Direct Antenna Modulation using Frequency Selective Surfaces

Stephen David Henthorn

A thesis presented for the degree of
Doctor of Philosophy in Engineering

The University of Sheffield
Faculty of Engineering
Department of Electronic and Electrical Engineering
July 2019

Acknowledgements

I am indebted to my supervisors Dr. Lee Ford and Professor Tim O'Farrell for the opportunity to carry out this research, as well as their continued support both academically and professionally. Thank you for all the opportunities you have pointed in my direction, I hope I made the best of them.

This work was funded by an EPSRC iCASE award, with industrial sponsors NEC Telecom Modus and BT Adastral. Many thanks to my industrial supervisors, Dr. Patricia Wells at NEC Telecom Modus and Mike Fitch at BT Adastral, for their input and guidance on this project. Further thanks go to all the people at NEC Telecom Modus who gave their insight and helped direct the project. Thanks also go to Simon Fletcher, now of Real Wireless, who was instrumental in the creation of this iCASE award.

This project is also affiliated with the EPSRC funded FARAD project, with academic partners at the University of Bristol, and industrial partners NEC Telecom Modus, Thales Ltd, uBlox UK Ltd, Mobile VCE, Orange Corporate Services Ltd, Cascoda Limited, Chemring Technology Solutions, Fujitsu and Harada Industries (Europe) Ltd. Many thanks to the organisers of the industrial-academic seminars for allowing me time to share my research at these events, and all of the delegates from all institutions for their helpful comments and guidance.

I also thank my family, who have always been a support when I need it. I apologise for continuing to fulfil their prediction that I would go to University and never leave. My greatest thanks go to my fiancée Emily, who has been a tireless support day in and day out through all the changing scenes of the past few years, in trouble and in joy.

Abstract

In the coming years, the number of connected wireless devices will increase dramatically, expanding the Internet of Things (IoT). It is likely that much of this capacity will come from network densification. However, base stations are inefficient and expensive, particularly the downlink transmitters. The main cause of this is the power amplifier (PA), which must amplify complex signals, so are expensive and often only 30% efficient. As such, the cost of densifying cellular networks is high.

This thesis aims to overcome this problem through codesign of a low complexity, energy efficient transmitter through electromagnetic design; and a waveform which leverages the advantages and mitigates the disadvantages of the new technology, while being suitable for supporting IoT devices. Direct antenna modulation (DAM) is a low complexity transmitter architecture, where modulation occurs at the antenna at transmit power. This means a non-linear PA can efficiently amplify the carrier wave without added distortion.

Frequency selective surface (FSS) are presented here as potential phase modulators for DAM transmitters. The theory of operation is discussed, and a prototype DAM for QPSK modulation is simulated, designed and tested. Next, the design process for a continuous phase modulating antenna is explored. Simulations and measurement are used to fully characterise a prototype, and it is implemented in a line-of-sight end-to-end communications system, demonstrating BPSK, QPSK and 8-PSK.

Due to the favourable effects of spread spectrum signalling on FSS DAM performance, cyclic prefix direct sequence spread spectrum (CPDSSS) is developed. Conventional spreading techniques are extended using a cyclic prefix, making multipath interference entirely defined by the periodic autocorrelation of the sequence used. This is demonstrated analytically, through simulation and with experiments. Finally, CPDSSS is implemented using FSS DAM, demonstrating the potential of this new low cost, low complexity transmitter with CPDSSS as a scalable solution to IoT connectivity.

Contents

List of Figures

List of Tables

List of Abbreviations

ADC	analogue to digital converter.
AM	amplitude modulation.
ASK	amplitude shift keying.
AWGN	additive white Gaussian noise.
BER	bit error rate.
BFSK	binary frequency shift keying.
BPSK	binary phase shift keying.
BS	base stations.
BST	barium strontium titanate.
CP	cyclic prefix.
CPDSSS	cyclic prefix direct sequence spread spectrum.
CSI	channel state information.
CSK	code shift keying.
CW	continuous wave.
DAC	digital to analogue converter.
DAM	direct antenna modulation.
DBPSK	differential binary phase shift keying.
DC	direct current.
DSSS	direct sequence spread spectrum.
EDGE	Enhanced Data for GSM Evolution.
EM	electromagnetic.
ES-OOK	energy synchronous on-off keying.
ESR	equivalent series resistance.
FFT	fast Fourier transform.

FSK	frequency shift keying.
FSS	frequency selective surface.
GPIB	general purpose information bus.
GPRS	General Packet Radio Services.
InterSI	intersymbol interference.
IntraSI	intrasymbol interference.
IoT	Internet of Things.
LoRaWAN	Long Range Wireless Access Network.
LoS	line of sight.
LPWAN	low power wide area network.
LR-WPAN	low range wireless personal access network.
MF	merit factor.
MIMO	multiple-in multiple-out.
m-MIMO	massive multiple-in multiple-out.
mmWave	millimetre wave.
MRC	maximum ratio combining.
NF-DAM	near-field direct antenna modulation.
OFDM	orthogonal frequency division multiplexing.
OFDMA	orthogonal frequency division multiple access.
OOK	on-off keying.
PA	power amplifier.
PAPR	peak-to-average power ratio.
PCB	printed circuit board.
PER	packet error rate.
PG	processing gain.
PSK	phase shift keying.
PWM	pulse width modulation.
QAM	quadrature amplitude modulation.
QPSK	quadrature phase shift keying.

RCS	radar cross section.
RF	radio frequency.
RMA	random multiple access.
RPMA	random phase multiple access.
SC-FDMA	single carrier frequency division multiple access.
SNR	signal to noise ratio.
TDD	time division duplexing.
TDMA	time division multiple access.
UMTS	Universal Mobile Telecommunications System.
UNB	ultra-narrowband.
UWB	ultra-wideband.
VHF	very high frequency.

List of Notation

α_l	Fading amplitude of lth path of channel.
A	Transmitted amplitude of message.
$A(\Lambda)$	Aperiodic autocorrelation with offset Λ.
B_c	Capacitive susceptance.
b_k	kth bit in bit stream.
c	Speed of light.
$\boldsymbol{c}$	Sequence vector.
C_{FSS}	Equivalent capacitance of FSS.
c_k	kth element of sequence vector.
C_v	Variable capacitance.
d	Distance between FSS layers.
δ	Loss angle of dielectric.
Δf	Difference between injected frequencies.
D_{max}	Maximum directivity.
e	Exponential constant.
E	Energy in autocorrelation sidelobes.
E_b	Signal energy per bit.
ϵ_{eff}	Effective relative permittivity.
ϵ_r	Relative permittivity.
F	Spreading factor.
f_0	Resonant frequency.
f_c	Carrier frequency (Hz).
g	Loop unit cell aperture width.

G	Gain.
G_r	Gain of receive antenna.
G_t	Gain of transmit antenna.
$\boldsymbol{h}$	Stationary channel vector.
h_I	In-phase component of channel.
h_Q	Quadrature-phase component of channel.
j	Imagninary unit.
K	Number of FSS unit cells in x direction.
l	Path l channel impulse response.
L	Number of channel paths.
Λ	Code offset.
L_{cav}	Length of waveguide antenna.
L_{FSS}	Equivalent inducance of FSS.
l_{probe}	Length of probe injecting energy into cavity.
L_v	Parasitic inductance of variable capacitor.
M	Number of FSS unit cells in y direction.
MF	Autocorrelation merit factor.
M_{mod}	Number of constellation points in modulation.
$n(t)$	Complex noise.
$\mathcal{N}(\mu, \sigma^2)$	Normal or Gaussian distribution with mean μ and variance σ^2.
N	Length of spreading sequence.
N_0	Spectral noise density.
η_a	Antenna efficiency.
n_b	Number of bits in a packet.
n_c	Number of chips in a packet.
N_{layers}	Number of FSS layers.
n_p	Number of pilot chips in a packet.
n_a	Number of postamble chips in a packet.
p	Unit cell periodicity.

ϕ	Phase change due to FSS.
P_{ep}	Packet error rate.
P_{in}	Power injected into antenna.
ϕ_l	Fading phase of lth path of channel.
ϕ_m	Phase of transmitted message.
P_r	Received signal power.
P_t	Signal transmit power.
$P_{T_b}(.)$	Pulse shaping function.
Q	Cyclic prefix length.
$r(t)$	Received baseband signal.
R	Distance between transmit and receive antennas.
$\Re(x)$	Real part of x.
R_v	Parasitic resistance of variable capacitor.
s	Loop unit cell inner patch dimension.
σ^2	Variance of distribution.
S	System throughput.
s_I	In-phase signal component.
S_{mn}	Scattering parameter describing power wave out of port m due to power wave incident on port n.
s_Q	Quadrature-phase signal component.
t	Time.
τ_l	Delay of lth fading path.
$\tan\delta$	Loss tangent of dielectric.
θ_c	Phase of pulse shaping or code sequence $\boldsymbol{c}$.
T_c	Chip duration.
T_{data}	Time duration of data section within a packet.
θ_n	Phase of symbol n.
$\mathrm{rect}(x)$	Rectangular function of x.
T_{packet}	Time duration of a packet.
T_s	Symbol duration.
t_{sub}	FSS substrate thickness.

$u(t)$	Complex baseband signal.
μ	Mean of distribution.
$v(t)$	Received signal envelope.
V	Bias voltage across diodes.
w	Unit cell element width.
W	Width of waveguide antenna.
$\boldsymbol{W}$	Periodic autocorrelation matrix.
ω_c	Angular carrier frequency (rads^{-1}).
$W(\Lambda)$	Periodic autocorrelation with offset Λ.
X	Number of 1s in a given binary sequence.
X_L	Inductive reactance.
λ	Wavelength.
Y	Number of 0s in a given binary sequence.
λ_0	Wavelength in free space.
λ_c	Wavelength in a given cavity.
λ_g	Wavelength in a given waveguide.
z	Decision variable.
$*$	Convolution operator.
$[\cdot]^H$	Hermitian transpose.

Chapter 1

Introduction

Since the rapid expansion in the number of wireless devices in the 1990s and 2000s, the amount of data sent over wireless channels has increased exponentially. Between 2011 and 2016 alone, the amount of global mobile data traffic increased by eighteen times according to CISCO, and the same company expects this to increase by a further seven times by 2021 [1]. In addition to this, the number of connected devices worldwide is predicted to reach over 35 billion by 2021, according to IHS [2]. This is driven by the Internet of Things (IoT), which aims to utilise connected objects and sensors for applications that require real-time monitoring, large-scale data collection, or remote and automated control [3].

In order to support these large increases in data and device capacity, new technologies are being developed, often under the collective label of 5G [4, 5]. These future wireless networks must make use of many different established and emerging technologies, including the use of millimetre wave (mmWave) frequencies for high-bandwidth transmission [6]; the expansion of the number of transmit and receive antennas in schemes known as massive multiple-in multiple-out (m-MIMO), which allows capacity increase through spatial multiplexing, spatial coding and diversity gain [7–10]; specific IoT protocols for supporting large numbers of devices with low data rate and latency requirements [11]; and finally network densification, increasing the number of base stations (BS) serving mobile devices [12, 13].

It is this final approach that is the most important and universal: the majority of capacity gain is expected to come from densification of the network [12]. However, this increases the importance of base station installation and energy costs, and presents opportunities for new technologies which may reduce these costs [14, 15]. The research presented in this thesis is drawn from the idea that these implementation issues with wireless communications systems may be solved through cooperation with neighbouring disciplines, in particular electromagnetics. This thesis presents the first in-depth study of one emerging technology in electromagnetics, direct antenna modulation (DAM) using frequency selective surfaces (FSS), and its application to wireless communications. DAM, where modulation occurs at the antenna at transmit power rather than in radio frequency (RF) electronics at low power, has been proposed previously for several specialised applications: for example allowing low profile antennas to transmit simple ultra-wideband (UWB) signals for on-body communications [16]; and producing direction-dependent modulation for improved physical layer security [17]. FSS are two-dimensional metamaterials which act as a frequency selective filter for incident electromagnetic waves. They are an established technology, used in situations as diverse as radar absorbers, reconfigurable antennas and scrambling mobile signals [18–20]. This thesis uses bandpass reconfigurable FSS to modulate the phase of a single-frequency carrier wave, producing phase shift keying (PSK) or continuous phase modulation.

FSS DAM as a technology has the potential to simplify base station transmitters, by replacing much of the RF electronics with a more complex antenna controlled at baseband, and by reducing the strain on the power amplifier (PA). In a conventional transmitter, the PA must amplify the whole modulated signal, so the PA must be linear to avoid distortion of the signal [21]. This distortion occurs, in typical class AB amplifiers, because the PA reaches saturation as it approaches its maximum output power (Fig. 1.1a), so peaky signals are not linearly amplified, and intermodulation products produce unwanted out-of-band radiation. As such, the PA is often operated at backoff from its saturation point, usually by the peak-to-average power ratio (PAPR) of the input signal, to ensure linear amplification of the signal. However, the PA becomes less efficient as back-off increases, as shown in Fig. 1.1b [22]. With contemporary waveforms, this back-off can be as much as 10dB, leading to average efficiencies of 30% even when digital pre-distortion techniques are used [23]. This can reduce to below 10% when they are not. In contrast, a PA in a DAM transmitter only amplifies the carrier wave, meaning a class D amplifier, with a theoretical maximum efficiency of 100%, can be operated in its non-linear region without distorting the signal [24]. This suggests that FSS DAM could be a simple, low-loss, energy efficient transmitter technology. This energy efficiency is of particular use in IoT applications, where there is expected to be hundreds of thousands of device connections per square kilometre [5]. As such, many BS will be required, increasing the energy cost of operation, unless energy efficiency is improved.

Many IoT schemes, such as Long Range Wireless Access Network (LoRaWAN) and Ingenu [25, 26], utilise some form of spread spectrum technique, where the transmitted bandwidth is greater than the message bandwidth [27]. This is often used to support multiple devices in the same channel; to overcome the limitations of fading in a wireless channel; and to provide interference rejection, which allows their use in unlicensed bands. FSS DAM lends itself well to spread spectrum techniques, as the signal bandwidth produced is limited only by the switching rate of the reconfigurable FSS, which theoretically can be in the order of 10s of MHz. In wideband fading channels, where copies of each transmitted symbol arrive at the receiver at delays greater than the length of each symbol, long spreading codes must

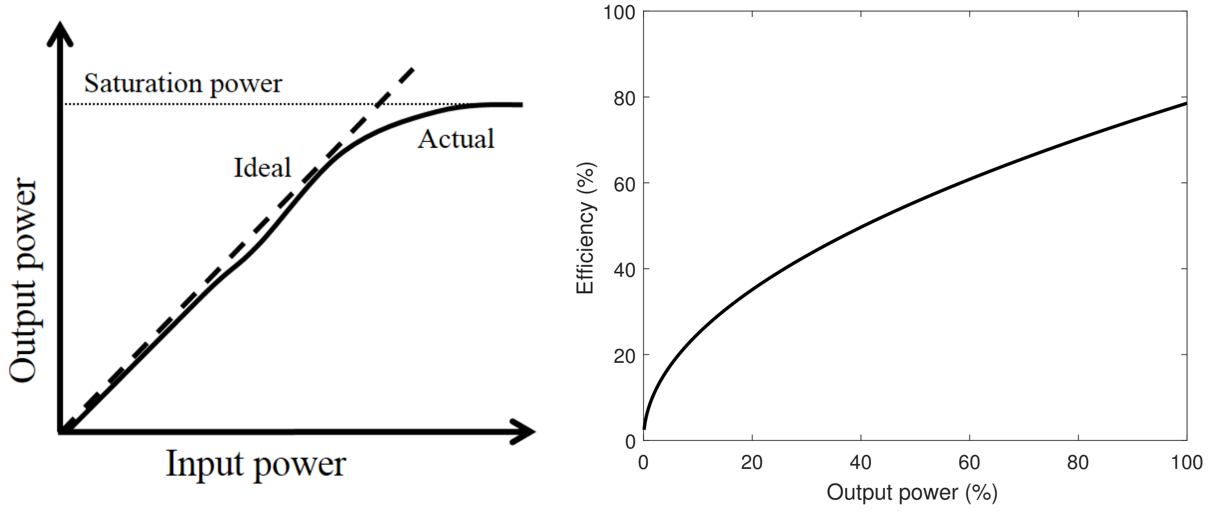

(a) (b)

Figure 1.1: (a) Output versus input power, and (b) Theoretical efficiency versus output power, of a class AB power amplifier

be used to overcome this interference, meaning the signal bandwidth must be many times greater than the message bandwidth, limiting throughput. The end of this thesis presents cyclic prefix direct sequence spread spectrum (CPDSSS), where the spreading sequence is a short code extended cyclically by the length of the wideband channel, analogous to a cyclic prefix (CP) being added to the start of each spread symbol. At the receiver, the CP is discarded, meaning each spread symbol is only distorted by copies of itself, not by the copies of preceding symbols. This means the interference experienced by each symbol is determined by the periodic autocorrelation function of the code, rather than being statistically dependent on the value of the preceding symbol and the aperiodic autocorrelation function of the code. Further, the periodic autocorrelation of some well-known codes are perfect, meaning that the interference of wideband fading can be removed entirely, while still benefiting from the time diversity of using a wideband signal.

In this thesis, FSS DAM units will be designed, simulated, fabricated and measured, being evaluated as antennas. They will also be implemented in simple end-to-end communications systems to explore their performance as transmitters. Comparisons will be made with the capabilities of current IoT communications protocols, and against other DAM technologies. A mathematical analysis of CPDSSS for IoT communications will then be provided, followed by exploration through simulation and experimental implementation using a conventional transmitter to validate the technique. Finally, the technique's use with an FSS DAM transmitter will be examined experimentally, demonstrating the novel technology with a new IoT transmission technique.

1.1 Motivation and objectives

1.1.1 Aims

This research aimed to demonstrate and implement Direct Antenna Modulation (DAM) using Frequency Selective Surfaces (FSS) as a solution for Internet of Things (IoT) downlink transmitters. In particular, continuous phase modulation with FSS DAM was targeted. A new IoT waveform, suitable for leveraging the advantages of FSS DAM while mitigating its weaknesses, should also be codesigned with the DAM unit to provide a complete solution.

1.1.2 Motivation

The number of connected devices is expected to increase dramatically over the coming years. There are many emerging approaches to this problem, such as standards based on coexisting with increasingly dense mobile cellular networks, and technologies supporting tens to hundreds of thousands of devices over large areas. However these are, respectively, expensive and reliant on mobile networks, and not scalable with ever increasing numbers of devices. As such, there is space for a new technology using low cost wireless access points for dense IoT networks. DAM has the potential to reduce the complexity and improve the energy efficiency of transmitters at these wireless access points significantly, by modulating after amplification to improve PA efficiency and remove much RF circuitry. In particular, the new technology presented here of FSS DAM could, through codesign of a new IoT waveform designed to leverage the advantages and mitigate the disadvantages of FSS DAM, provide the low cost, energy efficient transmitters required for scalable, affordable and dense IoT networks.

1.1.3 Objectives

The key objectives of this research were as follows:

1. ***Design and test QPSK FSS DAM:*** As a proof-of-concept, the first objective was to demonstrate that FSS DAM was capable of quadrature phase shift keying (QPSK) modulation. The FSS and antenna designs should be simulated, fabricated and measured, and then tested in an end-to-end communications system.

2. ***Characterise continuous phase FSS DAM:*** A fully operational FSS DAM unit capable of continuous phase modulation should be produced. The design principles should be examined with both theory and simulation. The final FSS unit should be fully characterised as an antenna and as a modulator, and again implemented in

an end-to-end communications system. Its suitability for IoT deployment should be assessed.

3. ***Explore CPDSSS for DAM transmission in IoT:*** Many waveforms have been developed to connect large numbers of devices requiring only low data rates, but the simplicity of DAM technology may restrict their use. FSS DAM may lend itself to variations on spread spectrum techniques, which may be particularly useful for transmitting data reliably in highly dispersive channels. The performance of these newly developed techniques should be investigated analytically, through simulation and through measurement, with both conventional modulation and with FSS DAM.

1.2 Original contributions

This research has made the following original contributions:

1. The design, fabrication and characterisation of an FSS DAM unit capable of producing QPSK modulation. The DAM unit was shown to be able to produce QPSK through simulation and measurement in an anechoic chamber. This was then used to build the first end-to-end communications system using FSS DAM, in a line-of-sight channel.

2. The full characterisation of the first continuous phase FSS DAM unit. The effects of all design questions for FSS DAM have been explored using simulation, and a prototype was fabricated and measured. This was then implemented in an end-to-end communications system to transmit data with binary phase shift keying (BPSK), QPSK and 8PSK modulation.

3. CPDSSS is introduced as an adaptation of spread spectrum techniques, which reduces the effects of frequency selective fading by using a cyclic prefix to protect each spread symbol. The scheme is analysed mathematically, and then validated with simulation and experimental implementation using a channel emulator.

4. CPDSSS is used with FSS DAM as a potential low-cost, energy efficient transmission scheme for Internet of Things applications. This is explored through experimentation.

1.3 Publications and engagement

1.3.1 Journal papers

1. S. Henthorn, K. L. Ford, and T. O'Farrell, "Bit error rate performance of quadrature modulation transmission using reconfigurable frequency selective surfaces," *IEEE*

Antennas and Wireless Propagation Letters, vol. PP, no. 99, pp. 1–1, 2017.

2. S. Henthorn, K. L. Ford, and T. O'Farrell, "Direct antenna modulation for high-order phase shift keying," *IEEE Transactions on Antennas and Propagation*, (Under Review)

1.3.2 Conference papers

1. S. Henthorn, K. L. Ford, and T. O'Farrell, "Frequency selective surface loaded antenna for direct antenna modulation," in *2017 11th European Conference on Antennas and Propagation (EUCAP)*, March 2017, pp. 731–734.
2. S. Henthorn, K. L. Ford and T. O'Farrell, "A low-loss reconfigurable frequency selective surface based antenna for direct antenna modulation," Loughborough Antennas & Propagation Conference (LAPC 2017), Loughborough, November 2017, pp. 1-4. (2nd Prize for Student Paper)
3. S. Henthorn, K. L. Ford, and T. O'Farrell, "A low–complexity array of directly phase modulating antennas," 12th European Conference on Antennas and Propagation (EUCAP), London, March 2018.
4. S. Henthorn, K. L. Ford, and T. O'Farrell, "Direct antenna modulation with frequency selective surfaces," 5th Colloquium on Antennas, Wireless and Electromagnetics (CAWE 2017), London, June 2017.

1.3.3 Further engagement

1. EPSRC Connected Nation Pioneers: Finalist in Intelligent Informatics category, 2018.
2. Demonstration at Fifth International Workshop on Next Generation Green Wireless Networks, 2018.
3. Demonstration at Innovate UK Knowledge Transfer Network: Advances in Metamaterials Workshop and Showcase, Solihull, March 2019.
4. Presentation at IET Antennas and Propagation for 5G and Beyond conference, Birmingham, February 2019.
5. Poster presentation at IEEE 5G Summit, Glasgow, May 2018.
6. Presentations at academic/industrial meetings for EPSRC FARAD project.

1.4 Outline of thesis

This thesis is composed of eight chapters. The first, this chapter, consists of an introduction to the research, including current trends in wireless communications, the research motivation, and aims and objectives for this thesis. Original contributions of this thesis are also detailed, along with publications to date. Next, important theoretical background for this thesis will be outlined in Chapter 2. This consists of a brief historical discussion of wireless transmitters, a discussion of the operation of FSS from an electromagnetics perspective, and an introduction to simple wireless communications systems, including spread spectrum as a solution to channel conditions. Chapter 3 is a literature review, which sets the space for the contribution of this thesis by discussing state-of-the-art DAM and IoT technologies, and demonstrates that the potential of low complexity, energy efficient DAM transmitters has yet to be exploited in IoT technology.

FSS DAM will then have its first full implementation discussed in Chapter 4, where a prototype QPSK modulating antenna is presented, simulated, fabricated, measured, and finally tested in an end-to-end, line-of-sight communications system. Chapter 5 develops this prototype into a continuous phase FSS DAM, detailing the design processes and fully analysing the DAM unit. A prototype DAM unit is then fabricated, measured, and tested in a line-of-sight communications system, producing BPSK, QPSK and 8PSK modulation. CPDSSS is fully introduced in Chapter 7, with full mathematical analysis, simulation, and experimental implementation with conventional modulation techniques. CPDSSS is then implemented using FSS DAM, and both simulation and experimental results are presented. Finally, conclusions of the thesis are drawn in Chapter 8.

Chapter 2

Background

2.1 Introduction

FSS DAM is a subject which straddles a number of neighbouring disciplines. The problem which this thesis is seeking to address is the scalability of Internet of Things (IoT) infrastructure, in particularly the energy and installation costs of base stations. As such, wireless communications theory is required to inform the reader on the challenges of transmitting information through the wireless channel, and some established approaches to this. Electromagnetics and antenna theory are here used to attempt to solve the complexity and inefficiency of conventional transmitters, which become increasingly problematic as networks densify, and provide a framework for the analysis of the operating principles of FSS and how they are used to produce modulation. Finally, RF circuit theory provides a comparison point with conventional transmitters as whole systems. This chapter will provide essential background on these areas; in particular the history of wireless transmitters, the fundamentals of FSS from an electromagnetics perspective, and finally an overview of communications theory and some modern techniques for data transmission over wireless channels.

2.2 Wireless transmitters and Direct Antenna Modulation

2.2.1 A historical view of wireless transmitters

The first radio transmitters, of the kind first experimentally demonstrated by Hertz [28] and commercialised by Marconi [29], produced radio waves by arcing current over a small spark gap. This was received as another spark, or an audible click, and interpreted by a trained operator. As such, these early transmitters were only suitable for wireless telegraphy, where information could be sent by Morse code. When the first attempts were made to

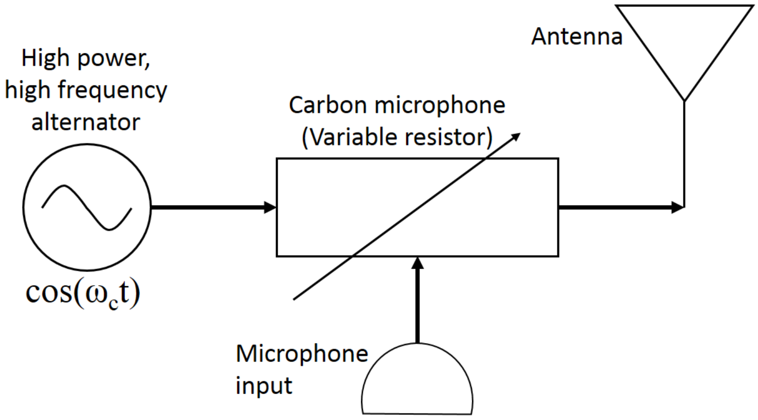

Figure 2.1: Fessenden's first CW AM transmitter

transmit audio using radio waves, these sparks alone were not able to carry this information. Fessenden realised that continuous wave (CW) radio signals would be required to carry such information, and implemented this first with a spark gap generator producing 20,000 sparks a second in 1904 [30], and then with an alternator producing true CW at 50kHz in 1906 [31]. He achieved amplitude modulation (AM) of the carrier by placing a carbon microphone in the transmission line, just before the transmit antenna, as shown in Fig. 2.1. Vibrations from a person speaking into the microphone varied the carbon's resistance, modulating the carrier wave passing through it. As such, the first wireless telephony was achieved by modulating at transmit power.

However, this came at a cost. In order to transmit at the kilowatts of power then required to make wireless telephony practical, the carbon microphone had to be submerged in cooling fluid, the transmit power was limited compared with wireless telegraphy, and the process was relatively inefficient. As such, when de Forest invented the three-input vacuum tube in 1908 and found it to be an effective radio frequency amplifier, the clear choice was to modulate at low power, where there was no need for cooling of the microphone, and then amplify the modulated signal [32].

Today, the majority of transmitters have been variations on this basic architecture. A conventional modern transmitter, using quadrature modulation and solid-state, semiconductor power amplifiers (PAs) is shown in Fig. 2.2a. In this architecture, the modulated signal must be amplified, radiate from an antenna and finally propagate through a channel with minimal distortion. While this form of transmitter has endured and been adapted for a variety of communications systems, amplifying the modulated signal places a restrictive requirement on the amplification stage. Increasingly, many modern communications systems use waveforms which have large peak-to-average power ratios (PAPRs) and large bandwidths [24].

To avoid distorting the signal, the PA must amplify all input levels in a linear fashion.

Often, this involves backing off the PA operating point from its maximum power to avoid the output being compressed and distorted, at the cost of reducing efficiency significantly (Fig. 1.1b). Two reduce the amount of back-off required, two main approaches have been followed. First, many PA designs have been introduced to improve efficiency, such as the Doherty amplifier, which uses a separate amplifier to produce the highest power outputs [33]. However, this comes at the cost of increased complexity and limited bandwidths. The second approach is to pre-distort the input signal around the compression point to allow operation at reduced back-off without producing a distorted output [34]. This can either be done in analogue RF circuitry, which has a limited bandwidth, or in the digital baseband. This second approach, however, often requires feedback to baseband of the distorted signal, including a digital demodulator, increasing the complexity of the transmitter significantly. As such, despite being able to reduce back-off by between 3dB and 6dB, they are often used only in large transmitters where the PA and cooling equipment account for more than 50% of the BS power output [35].

In all, this means the PAs used in wireless communications systems are often expensive and inefficient [35], increasing both the installation and operating costs for the transmitter. As such, the affordability of network densification is currently limited by the efficiency and initial cost of the PA.

2.2.2 Direct Antenna Modulation

In recent years, researchers have proposed moving away from conventional transmitter architectures in order to allow efficient, high bandwidth wireless communication. The problems faced by Fessenden's carbon microphone have been overcome to allow modulation to occur at or near the antenna in DAM transmitters, as shown in Fig. 2.2b. The CW carrier wave is amplified using a PA, then modulated at transmit power.

The principle benefits of DAM are from the PA running in its non-linear region without added distortion, improving the overall efficiency. Typical PA backoff for PSK signals is 3dB [22], meaning for a typical class AB radio frequency (RF) amplifier, the theoretical efficiency would be approximately 56% (Fig. 1.1b). Using a non-linear class D amplifier instead, which has a theoretical efficiency of 100%, reduces the amount of power wasted in the PA by 44%. The need for cooling of the PA will also be significantly reduced [24]. Further, the amount of RF electronics, such as mixers, filters and intermediate amplifiers, is reduced significantly, and replaced with some electronics operating at the symbol rate. This reduces the total size and power consumption of the transmitter. A number of approaches to DAM are now discussed.

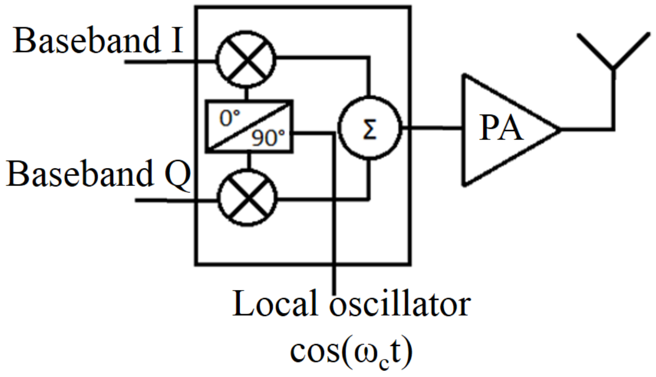

(a)

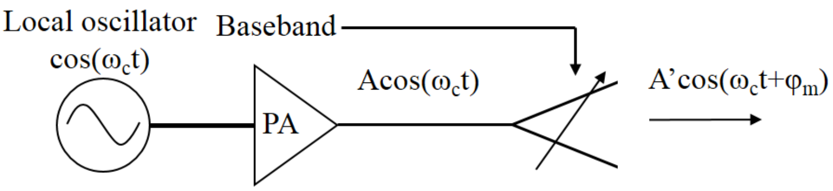

(b)

Figure 2.2: (a) Block diagram of a conventional homodyne quadrature transmitter, (b) Concept diagram of a DAM transmitter

DAM and efficiency

One of the key advantages of most DAM techniques is the improvement in PA efficiency, so a discussion of how to measure the efficiency of DAM transmitters is necessary. As the process of modulation, and with it much of the complexity, is moved from before the PA to after it, the majority of losses occur after the PA rather than within it. Because of this the PA, which will have an efficiency greater than 90%, will be assumed to be lossless. This is a fair comparison with the conventional PA efficiency models used as benchmarks, which do not take into account either component losses or cooling losses, but only the theoretical inefficiencies due to their mode of operation and use of back-off [35].

Instead, in most DAM techniques the losses can be considered to occur in the antenna. As such, the transmitter efficiency is approximately the antenna efficiency η_a. It could be argued that the antenna gain G, which is a measure of the amount of energy transmitted in the desired direction by an antenna, is a more useful measure of performance for DAM techniques. However, it then becomes difficult to compare with conventional transmitters, which could use an antenna with large gain without it being useful to say that it enhances the transmitter performance. Secondly, the DAM unit could be designed in ways that enhance the gain without improving its efficiency. This is because

$$G = D_{max}\eta_a \tag{2.1}$$

where D_{max} is the maximum directivity of an antenna, which can be increased by increasing the aperture of an antenna amongst other techniques. As such, while the gain will be given throughout this thesis and is an important parameter, the antenna efficiency is the key metric.

The measurement of η_a should also be considered. As suggested by Equation 2.1, the most accurate way to find it is to measure the antenna gain and directivity. Gain is easily found through the comparison technique, where the received power with the antenna under test is compared with the received power when an antenna with known gain is used [36]. However, calculation of the antenna directivity requires full measurement of the energy transmitted in all directions by the antenna, which may be difficult with bulk devices. While other approaches have been suggested, they all trade accuracy for ease of measurement.

As such, this thesis will use simulated efficiencies in CST, where available, to evaluate performance. These include losses from impedance mismatch, resistance in active devices and dielectric losses. However, the simulations will ignore ohmic losses in conductors, which are assumed to be minimal. Further, their accuracy relies on the models of active components provided by manufacturers. In all, they will supply a reasonable measure of the performance of DAM transmitters in comparison with conventional approaches.

DAM with integrated switches

Some of the first implementations of DAM were achieved by integrating active devices into antennas. One of the first to demonstrate this was [37], using a patch antenna with an integrated Schottky diode. The diode was formed by fabricating the patch antenna onto an appropriately doped silicon substrate. Switching the diode allows time-domain modulation of a CW carrier radiating from the patch, which the paper demonstrates with square wave modulation. This antenna is also able to receive similarly modulated incoming signals. This antenna was designed to operate at carrier frequency 10GHz.

The principle is further examined in [38], where the possibility of using such time-domain modulation to operate at bandwidths beyond those normally achievable with high Q antennas, such as patch antennas, is explored. Again pulse modulation is the only type explored, but fast switching rates allow data transmission in the order of 100s Mbit/s, well beyond what could normally be transmitted by a narrowband patch antenna, at a carrier frequency of 2.4GHz. It also achieves this while only amplifying a single frequency carrier, allowing more efficient operation. A similar approach is taken in [39], though here a physical varactor diode is soldered onto the microstrip feed of a patch antenna. Biasing of this diode allows tuning of the antenna's S_{11}, causing amplitude modulation of the signal as the narrowband resonance of the antenna moves away from the carrier wave passing through it. This technique was demonstrated at 2.45GHz with symbol rates of 1Mbit/s.

Another switched patch antenna technique for producing DAM is discussed in [16, 40]. PIN diodes - which are a semiconductor device consisting of P-type, Intrinsic and N-type material in that configuration and can act as a variable resistor or switch - are connected between the corners of a patch antenna and the ground plane. When they are unbiased they have very high resistance, so the antenna radiates as expected at the resonant frequency of 1.5GHz. However, when a 0.8V biasing signal is applied to the diodes, their resistance drops, shorting the patch and preventing it from radiating. This is simulated in [16], and then demonstrated experimentally in [40], producing amplitude modulated signals at up to 300MHz. However, beyond 200MHz the narrowband nature of the antenna starts to impair the transmitted signal, though this is still over two times greater than could be transmitted with a conventional amplitude modulation scheme and a patch antenna.

Other than diodes, some more exotic devices have been used in combination with patch antennas to achieve DAM. Reference [41] uses two memristors, the recently discovered fourth passive circuit element. The resistance of a memristor is determined by the previous resistance of the device, so it can be said to have memory. When the memristor is excited by a voltage signal its resistance changes, then returns to its original state some time after the voltage signal has stopped. When connected between the corners of a patch antenna and the ground, as PIN diodes were in [40], this change in resistance again causes the antenna to change its resonance. Due to the properties of the memristor, it was found that the amplitude modulation produced at 200MHz with a 1.45GHz carrier was less distorted than that produced using PIN diodes in the same setup.

This technique was then implemented in a full end-to-end communications system in [42], using PIN diodes as shown in Fig. 2.3a. It defines the modulation produced by the switching antennas as on-off keying (OOK), with some adjustment for the non-zero radiation in the 'off' configuration. The large baseband biasing signal is fed into the antenna at the same port as the RF carrier wave, which has significantly smaller amplitude. The DAM unit was designed to operate at 1GHz, and was demonstrated with a 5MHz OOK signal, producing a bit error rate (BER) with 2dB degradation over conventional OOK modulation at 10^{-3} error rate. Simulation in this work suggests that operation at 100MHz would produce unacceptable BER performance due to intersymbol interference (InterSI) from the finite time required for the antenna to charge when switching to the 'on' configuration. This challenges the potential advantages of using this technique, as operation beyond the bandwidth of the antenna is required for any performance gains over conventional modulation in this format.

A further development of this technique is energy synchronous on-off keying (ES-OOK) [43]. The switching may occur either within the antenna, as previously discussed, or in the RF feed. The switches are turned on and off only at times when the angle of the RF is 0. It is shown through simulation that this technique would provide almost instantaneous OOK,

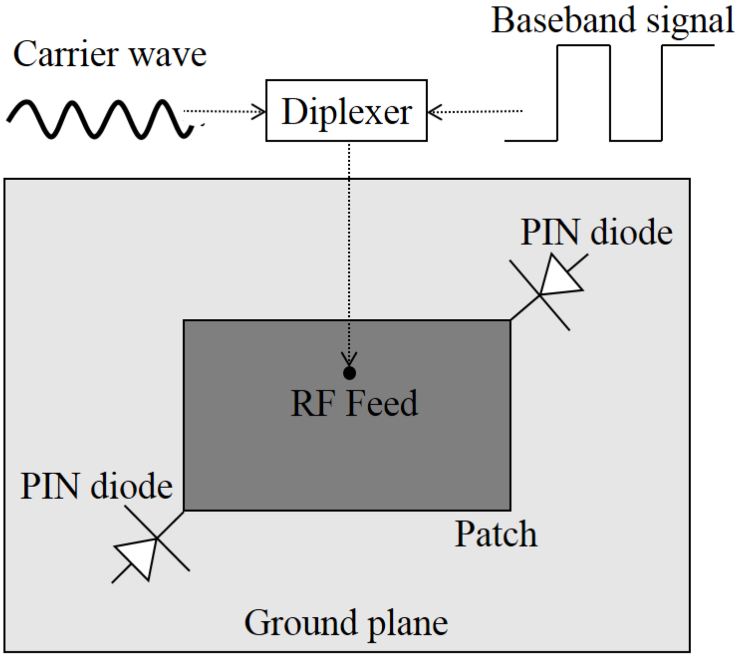

(a)

Figure 2.3: Diagram of integrated switch DAM [42]

as it prevents transients lasting significant amounts of time in the antenna and so causing InterSI.

The potential to operate at rates beyond the normal bandwidth of an antenna is particularly of interest to researchers looking to miniaturise antennas, as electrically small antennas tend to have narrower bandwidths. [44] introduces the concept of producing modulated RF using the transient characteristics of small antennas. As small antennas have high Q, they act as LC tank circuits. This circuit can then be charged by a switched capacitor, which is either being charged by a DC source, or discharging into the antenna. When the capacitor is charging and disconnected from the capacitor, it resonates at its own fundamental frequency, releasing its stored energy as RF at this frequency. When being charged by the capacitor, the resonant frequency is altered by this capacitor, causing transmission at a different frequency. This allows fast frequency shift keying (FSK) modulation to be produced in electrically small antennas. A 25MHz signal is produced at carrier frequencies 209MHz and 140MHz, far beyond the 400kHz bandwidth of the antenna.

This concept was further developed to allow amplitude modulation [45]. Two switches are used to control both the charging and discharging of the high Q antenna. As such, a pulse width modulation (PWM) signal may then be used to send arbitrary voltage levels across the capacitance within the antenna, allowing control of the transmitted amplitude. An analogue 1MHz signal was demonstrated on a 10MHz carrier wave from the electrically small antenna. This work also suggests using two such DAM units fed by the same pulse sequence, with a delay of a quarter of a pulse period, to produce circularly polarised QPSK modulation using this technique. This was not demonstrated here, however.

Recent advances in transistor technology have allowed shifting of the centre frequency of this form of DAM towards the very high frequency (VHF) range [46]. This work shows BFSK produced at a 50MHz carrier frequency with modulation rates at 10%. Further, efficiency performance is considered, giving 0.14%. While this is very small, it is at a similar level as a traditional electrically small antenna with a bandwidth 45 times smaller.

Near-field DAM (or Directional Modulation)

An alternative approach to DAM is near-field direct antenna modulation (NF-DAM), which was developed by Babakhani and Hajimiri [47]. This operates on the principle of varying the near-field environment of a passive driven element, in order to create arbitrary modulation at some point in the far-field. A key component of this approach is that, when some constellation is produced in a defined far-field direction, in other directions the constellation becomes distorted in ways that appear random. This adds physical layer security to point-to-point communications systems.

The first implementation of this was focussed on producing modulation at mm-wave, in order to overcome efficiency issues with amplifier design at these high frequencies [47]. A single driven dipole element, resonant at 60GHz, was designed, and surrounded by passive reflectors integrated with active components- either switches or varactors- in the same plane as the dipole feed. Changing the state of the switches and varactors alters the near-field of the driven element, causing changes in the farfield. With enough components, the setup is able to produce various constellation points in the complex plane. At 60GHz, the constructed reflectors are able to produce 20 constellation points, but all in the same quadrant of the complex plane. As such, a device for choosing the input phase to the driven element is used to determine the quadrant. The efficiency is also poor at around 1% due to losses in the substrate. However, the directional nature of the modulation produced by NF-DAM is proven [17]

Developing this technology, the same authors presented an implementation of NF-DAM at 2.4GHz, using two reflectors subdivided into sections by 11 and 8 MEMS switches, respectively [48]. This is used to again create 20 constellation points varying in amplitude and phase, though again in a single quadrant of the complex plane. The directionality of the modulation was again demonstrated. A full discussion of the achievable constellations using this technique is given in [49], demonstrating that the region of the complex plane available will always be limited with this technique.

To develop constellations using the whole complex plane, various researchers began using arrays of elements driven by the same RF source, but with some phase shift added inde-

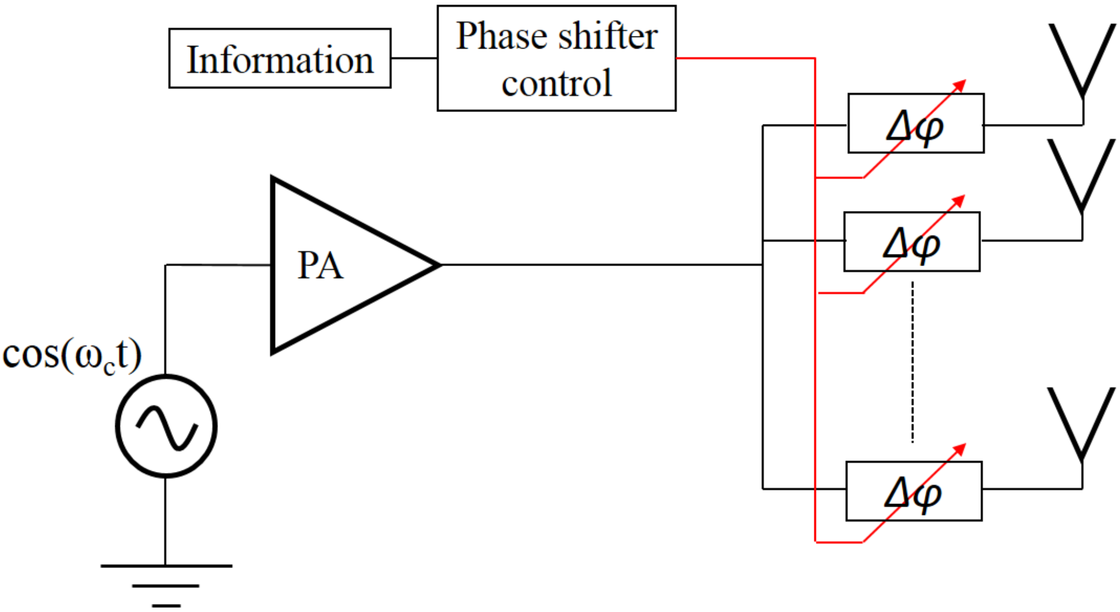

(a)

Figure 2.4: Diagram of generic driven NF-DAM transmitter

pendently to each element [50, 51] (Fig. 2.4a). Daly and Bernhard found that, where the patterns of the driven elements are known, the phase weighting on each required to produce a desired constellation point in some direction can be calculated [50]. This represented an advance over the switched reflectors discussed previously, which found their constellations through experimentation. This work simulated directional QPSK transmission using four elements at a carrier frequency of 7GHz, including BER measurements at different angles. Also discussed is a method for independently transmitting QPSK in different directions.

This concept was further developed by Shi and Tennant, who analysed the required number of elements needed to produce various constellation orders using two-bit diode phase shifters rather than continuous-phase ones [52]. This simplifies the implementation of this technique. Analysis of different orders of multi-directional independent modulation was also carried out. The authors also experimentally implemented a two-element active NF-DAM transmitter [51]. This was capable of producing non-standard 8- and 16-QAM modulation forms, covering the whole complex plane, and operated at 8.3GHz. Most recently, a two-element NF-DAM array has been implemented with continuous phase shifters at 2.45GHz comparing different methods of solving the equations to determine required phase shifts and producing QPSK modulation [53].

2.2.3 Metasurface modulation

Modulation using metamasurfaces, and in particular FSS, has been proposed previously. Kiani, Bird and Ford suggest that a transmissive FSS with integrated PIN diodes operating at high mm-Wave frequencies could be used to create amplitude shift keying (ASK) modulation [54]. Switching the diode from forward to reverse bias reduces the FSS transmission coefficient by 20dB at the operating frequency, allowing binary ASK modulation. The FSS is designed and simulated to operate at 60GHz, but no further work on the concept is presented. The work is developed to operate with switch MEMS gaining 30dB variation [55], and also extended to THz frequencies with design of a surface operational at 600GHz [56]. Again, no experimental implementation or exploration of this concept beyond simulation of the surface is presented.

Very recently, other approaches to using metasurfaces to produce modulation have been proposed. An electrically large single-layer reflective metasurface, with individual control of each unit cell, has been demonstrated to be able to produce various forms of modulation [57–59]. The first implementation was of binary frequency shift keying (BFSK), with each unit cell containing a single varactor diode controlled to produce one of four different values of phase shift [57]. The sum effect of all the unit cells produces the BFSK modulation, achieving symbol rates of 78.125 kSymbol/s. The surface used is electrically large, being $2.3\lambda \times 3.4\lambda$ at the 4GHz operating frequency, and requires a directive feeding horn, which in these experiments is placed 1.5m away from the surface.

An implementation producing QPSK modulation was then produced, with symbols rates of approximately 820 kSymbol/s claimed [58]. A single voltage is used to control all the unit cells equally, and it produces a distorted QPSK constellation, with the smallest constellation point 4dB smaller in magnitude than the largest. No BER performance is given to show the effect of this distorted constellation, or any losses in the surface given.

Most recently, an 8-PSK version of this reflective metasurface modulation has been presented [58] (Fig. 2.5). This implementation uses a 32×8 metasurface, with each unit cell containing two fixed capacitors and two varactor diodes (Fig. 2.5b). Each unit cell is biased by the same voltage to produce a single phase change of the whole incident plane wave. Maximum symbol rates of 4.096 MSymbol/s are shown, though with very high BERs of greater than 10^{-2}. BERs less than 10^{-3} are only achieved at symbol rates of 128 kSymbol/s, and this appears to be the error floor associated with this branch of metasurface modulation. Further, there is a 6dB difference in performance between using the metasurface as a modulator and using it as a conventional passive reflectarray. Only 0.7dB of this is due to loss in the surface, implying the rest of the loss is due to energy being directed in directions other than those intended, which may vary as the transmitted symbol varies. In addition to these losses, no account is given of losses due to imperfect illumination of the FSS by the horn antenna feed, where portions of the wave produced by the feed are not incident on the metasurface. Further, the effect of viewing angle on the modulation produced is not explored in any of the above papers.

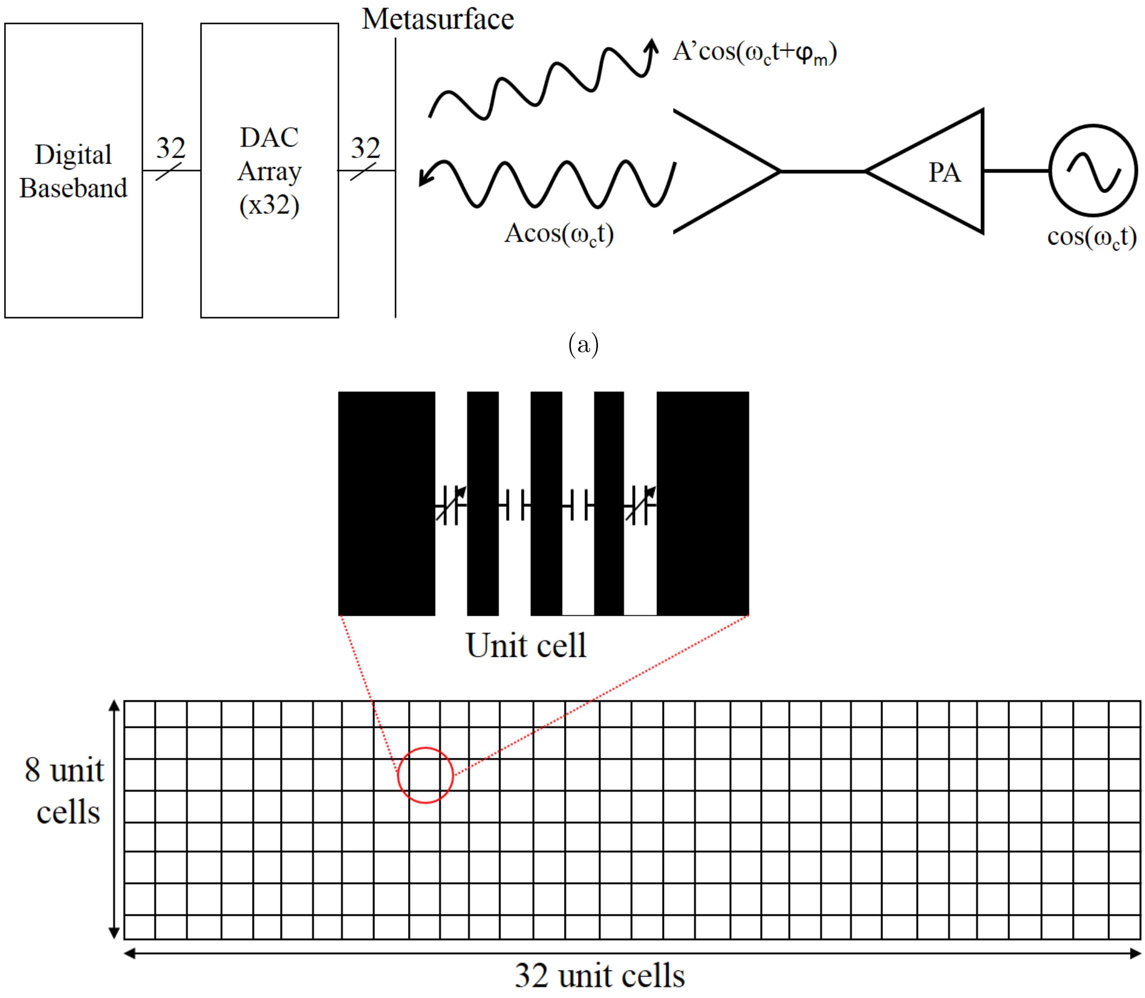

(a)

(b)

Figure 2.5: Diagram of 8-PSK reflective metasurface DAM transmitter [58], (a) Transmitter setup, (b) metasurface design

The state of the art - A comparison

Table 2.1 shows key metrics of state-of-the-art experimental implementations of each of the DAM techniques discussed in detail above. For integrated switches, the work of Srivastava and Adams, using a patch antenna with integrated PIN diodes, is considered [42]. This produces OOK with demonstration at 5 Mbit/s, though it is suggested that higher rates could be achieved with faster switching diodes. Other work has suggested QPSK modulation with switched small antennas, but these remain simulated only [45]. The efficiency is also not given, though due to the nature of using OOK, where the antenna will only be transmitting half the time, it is assumed that it will be less than 50% efficient.

As a point of comparison for near-field DAM, the work of Shi and Tennant producing directional QAM modulation at 8.3GHz provides a good description of the state-of-the-

DAM technique	Modulation format	Symbol rate (MSymbol/s)	Efficiency
Integrated switches [42]	OOK	5	<50%
Near-field [53]	directional QAM	0.1	63%
Reflective metasurface [59]	8PSK	2.048	25%

Table 2.1: Key metrics for experimentally implemented state-of-the-art DAM techniques

art [53]. The efficiency is calculated assuming that phase shifters with 2dB insertion loss were used to produce the constellation. Shi and Tennant do not discuss symbol rates, so the work of Daly et al, who showed QPSK NF-DAM transmitter operating at 100kSymbol/s, is used as a reference figure [50].

The state-of-the-art metasurface DAM is the most recently published work of Tie Jun Cui et al [59]. This produces an 8PSK constellation using a large reflective metasurface, operating at a carrier frequency of 4GHz. The maximum claimed symbol rate for transmission of data is 4.096 MSymbol/s, though this has a BER of around 3×10^{-2}. As such, the symbol rate of 2.048 MSymbol/s is used as a point of comparison, which is capable of reaching BERs of around 10^{-3}. The surface reflectivity is given as 85%, but while the BER of metasurface DAM is shown to perform equally with conventional modulation against the signal to noise ratio at the receiver, there is a 6dB performance drop when transmitted power is used as the variable. As such, it is assumed that this is a power loss of 6dB, giving an efficiency of 25%. Note that this ignores any possible losses from the imperfect illumination of the metasurface by the feed.

2.3 Frequency Selective Surfaces

2.3.1 Theory of operation

Metamaterials is a broad term for any material that has its properties, particularly its interaction with electromagnetic (EM) waves, determined by the design of the material rather than its chemical composition [60]. In particular, metamaterials are often composed of metallic (or magnetic) ‘subatoms’ of a given shape arranged in a non-metallic medium (Fig. 2.6). The geometry and placement of these subatoms determines the interaction of the metamaterial with EM waves, allowing control of the permittivity and permeability and so the refractive index of a material [61]. This has allowed the design of materials with negative or near-zero refractive indices [62], as well as other characteristics which do not occur naturally [63].

FSS are a subset of metamaterials, where the subatoms are metallic, two-dimensional, and repeat periodically on a two-dimensional surface (Fig. 2.7) [64]. The geometry of

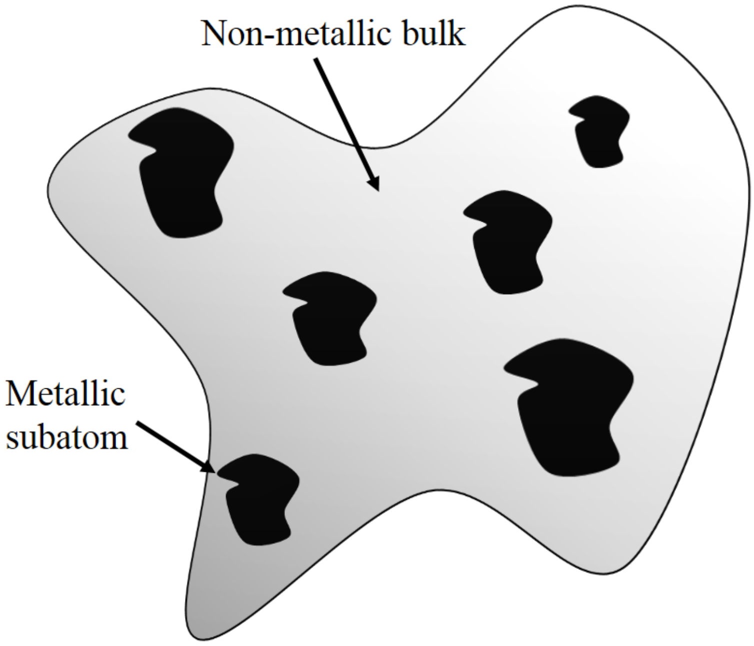

Figure 2.6: A generic metamaterial

the subatoms, conventionally referred to as the unit cell of the FSS, and the period of its repetition determines how the FSS interacts with incident EM waves. Their uses in practical applications includes artificial groundplanes for producing low profile directive antennas [65,66]; frequence selective reflectors for multiband reflectarrays [67–69]; and front-end filters in radomes for reducing the radar cross section (RCS) of radar systems and reducing out-of-band emissions. Recently, FSS have been integrated into waveguide antennas to control their RCS, particularly horn antennas. This is in order to take advantage of the filtering effects on received signals [70, 71].

The theory of operation of FSS can be seen with the simplest case, an infinite periodic array of infinitely long conducting strips in free space, aligned with the y axis (Fig. 2.8a) [72]. The strips are of width w and repeat with period p. An incident EM wave with normal incidence and its E-field parallel to the strips, in the y direction, will excite electrons in the conductor, causing currents to flow with the E-field along the strips. This is equivalent to a transmission line with the characteristic impedance of free space meeting a parallel inductance (Fig. 2.8b). The amount of energy reflected and transmitted by the surface is frequency dependent - at low frequencies the wave will be reflected, while at high frequencies it will be transmitted (Fig. 2.8c). As such, the surface is a high-pass filter with a corner frequency dependent on the equivalent inductance of the strips, with a larger inductance leading to a lower corner frequency. As with any conductor, the surface's inductance increases with greater p and smaller w, and decreases with smaller p and greater w. This can be inferred by the extreme cases - where p is very large or w is very small, the grating appears as mostly

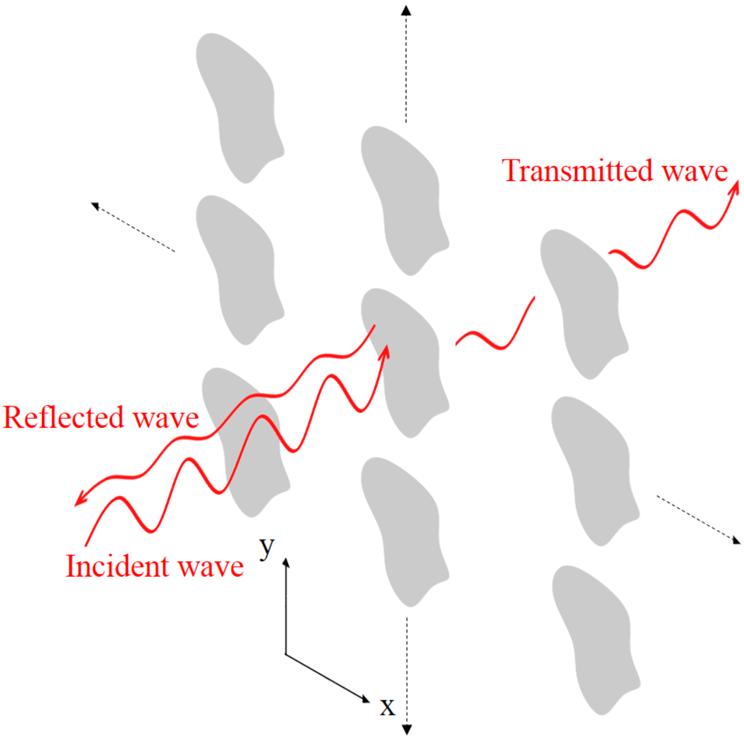

Figure 2.7: A generic frequency selective surface

free space so most frequencies will be transmitted; while a decreasing p or increasing w appears as an infinite conducting plane, which would reflect all frequencies.

Dividing the infinitely long strips into periodically repeating dipoles, as shown in Fig. 2.9a, alters the surface's behaviour. Each unit cell will be a conducting dipole of width w and length l, repeating along the x axis with period p_x and along the y axis with period p_y. An incident EM wave with the E-field aligned with the y axis will again excite electrons in the unit cells and cause currents. While the dipoles themselves can again be described as an inductance, the gaps between them introduce a capacitance in series with the inductance (Fig. 2.9b). This leads to a bandstop behaviour, where the incident wave is transmitted at low and high frequencies, but reflected at a central frequency where the impedance of the capacitive and inductive components are approximately equal (Fig. 2.9c). Note that the phase of the transmitted or reflected wave will also be altered by the FSS, as would be expected from an LC filter. As with any gap between conductors, the capacitance increases when the gap decreases (i.e. l increases and p_y decreases) and the area of the conductors separated by the gap increases (w increases). The dipole inductance behaves as in the strip grating scenario, though greater l also leads to greater inductance. This bandstop effect can also be considered as the incident wave being reflected when the array of patches is resonant, which again depends on the dipole geometry and periodicity.

In practice, the unit cell element can be almost any shape, which can vary depending on

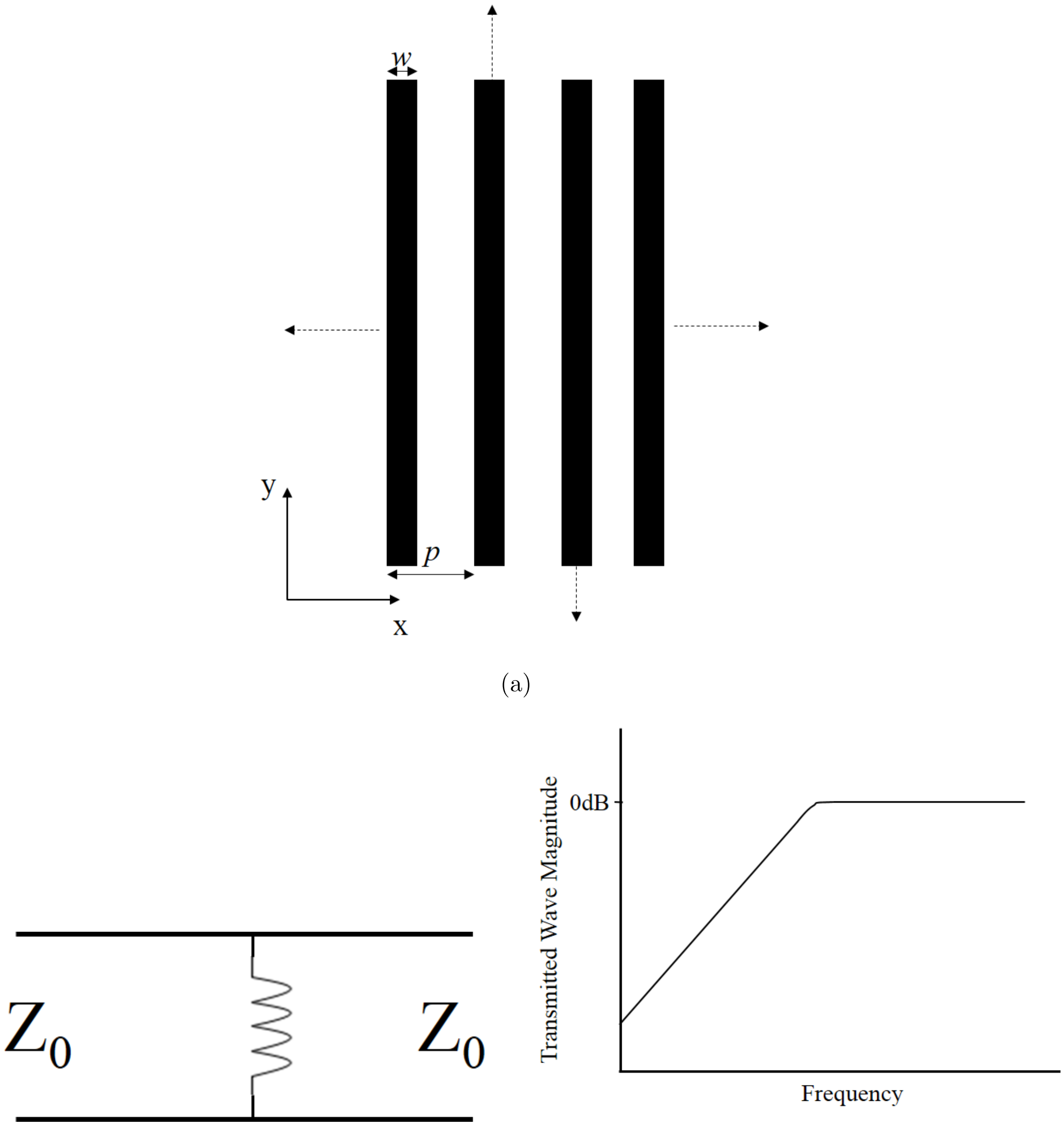

(a)

(b)

(c)

Figure 2.8: (a) A strip-grating FSS, (b) Equivalent circuit of a strip-grating FSS, (c) Magnitude of wave transmitted through strip-grating FSS

the application. For example, turning the dipoles into crosses of similar dimensions, as in Fig. 2.10a, adds rotational symmetry to the unit cell, meaning it will behave identically when the incident EM wave has its E-field aligned with either the x or y direction, reducing polarisation selective effects. Convoluting the elements, as is Fig. 2.10b, can also be performed to reduce the resonant frequency of the unit cell while maintaining the periodicity and physical size of the FSS, which is useful at longer wavelengths [73]. A further advance on this is the square loop unit cell, shown in Fig. 2.10c. This has a further reduced unit cell size for its resonant frequency, as resonance depends on the circumference of the loop. It also has

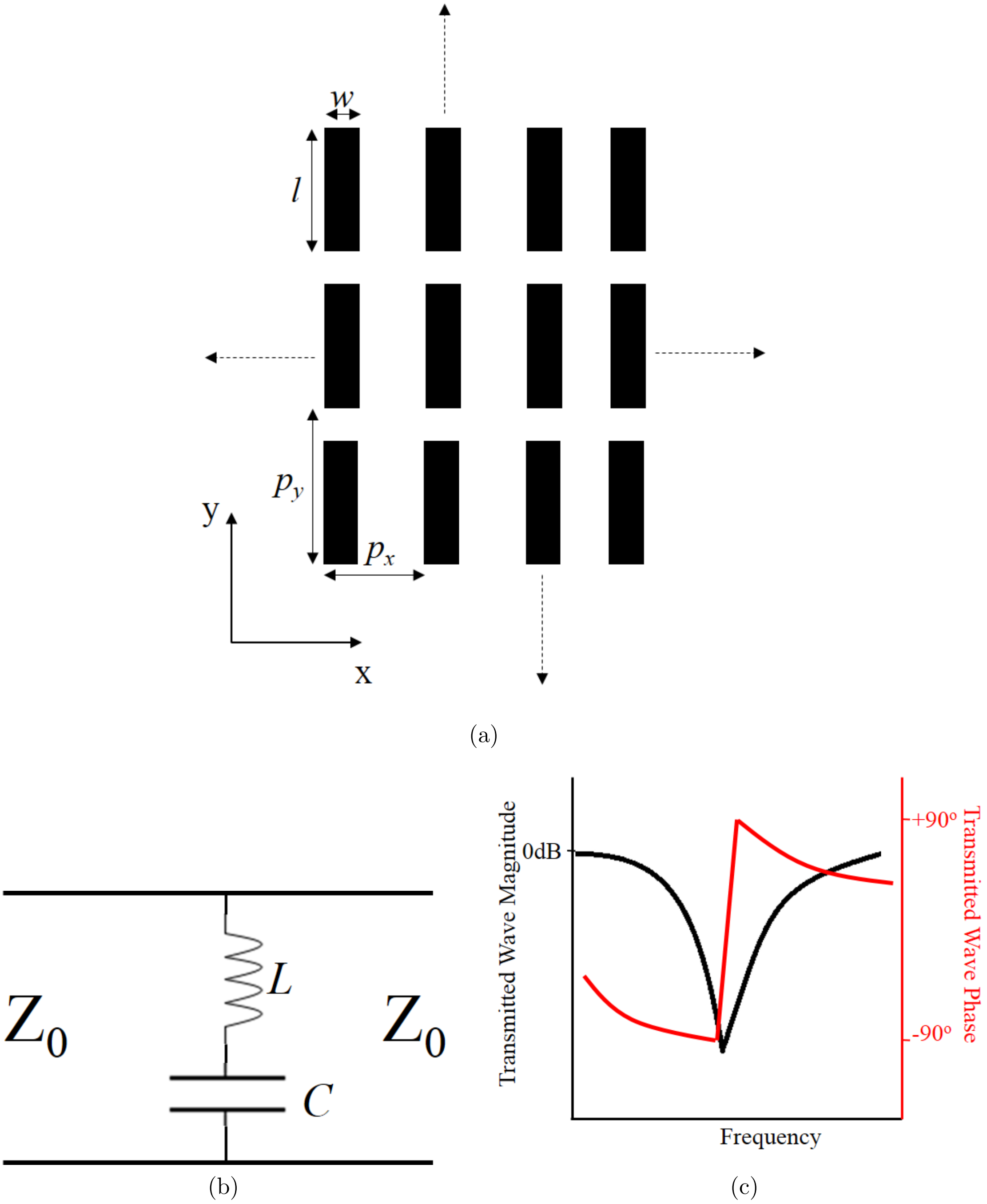

(a)

(b)

(c)

Figure 2.9: (a) A dipole patch FSS, (b) Equivalent circuit of a dipole patch FSS, (c) Magnitude and phase of wave transmitted through dipole patch FSS

good stability with non-normal angles of incidence, has rotational symmetry, has a relatively broad bandwidth, and is simple to model. Langley and Parker derived a set of equations for the equivalent circuit model of a square loop FSS at various angles of incidence, based on the generic LC model in Fig. 2.9b [74]. Assuming a wave of normal incidence, the inductive reactance X_L and capacitive susceptance B_c can be calculated as follows

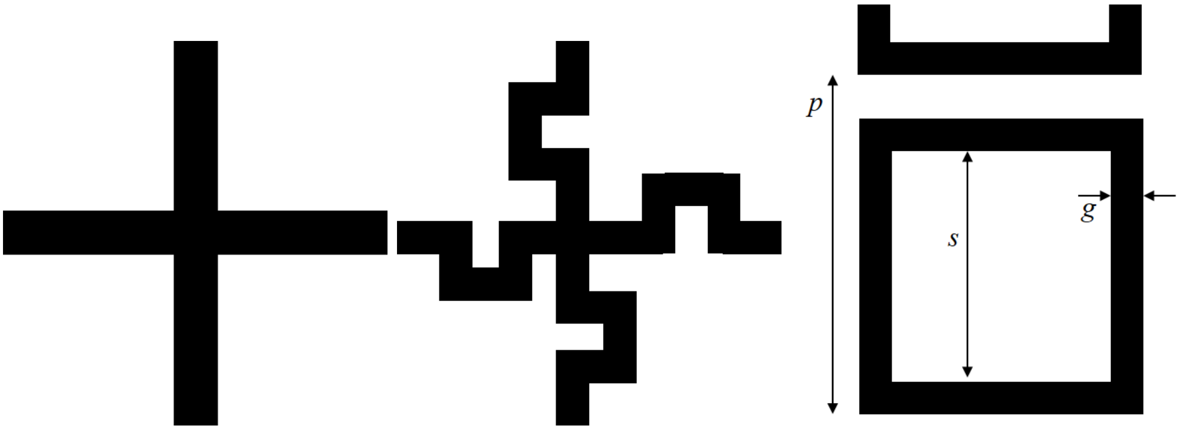

(a) (b) (c)

Figure 2.10: (a) A dipole cross unit cell, (b) A convoluted dipole cross unit cell, (c) A square loop unit cell

$$\frac{X_L}{Z_0} = \frac{(s+2g)}{p} F(p, 2g, \lambda) \tag{2.2}$$

$$\frac{B_C}{Z_0} = \frac{(4s+8g)}{p} F(p, p-s-2g, \lambda) \tag{2.3}$$

where p, s and g are the period, inner loop size and loop thickness respectively and λ is the wavelength of the incident wave (Fig. 2.10c). Function F is defined as

$$F(p, w, \lambda) = \frac{p}{\lambda}[\ln(\mathrm{cosec}(\frac{w\pi}{2p})) + G(p, w, \lambda)] \tag{2.4}$$

where

$$G(p, w, \lambda) = \frac{1}{2}\frac{(1-\beta^2)^2[(1-\frac{\beta^2}{4})(A_+ + A_-) + 4\beta^2 A_+ A_-]}{(1-\frac{\beta^2}{4}) + \beta^2(1+\frac{\beta^2}{2}-\frac{\beta^2}{8})(A_+ + A_-) + 2\beta^6 A_+ A_-} \tag{2.5}$$

$$A_\pm = \frac{1}{\sqrt{1 \pm \frac{p^2}{\lambda^2}}} - 1 \tag{2.6}$$

and

$$\beta = \frac{\sin(\pi w)}{2p} \tag{2.7}$$

The calculated values for X_L and B_C can then be used in the equivalent circuit model to find the resonant frequency of a square loop FSS in free space at a given frequency.

If bandpass characteristics are required for an FSS, Babinet's principle can be used [75]. In optics, this principle states that the diffraction of a beam around a planar opaque object is identical but inverse to the diffraction of a beam through an aperture, in a planar opaque sheet, of identical proportions to the object. The object and the equivalent aperture are referred to as complementary surfaces, and the two diffraction patterns sum to produce the same effect as if the beam faced no impediment. Booker noted that for electromagnetics, this principle allows us to say that an array of planar conducting elements is complementary to an array of apertures in a conducting screen (Fig. 2.11a) [76]. As such, the frequency responses should be identical but inverse - going from bandstop to bandpass, but with the same corner frequencies and bandwidth (Fig. 2.11c). Again note the phase change caused by the FSS, particularly in the pass region. In the circuit model of FSS, the array of apertures appears as the same inductance and capacitance as in the patch case, but in parallel with each other (Fig. 2.11b). However, Booker also noted that the polarisation of the array would also change - for an array of dipole apertures, the H-field would be aligned with the dipoles to experience the complementary effect. This is because electric currents cannot occur in an aperture, but we can consider magnetic currents - in reality caused by the flow of electrons around the aperture - to operate in an analogous way. As such, we can derive a square loop aperture FSS, as shown in Fig. 2.12a, which is described by the Langley and Parker equations, retains the desirable characteristics of the square loop unit cell, but has a bandpass behaviour.

2.3.2 Practical considerations

The above discussion and analysis considers FSS as infinite arrays of periodically repeating unit cells, consisting of perfectly conducting material, suspended in free space. Clearly, some discussion must be made of practical implementations of FSS. First, FSS are often fabricated onto a dielectric substrate. This is in many ways an advantage, as it makes them easy to manufacture cheaply with conventional printed circuit board (PCB) etching techniques, and provides a firm mechanical structure which may be useful in some applications. However, it also means that the assumption of the FSS as in a transmission line with the characteristic impedance of free space is untrue, as the dielectric will have a different, usually notably higher, permittivity. If the FSS is embedded in an infinitely thick dielectric with relative permittivity ϵ_r, this produces a shift downward in resonant frequency by a factor of $\sqrt{\epsilon_r}$ [77]. However, FSS are more often mounted on a material rather than embedded within one, so the effective permittivity ϵ_{eff} becomes the average ϵ_r of the dielectrics on either side, noting that the relative permittivity of air is 1. Further, practical thicknesses, of the order of 1 or 2mm, see a smaller effect than the infinitely thick dielectric.

Also, practical FSS must be of a finite size. As such, for the analysis above to hold, the FSS must appear infinite to the incident wave so the unit cells couple to each other. Further, when a small FSS is used diffraction around the surface may occur, leading to unexpected behaviour and poor frequency selectivity. To avoid these effects, FSS are usually designed to

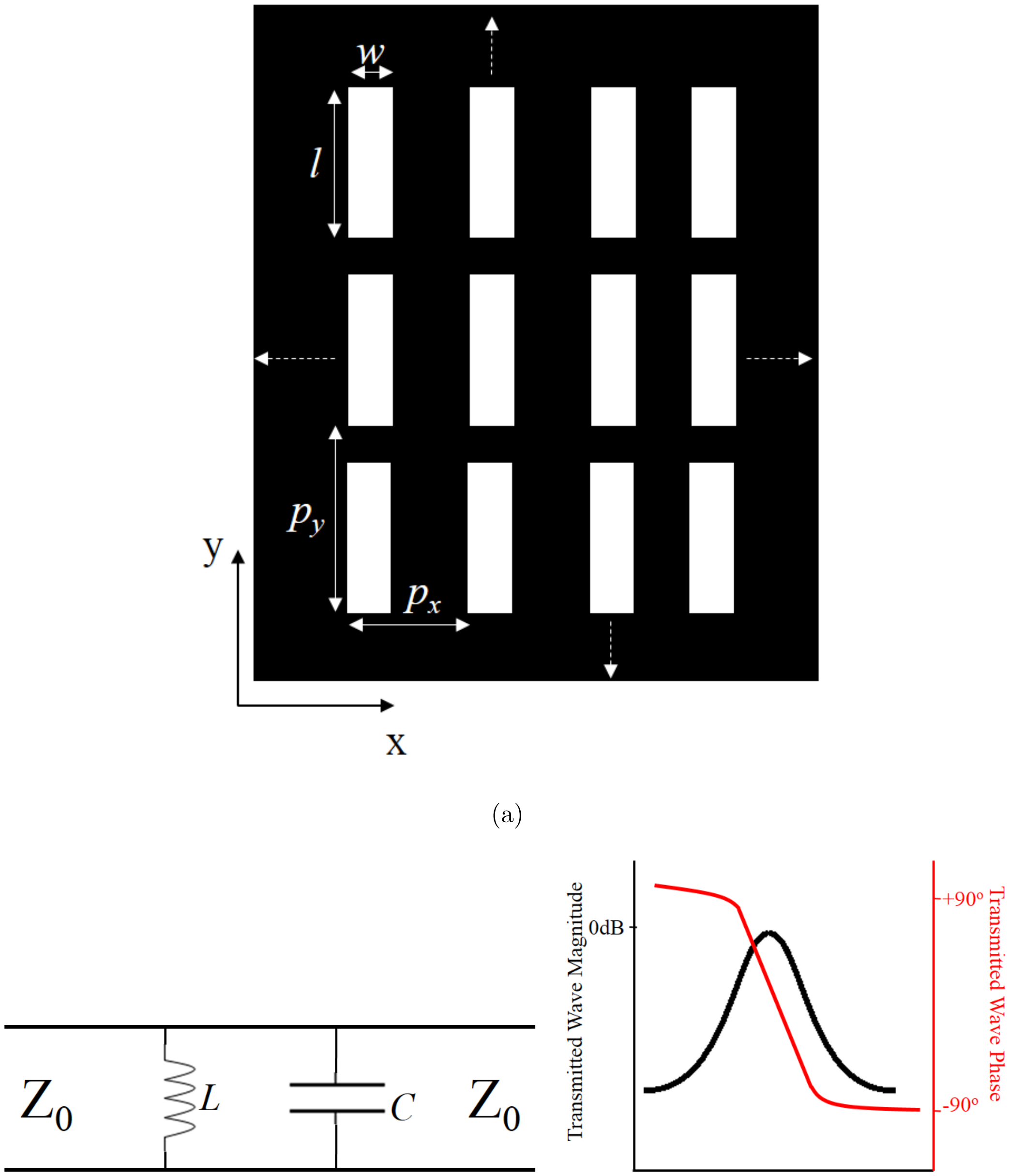

(a)

(b)

(c)

Figure 2.11: (a) A dipole aperture FSS, (b) Equivalent circuit of a dipole aperture FSS, (c) Magnitude and phase of wave transmitted through dipole aperture FSS

have length of at least 10λ, though reasonable performance can sometimes be obtained with smaller FSS [72]. Otherwise, an FSS may be inserted into a waveguide, though behaviour will be notably different from that in free space and must be designed as such [78].

It should also be noted that with non-perfect conductors, loss is introduced to the FSS. The E-field of the incident wave induces currents in the conductor, which experience resistance and so disperse some energy as heat. This can be modelled as a resistor in series with the inductance in the circuit model (Fig. 2.12b) [79]. As such, even in a peak transmission region, there is not perfect transfer of energy through the surface. Loss also occurs in the

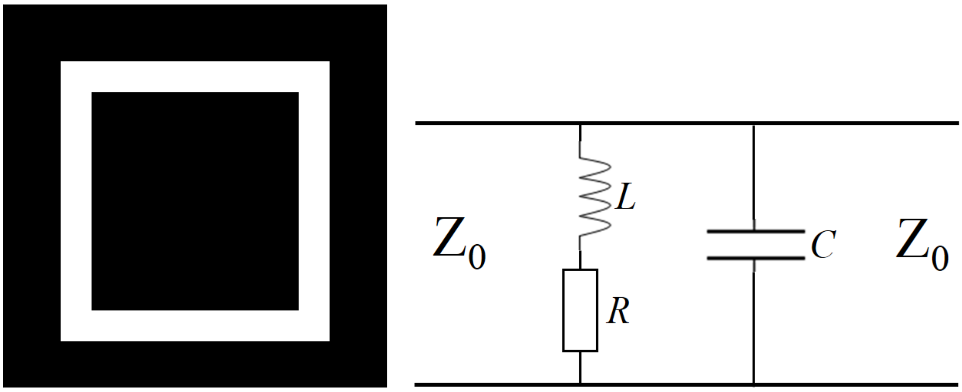

Figure 2.12: (a) A square loop aperture unit cell, (b) Equivalent circuit of a lossy aperture FSS

dielectric, due to the material's opposition to charges moving around within in [80]. The lost energy is dissipated as heat. Loss and edge effects also compromise Babinet's principle slightly - a practical aperture FSS will not perfectly match its complementary patch FSS, with a shift in resonant frequency being the most common effect.

Finally, due to the lattice configuration of FSS, when the unit cells have a large enough period they act as a diffraction grating [72]. The incident wave diffracts through the FSS, causing the transmitted wave to propagate in unintended directions away from and in addition to the main beam. These undesired emissions are called Grating lobes, in analogy with array theory [64]. They can be avoided by limiting the period $p < \lambda_0$ for normal incidences, though this decreases to $p < \dfrac{\lambda_0}{1 + \sin(\theta)}$ where θ is the angle of incidence.

2.3.3 Reconfigurable FSS

The design of FSS can be altered in several ways to make them reconfigurable. This can be by making them alterable mechanically, such that the dimensions of the FSS appear to alter [81]; using a substrate which is itself reconfigurable, so its effect on the FSS properties becomes tunable [82]; or by integrating active components such as switches or variable capacitors [83, 84]. These approaches can make the FSS switch between two or more distinct states, changing its fundamental operation, or allow tuning of the structure's resonant frequency. This subsection will overview the variety of reconfigurable FSS techniques and some of their applications.

It has long been known that the resonant frequency of an FSS depends on the dimensions of its elements and how they appear to an incident plane wave [72]. However, the idea of using mechanical means to alter them is relatively recent, with a key early development being the work of Fuchi et al on origami FSS [81]. Conventional FSS unit cells are fabricated onto a paper substrate, which, when folded, alters the resonant frequency of the FSS. Increasing the folding angle increases the resonant frequency, with shifts of 19% from 10GHz achieved.

This has use in space applications where an FSS may need to be deployed from a small size and then tuned.

For applications where faster tuning may be required, such as beamscanning, quicker and smaller tuning approaches must be taken than large scale change of the FSS structure. One recent suggestion is using piezoelectric actuators to support an FSS layer above the ground plane to create a tunable high impedance surface [85]. By altering the distance between the FSS and the ground plane, the centre frequency, and so the reflected phase at a given frequency, is altered. By placing the actuators outside the FSS region, they have little effect on the reflected wave, and so are advantageous at mm-Wave frequencies where tunable components are often lossy [86]. This design has recently been incorporated into a beam-scanning leaky wave antenna operating at mm-Wave, with potential applications in satellite communications [87].

The use of substrates with variable properties has been proposed to allow low-profile implementation of tunable FSS [82, 88]. This usually operates by altering the relative permittivity or permeability of the substrate, so changing the resonant frequency of the FSS fabricated onto it. The first attempt to make use of this process was by Lima, Parker and Langley [89]. Here, a supporting structure allowed the FSS to be backed by a liquid substrate, which altered the dipole slot FSS resonance by 40% compared with when no liquid was present. This is a slow approach to tuning, and similar approaches have only recently been suggested, using metallic microfluids to alter the operation of an FSS from bandpass to bandstop [90].

A more practical approach to tunable substrates was suggested by Parker et al, who suggested using ferroelectric materials as an FSS substrate [88]. Biasing the substrate, and so placing a magnetic field across it, alters the substrate's effective permeability, so changing the resonance of the FSS fabricated on it. This is further developed in [91], where it is found that 8% tuning can be achieved. However, this material was then largely abandoned, due to the large magnetic fields required for tuning and the high losses in the substrate.

Liquid crystal substrates then emerged as a new method of tuning FSS [82]. Applying an electrostatic field across liquid crystals causes the molecules to align with the field, changing the material's relative permeability [92]. [82] was the first demonstration of this, showing that a dipole bandpass array could realise tuning of 4% at around 130GHz with a bias voltage of 10V. This high frequency of operation is a useful factor in the choice of liquid crystals, however, the loss change with tuning is large, with 10dB difference between the extreme states in [82]. Liquid crystal tuned FSS have also been demonstrated at THz frequencies [93] and at standard microwave frequencies [94], with similar levels of performance.

However, what both mechanical and substrate-based tuning suffer from as approaches are the achievable switching rates of the different methods. While for many applications the rates achievable are acceptable, such as beamsteering [95], others require rates only achievable with electronic switching. For this reason, and for ease of manufacture, many approaches to reconfigurable FSS use active electronic components. The equivalent circuit model of FSS suggests that integrating active electronic components into the unit cells should allow control of the FSS properties. Some of the earliest research to do this used PIN diodes, which increase their resistance with decreasing forward currents through them [83]. When used with square loop aperture unit cells, with one diode across each side of the square, biasing the diodes in their high resistance state produces the expected bandpass response [96]. However, switching the diodes to low resistance allows currents to flow between each patch and across the apertures, causing the FSS to act as an inductive high-pass surface. Careful design of the unit cell allows this switching to cause the FSS to go from transmissive to reflective at the desired frequency. It should be noted that the addition of any active component, all of which have some parasitic resistance, introduces more loss to the FSS.

This effect, which has also been performed with different unit cell configurations, has been used to create beam-steering antennas, by surrounding an omnidirectional antenna with a cylindrical FSS, which is switched to its transmissive state only in the desired transmit direction [97]. Switching PIN diodes can also be used to change the effective FSS unit cell, so tuning its centre frequency [98]. Using transmissive FSS, this switching effect has been suggested as a way to allow electromagnetic reconfigurability of buildings [99], while using the diodes as variable resistors in reflective FSS has been used in active radar absorbers, allowing tuning of the reflectivity within a certain bandwidth [100].

PIN diodes tend to have relatively high loss, however, and suffer from non-linear effects [101]. As such, some research has turned to micro-mechanical electromagnetic systems (MEMS), which have much lower loss and better power handling capabilities than conventional semiconductor devices [102]. They are fabricated using lithographic techniques usually used to create integrated circuits, and often consist of some conducting bridge between contacts, which is moved to meet them by an electric field due to a bias voltage. It has been shown that MEMS switches can be used to create reconfigurable FSS in the microwave region able to operate at over 20 watts of power without affecting the resonant frequency [103]. Applications for this technology include reconfigurable reflectarrays [104], and as switchable substrates for enhancing the bandwidth of reconfigurable antennas [105]. MEMS that produce variable capacitance have also been developed, where a conductive bridge above a contact is deflected by a biasing electric field, with the gap between the bridge and the contact creating a variable capacitor [106].

Integrating one of these devices into an FSS unit cell, as shown in Fig. 2.13a for a square loop aperture, places a variable capacitance in parallel with the intrinsic capacitance of the FSS (Fig. 2.13b). Note again that parasitic inductances and resistances are also

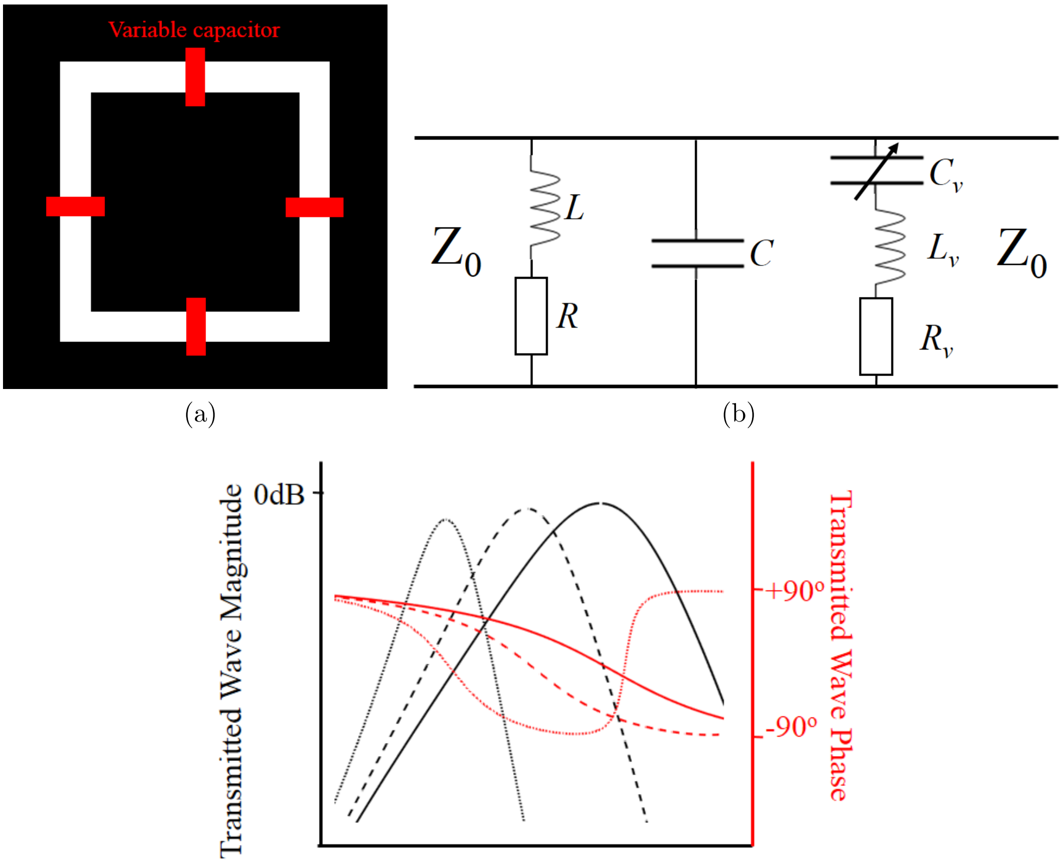

(a) (b)

(c)

Figure 2.13: (a) A reconfigurable aperture square loop FSS, (b) Equivalent circuit of a reconfigurable aperture FSS, (c) Magnitude and phase of wave transmitted through reconfigurable aperture FSS with varying capacitance

introduced, which will vary depending on the type of device used. This additional capacitance allows tuning of the FSS resonant frequency, as shown for a square loop FSS in Fig. 2.13c [107]. Adding this additional capacitance reduces the resonant frequency significantly from its intrinsic resonance, and increasing the tunable capacitance further reduces the resonant frequency. It also begins to increase the loss through the surface, as more current passes through the parasitic device resistance R_v as the variable capacitor (C_v) reduces in impedance, increasing I^2R losses. Also note that the phase response of the FSS moves with its magnitude response. This reconfigurable FSS is now a bandpass FSS with a tunable centre frequency.

At microwave frequencies, however, varactor diodes are more established as variable capacitors for tuning of FSS [108]. FSS using varactor diodes have been used in multiple applications, from high impedance surfaces for tunable low-profile antennas [109], to radar cross-section reduction [110]. Barium strontium titanate (BST) capacitors, which use thin-film ferroelectrics to produce a variable capacitance, have also been suggested for these

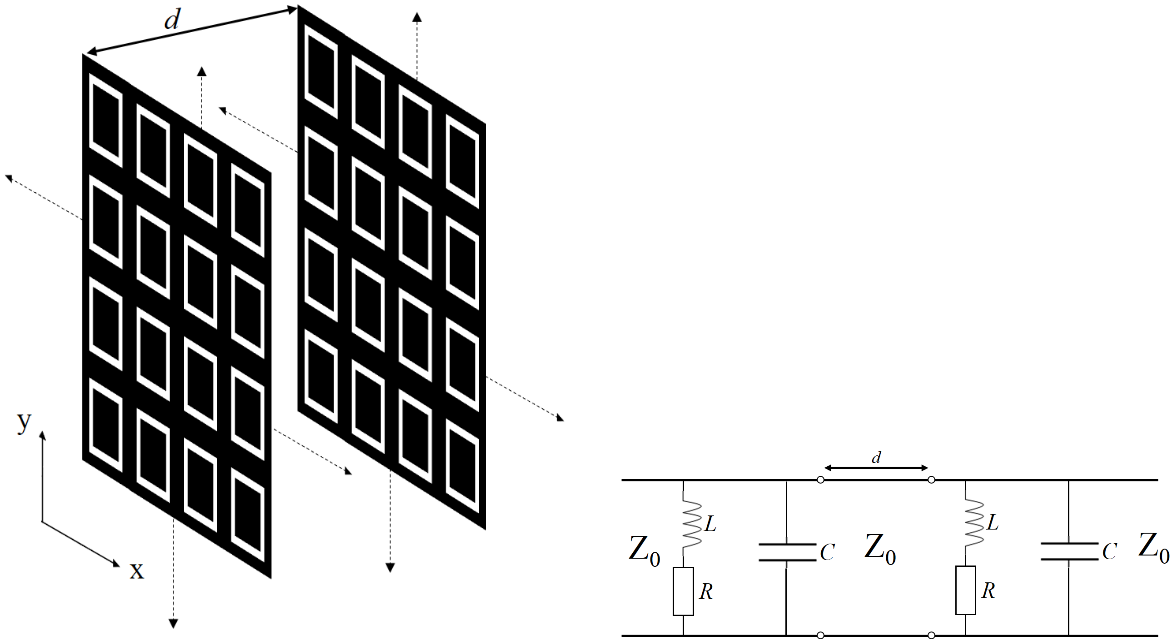

(a) (b)

Figure 2.14: (a) A 2-layer aperture square loop FSS, (b) Equivalent circuit of a 2-layer aperture FSS

tunable FSS applications [84].

2.3.4 Multiple-layer FSS

Some applications require a broader passband than single layers of FSS are able to provide [111]. Spacing identical FSS layers some distance d apart in free space, both at normal incidence to an incident EM wave as in Fig. 2.14a, is equivalent to adding a free space transmission line of length d between two identical LC circuits, as shown in Fig. 2.14b. Where $d = \lambda/4$, with λ the wavelength of the incident EM wave, the wave transmitted through the first layer has rotated through 90^o when it reaches the second layer. This produces a frequency response which has a broader pass band than the single layer, while maintaining a linear phase change with frequency within the passband.

This extended bandwidth is of particular interest in cases where reconfigurable FSS are required to produce a phase change for minimal magnitude variation. The single-layer FSS designs discussed so far provide a maximum of 180^o phase change across all frequencies, while the transmitted magnitude changes more than 10dB (Fig. 2.13c). Using multiple FSS layers can overcome this problem, as discussed at length by Abdelrahman, Elsherbeni and Yang [112].

Multiple layers can be cascaded together to further increase the FSS pass bandwidth, so increasing the accessible phase change for a given magnitude variation (Fig. 2.15). For 1dB of magnitude variation, two FSS layers gives 128^o phase variation, three layers gives 266^o

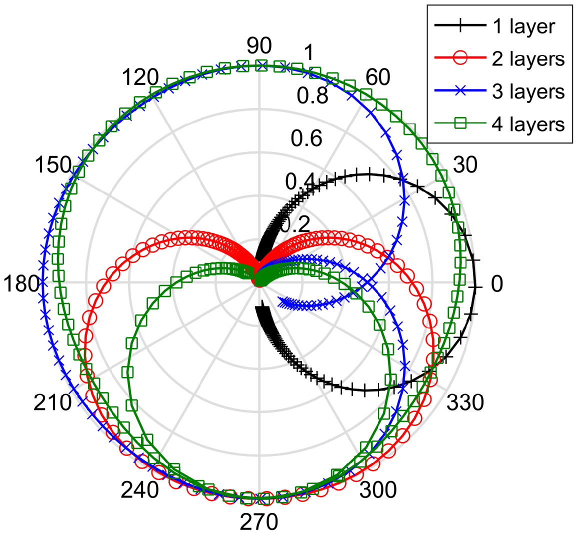

Figure 2.15: Polar plot of theoretical transmitted wave magnitude and phase through different numbers of bandpass FSS layers

phase variation, and four layers gives more than 360^o phase variation [112]. However, note that if a single layer has some transmission loss XdB, each added layer increases the loss by a further XdB, affecting the total performance of the FSS.

2.3.5 Phase change with FSS

By allowing control of a centre frequency, tunable FSS also allow control of a reflected or transmitted phase at a given frequency. As described in Section 2.3, the filter response of a bandpass FSS has a linear phase change in the passband. This means that as the FSS centre frequency is varied, at a single frequency within the passband the transmitted phase is also varied. One of the first uses of this was in an active radar absorber called the Phase Switched Screen, which is an FSS loaded with varactor diodes which tune back and forth to change the phase of the signal transmitted through the screen [113]. This spreads the incident RF energy across different frequencies, reducing the radar cross-section, particularly in combination with conventional resistive absorbers. Another application is in electromagnetically secure buildings, where changing the phase transmitted through a building's walls in GSM bands is shown to scramble the signal and so greatly increase error rates [114]. It is also shown that the effect is preserved at tuning rates well below the symbol rates of the GSM signal.

One application of phase tuning FSS that has attracted growing attention in recent years is reconfigurable transmitarrays. These have a similar operation to reflectarrays, in that the FSS is used to beamform an incident, modulated RF signal [115]. However, as the name suggests, the beam is formed by transmitting the RF through one or more FSS layers, analogously to lenses, rather than reflecting off a surface, analogously to a concave reflector. In order to act as lenses, the phase of each unit cell must be controlled to cause constructive interference in the desired beam direction. This is conventionally done by varying the dimensions or orientation of each unit cell [116]. The planar nature of FSS means that low-profile, highly directive antennas can be developed [117], which are of particular interest at mm-Wave frequencies.

Reconfigurable FSS-based transmitarrays use the same unit cell across the surface, but vary the tuning of each cell using an active element to alter the cell's phase response [118]. Variation of these unit cell responses allows beamsteering. Usually multiple-layer FSS are used to ensure enough phase rotation is obtained [112]. These were first suggested with one-dimensional beamsteering using four layers of varactor-loaded dipole slot arrays, which achieved a simulated phase variation of over 360^o at 4.2GHz [119]. A similar transmitarray was experimentally implemented using eight layers of a varactor-tuned FSS to achieve nearly 400^o phase change for 6dB magnitude variation [120]. Further work has shown that layering two tunable capacitive FSS, with integrated ferroelectric varactors, with a passive inductive layer in between, can achieve $\pm 10^o$ beamscanning in one dimension, though the absolute phase change achieved is not given [121].

It has also been suggested that placing the FSS layers very close to a directive antenna can reduce the required size of each FSS layer, and reduce the form factor of the whole beamsteering system [122]. This work uses five closely spaced varactor-loaded square-loop aperture FSS over the aperture of a horn antenna. This achieves 200^o phase change for 1dB magnitude variation at 5.3GHz, allowing beamsteering in two dimensions of up to 31^o. Two-dimensional control is achieved by having gaps between adjacent columns of FSS unit cells, and a biasing line running along the reverse of each row of unit cells which connects to the central patch. As such choosing the bias voltages on each row and column allows beamscanning in the E-plane, H-plane and along the 45^o axis. However, for full independent two-dimensional beamscanning, each unit cell must be biased independently. The first analysis of the effects of this used a 5 layer square-loop FSS again over the aperture of a horn antenna, and demonstrated over 360^o phase change and achieving $\pm 25^o$ phase change independently in both azimuth and elevation [95]. However, this used fixed capacitors as a proof of principle. Work has since been presented using varactor diodes and a six layer FSS, with a single complex biasing network on the reverse of the final FSS layer connected to the patches of all the FSS layers [123]. This achieves 400^o phase change, and allows independent two-dimensional beamsteering of up to 28^o in azimuth and 26^o in elevation.

2.3.6 Summary

This collection of work on reconfigurable FSS-based transmitarrays shows how producing phase change with transmissive FSS is an active topic of interest. However, in comparison

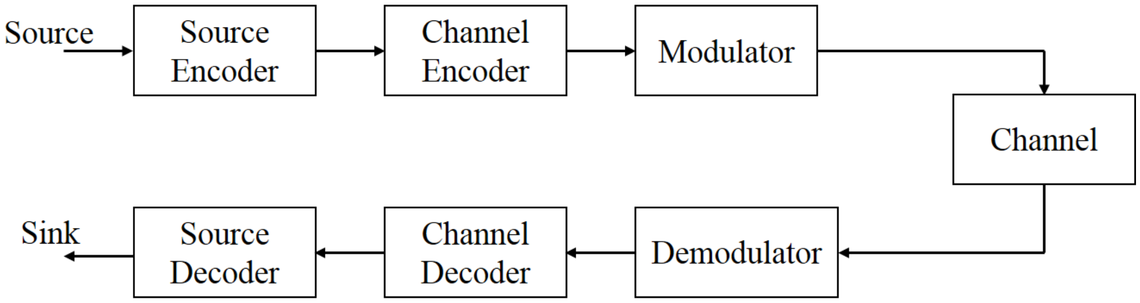

Figure 2.16: Flowchart of a generic communications system

with using FSS for modulation, there are some key differences. First, DAM aims to produce one phase change across the whole FSS, reducing requirements of biasing networks. Second, the rates of change of beam direction are in the order of milliseconds, rather than the sub-microsecond tuning speeds required by modulation. Finally, the requirements for the bandwidth of the FSS differs between transmitarrays and modulating FSS. As transmitarrays must steer a whole modulated signal, which may be wideband, it should have the same phase response over the signal bandwidth to avoid steering different frequency components in different directions. A modulating FSS, however, is fed by a single frequency RF signal, and creates a wideband signal through tuning of the FSS. Nonetheless, the works described above contribute significantly to the development and understanding of phase modulating FSS.

2.4 Wireless communications systems

The purpose of any digital communications system, including for IoT connectivity, is to obtain, at a data sink, an identical copy of the stream of binary data bits at a data source. The generic flowchart for this is shown in Fig. 2.16. The source encoder reduces the number of bits to be transmitted, by removing any redundancy or information which may be discarded without drastically affecting the output; while the channel encoder manipulates the bits to be transmitted to allow detection or correction of errors in transmission at the receiver, usually by adding redundancy [124]. These processes are reversed at the receiver by the source and channel decoders, and neither will be considered in this thesis - all data bits will be assumed to contain equal amounts of information, and no error detection or correction will be utilised. The other key processes - modulation, demodulation, and the channel - will be discussed in more detail.

2.4.1 Digital modulation and the wireless channel

Modulation is the process of converting binary bits into a form which can pass through the medium between the transmitter and receiver, known as the channel. For wireless communications, this form is usually an EM wave which propagates through the environment. When using coherent radio transmitters, a given sequence of bits is represented as some RF signal

$$s(t) = \Re\left\{u(t)e^{j\omega_c t}\right\} \tag{2.8}$$

where $e^{j\omega_c t}$ is a carrier wave with frequency $f_c = 2\pi\omega_c$ and the complex baseband signal

$$u(t) = s_I(t) + js_Q(t) \tag{2.9}$$

contains the information. s_I and s_Q are known as the in-phase and quadrature-phase components of the baseband signal, as the total transmitted signal can be represented as

$$s(t) = s_I(t)\cos(\omega_c t) - s_Q(t)\sin(\omega_c t) \tag{2.10}$$

with $\cos(\omega_c t)$ representing the in-phase part of the carrier signal and $-\sin(\omega_c t)$ representing the quadrature phase part.

At some receiver, the incoming signal is given by

$$r(t) = \Re\left\{v(t)e^{j\omega_c t}\right\} + n(t) \tag{2.11}$$

where $n(t)$ is the additive white Gaussian noise (AWGN) produced by the channel, mainly by thermal processes in the receiver. The envelope of the received signal, $v(t)$, is a combination of the transmitted baseband envelope and the channel response. Assuming the channel impulse response $\boldsymbol{h}$ is linear and time-invariant for the length of the signal,

$$v(t) = u(t) * \boldsymbol{h} \tag{2.12}$$

where $*$ denotes convolution.

This channel impulse response is defined by several key phenomena. The first is free-space path loss, which is caused by the dispersing energy of a propagating electromagnetic wave. This leads to a drop in received power proportional to the distance from the transmitter and the frequency of the carrier wave:

$$\frac{P_r}{P_t} = \frac{G_t G_r \lambda^2}{(4\pi R)^2} \tag{2.13}$$

where P_r and P_t are the received and transmit power respectively, G_t and G_r are the gain of the transmitting and receiving antennas respectively, λ is the carrier wavelength and R is

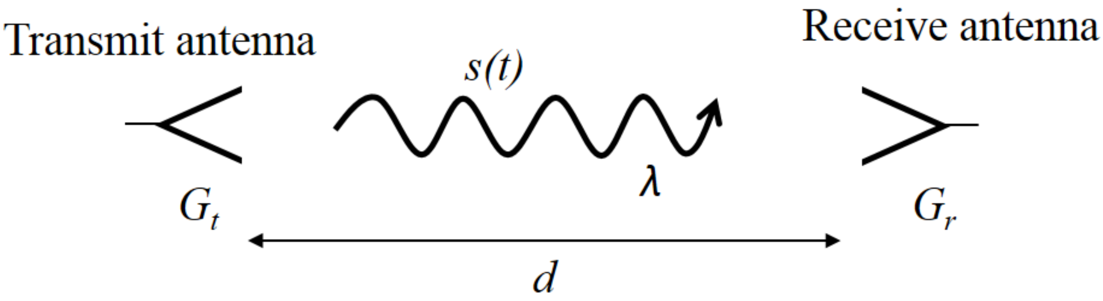

Figure 2.17: Propagation of a wireless signal in free space

the distance from the transmitter (Fig. 2.17). This free space path loss model is also known as the Friis equation. There is also a phase shift from propagation in free space, giving a transfer function between the transmitted and received signals of

$$h = \frac{\lambda\sqrt{G_t G_r}}{4\pi R} e^{\frac{-j2\pi R}{\lambda}} \tag{2.14}$$

This power reduction is predictable and easy to plan for in designing communications systems, while the phase shift can be measured by sending a known signal, allowing it to be accounted for before detection of signals. Some experiments in this thesis will use these ideal channels to evaluate the developed FSS DAM systems, usually by placing the experiment inside an anechoic chamber to recreate free-space conditions. These ideal channels are known as AWGN channels as the errors caused are dominated by the effect of thermal Gaussian noise.

Fading channels

However, most real-world wireless communications systems face more complicated channel effects. One of these is shadowing, which is caused by objects blocking the propagating wave and so reducing its power. This varies slowly with time as the environment around a receiver changes. It is often described statistically as a slow variation in received power. However, the most difficult channel effect to account for is known as multipath. This is where, due to reflections from the environment, multiple copies of a signal arrive at the receiver over different paths with different delays, causing self-interference (Fig 2.18). While for simple scenarios as depicted in Fig. 2.18 $r(t)$ can be calculated analytically by summing the different paths the wave takes, in practice it is much easier to express this process statistically:

$$r(t) = \Re(x)\{[\sum_{l=0}^{L(t)} \alpha_l(t) e^{-j\phi_l(t)} u(t-\tau_l(t))] e^{j\omega_c t}\} \tag{2.15}$$

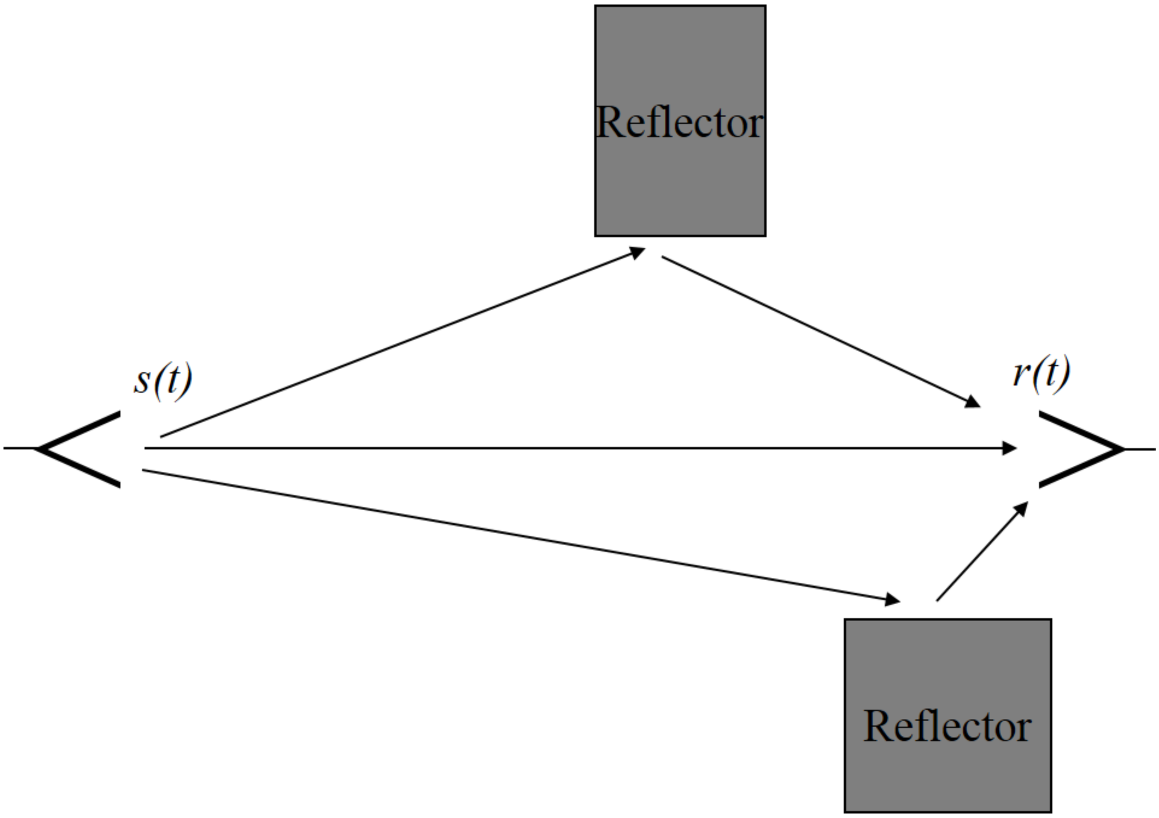

Figure 2.18: Propagation in a multipath environment

where l is the path number, $L(t)$ is the total number of paths the signal takes, $\alpha_l(t)$ is the fading amplitude of this path, $\phi_l(t)$ is the fading phase of the lth path and $\tau_l(t)$ is the delay of this path relative to the 0th path. Note that $L(t)$, $\alpha_l(t)$, $\phi_l(t)$ and $\tau_l(t)$ are all functions of t, which indicates that these values change over time due to changes in the channel environment. The fading amplitude $\alpha_l(t)$ is determined by the free space pathloss caused by the path length R_l, the product of the gain of the antennas in the direction of transmission and reception for this path, and any reduction in amplitude due to lossy reflections and shadowing. The fading phase $\phi_l(t)$ is determined by the length of the path taken, the wavelength λ, any phase shifts due to reflection and Doppler phase shifts due to the relative movement of the receiver and reflectors. Finally the delay $\tau_l(t)$ is determined only by the length of the path and the speed of the propagating wave in the medium, which is assumed to be the speed of light, c.

Summing these paths leads to two possible fading effects. If all the delays τ_l are much smaller than one symbol length T_s of the transmitted signal, the receiver resolves all paths into a single path. In this case, the differently delayed copies of the carrier wave interfere with each other constructively and destructively in a process called narrowband fading. As the difference between two copies of the carrier adding constructively or destructively is a small distance at microwave frequencies (15cm at 1GHz), the magnitude of the received

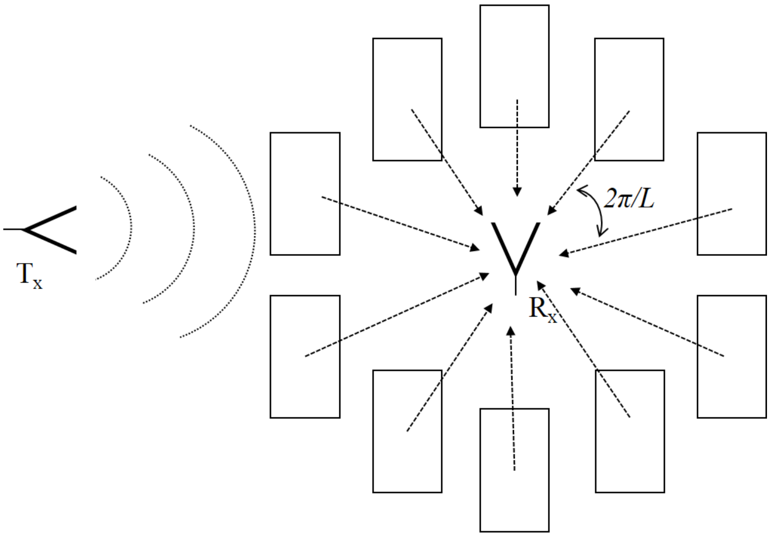

Figure 2.19: Clarke's model of Rayleigh fading

signal varies very quickly. This causes significant problems for maintaining acceptable error rates in communications systems. The most commonly studied form of narrowband fading is Rayleigh fading, which is derived from Clarke's model (Fig. 2.19) [125]. It is assumed that no line-of-sight path is present, but that the receiver is surrounded by L reflectors equally spaced $\frac{2\pi}{L}$ radians apart, which provide the signal. As $L \xrightarrow{\infty}$ the channel $h(t) = h_I(t) + h_Q(t)$ with power normalised to 1 has a distribution $h_{I,Q} \sim \mathcal{N}(0, 0.5)$ where $\mathcal{N}(\mu, \sigma^2)$ is the Gaussian distribution with mean μ and variance σ^2.

When some delays τ_l are greater than T_s, the receiver resolves these into multiple different paths. This means that symbols are interfering with subsequently transmitted symbols, which is known as intersymbol interference (InterSI) or wideband fading. Note that this manifests as a random interference, as the order of data symbols is essentially random. The different paths also undergo variation in magnitude and phase, and may have similar or different average powers (Fig. 2.20).

The effects of two different channels - AWGN and narrowband Rayleigh fading- on binary signalling is shown in Fig. 2.21. In AWGN the BER drops quickly as the noise power required to cause a symbol error becomes greater. In a Rayleigh channel the decay is significantly slower, as errors occur when the symbol power is much less than the average power even for high signal to noise ratio (SNR).

Digital modulation schemes

With this knowledge of the distorting effects of wireless channels, the signals for carrying information through them can be designed appropriately. This subsection will focus of signalling for AWGN channels, and some approaches to fading channels will be discussed in

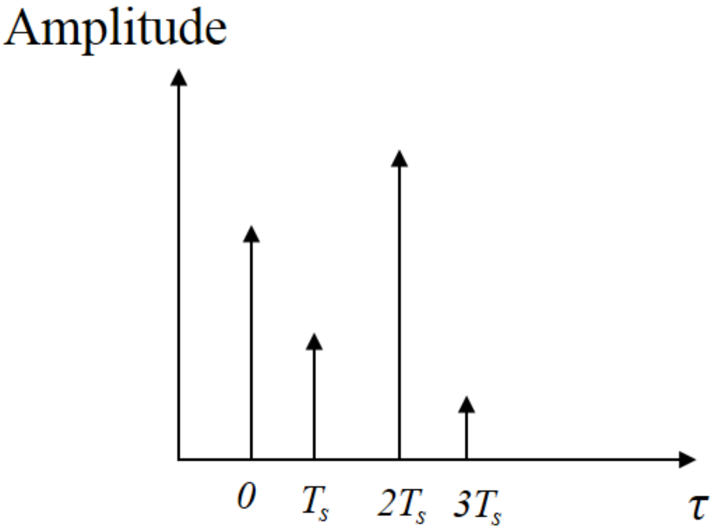

Figure 2.20: A resolved wideband channel

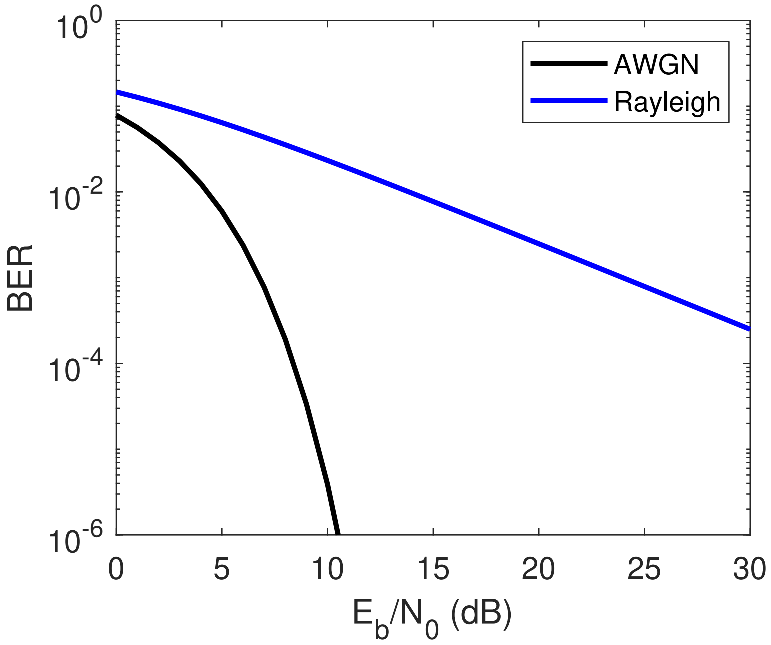

Figure 2.21: Theoretical error rates for binary signalling in AWGN and narrowband fading channels

Section 2.4.2. The generic wireless signal described in Equation 2.8 can be rearranged as

$$s(t) = A(t)\cos\left(\omega_c(t)t + \phi_m(t)\right) \tag{2.16}$$

where $A(t) = |s_I(t) + js_Q(t)|$ and $\phi_m(t) = \angle(s_I(t) + js_Q(t))$. This suggests there are three variables that can be altered in a transmitted signal: the carrier frequency $\omega_c(t)$, the amplitude of the signal $A(t)$, and the phase of the signal $\phi_m(t)$. While varying the carrier frequency to represent information is an accepted form of modulation, which in digital terms

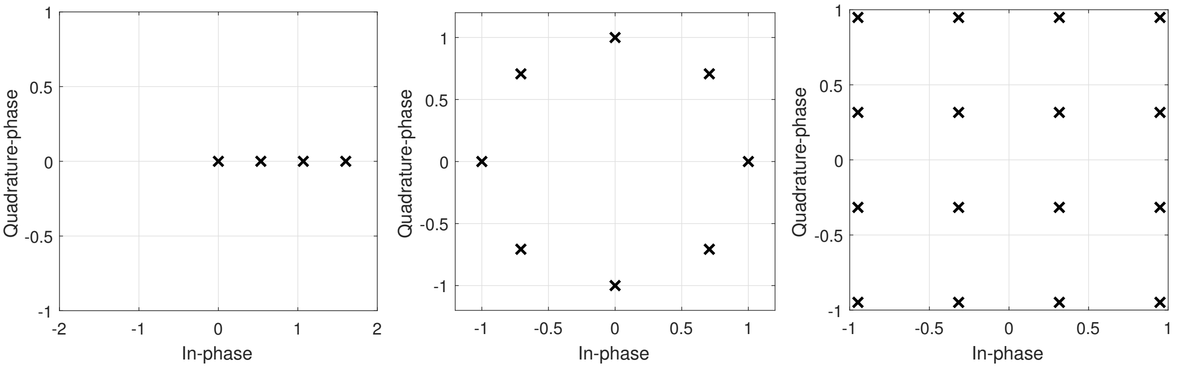

(a) (b) (c)

Figure 2.22: Constellation diagrams of conventional digital modulation schemes (a) 4-ASK, (b) 8-PSK, (c) 16-QAM

is known as frequency shift keying (FSK), it is generated using non-linear techniques which produce spectral broadening, reducing the spectral efficiency of the modulation in comparison with the alternative linear approaches.

These schemes vary $A(t)$, $\phi_m(t)$ or both between different discrete states to represent different bits of information. These can all be represented in signal space on IQ diagrams, where the I represents the different values $s_I(t)$ can take and Q represents the values $s_Q(t)$ can take in the signal set. Where $A(t)$ only is varied, this is known as amplitude shift keying (ASK), and all the possible signal values, or constellation points, usually exist on the positive real axis (Fig. 2.22a). Where only $\phi_m(t)$ is varied, all the constellation points exist on the unit magnitude circle (Fig. 2.22b). When both are varied, this is known as quadrature amplitude modulation (QAM) as $s_I(t)$ and $s_Q(t)$ are varied independently (Fig. 2.22c). These constellation points can exist anywhere on the IQ plane.

The choice of where to place these constellation points is taken to maximise the chance of successfully retrieving the data at the receiver. In an AWGN channel with $h(t) = 1$, the transmitted signal s_i from possible set $\{s_0, s_1, \ldots, s_{M_{mod}-1}\}$ is correctly detected by a receiver when the received signal $r = s_i + n$

$$|r - s_i|^2 < |r - s_j|^2 \tag{2.17}$$

where s_j is any other possible signal in the set. As such, to minimise the chance of error, the Euclidean distance between constellation points

$$||s_i - s_j|| = \sqrt{(s_i - s_j)^2} \tag{2.18}$$

should be maximised. In PSK systems this is done by placing the constellation points $\frac{M_{mod}}{2\pi}$ apart. Note that reducing this spacing reduces the Euclidean distance between neighbouring

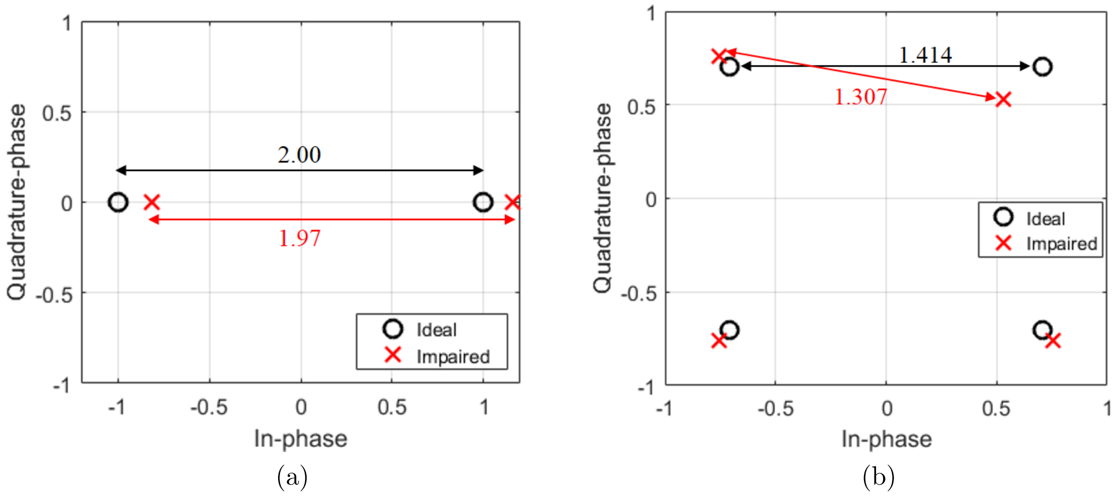

Figure 2.23: Normalised constellation diagrams of distorted (a) BPSK and (b) QPSK where one constellation point is 0.7 the amplitude of the others

constellation points, increasing the chance of error. As such phase error and additional phase variation from a transmitter should be minimised in order to maximise performance. Increasing M_{mod} also reduces the Euclidean distance between constellation points, though with the benefit of increasing the spectral efficiency of the signal.

Less intuitively, if a PSK constellation has perfectly distributed constellation points in phase but the magnitude of each of them varies, this also reduces the Euclidean distance between them for a given total constellation power, increasing the error. This can be demonstrated with a BPSK constellation where one point is 0.7 of the amplitude of the other (Fig. 2.23a). Normalised to 1, an ideal BPSK constellation takes values $[-1, 1]$, and the two points have a Euclidean distance of $||s_0 - s_1|| = 2$ between them. However, if the negative value is 0.7 of the amplitude of the other, normalised to 1 the constellation becomes $[0.811, 1.159]$. This decreases the Euclidean distance between the two to $||s_0 - s_1|| = 1.97$. That this is a small decrease shows the robustness of BPSK - with a similar analysis for QPSK the distance between two neighbouring constellation points reduces from $\sqrt{2}$ to 1.31 (Fig. 2.23b). This decreased Euclidean distance will increase the error probability at a given constellation power. This will become important when the distorting effects of FSS DAM are considered throughout this thesis.

2.4.2 Spread spectrum communications

Signal design for overcoming the effects of fading, both narrowband and wideband, has been a focus of wireless communications for many years. One key innovation was direct sequence spread spectrum (DSSS), which emerged from defence communications [126], and a form was used in the 3G mobile communications standard Universal Mobile Telecommunications System (UMTS) [127]. While previously wideband fading had been avoided by ensuring the symbol period T_s is greater than the maximum relative delay τ_L of the channel, DSSS transmits a signal that occupies a significantly greater bandwidth than the message requires. This is done by multiplying each data symbol by some code $\boldsymbol{c}(t)$, which consists of N chips (Fig. 2.24). As such, each data symbol is represented by a sequence of N (Fig. 2.25a).

A stream of binary data is mapped to complex baseband symbols

$$b(t) = \sum_{i=-\infty}^{\infty} b_k P_{T_b}(t - iT_b) \tag{2.19}$$

where b_k is the kth symbol and $P_{T_b}(.)$ is the symbol pulse shaping function. Here it is assumed that unit rectangular pulses are used. The spreading sequence stream is given by

$$c(t) = \sum_{i=-\infty}^{\infty} c_{i(modN)} P_{T_c}(t - iT_c) \tag{2.20}$$

where c_k is from the length N spreading sequence vector $\mathbf{c} = [c_0, c_1, ..., c_{N-1}]$, which in this thesis may be binary or polyphase, and the chip pulse shaping factor $P_{T_c}(.)$ is again rectangular. The baseband transmitted signal is given by

$$s(t) = \sqrt{2P} b(t) c(t) \tag{2.21}$$

where P is the transmit power.

The aim is that each symbol undergoes wideband fading within the length of the code, causing intrasymbol interference (IntraSI). This means that, firstly, the InterSI is limited to a small portion of each symbol, reducing its influence. Secondly, once the received signal is correlated with the same $c(t)$, the magnitude of the IntraSI is determined largely by the autocorrelation properties of the code. In the ideal scenario, the code will have an autocorrelation with a large peak when the code has a zero shift, and all zeros elsewhere, like an impulse (Fig. 2.25b). This situation removes IntraSI completely, while codes with small sidelobes reduce the IntraSI significantly. Sequences with suitable properties for use as codes in DSSS systems are discussed later in this Chapter.

Finally, the interference-suppressing characteristics of the code allows the receiver to take advantage of the multiple copies of the signal. As each path is likely to fade differently, if not independently, when one path is heavily faded it is statistically likely that there is another path which has a greater power. Choosing the strongest path is known as selection diversity, and reduces the statistical chance of an error, as all paths must have low power to cause errors, which is less likely. Further, a RAKE receiver may be used to collect energy

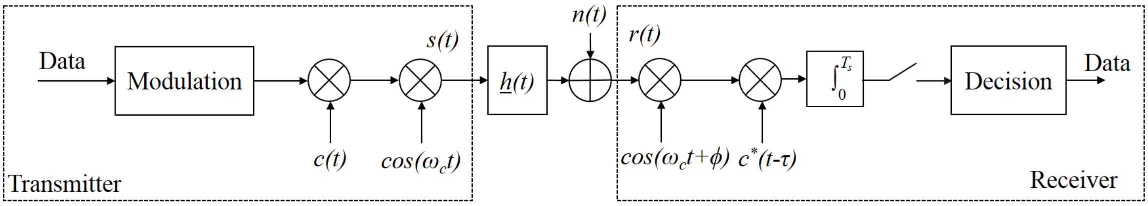

Figure 2.24: A Direct Sequence Spread Spectrum communications system

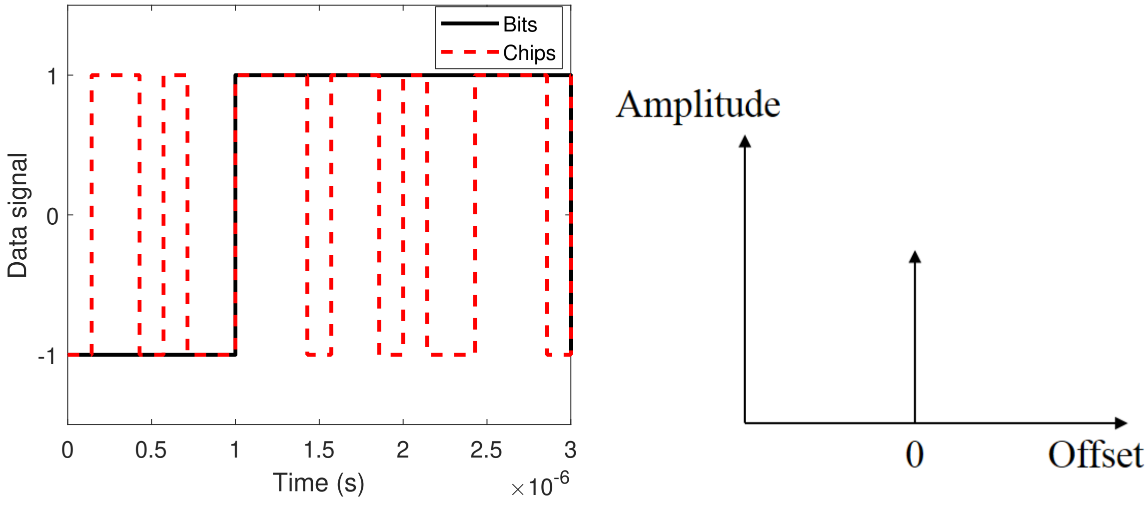

(a)

(b)

Figure 2.25: (a) Time domain waveform of BPSK data and that data spread by a length 7 Barker sequence, (b) Ideal autocorrelation response

from multiple paths simultaneously in a DSSS system, taking advantage of all the incident power and so improving performance (Fig. 2.26) [128]. Maximum ratio combining (MRC) is often used, multiplying each delayed path by the conjugate of its own channel response to maximise the effect of strong paths on the final decision, while minimising the effects of heavily faded paths which are likely to add more noise than signal.

2.4.3 Sequences

In order for DSSS to operate, sequences with 'good' autocorrelation properties must be chosen as the spreading codes. In addition to use in DSSS, sequences with good autocorrelation properties are also useful for use as pilots - known sequences sent by a transmitter to allow the receiver to estimate the channel response and latch on to the transmitted signal. As what is good for one use is good for the other, they will be treated together here.

The aperiodic autocorrelation $A(\Lambda)$ of sequence $\boldsymbol{c}$ consisting of elements c_i, for $0 \leq i \leq$

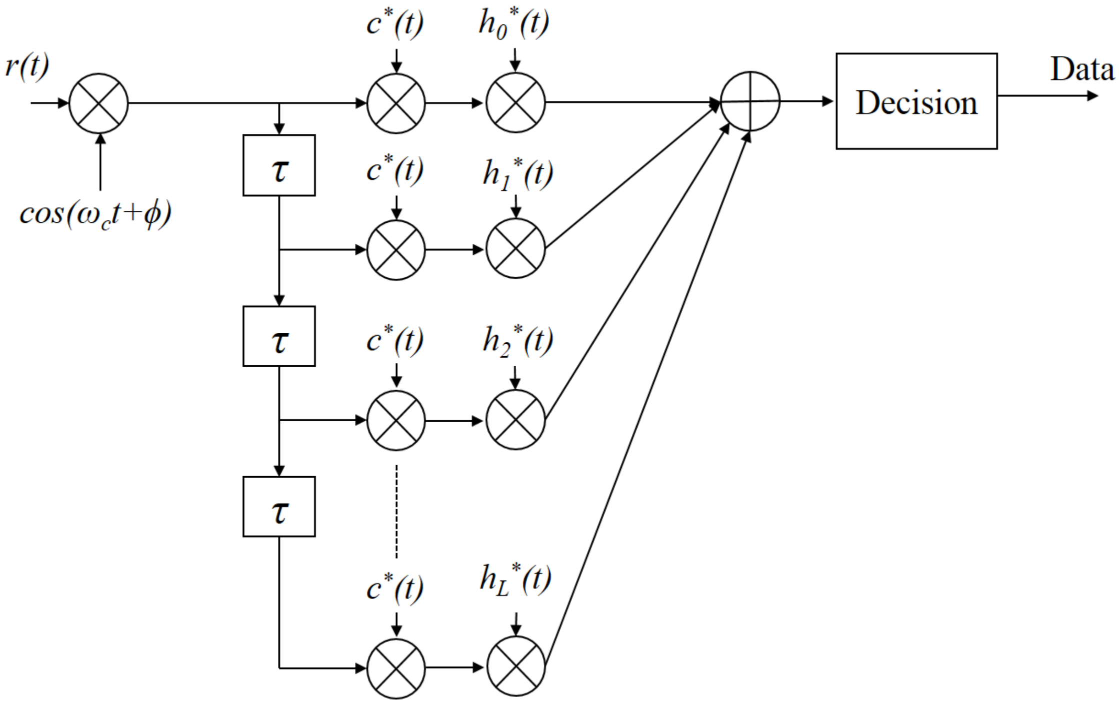

Figure 2.26: A RAKE receiver

$N - 1$ at offset Λ is given by

$$A(\Lambda) = \begin{cases} \sum_{j=0}^{N-1-\Lambda} c_j c_{j+\Lambda}^*, & \text{if } 0 \leq \Lambda \leq N-1 \\ \sum_{j=0}^{N-1+\Lambda} c_{j-\Lambda} c_j^*, & \text{if } 1-N \leq \Lambda \leq 0 \\ 0, & \text{if } |\Lambda| \geq N \end{cases} \tag{2.22}$$

while the periodic autocorrelation $W(\Lambda)$ of the same sequence is

$$W(\Lambda) = \sum_{m=0}^{N-1} c_m c_{m+\Lambda}^* \tag{2.23}$$

The aperiodic autocorrelation is useful for analysing the effect of a single sequence on its own, while the periodic usually occurs when multiple copies of the sequence are transmitted after each other. For sequences with all elements of unit magnitude, including binary sequences, both autocorrelations give $A(0) = W(0) = N$ as the peak of their response, which is the in-phase correlation of any sequence. The other values, however, depend on the sequence under test. As has already been stated, an ideal unit magnitude sequence would have an autocorrelation of N at $\Lambda = 0$ and 0 elsewhere. In practice, there are very few codes that achieve this. If the sequence is binary, only the length four Barker code has this property, and only in the periodic domain [129]. How close a sequence is to the ideal aperiodic autocorrelation is often represented by its Merit Factor:

$$MF = \frac{N^2}{E} \tag{2.24}$$

where the energy in the sidelobes, E, is given by

$$\begin{aligned} E &= \sum_{\Lambda=-N+1,\Lambda\neq 0}^{N-1} A(\Lambda)A^*(\Lambda) \\ &= 2\sum_{\Lambda=1}^{N-1} A(\Lambda)A^*(\Lambda) \end{aligned} \tag{2.25}$$

As such a sequence with a high MF has significantly more energy at zero correlation than across the rest of the sequence phase shifts. This means that when the sequence is used as a code in a DSSS system, the energy in each path after correlation will mostly be due to the desired correlated signal, rather than due to InterSI. This reduced interference improves error performance. When used as a pilot, a high MF means that the sequence will produce a strong signal when the receiver is synchronised with the transmitted signal and a weak one when it is not, making it easier for the receiver to synchronise appropriately. When estimating multipath, it also reduces the influence of other paths on a channel estimate in the same way the sequence suppresses InterSI in DSSS, increasing the accuracy of the estimate.

The binary sequences with the nearest autocorrelation response to the ideal are called the Barker sequences [130]. These have responses with sidelobes which take values of either 0 or ±1 (Fig. 2.27). This gives them very good merit factors, giving values of 8.17 and 14.1 for length 7 and 13 codes respectively. Because of this stringent condition there a very few of these sequences, with the longest known being 13, and for each length there exists only one sequence and its reciprocal. This restricts their use, as often long codes are used to overcome very wideband fading in dispersive environments, and multiple access approaches to spread spectrum require more than one code in a set [128]. Further, not all the Barker codes are balanced or pseudobalanced - properties of binary codes where the number of 1s is equal to or one greater than the number of 0s, respectively.

Balanced and pseudobalanced sequences are useful for security, as balanced codes appear pseudorandom, and unbalanced sequences cause an effective direct current (DC) offset in transmitters as more of some values are transmitted than of others. As such, m-sequences (from 'maximum length') are often used [131]. These are generated using shift registers, and as such long codes can be generated while using minimal storage space on a device. m-sequences are then used to generate large sets of Gold codes, though this is beyond the scope of this thesis. They do, however, have good autocorrelation properties, with merit factors of 4.17 and 4.67 for lengths 15 and 31 respectively (Fig. 2.28). Note that the length

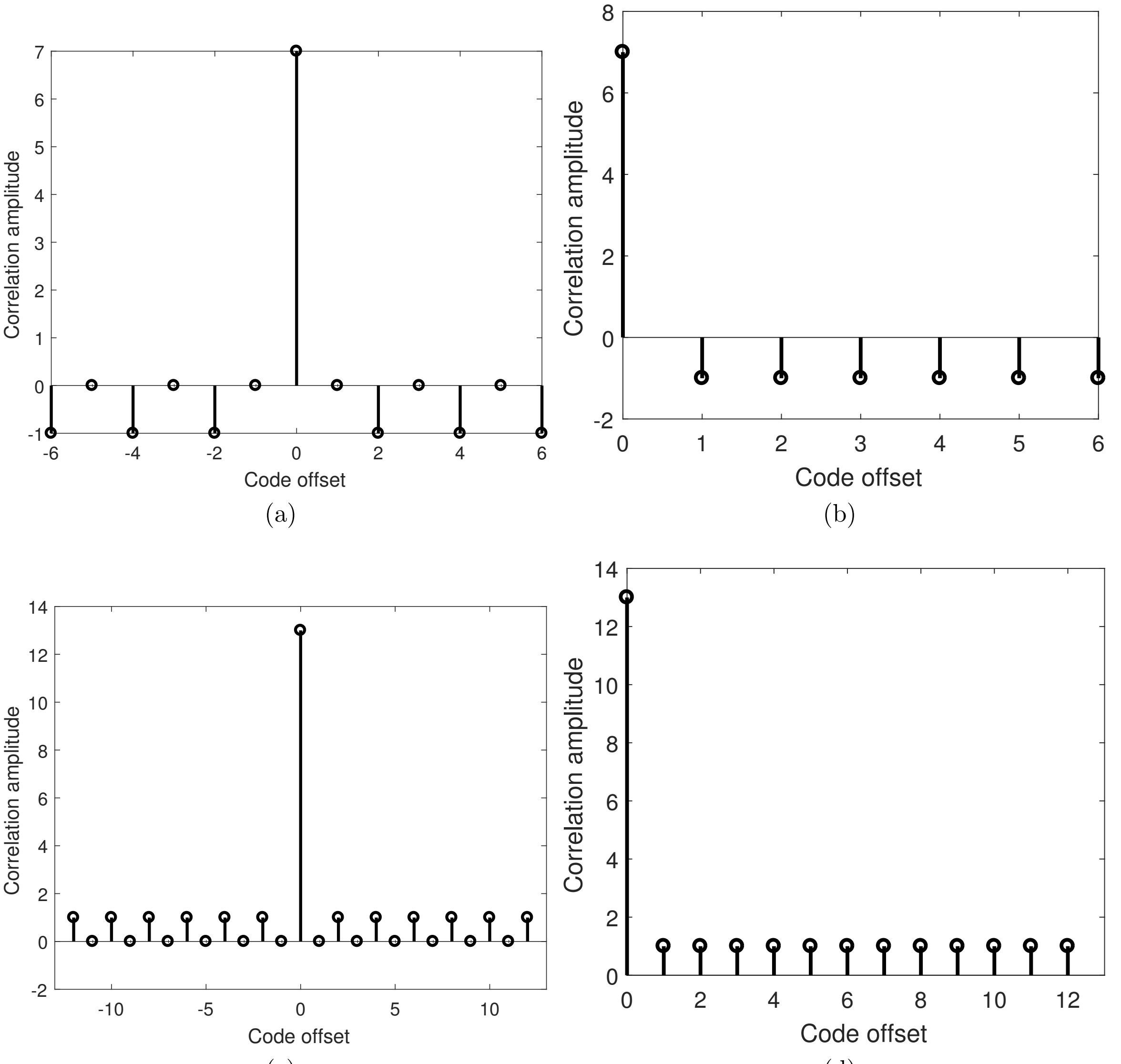

(a) (b)

(c) (d)

Figure 2.27: Autocorrelation of Barker sequences, (a) Length 7 aperiodic, (b) Length 7 periodic, (c) Length 13 aperiodic, (d) Length 13 periodic

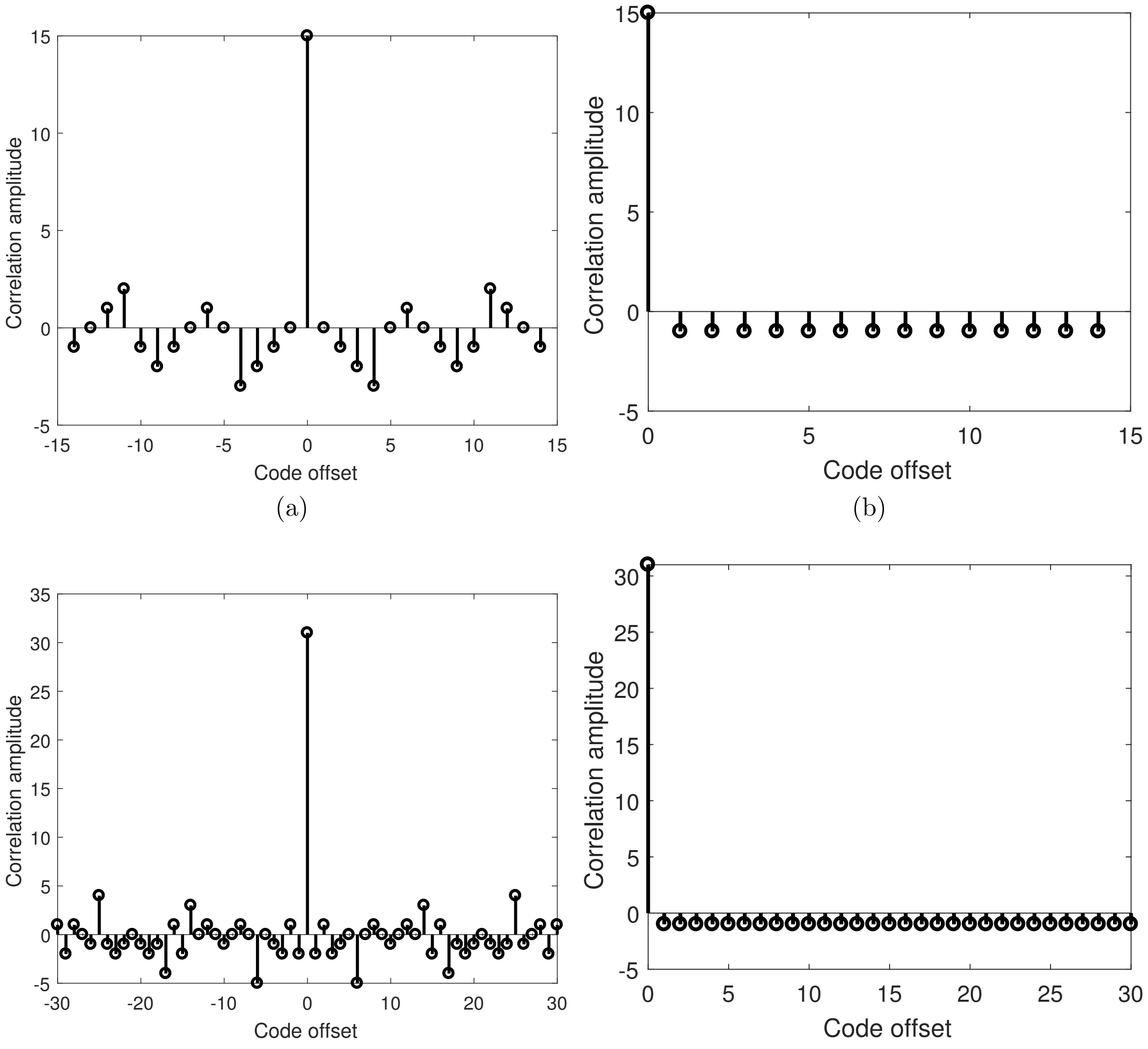

(a) (b)

(c) (d)

Figure 2.28: Autocorrelation of m-sequences, (a) Length 15 aperiodic, (b) Length 15 periodic, (c) Length 31 aperiodic, (d) Length 31 periodic

	EC-GSM-IoT [135]	LTE-M [136]	NB-IoT [137]
Frequency bands (MHz)	900, 1800	800, 900, 1800, 2100, 2600	800, 900, 1800, 2100, 2600
Modulation format	GMSK, 8PSK	QPSK, 16QAM	BPSK, QPSK
Bandwidth (kHz)	200	1080	180
Data rates (kbit/s)	70, 240	$\leq$1000	20, 240
Multiple access	TDMA, RMA	OFDMA (128), SC-FDMA	OFDMA (128), SC-FDMA
Latency (ms)	700 - 2000	10 - 15	1060 - 10000
Urban coverage (km)	1	0.5	1
Devices per gateway	50,000	50,000	55,000

Table 2.2: Comparison of metrics for various cellular IoT standards

7 Barker sequence is also an m-sequence.

This thesis uses the length 15 m-sequence for two purposes. First it is used as the pilot sequence for the designed DAM systems. It is appropriate for this due to its high merit factor for its length, allowing easy synchronisation with the received signal and also accurate channel sounding. Second, it is used as part of a DSSS DAM system in order to ameliorate the distorting effects of FSS DAM. Here the pseudobalanced property of the m-sequence are particularly useful.

2.5 Communications systems for the Internet of Things

The Internet of Things (IoT) is an emerging paradigm where many devices are connected together with minimal human intervention, allowing simple monitoring of industrial or agricultural equipment, improved provision of utilities and public services, and more efficient running of people's home lives [3]. In order to enable this, these devices must be able to connect to each other through some network, which, to aid mobility and flexibility, often include wireless links. As such, many different public standards and proprietary systems have been developed to provide these links in different situations. These can be considered in two distinct categories. First, low range wireless personal access network (LR-WPAN) are short-range, low-throughput standards for device-to-device communications [132]. These will not be examined in depth in this thesis, as size limitations mean FSS DAM is not suitable for many applications in which these standards are used. The second is low power wide area network (LPWAN), which aim to connect large numbers of devices over an area over 1km with low to mid-rate throughputs [133, 134]. These technologies require base stations or access points, meaning potential energy savings may be made with FSS DAM technology. This Section will explore some of the key existing standards in LPWAN.

EC-GSM-IoT is a 3GPP standard which operates within the bands licenced for use by GSM mobile communications (Table 2.2) [135]. It was designed as an enhancement to the General Packet Radio Services (GPRS) data transfer protocol, extending the number of

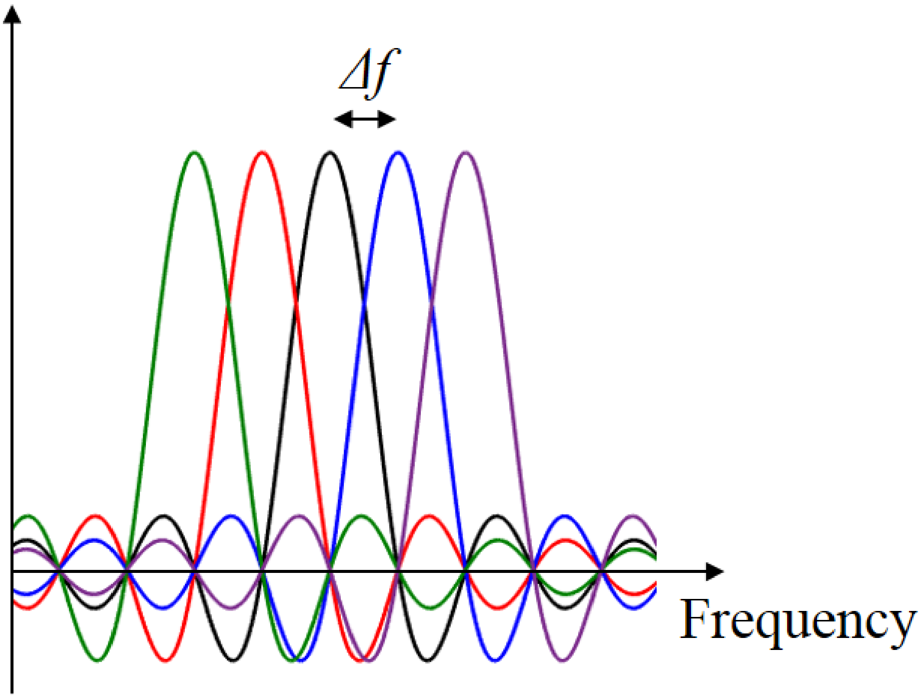

(a)

Figure 2.29: Frequency domain diagram of OFDMA multiple-access technique

devices that could be supported with time division multiple access (TDMA) and random multiple access (RMA) techniques to around 50,000 per cell. Further, the data rates were enhanced by allowing 8PSK modulation as an alternative to GMSK, increasing data rates from 70kbit/s to 240kbit/s while maintaining compatibility with existing Enhanced Data for GSM Evolution (EDGE) transmitters. This allows relatively small amounts of data to be transmitted over wide areas in situations where latency requirements are relaxed, while allowing the devices to be simple and have long battery lives of around 10 years. These requirements are common in applications involving remote data collection from sensors. EC-GSM-IoT also leverages the ubiquity of GSM base stations across the world. Note, however, that this scheme requires an equaliser at the receiver, which increases the complexity of the system.

At the other end of the scale is LTE-M, another 3GPP standard which aims to provide medium data rate, low latency machine communications, targeting applications requiring continuous and real-time data transfer, such as precision asset tracking [136]. To do this, it uses existing LTE infrastructure, spectrum and waveforms, utilising a portion of LTE resource in a given cell (Table 2.2). It also uses orthogonal frequency division multiple access (OFDMA) on the downlink, and its close relation, single carrier frequency division multiple access (SC-FDMA), on the uplink, as in mobile LTE [138]. These waveforms will not be explored in detail here, but they use multiple narrowband, closely spaced but orthogonal

	Sigfox [139]	Ingenu [26]	LoRaWAN [25]
Frequency bands (MHz)	868,902	2400	433, 868
Modulation format	DBPSK	DBPSK	CSS
Bandwidth (kHz)	0.1	1000	125, 250, 500
Data rates (kbit/s)	0.1 - 0.6	0.01 - 8	0.3 - 37.5
Multiple access	RMA	RPMA	RMA
Urban coverage area (km)	3 - 10	5	3-15
Devices per gateway	10^6	10^4	10^4

Table 2.3: Comparison of metrics for various proprietary LPWAN IoT technologies

carriers to divide spectrum between users efficiently (Fig. 2.29a). In LTE based systems, each subcarrier is spaced by 15kHz. It also supports both QPSK and 16-QAM modulation formats. LTE-M differs from mobile LTE in using a narrower bandwidth of 72 subcarriers, giving a total bandwidth of 1.08MHz instead of the standard 20MHz, in order to reduce the cost and energy consumption of the devices. In order to reduce the complexity of the system, the size of the Fast Fourier transform (FFT) used for orthogonal frequency division multiplexing (OFDM) is reduced from the LTE standard 2048 to 128, though the processing required is still relatively complex. Further, the battery life is extended up to 10 years by introducing deep sleep modes for the wireless devices. This all allows relatively low average power operation while enabling low latency communications with IoT devices when they are active.

The final 3GPP IoT standard is NB-IoT, which also makes use of LTE infrastructure, but transmits narrowband signals either within the operating bandwidth of mobile LTE, or in the guard bands surrounding them [137]. As with LTE-M, the uplink and downlink are designed to retain orthogonality with LTE, using OFDMA on the downlink and SC-FDMA on the uplink with the same numerology as LTE. The main difference is the much smaller bandwidth, using up to 12 15kHz channels to give a total bandwidth of 180kHz (Table 2.2). The FFT size for OFDM is again 128, allowing operation over a broader set of subcarriers than required in order to allow coexistence with mobile LTE systems. This increases the complexity of the system. BPSK and QPSK are used to reduce the PAPR and so increase the energy efficiency of devices, though this reduces the data rate to 20kbit/s per channel. The narrow bandwidth means an estimated 10,000 devices can be connected in a single cell, enabling low-throughput and sporadic transmission of data with latencies in the order of seconds, suitable for applications such as smart metering and other sensor networks.

Proprietary IoT standards have also been developed. One of these, Sigfox, uses an ultra-narrowband (UNB) approach, transmitting very small packets of up to 12 Bytes in the uplink with channel bandwidth of 100Hz [139]. This means that, by putting all the transmitted energy into a small bandwidth, the signal is decodable even when coexisting with high power but more spectrally spread signals. This may occur often, as Sigfox signals are transmitted in unlicensed bands, specifically sub-GHz bands to increase coverage range. In addition, the robust differential binary phase shift keying (DBPSK) modulation format is used- where the data bit transmitted is determined by the change in phase from the previous bit of either 0 or π. This all makes the coverage area for Sigfox very large- up to 10km in urban environments and 50km in rural ones. Further, DBPSK removes the need for pilot signals, reducing the length of the packets transmitted. Packet length is also reduced by not using any error detection coding. However, to maximise the number of device connections, each device is limited to 140 uplink and 4 downlink packets per day. This allows around 1 million devices to connect to a single gateway, but means the practical latency may be very high. As such, Sigfox is best suited to applications requiring occasional transmission of small packets of data, such as soil monitoring sensor networks in agriculture.

Ingenu is another company with a proprietary solution to IoT connectivity [26]. The underlying technology, random phase multiple access (RPMA), was developed for connecting devices in the oil industry, and has since been adjusted for more general LPWAN solutions. RPMA uses a Gold code- a pseudo-random binary sequence derived from an m-sequence [140]- of length between $2^9 = 512$ and $2^{13} = 8192$ on the uplink or between $2^4 = 16$ and $2^{11} = 2048$ on the downlink, to spread the DBPSK modulated data as in DSSS techniques [141]. This provides both a very high processing gain, giving robustness against interference in the unlicensed 2.4GHz band while enabling data rates between 10bit/s and 8kbit/s, and allows multiplexing through choice of a random offset sequence phase for each device to transmit on. As such, it is likely that every device will be transmitting the same Gold code with a different code offset. Due to the low sidelobes of Gold codes, this means that the messages from each device will be nearly orthogonal to each other, with only small amounts of interference added. This allows approaching 10^4 devices to be connected to a single access point, while the large processing gain gives a coverage range of around 5km in urban environments. The length of the codes makes the latency large compared with some cellular approaches, but the unlimited messages per device means there is significant advantages over Sigfox. Convolutional coding is also used to increase the receiver sensitivity and so increase the coverage range. RPMA supports both uplink and downlink, using time division duplexing (TDD) with 50% of the time use by each, and uses a 1MHz bandwidth. Also, the variability of spreading rates allows greater resilience to fast variation in the channel. As such, this is suitable for applications requiring constant low rate data transfer, such as smart metering and building monitoring.

The final approach explored here is the Long Range Wireless Access Network (LoRaWAN) [25]. LoRa is the proprietary physical layer technology belonging to Semtech, while LoRaWAN describes the higher layer protocols, which are open access [142]. It oper-

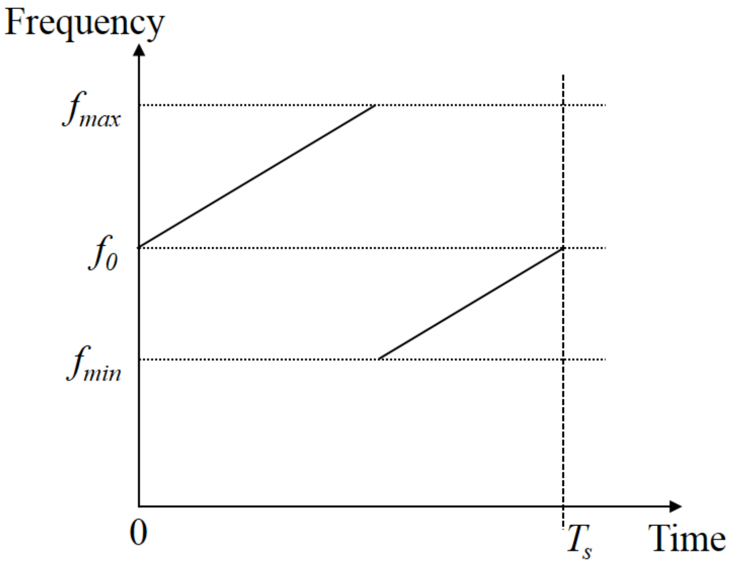

(a)

Figure 2.30: Representation of a chirp spread spectrum symbol

ates within the unlicensed sub-GHz ISM bands. LoRa uses CSS as its modulation format, meaning the bandwidth describes the distance between the maximum and minimum frequency each symbol can take. Every symbol begins with some start frequency determined by the data bits, and increases linearly with time to the maximum frequency of the channel, before dropping to the minimum frequency and rising at the same rate to the start frequency (Fig. 2.30a). This is known as a chirp, or Compressed High Intensity Radar Pulse. The rate of change of frequency during the chirp- and so its duration- depends on the spreading factor F, which in LoRa takes on powers of 2 between $2^6 = 64$ and $2^{12} = 4096$, while the starting frequency depends on the values of $log_2(F)$ data bits [143]. Each signal with a given F is orthogonal to the other, while signals with different values of F are nearly orthogonal, allowing recovery of the transmitted data using a correlator receiver [144]. The pseudo-orthogonality of CSS symbols is used to increase multiple access to the channel, in addition to using RMA techniques, allowing around 10000 devices to connect to a single access point. This is similar to that achieved by Ingenu's RPMA but much less than the number of connections supported by Sigfox. The variable spreading rates allows variation in the data throughput from 0.3 to 37.5kbit/s, similar to the performance of Ingenu and greater than that of Sigfox.

2.6 Direct Antenna Modulation for the Internet of Things

Finally, this Chapter will examine how currently existing DAM technologies may be useful in the implementation of IoT networks. The low-cost, energy efficient modulation provided by some DAM approaches is of particular interest, both in devices, where battery life and cost per unit are key concerns; and in access points, where the energy efficiency and complexity of the transmitters impacts on the costs of the IoT service provider. Different DAM technologies will be evaluated for their ability to recreate the modulation formats, symbol rates and multiple access schemes of the IoT protocols explored above, and their suitability for use in devices or access points in different application scenarios.

NF-DAM requires the use of antenna arrays, though here to produce directional modulation [17]. It is notable amongst DAM techniques for having demonstrated simultaneous transmission of different channels [53]. While higher order constellations are possible using this technique, multiple antennas goes against the low complexity, low form factor approach taken by all IoT protocols. Further, finding the appropriate direction to transmit constellations in adds more complexity to any IoT system using NF-DAM.

DAM using integrated switches, as in [42], appears to be more favourable to use in IoT communications. The low form factor of the planar devices used is of particular interest, with electrical sizes of $0.32 \times 0.39 \times 0.01\lambda^3$ being typical. This suggests that integrated switch DAM may be of particular use within devices. However, the limited modulation types preclude the use of integrated switch DAM from LP-WAN communications.

Finally, reflective metasurfaces have been used to BFSK [57] and 8PSK modulation [59]. This is promising for the EC-GSM-IoT standard, which uses both 8PSK and GMSK, as well as for most proprietary LPWAN technologies, which use DBPSK, GMSK and QPSK. It should be noted here that GMSK is continuous phase, so should be producible by any continuous phase modulator. However, the metasurface used is electrically large, though thin, at $5.44 \times 1.36 \times 0.07\lambda^3$. This means it is unlikely to be used in devices and so the mesh networks of LR-PWAN technologies. It could still be used as an access point, perhaps mounted on top of a building. If so, the size of the required feed should be taken into account, which must illuminate the metasurface with a plane wave from the metasurface's farfield, though the distance of the feed from the surface is not given in [59]. Further, while the directivity and modulation performance outside the beamwidth is not considered in any of these papers, due to the electrical size of the surface we can expect the directivity to be high or the modulation to be directive, or both. As such, the suitability for using a modulating metasurface as an LPWAN downlink transmitter, which must cover large areas equally, is uncertain.

This demonstrates that the potential benefits of DAM transmitters for IoT networks, in particular their potentially high efficiency and low complexity, remain largely unexploited. This is despite the expected growth in the number of connected devices, which is likely to mean the number of devices supported by LPWAN technologies will limit their range of deployment [3]. As this occurs, the number of access points required to provide IoT services will have to increase, and the installation and running costs of transmitters at the base stations will become more significant for the service provider [14]. The challenge of energy efficient, cost effect connectivity for IoT service providers is an opportunity for the emerging technology of FSS DAM.

Chapter 3

FSS DAM: Concept and development

3.1 Introduction

This thesis has already shown that the solution to increasing capacity for increasing numbers of Internet of Things (IoT) devices might be found through cost-effective densification of wireless access points using direct antenna modulation (DAM). However, as has also been outlined, this potential is yet to be leveraged with existing DAM technologies. This Chapter will explore the process for designing a DAM unit using transmissive frequency selective surfaces (FSS) which has the potential low complexity, energy efficient characteristics required for use in dense IoT wireless networks.

The design requirements for this DAM unit are outlined in Table 3.1. The key parameter is that the FSS DAM design should produce generic phase modulation, and could then be used for phase shift keying (PSK) in particular. The frequency of operation chosen is 1.8GHz as it is a licensed mobile frequency band recently opened up for EC-GSM-IoT communications, so the DAM unit designed will operate in an accepted IoT band [135]. However, the performance will be similar across the microwave region used by IoT communications. The unit will also be designed to operate at over 1MSymbol/s, which is of a similar order to spread spectrum IoT techniques Ingenu and LoRa [25, 26]. For demonstration purposes, the design will focus on producing a single linear polarisation. Finally, the unit should have an aperture of approximately $\lambda_0/2$ in order to facilitate the use of these units in arrays, where the antenna spacing is usually around $0.6\lambda_0$. The depth of the unit is more flexible, but will be kept as small as possible.

First, the concept of using transmissive FSS to phase modulate is presented, and some of the advantages are discussed. The requirements and design of FSS for achieving various types of phase modulation is then examined. Finally, a general design is produced for a reconfigurable antenna, which can act as the modulator in a phase FSS DAM transmitter.

Parameter	Requirement
Modulation format	Phase (PSK)
Frequency of operation	1.8GHz
Symbol rate	> 1MSymbol/s
Polarisation	Linear
Size	$\frac{\lambda_0}{2} \times \frac{\lambda_0}{2} \times \lambda_0$

Table 3.1: Key design requirements for FSS DAM

3.2 Concept and advantages of FSS DAM

This thesis has previously discussed the overall design and potential advantages of DAM as a transmitter technology (Section 2.2). Fig. 2.2b shows a generic DAM transmitter, where a CW carrier is amplified to transmit power, and modulation occurs at or after the antenna. For phase FSS DAM, this broad architecture remains, but the modulation process is a reconfigurable, multilayer FSS in front of a passive antenna (Fig. 3.1a). This FSS acts as a tunable bandpass filter, with its centre frequency varying with the capacitance of the variable capacitor (Fig. 3.1b). By varying the filter's centre frequency, while keeping the CW carrier within the passband, the changing phase response of the FSS alters the phase of the transmitted signal. As such, the phase of the wave transmitted by the FSS is controlled by a baseband modulating signal sent to the variable capacitors integrated into the FSS. For barium strontium titanate (BST) based and diode variable capacitors, this control signal is a bias voltage waveform, where any continuous voltage level corresponds to a capacitance, which also varies continuously. For microelectromechanical systems (MEMS) or digitally tuned variable capacitors, the control signal would be a digital word describing the desired capacitance, which changes discretely. The FSS, which now acts as an analogue phase modulator, can be made to produce a PSK modulation by choosing appropriate control signals for each desired PSK constellation point, and sending these signals to the FSS to transmit.

This process has several advantages over conventional modulation, and over other state-of-the-art DAM technologies. First, as with all DAM techniques, FSS DAM benefits from the power amplifier (PA) running in its non-linear region without added distortion due to the constant evelope of the carrier, improving the overall efficiency. In addition, the amount of energy used on cooling will be reduced. Further, the amount of RF electronics required is reduced significantly, and replaced with baseband electronics operating at the symbol rate providing the signals for the variable capacitors. This reduces the total size and power consumption of the transmitter.

FSS DAM is also able to reproduce conventional, and higher order, modulation schemes,

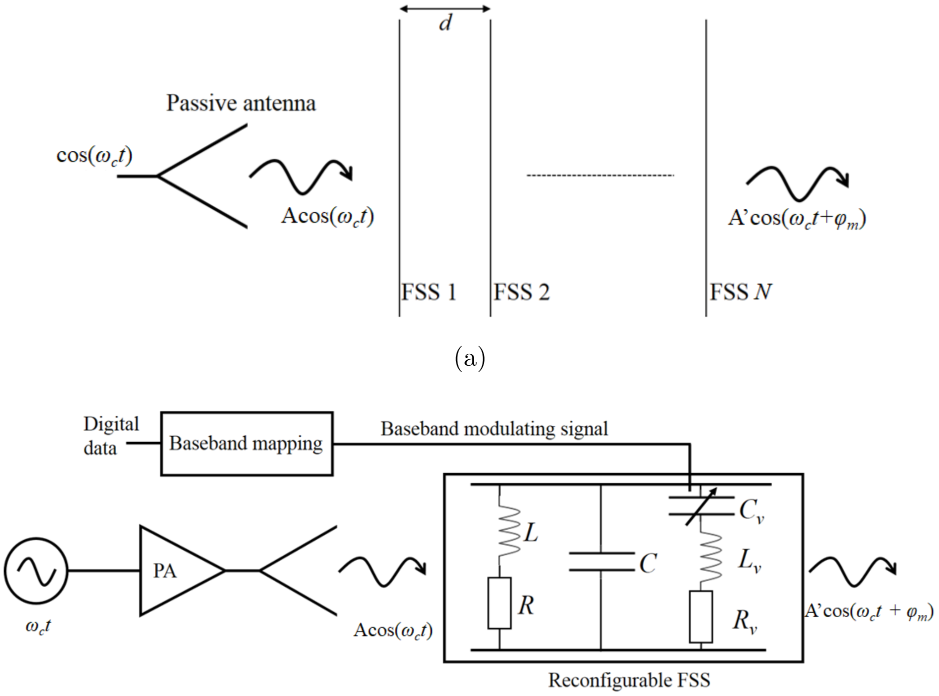

(a)

(b)

Figure 3.1: A PSK FSS DAM transmitter, (a) Physical overview, (b) Conceptual diagram

in particular PSK. This is an advantage over the DAM transmitters using components integrated into antennas, which can only produce OOK or basic amplitude modulation, as discussed in Chapter 2.2. FSS also have the advantage of using variable capacitors to produce the modulation, which in some cases, particularly for diode-based capacitors, can achieve switching speeds of less than 100ns [145]. This allows bandwidths in the order of 10MHz to be output, significantly more than has been achieved by NF-DAM. The modulation produced by FSS DAM is also non-directional, making it more easily applicable in IoT and broadcast applications than NF-DAM. Finally, a well-designed FSS DAM unit will always keep the carrier wave within the passband of the FSS. This means that there are minimal reflections from the DAM unit back toward the PA.

3.3 Designing frequency selective surfaces for DAM

The FSS in a PSK DAM transmitter must be capable of producing at least the amount of phase change required for the desired constellation, while minimising the amount of magnitude distortion of constellation points. This distortion reduces the Euclidean distance between constellation points, and so impacts on the transmitter performance. It should also have minimal transmission loss, in order to benefit from the efficiency gains of using DAM. This section discusses the design questions for the FSS, such as the unit cell element shape,

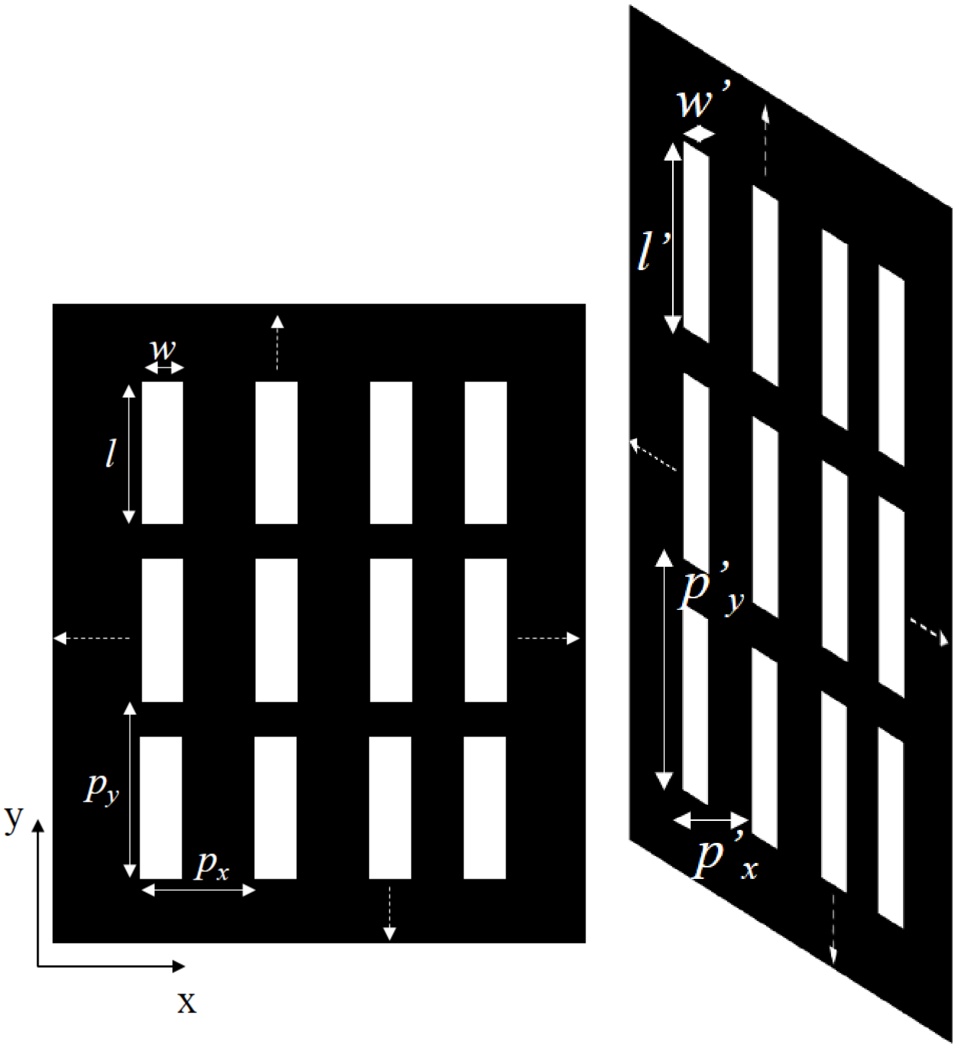

(a) (b)

Figure 3.2: Effect of varied angle of incidence on effective aperture geometry for dipole unit cells. (a) Orthogonal incidence, (b) oblique incidence

the dimensions of the unit cell geometry, the choice of devices to add reconfigurability, and the number of layers required.

3.3.1 Unit cell design

As discussed in Section 2.3, an FSS consists of periodically repeating metallic elements on a two-dimensional surface. The choice of the type of element depends on whether the desired effect is bandpass or bandstop, the bandwidth produced by the element and the stability of the element's response with different angles of incidence. Practical considerations should also be considered, such as the physical size of the element and its ease of modelling and fabrication.

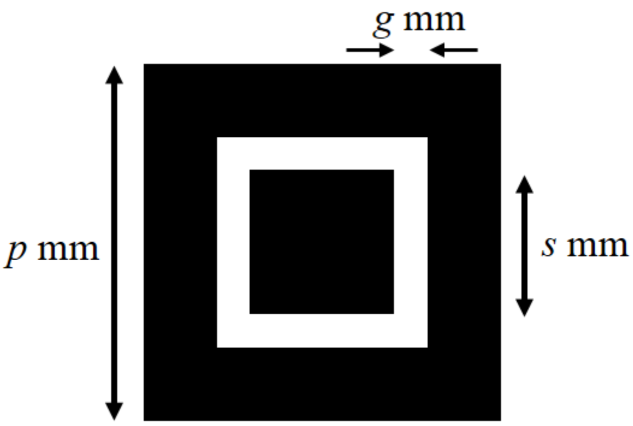

Figure 3.3: Geometry of a square loop aperture unit cell

Throughout this thesis, a transmissive FSS modulator has been chosen. This is principally because it allows simple implementation of multiple layers to increase the bandwidth and phase change available. As such, the unit cell should be an aperture, giving a bandpass response. While the simplest aperture element is a dipole, this element has a narrow bandwidth and is unstable with changing angles of incidence. This can be seen by picturing how quickly the geometry of the aperture 'visible' to an incident wave changes as the angle of incidence changes (Fig. 3.2). When the incident wave is travelling in the z direction while the surface is in the $y-x$ plane, so orthogonal to it, the surface has elements with length l, width w and periodicities in the x and y directions p_x and p_y respectively (Fig. 3.2a). However, when the surface is rotated around the y axis such that the incidence is now oblique, the element width appears to reduce from w to w', the length l appears to change to l', and periodicities p_x and p_y reduce to p'_x and p'_y (Fig. 3.2b). The element shape also appears to have altered. As such, the incident wave interacts differently with the surface at oblique angle to how it does at orthogonal incidence, shifting the resonant frequency. These problems can be mitigated by using a loop aperture unit cell, which has a broader bandwidth and is more stable with changing angles of incidence (Fig. 3.3) [72]. Loop apertures also have the advantage of being electrically smaller than dipole apertures. Choosing a square loop shape makes the element simple to model, simulate and fabricate due to their straight lines; while the rotational symmetry of the element means the performance changes only minimally with the polarisation of the incident wave. They also have an established equivalent circuit model, discussed in detail in Section 2.3.

There are three dimensions that can be varied to alter the geometry, and so reflection characteristics, of a square loop FSS: the periodicity p, the inner patch dimension s, and the width of the aperture g (Fig. 3.3). The unit cell will resonate when the largest circumference of the loop $c \approx \lambda/2$ where λ is the wavelength of the incident wave. This suggests that the

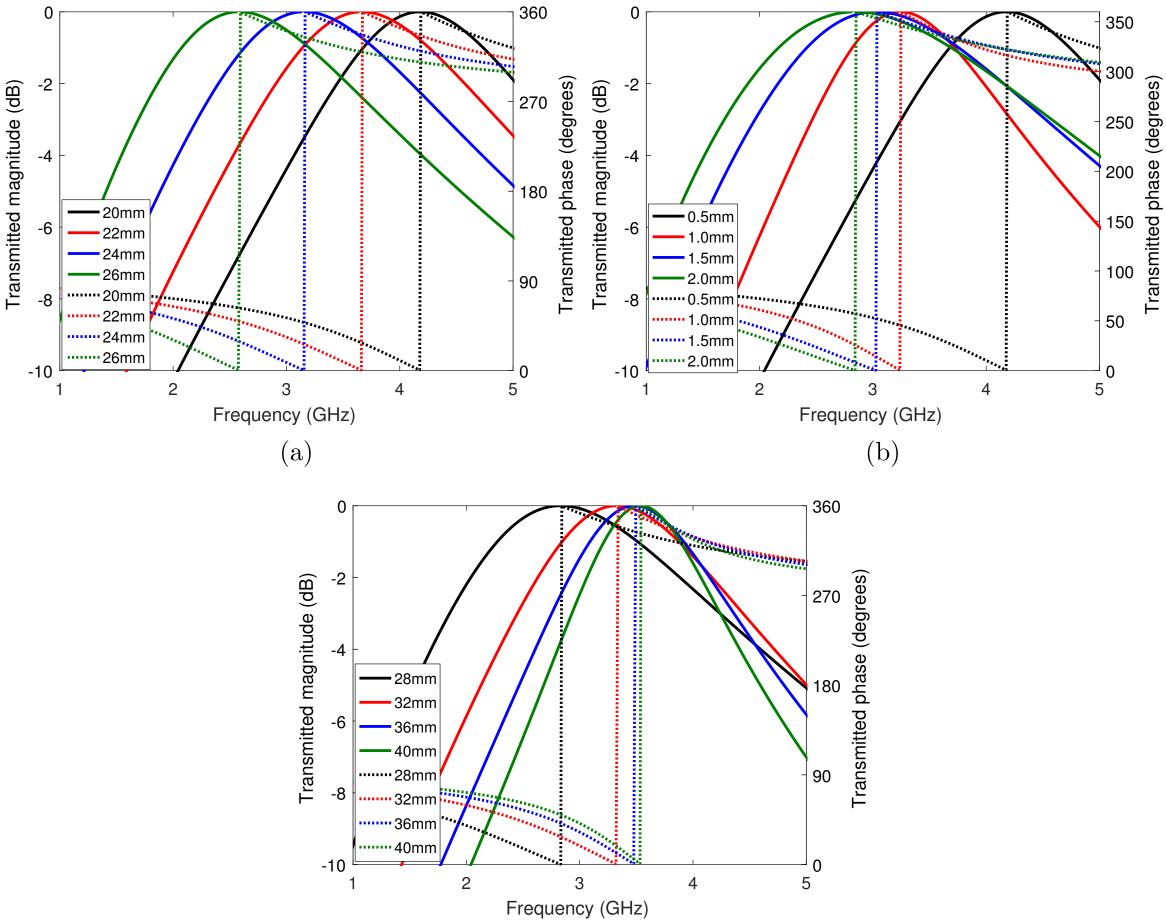

(a) (b) (c)

Figure 3.4: Simulated magnitude (solid lines) and phase (dashed lines) of lossless square loop aperture FSS S_{21} in free space with Floquet mode boundaries, s=24mm, p=30mm, g=1mm, while varying (a) s, (b) g and (c) p.

most important dimensions for determining the resonant frequency f_0 are s and g, with larger values of each resulting in a lower resonant frequency. This is supported by simulation of a lossless, single-layer, infinitely sized square-loop FSS in free space using Floquet boundaries in CST (Fig. 3.4a). It should be noted, however, that the increasing g while keeping s fixed eventually causes the decrease in resonant frequency to slow and saturate (Fig. 3.4b). However, in addition to this, the value of p also affects the response, with increasing p resulting in an increase in the resonant frequency. This effect lessens as p gets larger relative to s, as the resonance of the unit cells alone becomes dominant over the resonance of the whole array due to coupling between adjacent elements becoming smaller (Fig. 3.4c). This also accounts for the reduction in bandwidth as p and s move further apart. These effects are also described by the equivalent circuit model of Langley and Parker, discussed in Section 2.2 [74].

Note that the transmitted magnitude and phase through the FSS may also be defined

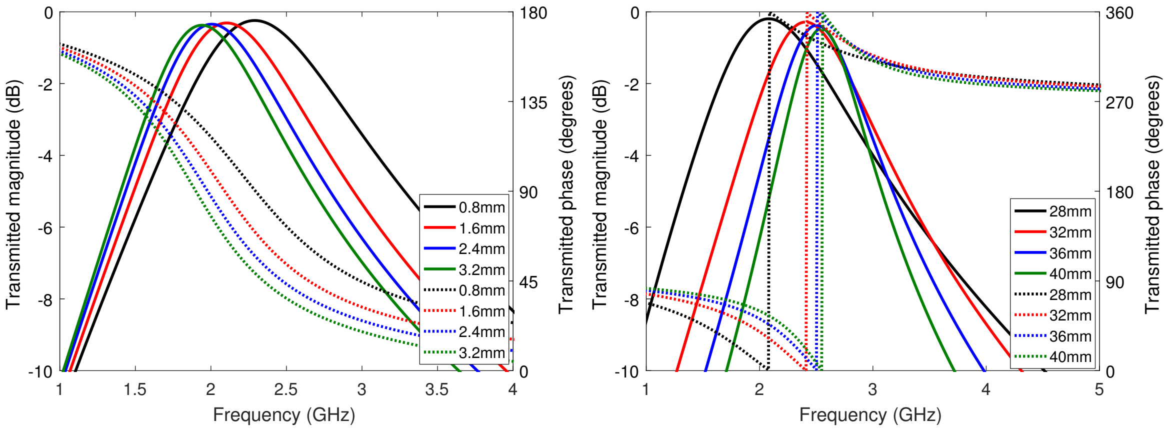

(a) (b)

Figure 3.5: Simulated magnitude (solid lines) and phase (dashed lines) of dielectric-backed square loop aperture FSS S_{21} in free space with Floquet mode boundaries, s=24mm, p=30mm, g=1mm, t_{sub}=0.8mm while varying (a) t_{sub}, (b) p

in terms of the scattering or s-parameters, in particular the S_{21} values. This is a complex value which describes the portion of the power wave travelling away from the FSS in one direction due to the power wave incident on the other side of the FSS. As FSS are reciprocal, $S_{21} = S_{12}$. To maximise transmission through the FSS at the desired frequency of operation, an S_{21} with magnitude approaching 1 is preferred, though change in the phase at different frequencies may be desirable. Generally, S_{mn} describes the power wave away from port m of a network due to the power wave incident at port n.

When a dielectric is added to one side and the other is left in air, as discussed previously in Section 2.3.2, an infinitely thick dielectric causes a shift down of resonant frequency by a factor of $\sqrt{(\epsilon_{eff})}$ where $\epsilon_{eff} = \dfrac{\epsilon_r + 1}{2}$. Using thin dielectrics, where the thickness $t_{sub} \ll \lambda_0$, has a much smaller shift. The simulation in Fig. 3.5a shows the same FSS as above, but with an FR4 substrate. The FR4 is modelled as having effective permittivity $\epsilon_r = 4.4$ and loss tangent tan$\delta = 0.025$. The simulation shows a shift in resonant frequency of 1.38 for t_{sub}=0.8mm, and up to a factor of 1.63 for t_{sub}=3.2mm. These thicknesses are an appropriate range for the structural stability required for the modulating FSS, and all show less shift in resonant frequency than the theoretical limit of 2.1 for FR4. Also, the losses introduced by the dielectric reduce the peak S_{21} due to the dielectric's resistance to the electric field. This increases as t_{sub} increases, such that a 3.2mm dielectric adds 0.4dB loss through the surface compared with an FSS with no substrate. This suggests thinner dielectrics should be used to minimise loss. Further, Fig. 3.5b shows that in an FSS backed by FR4 with t_{sub}=0.8mm, the peak S_{21} reduces as the difference between p and s increases, due to the reduced coupling between neighbouring unit cells. As such, a square loop FSS design should keep p and $s + 2g$ of similar sizes in order to minimise loss.

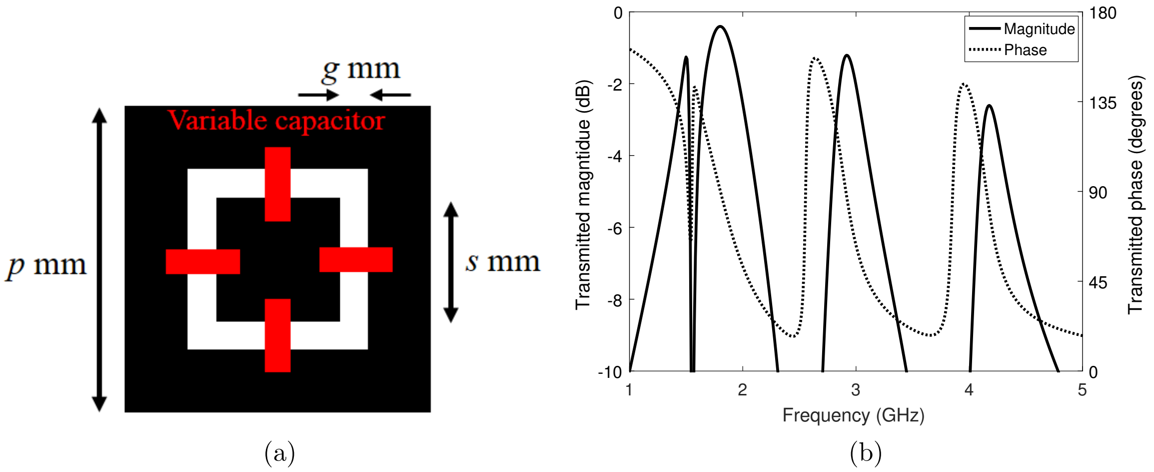

Figure 3.6: (a) Geometry and layout of a reconfigurable square loop aperture FSS, (b) Simulated S_{21} of square loop aperture FSS with only one diode

3.3.2 Design of reconfigurable FSS for DAM

In addition to the choice of FSS element and the design of the unit cell geometry, the choice of variable capacitor is an important design questions for an FSS modulator. As discussed in Section 2.3, adding variable capacitors to an FSS allow tuning of the resonant frequency of the surface. The capacitance of the device C_v is added in parallel to the natural capacitance of the FSS, meaning the minimum resonant frequency is reduced. For DAM, the important characteristics of the variable capacitor are the range of capacitive tuning provided, the rate at which that tuning can be provided, the types of signal required to produce this tuning, and the losses in the device. For a square loop aperture FSS which is polarisation agnostic, four diodes per unit cell are required, as in Fig. 3.6a. This can be reduced to two diodes, both in line with the incident E-field, when the polarisation of the incident wave is known. Diodes are required on each edge of the loop to avoid multiple different resonances occurring, as in Fig. 3.6b.

The range of capacitance C_v required for tuning an FSS over the whole of its bandwidth is quite small, with a factor of 3 enough to tune across the 3dB bandwidth (Fig. 3.7a). Note that as the capacitance increases, the shift in f_0 decreases quickly at first, but eventually saturates as the lower limit of the FSS tuning is reached. There is also a narrowing of the absolute bandwidth as C_v increases, though the steeper phase change within the bandwidth means the same amount of phase change is achieved within each tuning bandwidth (Fig. 3.7b). Also, the peak S_{21} reduces as the capacitance increases. This is because the capacitive impedance decreases as the capacitance increases, allowing more current to pass through the devices. This increases the I^2R_v losses in the variable capacitors, increasing the loss through the surface. This suggests that variable capacitors with low capacitance are preferred, and with a minimum tuning ratio of 3.

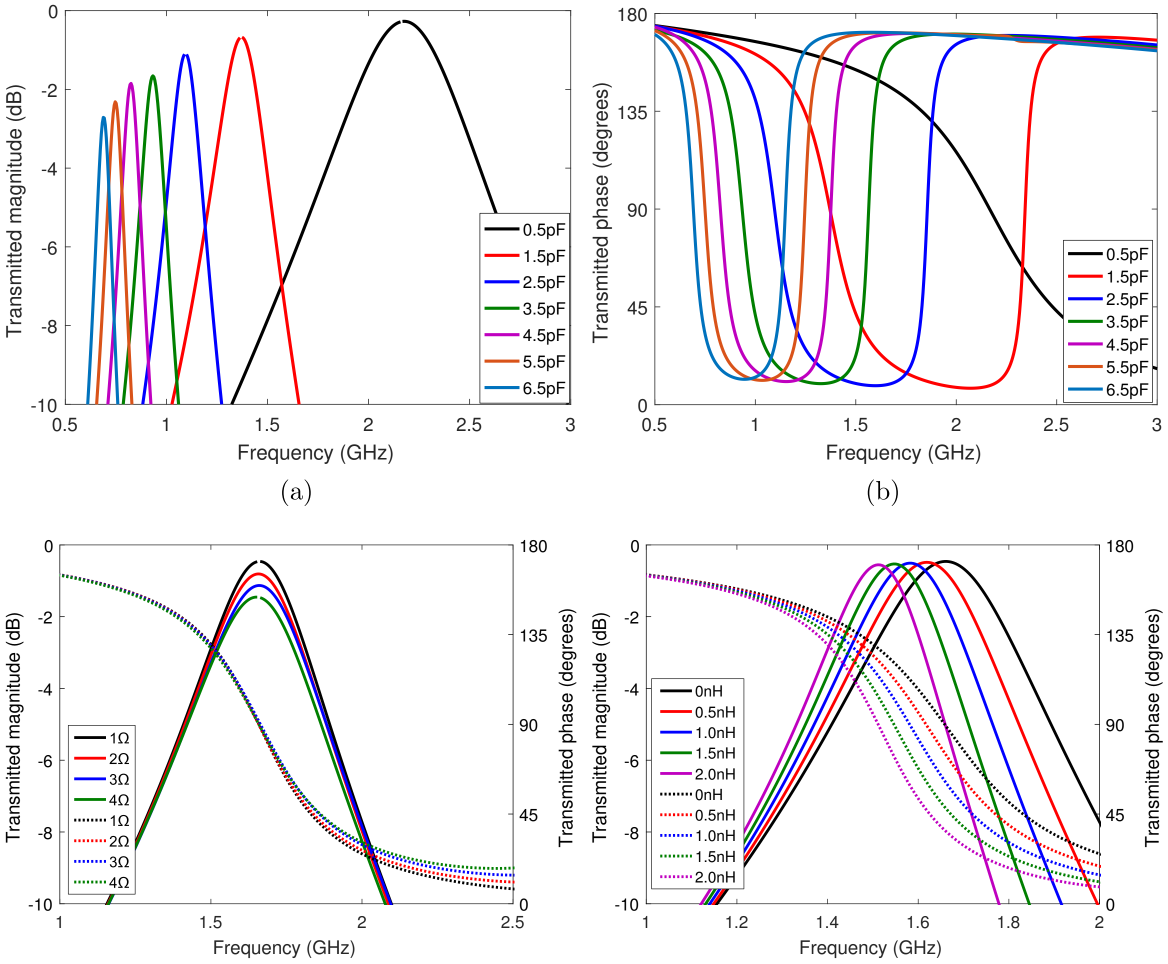

(a) (b)

(c) (d)

Figure 3.7: Simulated magnitude (solid lines) and phase (dashed lines) of reconfigurable square loop aperture FSS S_{21} in free space with Floque mode boundaries, s=24mm, p=30mm, g=1mm, t_{sub}=0.8mm, R_v=1Ω, C_v=1pF, L_v=0nH. (a) Magnitude while C_v varies, (b) phase while C_v varies, (c) varying R_v, and (d) varying L_v.

The effect of different values of R_v on FSS performance is shown in Fig. 3.7c, with increased equivalent series resistance (ESR) in the capacitors reducing the peak S_{21}. For this FSS at this capacitance, each 1Ω increase in R_v leads to 0.4dB increase in loss. The phase change within the passband also reduces slightly as the ESR increases. As such, variable capacitors with low ESR should be chosen. The parasitic inductance, L_v, of the variable capacitors should also be considered. Fig. 3.7d shows a simulation of the above FSS with varying L_v, showing that a higher inductance lowers the resonant frequency of the surface. The effect on loss and the phase change within the passband are minimal. This implies that the L_v of variable capacitors should be considered alongside the tuning range of C_v to accurately predict the tuning of f_0.

Another important factor in the choice of variable capacitor is the rate and accuracy of tuning possible, which is closely related to the method of tuning the device uses. Types such as MEMS and BST tunable capacitors have been demonstrated for use on FSS [84, 104]. While MEMS and other digital capacitors have high linearity and low R_v, they have slow switching speeds and require complicated bias networks. The digital tuning also adds complexity to the control circuitry for the FSS modulator. BST capacitors are low loss, but due to their tuning mechanism, where the material properties of BST change in response to an electric field, the maximum switching rates with current commercial devices is in the kHz. They also often require high voltages to produce the required change in C_v. Semiconductor-based variable capacitors can have very fast switching rates depending on the materials used to construct them, to the order of 100MHz. They also only require voltages in the low 10s of Volts to produce significant change in capacitance. The ESR of diode-based variable capacitors tends to be higher, however, and increases when the tuning range of C_v is increased. Varactor diodes are designed particularly for this broad tuning range, though all semiconductor diodes exhibit variable capacitance when in reverse bias. The choice of device should be taken carefully for each design.

3.3.3 Multilayer reconfigurable FSS design for DAM

Increasing the number of layers of an FSS increases the bandwidth, and the amount of phase change within that bandwidth, of the filter. This was previously discussed theoretically, but here will be analysed with simulations. The choice of the number of layers is important for a phase modulating FSS, as it must be capable of producing the desired output phases with as little magnitude impairment as possible. These impairments reduce the Euclidean distance between the constellation points, so minimising them maximises the BER of the total system.

The simulated S_{21} and S_{11} of a lossless reconfigurable FSS with different numbers of layers is shown against frequency in Fig. 3.8. The S_{11} value describes the power wave reflected from the FSS compared with the incident wave, and should be minimised at the frequency of interest to maximise energy transmitted forward. Good performance is often assumed for $|S_{11}| < -10\text{dB}$ where $| \cdot |$ takes the magnitude, though in some circumstances -6dB may be deemed acceptable. Fig. 3.8 shows increasing bandwidth as the number of layers increases. However, the roll-off also becomes steeper as the number of layers increases. As such, care should be taken near the edges of a multi-layer filter response, where small changes in the frequency of interest can lead to large changes in magnitude. The broad bandwidth produced by multi-layer FSS suggests that there will be greater phase change across the filter bandwidth, as is shown in polar form in Fig. 3.9. It suggests that a single layer FSS is only suitable for ASK, as the phase change for 3dB variation in magnitude is only 90^o. Two layers is capable of producing two constellation points 180^o apart, equivalent to BPSK, with no magnitude impairment; but these constellation points are 3dB below the

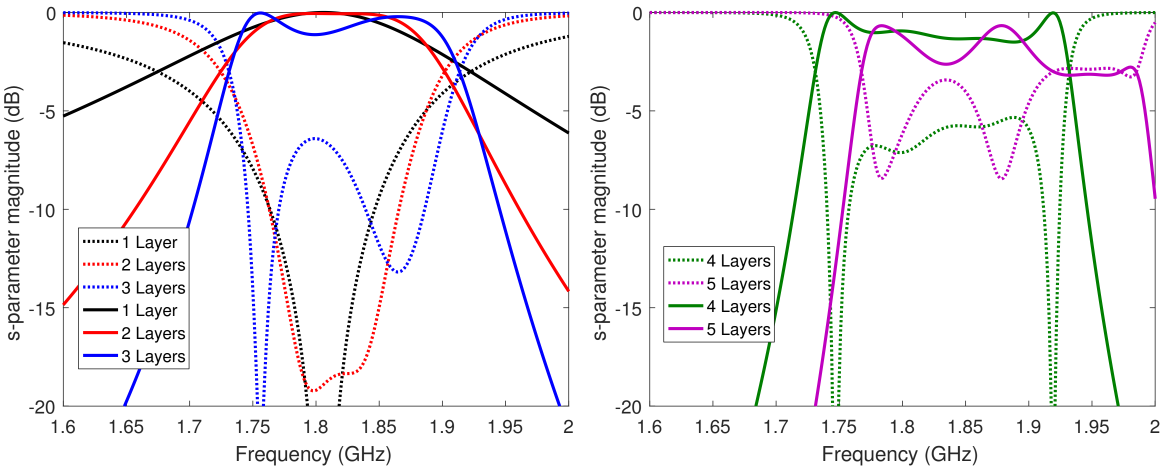

(a) (b)

Figure 3.8: Simulated S_{21} (solid lines) and S_{11} (dashed lines) of multilayer reconfigurable FSS in free space. p=15mm, s=12mm, g=0.6mm, t_{sub}=1.6mm, C_v=1.3pF. (a) 1-3 layers, (b) 4-5 layers.

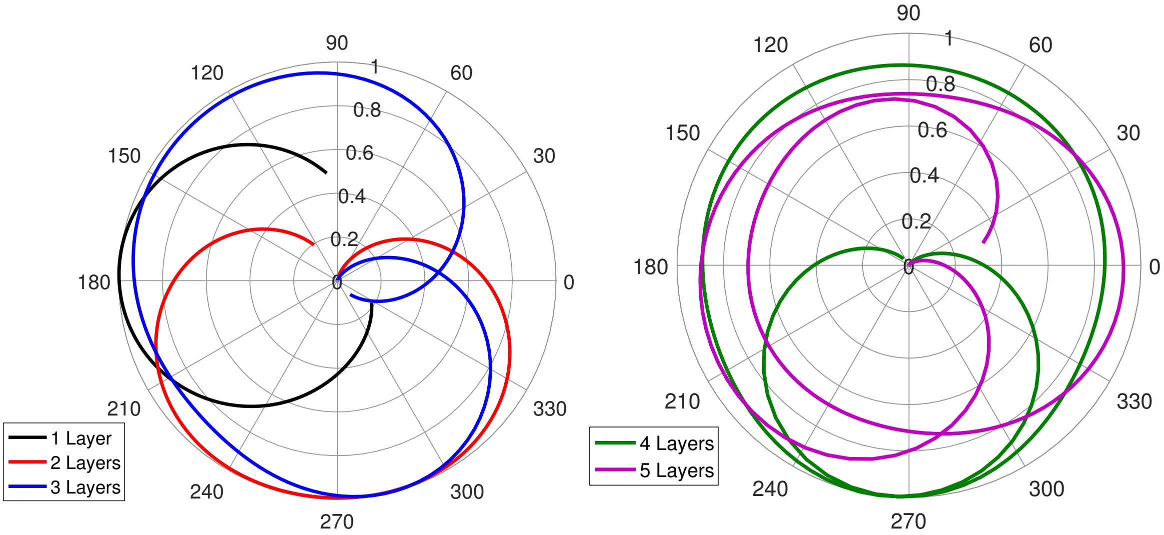

(a) (b)

Figure 3.9: Simulated S_{21} of multilayer reconfigurable FSS in free space against frequency. p=15mm, s=12mm, g=0.6mm, t_{sub}=1.6mm, C_v=1.3pF. (a) 1-3 layers, (b) 4-5 layers.

peak transmission of the FSS. QPSK could be achieved with 3 layers for 1.3dB variation in the constellation points, and 4 layers achieves continuous phase modulation with 1dB variation.

However, increasing the number of layers also increases the loss through the whole FSS. This is illustrated by Fig. 3.10a, showing simulated S_{21} of different numbers of layers. Where a single layer has some transmission loss, in this simulation 0.8dB, every added layer increases the loss by a futher 0.8dB. Further, as the amount of loss through the FSS varies with changing C_v and adding ESR decreases the phase change within the bandwidth, the

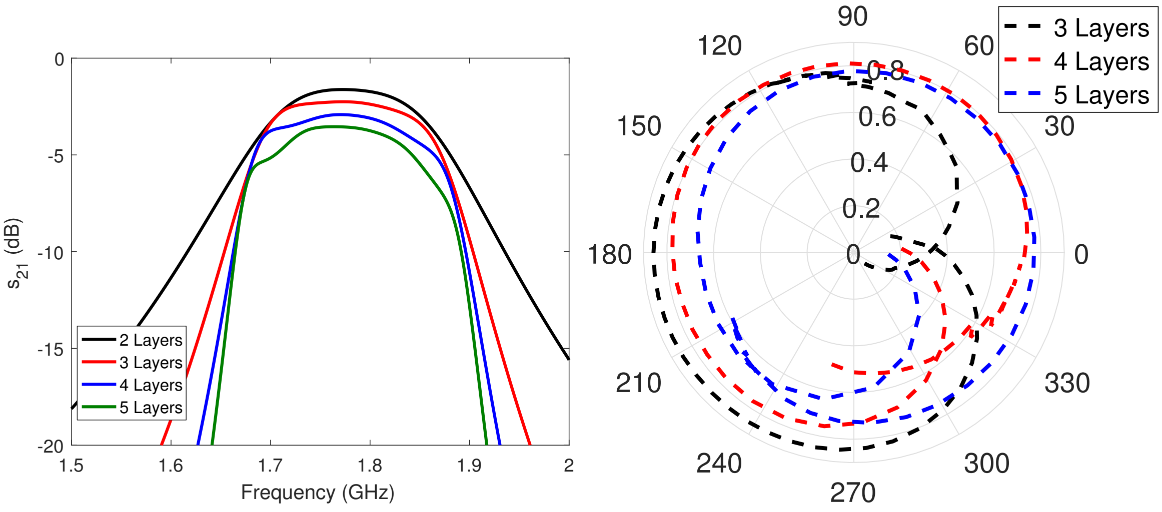

(a) (b)

Figure 3.10: Simulated S_{21} of multilayer reconfigurable FSS in free space, p=15mm, s=12mm, g=0.6mm, t_{sub}=1.6mm. (a) Magnitude against frequency at C_v=1.3pF, (b) Polar plot with changing capacitance at 1.8GHz.

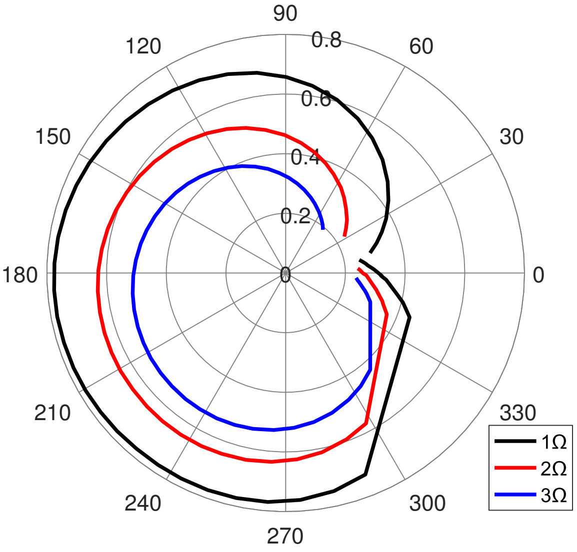

Figure 3.11: Simulated S_{21} of multilayer reconfigurable FSS in free space, p=15mm, s=12mm, g=0.6mm, t_{sub}=1.6mm. (a) Magnitude against frequency at C_v=1.3pF, (b) Polar plot with changing capacitance at 1.8GHz.

amount of magnitude variation for a given phase change is altered by the presence of loss. This effect is shown in Fig. 3.10b, which shows that, where R_v=0.44Ω, an allowance of 3dB variation means 3 layers can achieve 275^o phase change, 4 layers can achieve 345^o, and 5 layers can achieve 405^o. However, the total loss through the FSS increases from 1.34dB for 3 layers, through 1.77dB for 4 layers, to 2.16dB for 5 layers.

This reduction in phase change for a given magnitude variation continues as the loss in the surfaces increases. Taking a three-layer FSS with an FR4 substrate, where R_v=1Ω

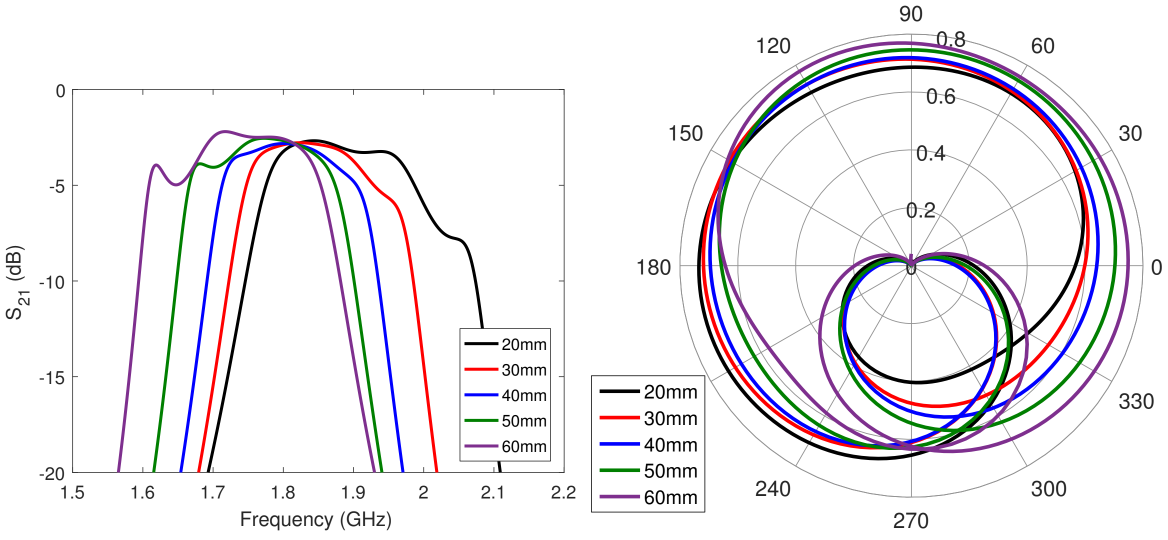

(a) (b)

Figure 3.12: Simulated S_{21} of 4-layer reconfigurable FSS in free space with varying spacing d between layers, (a) Magnitude against frequency, (b) Polar plot against frequency. Note that at 1.8GHz $\lambda_0/4 \approxeq$ 41mm

gives 260^o phase change for 3dB variation, with 2.2dB total loss through the FSS (Fig. 3.11). As the ESR increases through 2Ω and 3Ω, this decreases to 235^o and 210^o, while total losses increase to 3.8dB and 5.4dB, respectively. As such, the choice of the number of layers required to produce a desired constellation should be taken once the ESR of the variable capacitors and the loss tangent of the dielectric substrate used are known.

The spacing between layers, d, should also be considered. Up to this point, it has been assumed that each FSS layer was placed $\lambda_0/4$ apart, as this gives theoretically the flattest passband filter response. Varying d produces a frequency response which has a less flat passband (Fig. 3.12a). However, at times this may be useful in order to increase the amount of phase change for a given magnitude variation- for example, in Fig. 3.12b, a spacing of $3\lambda_0/10 = 50$mm gives 2.1 dB magnitude variation for 360^o phase change, while d = 40mm$\approxeq$ $\lambda_0/4$ gives 2.5dB magnitude variation, despite the second giving a flatter response. A decision may also be made to reduce the spacing between layers to reduce the form factor of the modulator.

3.4 Reconfigurable antenna design for DAM

In order to build a DAM transmitter, an RF source must be included with the modulating FSS. This integration of a reconfigurable FSS with a radiating element can be considered as a single reconfigurable antenna. Some different approaches to the design of a DAM reconfigurable antenna are considered here.

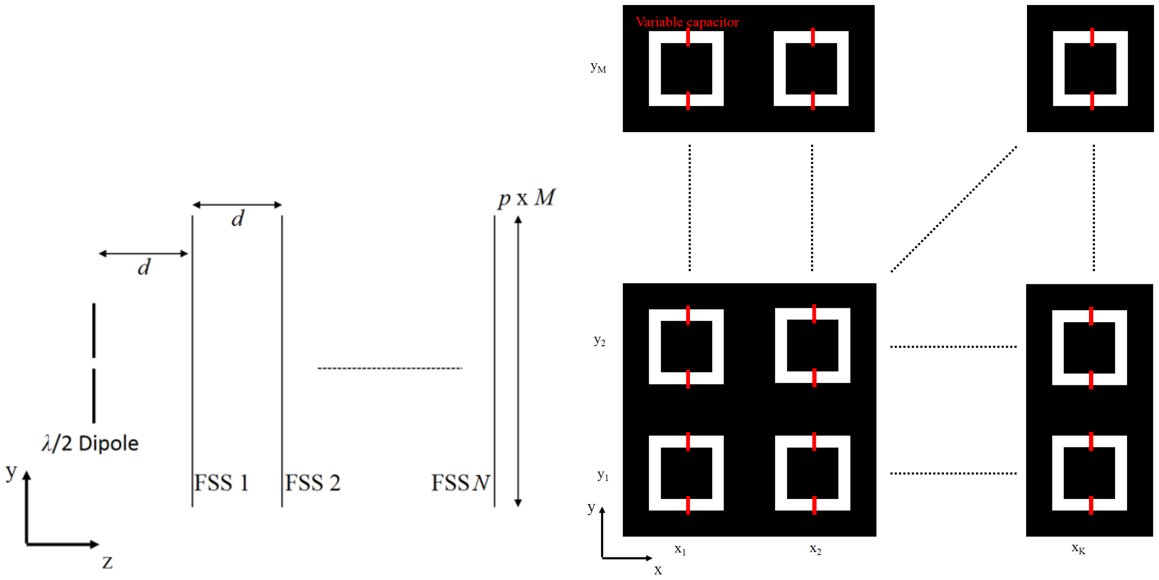

(a) (b)

Figure 3.13: Diagram of dipole-based free space reconfigurable antenna. (a) y-z plane, (b) x-y plane.

3.4.1 Free space FSS with dipole

The simplest possible reconfigurable antenna design would be that suggested by Fig. 3.1a, where the multilayer FSS is placed in free space in front of a radiating element. A generic implementation of this, using a $\lambda/2$ dipole as a feed, and with a N_{layers} layer FSS with each layer a $M \times K$ array of unit cells and placed distance d apart, is shown in Fig. 3.13. This was simulated in CST using 3-layer FSS consisting of 6×6 arrays of unit cells 40mm away from it. The chosen FSS parameters were p=15mm, s=12mm, g=0.6mm and t_{sub}=1.6mm, while the variable capacitor was modelled with R_v=1Ω, L_v=0.5nH and C_v=1.3pF. When an E-field probe was placed in the farfield aligned with centre of the FSS array, as shown in Fig. 3.14, response against frequency does not show the expected change in phase and magnitude, giving only 180^o phase change for 3dB impairment of magnitude, rather than the expected 260^o, and the magnitude variation is erratic (Fig. 3.15a). The response is further degraded at different viewing angles: at 25^o from the intended boresight in the H-plane there is still 180^o phase change for 3dB impairment of magnitude, but there are nulls present in the response, which could cause issues in implementing the antenna as a modulator. Also, due to reflections from and loss through the FSS, the antenna pattern is distorted, with more energy going away from the intended direction than toward it (Fig. 3.15b).

Examining the simulated E-field leads to further understanding of this behaviour. Looking from the y-z plane, where the dipole appears as a point source, the field seems to pass through all layers of the FSS (Fig. 3.16a). However, viewing in the x-z, it can be seen that the farfield contains fields which have refracted around at least one of the FSS layers (Fig.

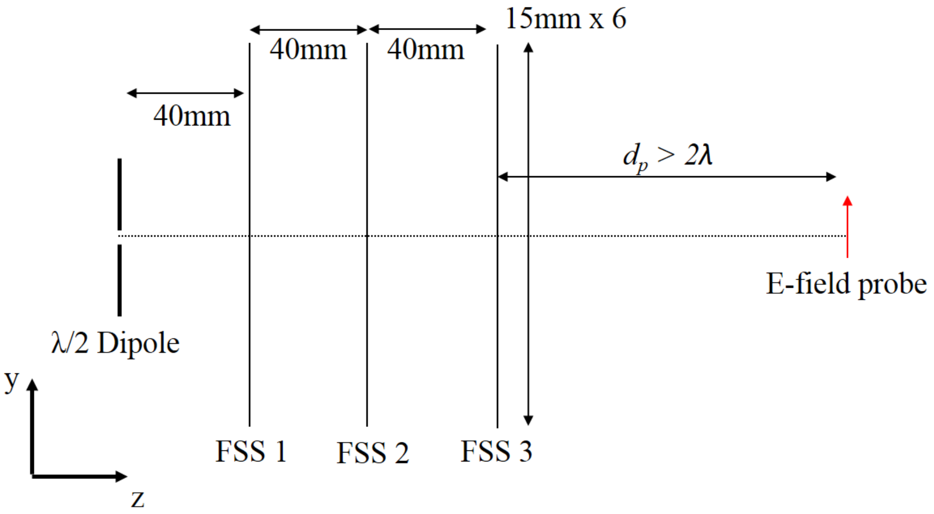

Figure 3.14: Diagram of dipole-based free space reconfigurable antenna. (a) y-z plane, (b) x-y plane.

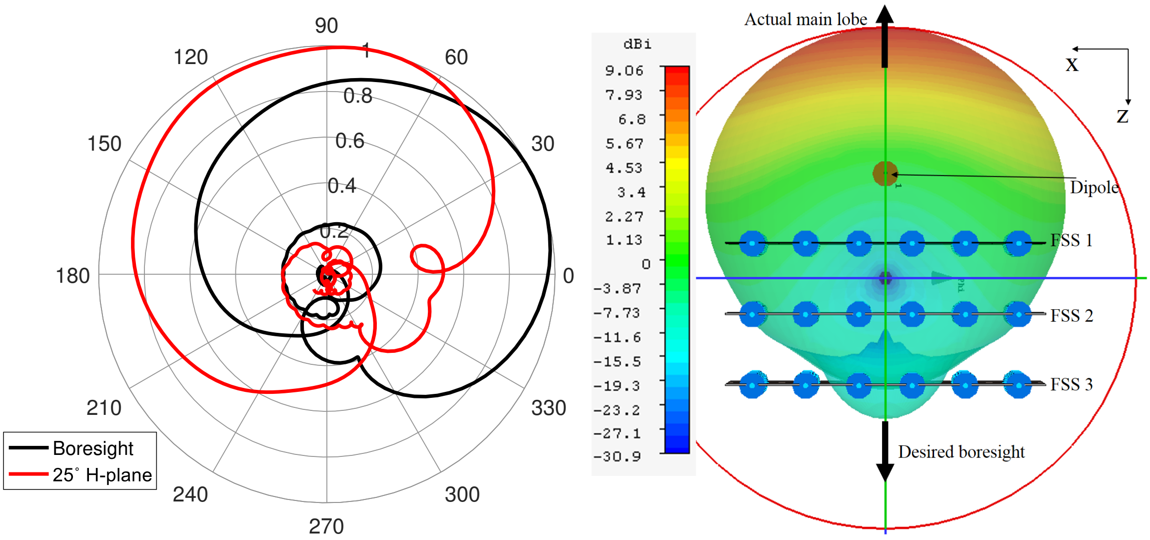

(a) (b)

Figure 3.15: Simulated free-space reconfigurable antenna with dipole. (a) Magnitude and phase of E-farfield at viewing angles, (b) Radiation pattern viewing from x-z plane

3.16b). This leads to the degradation of the filter performance. It could be mitigated by using a more directive antenna or larger FSS. However, a more directive antenna may not solve the issues with the antenna pattern, or variation in the transmitted signal at different viewing angles. Also, the FSS is in this simulation is already of size $1.1\lambda_0$, which may restrict its use in applications requiring a more limited form factor.

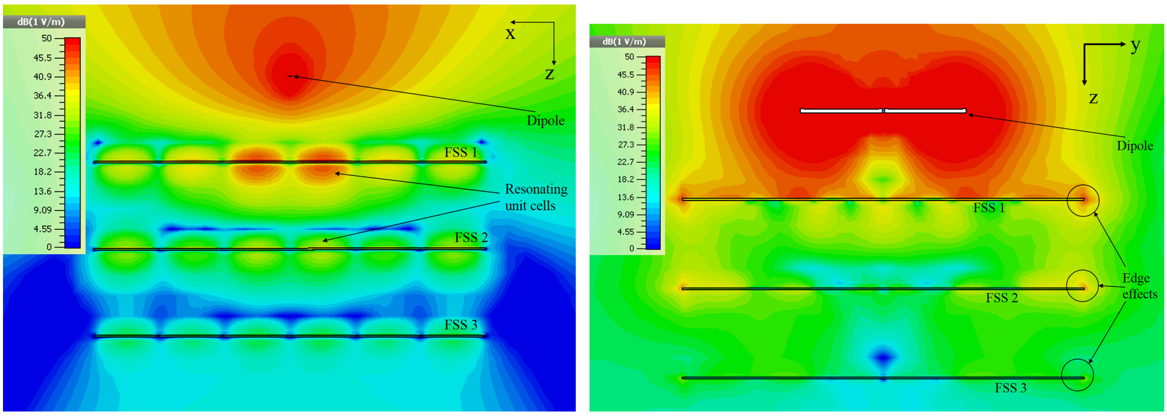

(a)

(b)

Figure 3.16: Simulated E-field of free-space reconfigurable antenna with dipole in (a) x-z plane, (b) y-z plane

3.4.2 Reconfigurable waveguide antenna

Due to the findings above, the integration of all FSS layers into a waveguide antenna, making it reconfigurable, was explored (Fig. 3.17). This ensures that all transmitted fields pass through all layers of the FSS, while limiting the size of FSS required. While many different types and shapes of waveguide could be used, this thesis will focus on rectangular waveguides with square apertures for ease of modelling and fabrication.

An important parameter for this design of reconfigurable antenna is the number of unit cells each FSS layer consists of, which will be referred to as K in the x direction and M in the y direction (Fig. 3.17b). There are two factors to account for in this. The first is that the waveguide must have a large enough aperture to allow the propagation of fields at the desired frequency. In a rectangular waveguide, this cutoff frequency is determined by the width of the waveguide in the x-direction, as it must be able to support a standing E-field wave across it [146]. For a desired frequency of operation f_c, and FSS period p, there must be $K \geq \dfrac{c}{2pf_c}$ unit cells in the x-direction, where c is the speed of light in the waveguide medium. This ensures that the frequency of operation is above the waveguide cutoff frequency. However, where the total waveguide width $pK \geq \dfrac{c}{f_c}$, higher order modes will propagate within the waveguide, possibly producing unwanted effects. As such, the values of p and K should be chosen to be between these values. All antennas simulated in this thesis will operate within these boundaries.

As the fields in a waveguide are setup in a different way from how a free space wave propagates, the effect on FSS performance in a waveguide should be considered. Passive FSS have long been placed inside waveguides in order to characterise them while reducing the required size of the FSS [147]. Previous work has shown that an FSS with two orthogonal axes of symmetry, such as a square loop, resonates at a similar frequency inside a waveguide

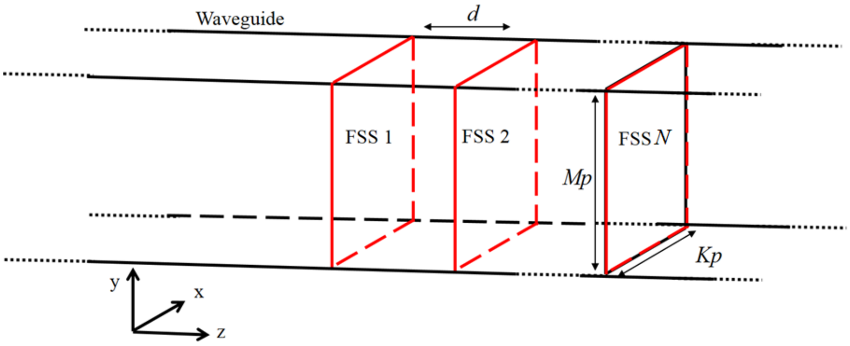

(a)

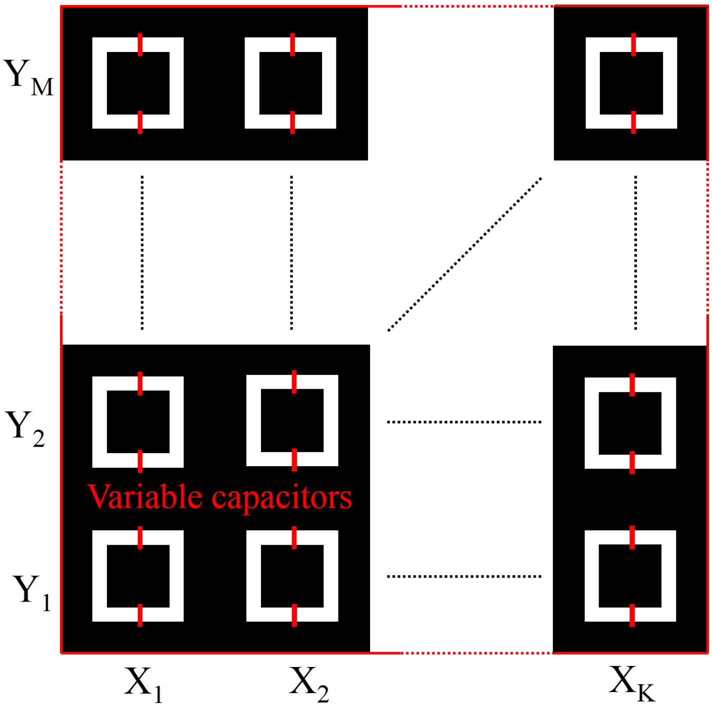

(b)

Figure 3.17: Diagrams of waveguide-based FSS concept. (a) 3D waveguide structure, (b) FSS structure in waveguide

as in free space. This is corroborated by Fig. 3.18a, which shows the S_{11} of a single-layer square loop FSS with parameters p=22mm, s=15mm and g=1mm in free space and in an infinitely long waveguide shaped to fit a 5 × 5 FSS. The resonant frequency is shifted upward by only 4% when the FSS is in a waveguide, a difference which holds over a range of thicknesses t_{sub} of FR4 substrate. It should be noted that all the investigated values of t_{sub} are electrically small, with a maximum of 0.032λ.

However, this changes when active devices are integrated with the FSS to make them reconfigurable. This is shown by Fig. 3.18b, which shows that the resonant frequency of a lossless FSS with the above dimensions resonates at significantly different frequencies in free

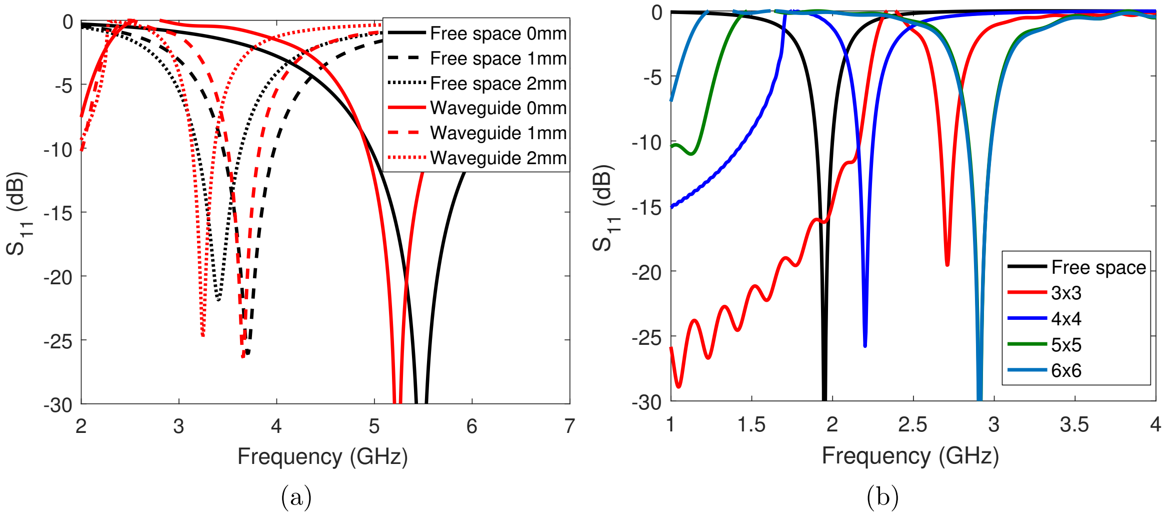

Figure 3.18: Simulated S_{11} of lossless single layer FSS in free space and in different waveguide configurations, (a) passive with varying FR4 substrate thickness t_{sub}, (b) lumped element capacitors of C_v=1pF included in model, substrate t_{sub}=0. Unit cell dimensions p=22mm, s= 15mm, g=1mm

space compared with various different waveguide configurations when lossless capacitors of 1pF are integrated into each unit cell. There seems to be no fixed pattern as to how the dimensions of the FSS and waveguide affect the resonant frequency, as the 5×5 configuration resonates at the highest frequency, but the 4×4 configuration resonates lower than the 3×3 configuration. However, all waveguide implementations resonate at a higher frequency than the free space reconfigurable FSS, and there appears to be saturation for configurations with more unit cells than 5×5.

The reasons for this can be seen in analysis of the surface currents on the FSS at resonance (Fig. 3.19). It can be seen that in free space, the currents are strongest around the loop of the FSS and through the diodes, and that each unit cell resonates in the same way (Fig. 3.19a). In the waveguide case, however, as well as currents being unevenly distributed between each unit cell due to the sine-like E-field distribution in the waveguide, the currents are strongest along the strips of conductor between unit cells (Fig. 3.19b). This suggests that there is a sampling effect where the number of unit cells resonating properly in the waveguide is not equivalent to a large number of unit cells resonating in the same way.

The shift in resonant frequency remains fairly constant as capacitance varies, with the difference between resonances in free space and the waveguide configurations changing from 976MHz to 870MHz between 1pF and 1.5pF for the 5×5 case (Fig. 3.20a). Note that as a function of the resonant frequency in the 5×5 waveguide this is a consistent 34% downward shift. The simulated results are shown only over a small range of capacitance due to the cutoff frequencies of the smaller waveguides preventing further investigation. The shift is also constant for different values of p, which also changes the waveguide dimensions (Fig. 3.20b).

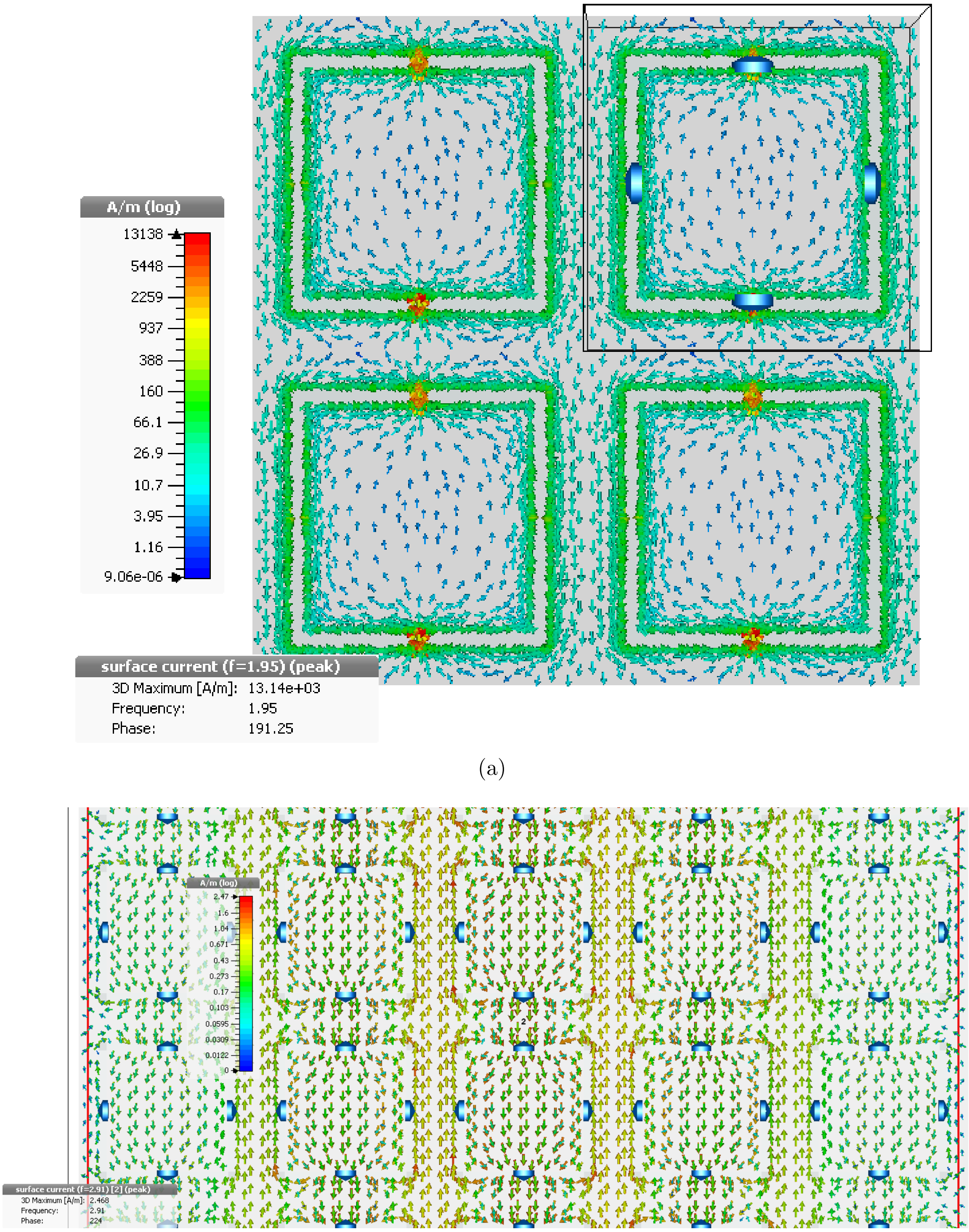

(a)

(b)

Figure 3.19: Simulated surface currents on lossless single layer reconfigurable FSS, (a) in free space, (b) in 5×5 waveguide configuration. Unit cell dimensions p=22mm, s= 15mm, g=1mm, t_{sub}=0, C_v=1pF.

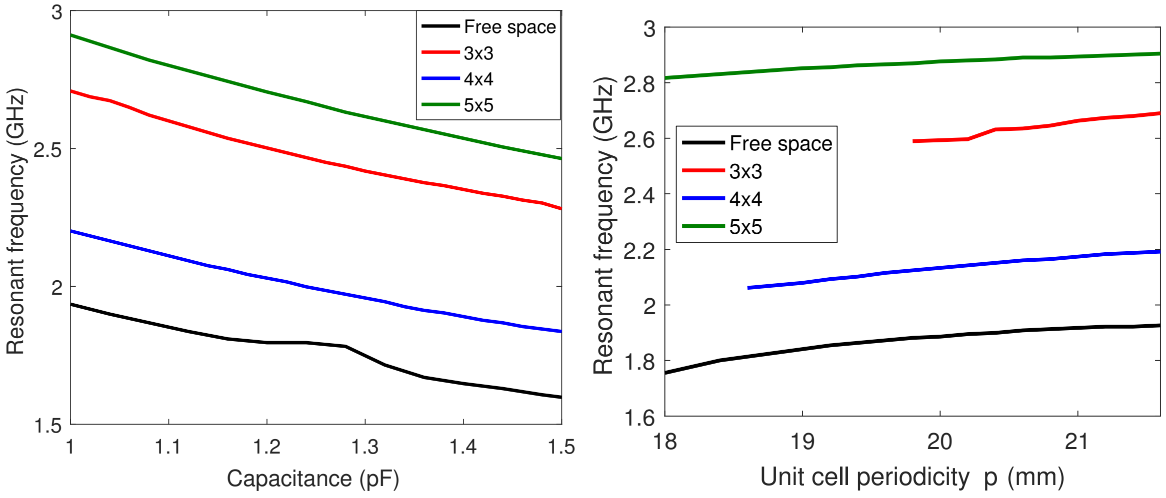

(a) (b)

Figure 3.20: Simulated resonant frequency of single-layer lossless reconfigurable FSS in free space and in different waveguide configurations, (a) Varying capacitance, (b) varying p. Non-varying dimensions p=22mm, s= 15mm, g=1mm, t_{sub}=0, C_v=1pF.

This suggests that the shift in resonant frequency is due to the sampling and coupling effect of different numbers of unit cells in a waveguide, rather than the waveguide cutoff frequency. Note in this figure some smaller values of p lead to resonance below the cutoff frequency of different configurations, in these cases the resonance is not shown. As a result of this, care should be taken when designing a reconfigurable FSS to operate inside a waveguide, as the dimensions of the FSS will affect the frequency of operation.

The coupling of unit cells in a waveguide-embedded FSS can also affect the amount of phase change produced by the FSS. Some coupling between unit cells is required for any resonance at all, which is not fulfilled when $M = K = 1$. The bounds for this are explored by simulating a single-layer, lossless FSS in an infinitely long waveguide (Fig. 3.21). The aperture of the waveguide is kept constant at 160mm^2, while the number of unit cells occupying that space is varied, with g=1mm and the ratio s/p=0.8. The performance is similar for 4×4 and 5×5 arrays of unit cells, giving 180^0 and 170^o of phase change over 6dB magnitude variation. However, this degrades when $M = K = 3$ or 2, giving 155^o and 150^o respectively.

The reasons for this can be seen by examining the E-field within the waveguide and the surface currents on the FSS at resonance for the 2×2 and 5×5 cases (Fig. 3.22). The 5×5 case shows an E-field with the classic strength distribution in a waveguide, illuminating the central unit cells more than the ones towards the edges in the x-direction, but with fairly even E-field strength across the three central columns of unit cells (Fig. 3.22a). This induces strong currents in each column, clearly showing the unit cells coupling both vertically and horizontally (Fig. 3.22b). In contrast, the 2×2 case shows the strong E-fields on all four unit

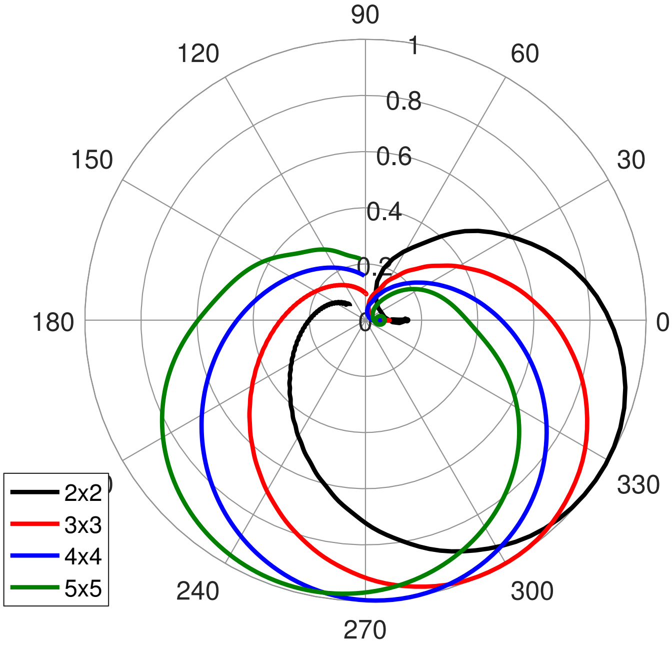

Figure 3.21: Simulated S_{21} of single-layer lossless reconfigurable FSS of different number of unit cells $(M \times M)$ in 160mm×160mm infinitely long waveguide. g=1mm, p=160/M mm, C_v=1pF and ratio s/p=0.8

cells being abruptly pulled to zero at the edges, due to the condition that at the conducting waveguide wall the tangential E-field must be 0 (Fig. 3.22c). This means that the induced currents through the middle of the unit cells are small compared with those at their edge, suggesting they are not resonating as well as in the 5×5 case (Fig. 3.22d). This indicates that more unit cells is advantageous, however limits on space, the number of variable capacitors required, and avoiding higher-order modes in the waveguide may lead to a design choice of smaller numbers of unit cells.

The design of the feed into, and radiating end of, the waveguide antenna should also be considered. The radiating aperture could be tapered to increase gain, or otherwise shape the radiation pattern. However, this is outside the scope of this thesis. As such, the antennas examined in this thesis will be rectangular, having a consistent aperture across their length, with the final FSS layer placed at the opening of the antenna into free space. To provide an RF source to the antenna, many different feed types could be used, such as planar crossed dipoles integrated inside the antenna. For simplicity of modelling and fabrication, a single monopole feed is used to provide a linearly polarised RF source throughout this thesis.

A cavity backing is placed $\lambda_c/4$ away from the feed to maximise the energy transmitted forward through the FSS, where λ_c is the wavelength inside the cavity. Waves transmitted away from the FSS will undergo 90^o phase rotation for travelling $\lambda_c/4$, 180^o phase change due to reflection off the electrical conductor of the cavity backing, and a further 90^o rotation as the $\lambda_c/4$ is travelled by the reflected wave back to the feed, adding to 360^o. As such the reflected wave will interfere constructively with waves transmitted towards the FSS from the

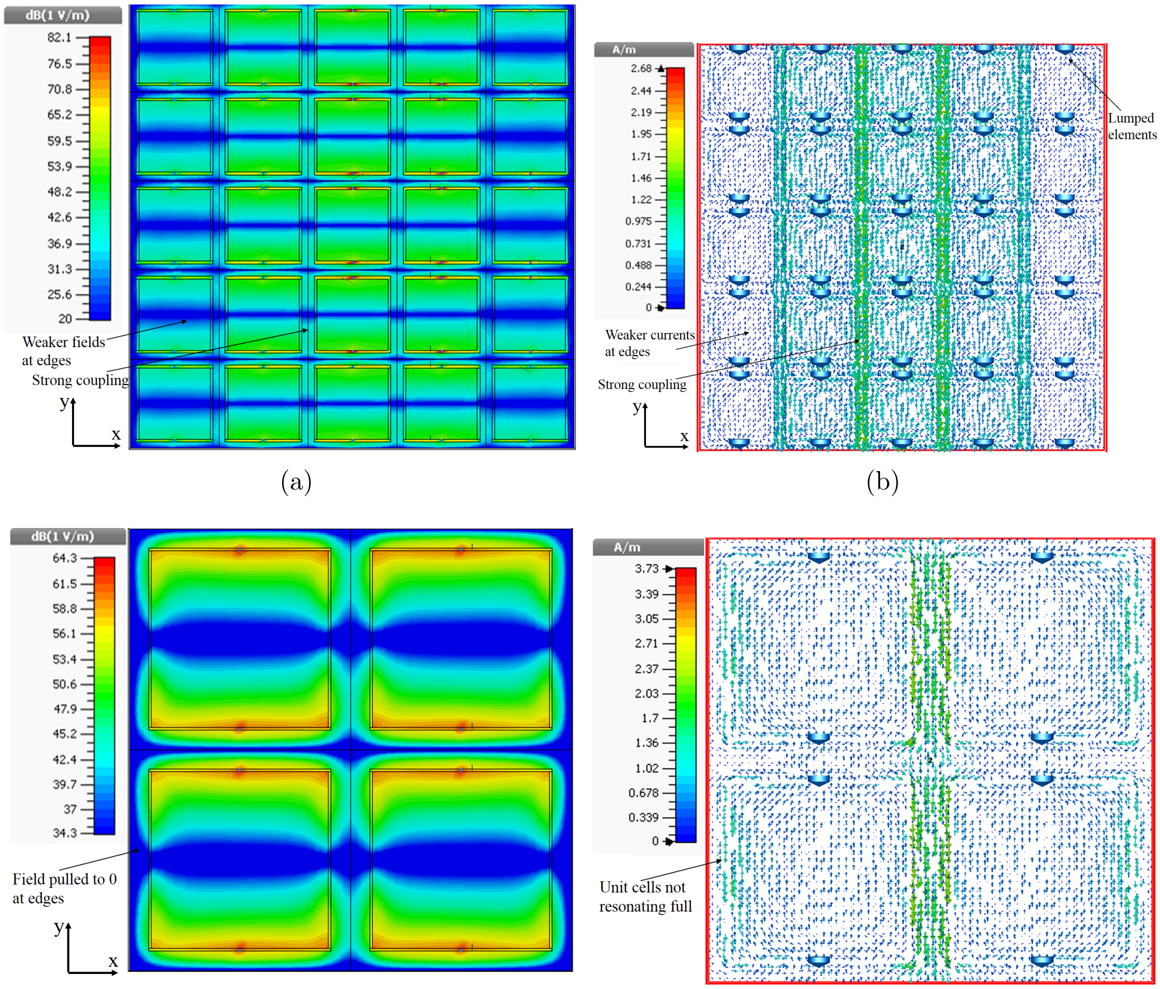

(a) (b)

(c) (d)

Figure 3.22: Simulated single-layer lossless FSS of varying unit cell sizes in infinitely long, 160mmx160mm waveguide. (a) E-field of 5 × 5 FSS, (b) Surface currents on 5 × 5 FSS, (c) E-field of 2 × 2 FSS, (d) Surface currents on 2 × 2 FSS

feed. The backing also serves to limit the physical size of the antenna. The length of this feed affects the match of the total antenna, and should be designed to minimise the S_{11} once the FSS has been designed within the cavity. This final antenna design is shown in Fig. 3.23.

3.5 Discussion

A generic design of a FSS DAM unit has been produced which broadly meets the design criteria set out at the start of this Chapter (Table 3.1). The main objective, of producing a reconfigurable antenna capable of producing phase modulation, has been met. By using tunable FSS, the phase of the carrier can be altered through the control of variable capacitors embedded into the FSS. Increasing the number of FSS layers increases the amount of phase variation available for a given amount of magnitude variation, in trade off with the total loss through the FSS.

The frequency of operation of the FSS DAM unit has not yet been set in this generic design, but all simulation has taken place in the microwave region. As such, 1.8GHz should be achievable as desired with good choice of variable capacitors. This also applies to the achievable symbol rate, which will be largely determined by the tuning rate of the variable capacitors. The unit produces a single linear polarisation, using a monopole feed to feed the unit. This also allows the variable capacitors to be placed only in alignment with the E-field, reducing the number required.

The size requirement needs deeper discussion. By enclosing the FSS in a cavity, the risk of diffraction of signals around the FSS has been eliminated, most likely reducing the required size of the FSS. However, in order for energy to propagate through the cavity, its aperture must be greater than $\lambda_0/2$. Through design, it is possible to make the dimensions as close to this requirement as possible. The depth of the unit is largely determined by the number of FSS layers used, as for the flattest frequency response the layers should be spaced $\lambda_c/4$ apart. As such, the depth of the unit should be traded off with the quality of phase modulation produced. In all, however, the generic design is able to broadly meet the requirements of an FSS DAM transmitter for IoT applications.

3.6 Conclusion

The fundamental design for the reconfigurable antenna for FSS DAM studied in this thesis has been established through analysis and simulations. It integrates a square-loop aperture multilayer FSS of $M \times K$ unit cells into a waveguide antenna, fed by a cavity-backed monopole. Some of the options for this design, such as the geometry of the unit, the choice

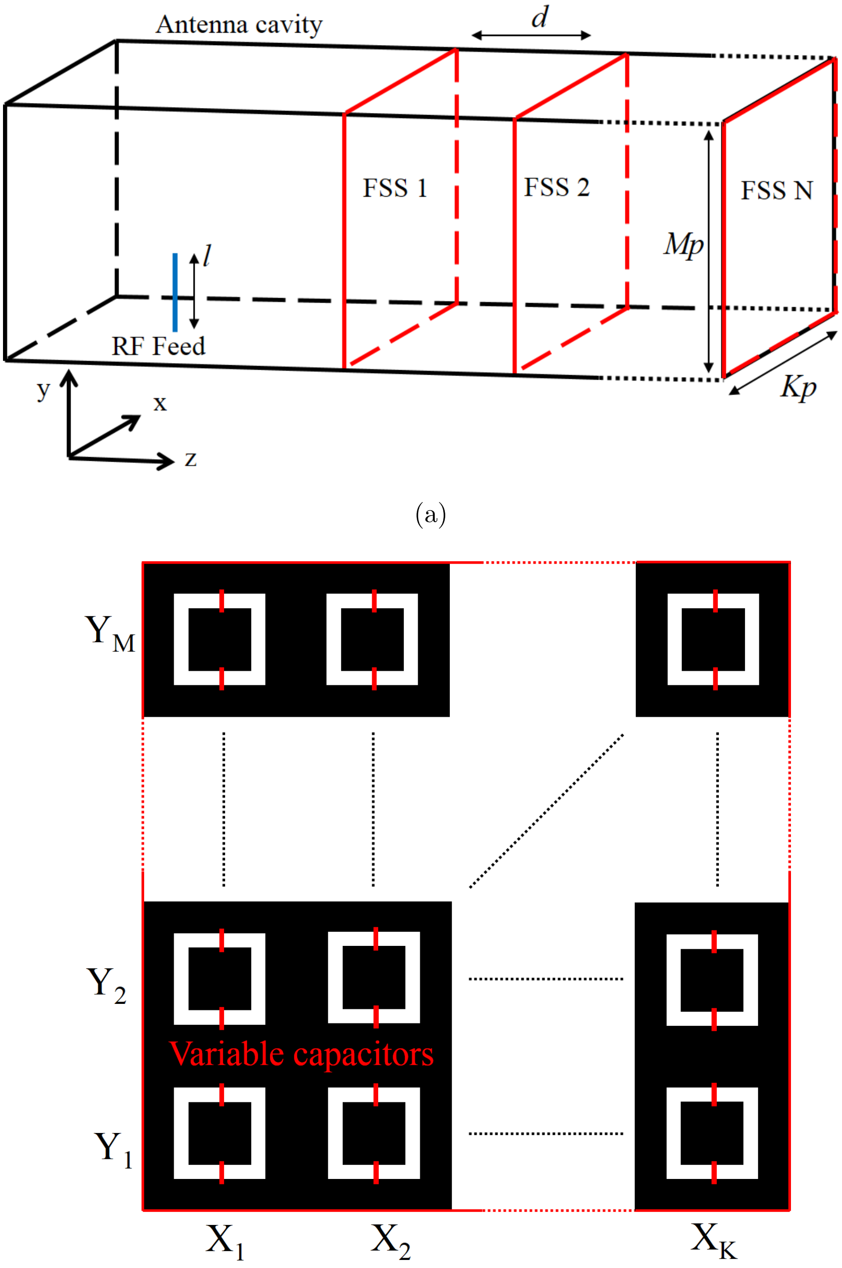

(a)

(b)

Figure 3.23: Diagrams of modulating antenna concept. (a) 3D antenna structure, (b) FSS structure in antenna

of variable capacitors and the values of M and K, have been discussed in detail. The design has been created for the potential to provide low complexity, energy efficient phase modulation over broad bandwidths in comparison with conventional modulators, whilst limiting the unit form factor. These characteristics may allow the use of the DAM unit produced through this thesis to affordably densify IoT wireless networks.

Chapter 4

QPSK DAM: A demonstration

4.1 Introduction

The previous Chapter developed a general design of a direct antenna modulation (DAM) unit, using reconfigurable transmissive frequency selective surfaces (FSS). This template has the potential to produce wide bandwidth phase modulation efficiently and with low complexity, while maintaining a reasonable form factor. This presents opportunities for the use of this DAM template as transmitters for Internet of Things (IoT) access points, reducing the costs of network densification. In this chapter, the general template will be implemented as a proof-of-concept QPSK modulating FSS DAM unit.

A prototype antenna will be designed to achieve QPSK modulation at symbol rates in the MHz, and operating at 1.8GHz, which is a licensed mobile frequency band used for both GSM and LTE (Table 4.1). Further, it will again produce a single linear polarisation and have an aperture of as close to $(\lambda_0/2)^2$ as possible, and a depth of approximately λ_0. The efficiency should be greater than 30%, the average PA efficiency in large base stations.

This Chapter contains the design of the FSS, its incorporation into an antenna, and measurement of the DAM unit's performance as an antenna. A conventional end-to-end communications system, based around the QPSK DAM unit, will be designed and implemented, in order to measure the FSS DAM unit's performance as a modulator over a line of sight (LoS) channel. This work was undertaken as a proof-of-concept for "phase FSS DAM", and will be used as the basis for a preliminary discussion of the potential for FSS DAM to be used in IoT networks. Some of this work has previously been published in [148–150].

4.2 FSS modulator design and simulation

In this section, a reconfigurable antenna capable of acting as the modulator in a QPSK FSS DAM transmitter will be designed and simulated. It will be based on the general design set

Parameter	Requirement
Modulation format	QPSK
Frequency of operation	1.8GHz
Efficiency	¿30%
Symbol rate	$>$ 1MSymbol/s
Polarisation	Linear
Size	$\frac{\lambda_0}{2} \times \frac{\lambda_0}{2} \times \lambda_0$

Table 4.1: Key design requirements for QPSK FSS DAM

out in detail in Chapter 3, and its expected performance will be predicted through simulation.

4.2.1 FSS design

For an FSS DAM transmitter to achieve QPSK modulation, the FSS is required to provide four orthogonal constellation points, each separated by 90^o of phase, where the relative differences in the magnitude of each point, and so the distortion of the constellation, is minimised. A square-loop reconfigurable FSS was designed to achieve this (Fig. 4.1a). It was designed to resonate higher than the frequency of interest, such that the tuning capacitance of a variable capacitor will reduce the resonant frequency to around 1.8GHz. Using Langley's equations [74] and assuming the EM wave has orthogonal incidence, the FSS unit cell dimensions in Fig. 4.1a give an equivalent inductance, L_{FSS}, of 19pH and capacitance, C_{FSS}, of 64pF giving a static resonance at 4.5GHz. This is corroborated by simulation of an infinite layer of these unit cells using Floquet boundaries in free space, as shown in Fig. 4.1b. The supporting dielectric was chosen as FR4, for ease and cost of fabrication, with a thickness of t_{sub}=0.8mm, which is the thinnest standard thickness. This was chosen to minimise losses in the dielectric.

Varactor diodes were chosen as the variable capacitors for their broad tuning range, potential high switching rate, and the low voltages needed to vary their capacitance. In particular, SMV1247 varactor diodes, with equivalent series RLC circuit parameters of R_v=4.9Ω, L_v =0.7nH and tuning capacitance of C_v=0.6pF-7pF, were chosen. They also tune fully over their range for bias voltages less than 6V, which eases implementation. These diodes have a comparatively high ESR, but this was chosen as a trade-off with low minimum capacitance, which on balance decreases loss in the diodes. This is shown by simulation of a single-layer FSS with SMV1247 diodes, versus the same FSS with BB202 diodes, with characteristics shown in Table 4.2 (Fig. 4.2a). The SMV1247 diodes show an improvement of 0.3dB in transmitted magnitude over the BB202 diodes.

The number of layers required to achieve QPSK was then explored. The theoretical

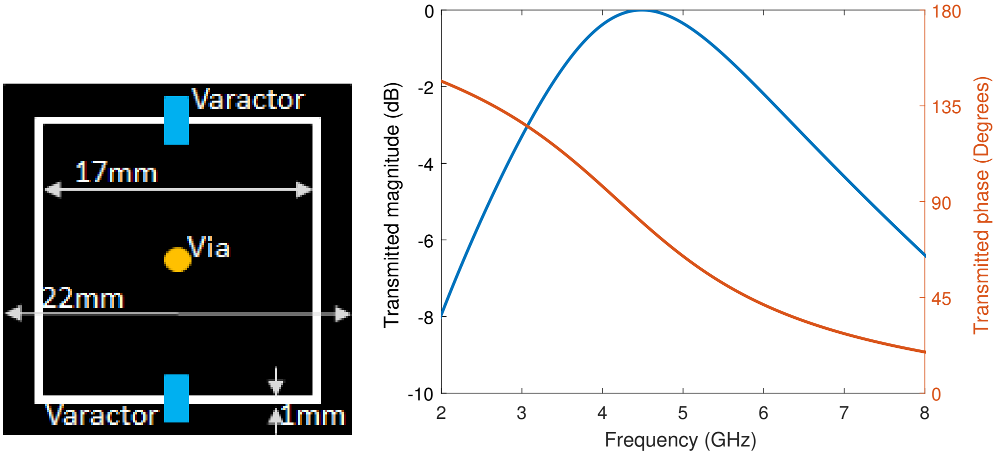

(a) (b)

Figure 4.1: (a) Design and geometry of FSS unit cell, (b) Simulated S_{21} of ideal static FSS design with Floquet modes in free space.

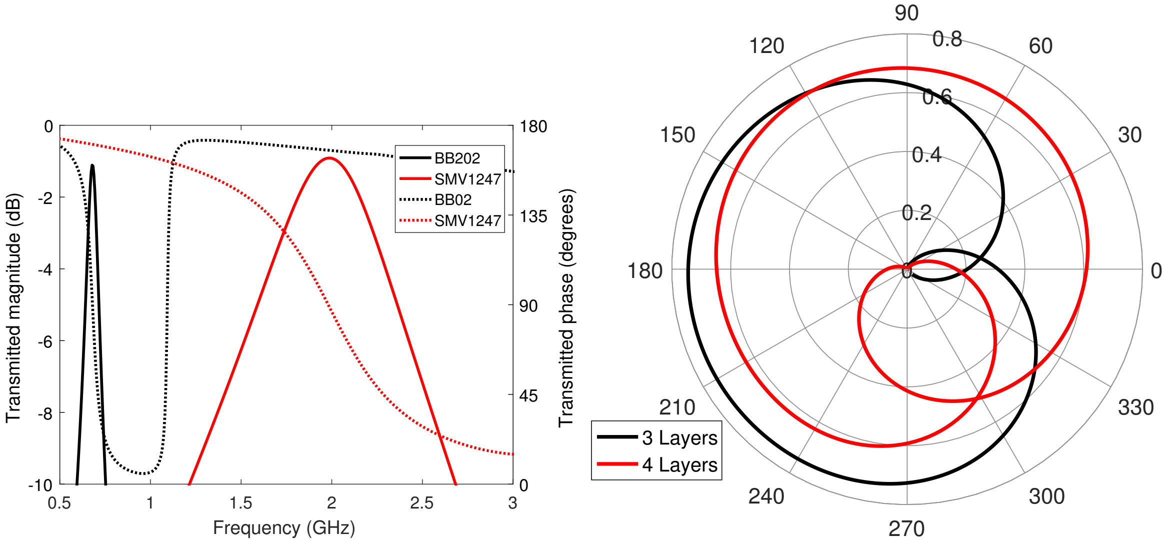

(a) (b)

Figure 4.2: Simulated lossy FSS S_{21} against frequency, (a) single layer with SMV1247 and BB202 diodes (magnitude- solid lines, phase- dashed lines), (b) multiple layers with SMV1247 diodes

Diode name	C_v range (pF)	Typical R_v (Ω)	L_v (nH)	Tuning voltages (V)
SMV1247	0.6 - 7	4.9	0.7	0.3 - 4.7
BB202	6.4 - 30	0.4	0.5	0.2 - 6.0

Table 4.2: Comparison of possible varactor diode characteristics

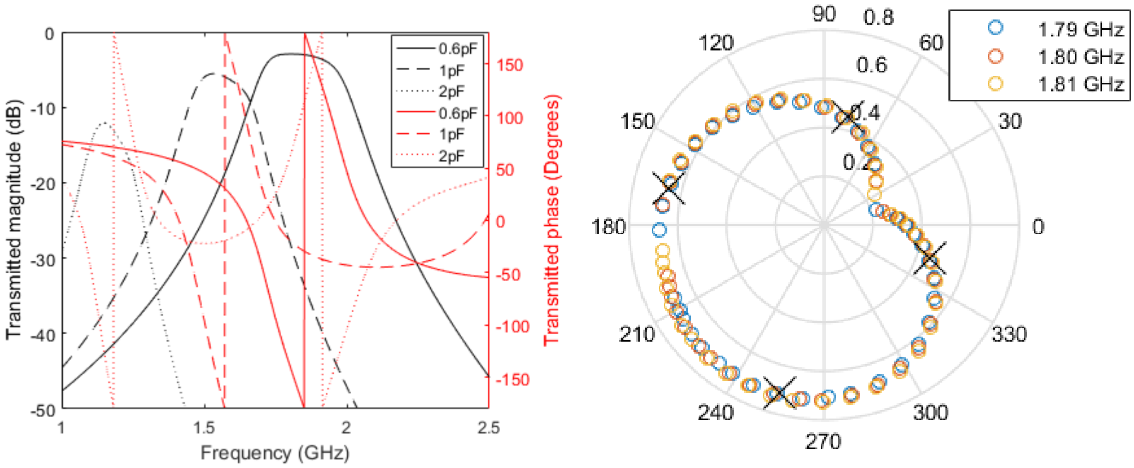

(a) (b)

Figure 4.3: Simulated S_{21} of final, three-layer, reconfigurable FSS design in free space, (a) against frequency, (b) against capacitance across 20MHz bandwidth with potential QPSK constellation marked (x)

minimum, as discussed previously, is 3 layers, so simulations of 3 and 4 layers of the designed FSS in free space were used to explore the behaviour (Fig. 4.2b). For 3 layers, the total loss through the FSS is 2.5dB at 0.6pF, with 3.2dB variation across the 270^o phase change required for QPSK. This is in comparison with 4 layers, which has 3.3dB total loss, but only 1.2dB magnitude distortion across a QPSK constellation. While the constellation produced by a 4-layer design would be less distorted than that from a 3 layer, the loss is greater and the antenna form factor also increases by a further $\lambda/4$. As such, the 3 layer design was chosen, with 3.2dB distortion seen as acceptable for proof-of-concept.

The final FSS design in free space is shown simulated over a range of capacitances in Fig. 4.3. This shows that, once magnitude variation due to additional losses at higher capacitances are factored in, the expected magnitude distortion across the QPSK constellation (shown in crosses in Fig. 4.3b) is 4.2dB. Note also that the performance is almost identical over a 20MHz channel bandwidth.

4.2.2 Antenna design and simulation

The next step in the design of the QPSK DAM unit is to integrate the reconfigurable FSS into an antenna. Using the general design produced in Chapter 3 (Fig. 3.23), the key design

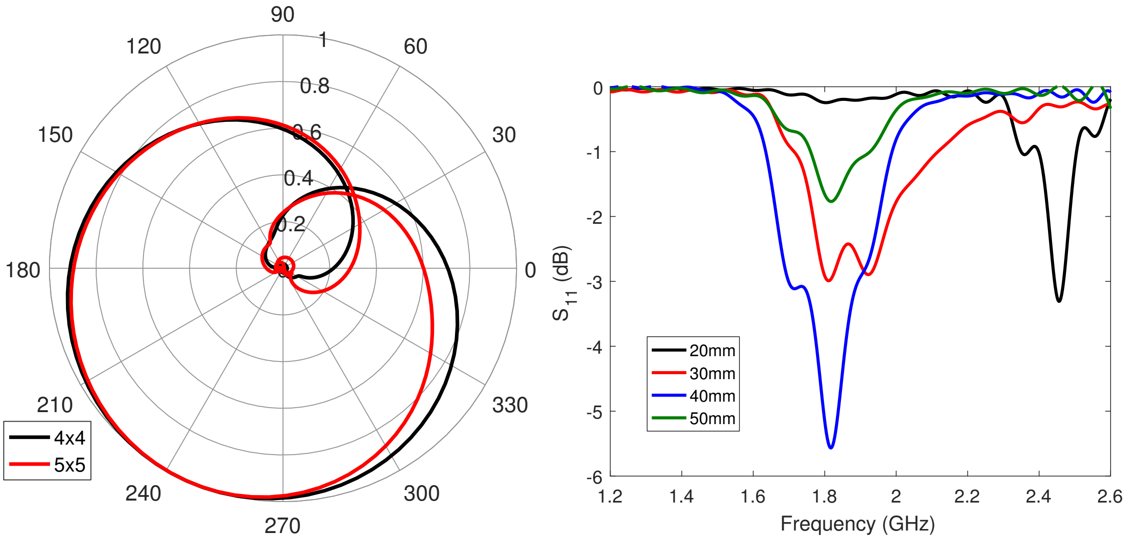

(a)

(b)

Figure 4.4: Simulated antenna, (a) E-field at boresight against frequency while varying K, (b) Antenna S_{11} against frequency with varying probe length l

questions are the number of unit cells per FSS layer to be used (M and K), the spacings between the layers (d), and the length of the probe (l_{probe}). In order to simplify the possible future transition from a design with single linear polarisation to dual polar designs, it was decided that the antenna aperture should be square, such that $M = K$. Fig. 4.4a shows the simulated normalised E-field at the antenna boresight in the farfield against frequency with different values of K. In this case, the 4×4 arrangement gives better performance than where K=5, giving 3.7dB distortion as opposed to 4.4dB over the QPSK constellation. As such, the 4×4 arrangement was chosen.

This 4×4 antenna was then simulated with various probe lengths, with the antenna S_{11} shown in Fig. 4.4b. The best performing length is 40mm at 1.8GHz, with a match of 6dB. Normally a match of 10dB or better would be preferable in an antenna, but this was considered less important for the purposes of demonstrating QPSK DAM. It could be improved by using a matching network on the antenna input, reducing the loss in performance.

The effect of altering the spacing between layers is shown in Fig. 4.5. The wavelength within the antenna at the frequency of interest, 1.8GHz, will be between λ_0=167mm and λ_g=519mm, where the antenna width $K \cdot p$=88mm. This is because the cavity on the antenna is neither free space, nor an infinitely long waveguide. As such, layer spacing d should be between $\lambda_0/4$=41.7mm and $\lambda_g/4$=130mm. The flattest response is where d=60mm, suggesting the wavelength in the cavity is around 240mm. However, the magnitude change for 270^o phase change appears to be less where d=40mm, giving 2.5dB distortion instead of 3.2dB distortion at C_v=1.05pF. As such, and to reduce the antenna form factor, the spacing for the final design was chosen as d=40mm.

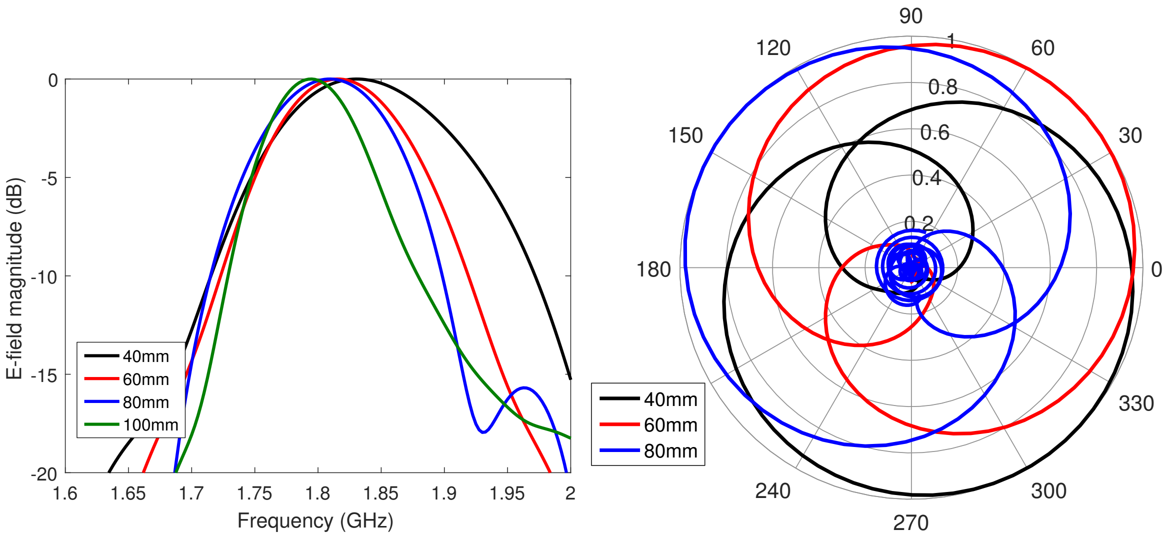

(a) (b)

Figure 4.5: Simulated E-field at boresight of antenna against frequency with distance d between layers as a parameter, (a) Magnitude, (b) Polar plot of magnitude and phase

Finally, one element of the design which has yet to be considered is the method of biasing the diodes on the FSS. Each FSS will be connected to the bias voltage signal by a twisted pair of wires, and biasing lines fabricated on the reverse of the FSS will connect the signal to each FSS patch through vias. The design for the biasing network of this antenna is shown in Fig. 4.6a. The majority of biasing lines are placed orthogonally to the incident E-field, in order to minimise their impact, and a single line connects them together. The effect of these biasing lines is to introduce extra loss of 0.5dB through the whole antenna, and to shift the resonant frequency of the antenna upwards by 20MHz, due to the added inductance (Fig. 4.6b).

The final antenna design is shown in Fig. 4.7. Its operation can be shown by simulation of its behaviour at resonance (Fig. 4.8). Fig. 4.8a shows the monopole probe injecting energy into the cavity, which reflects off the reverse wall and interferes constructively with the forward-travelling part of the injected wave. The E-fields then pass through the three FSS layers, with resonance around the FSS patches, as can be seen more clearly in Fig. 4.8b. Note here that the central columns of unit cells are subject to stronger E-fields, due to the E-field distribution inside the cavity, as discussed previously. The greater importance of the central FSS unit cells is further demonstrated in Fig. 4.8c. Note that the energy inside the cavity reduces after each FSS layer, due to the losses in the varactor diodes and in the FSS substrate.

The change in E-field magnitude and phase due to changing diode capacitance was simulated by placing an E-field probe at boresight outside of the model bounding box, and normalising the result against the field strength at the same point when the FSS is removed

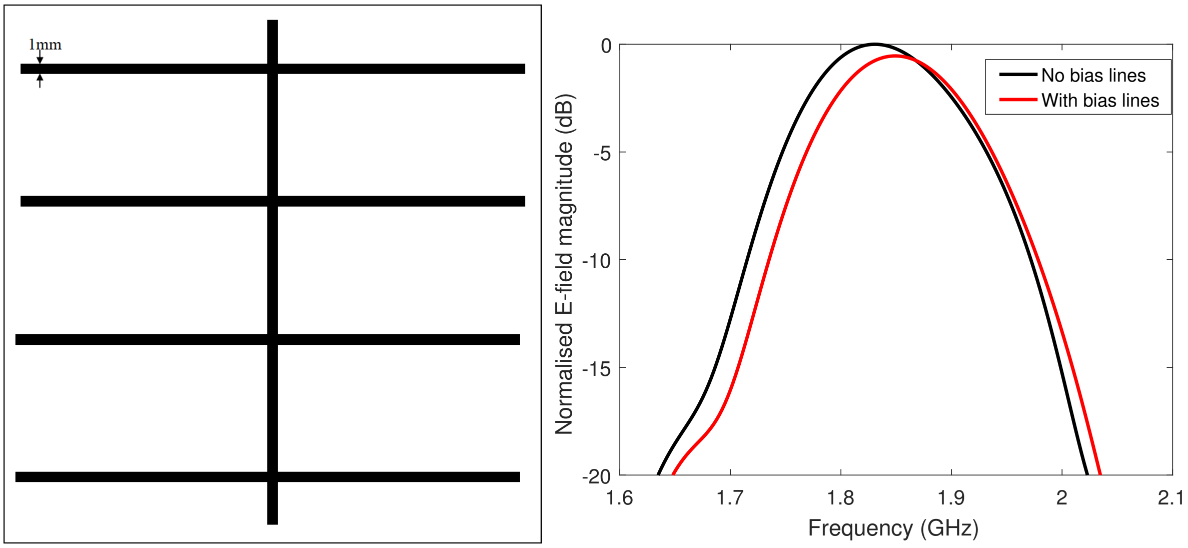

(a) (b)

Figure 4.6: (a) Diagram of bias line configuration on FSS, (b) Simulation of reconfigurable antenna E-field at boresight with and without bias lines, against frequency at C_v=1.05pF

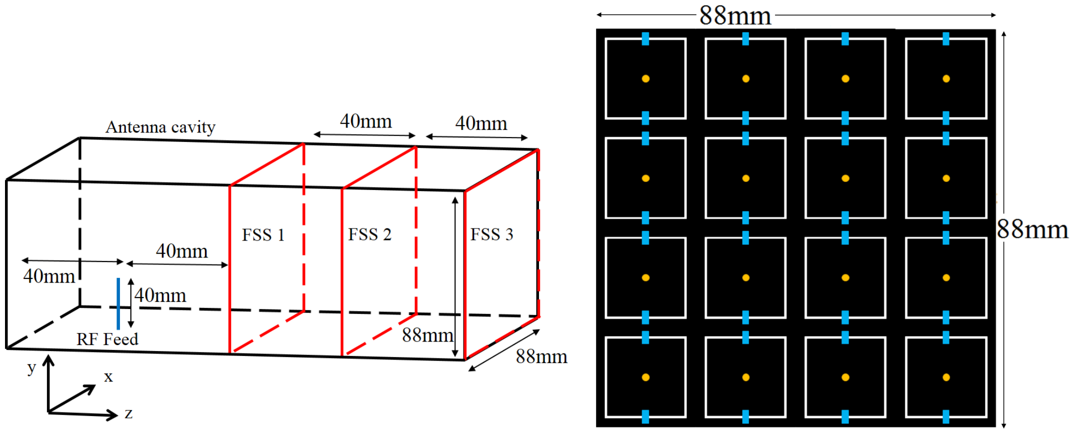

(a) (b)

Figure 4.7: Reconfigurable antenna design, (a) Side view, (b) Front view

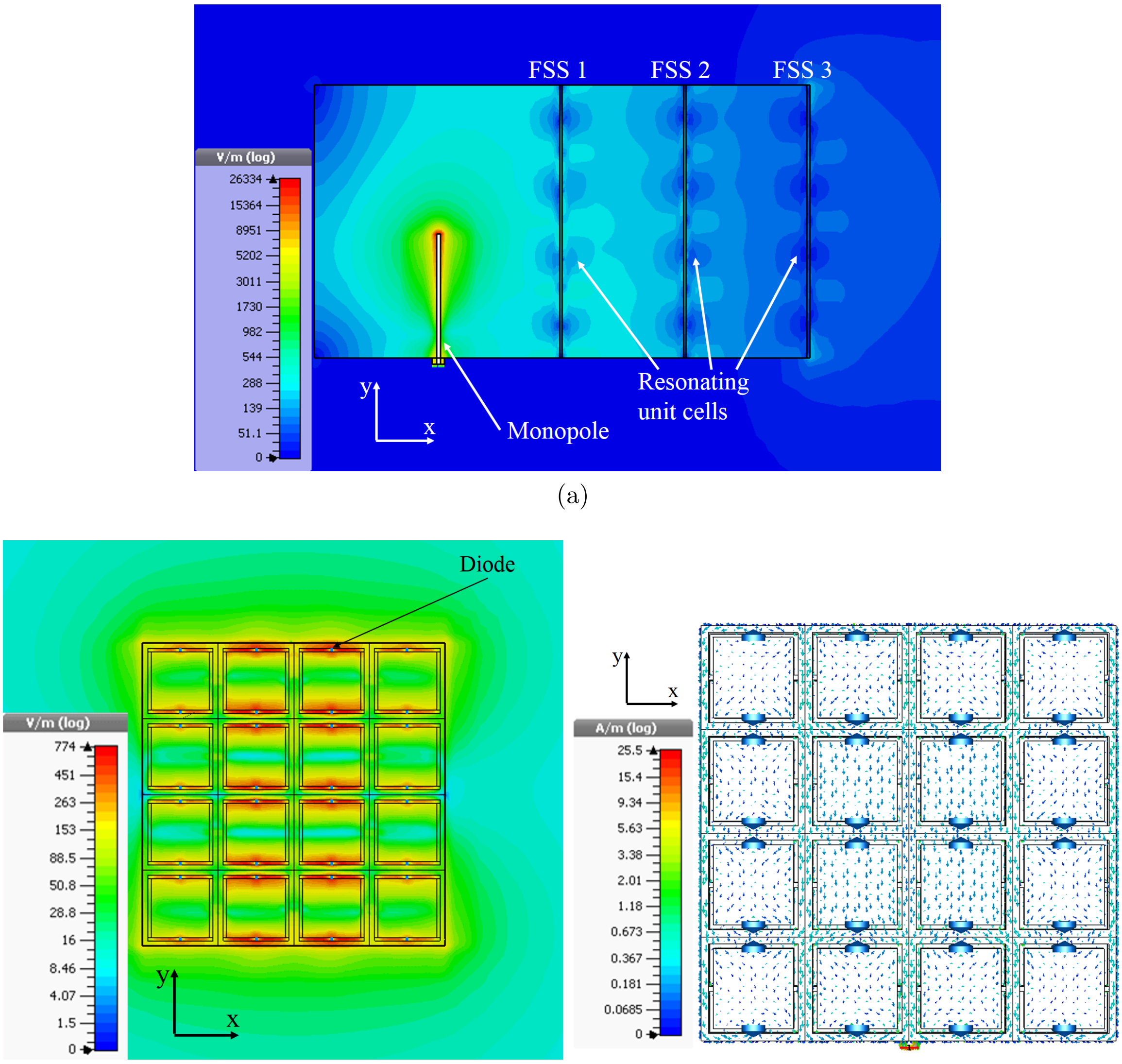

(a)

(b)

(c)

Figure 4.8: Simulated fields and currents of final antenna at 1.8GHz with C_v=1.11pF, (a) E-field side profile, (b) E-field antenna front, (c) Surface currents of final FSS layer

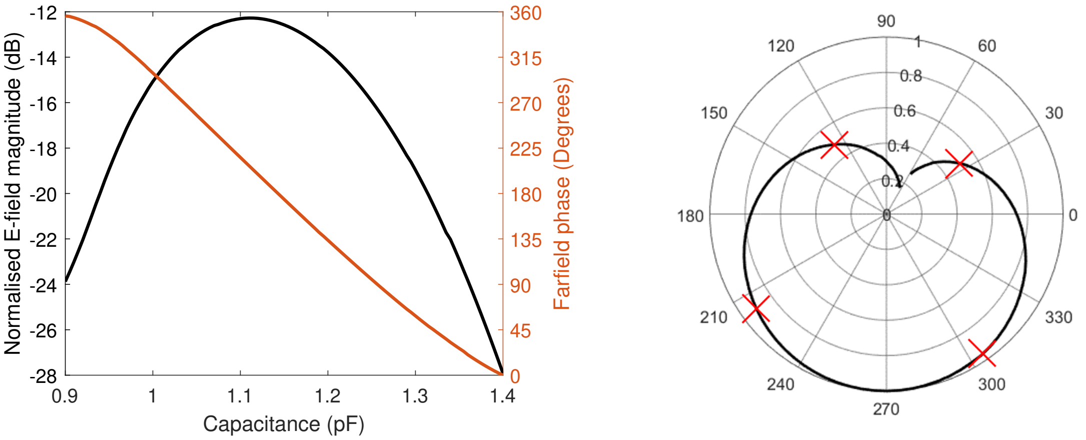

(a) (b)

Figure 4.9: Simulated E-field at antenna boresight normalised to empty cavity, (a) Magnitude and phase plots, (b) Polar plot with possible constellation points shown as 'x'

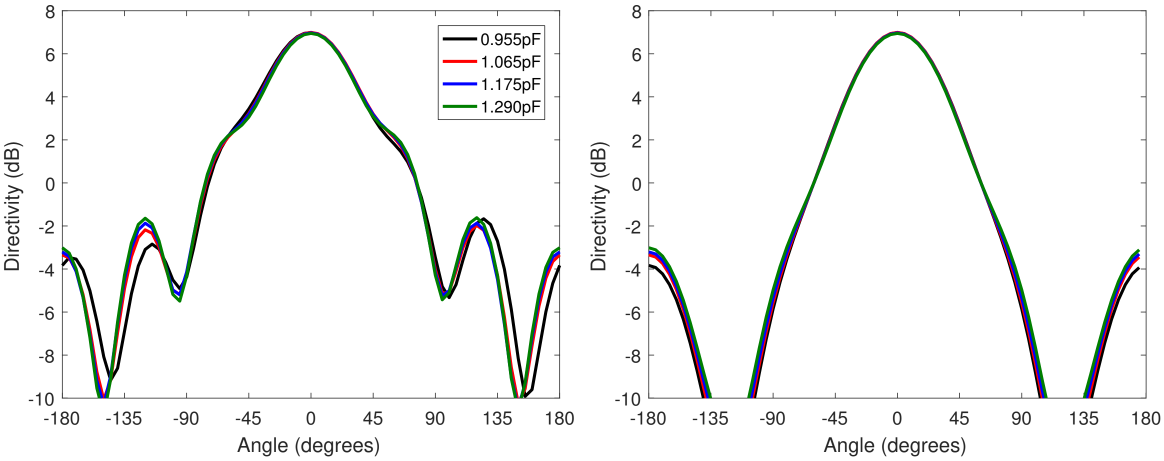

(a) (b)

Figure 4.10: Simulated antenna directivity, (a) E-plane cut, (b) H-plane cut

from the cavity (Fig. 4.9a). It shows 6.2dB magnitude variation is expected to occur across 270^o of phase change at 1.8GHz, over the range 0.955-1.290pF (Fig. 4.9a). Note also the large loss over an empty cavity of minimum 12dB, due to losses in the varactor diodes and substrate. This will be discussed further later in this Section. A QPSK constellation has been drawn out from this, at $C_V=$ 0.955pF, 1.065pF, 1.175pF and 1.290pF. These chosen constellation points show 5.75dB distortion between the largest and the smallest, with two points with a low amplitude and two with a large amplitude (Fig. 4.9b).

The antenna's directivity at these four constellation points is shown in Fig. 4.10. This shows an expected 3dB beamwidth of around 75^o in both the E-plane and in the H-plane, with peak directivity of 7dB at boresight. The pattern is constant across the four constellation points, with especially good agreement within the main beam of the antenna. However, note

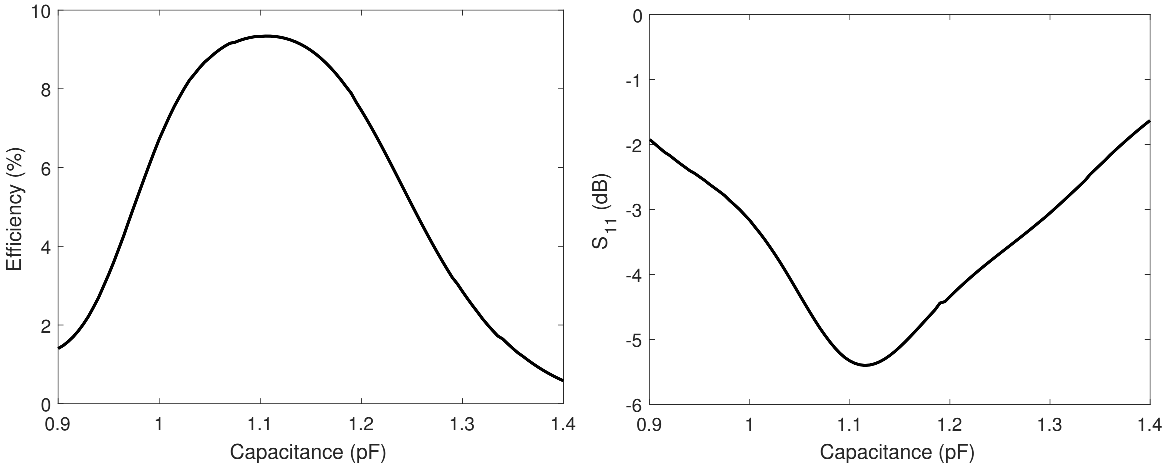

(a) (b)

Figure 4.11: Simulated antenna characteristics with varying capacitance, (a) radiative efficiency, (b) S_{11}

that the peak gain for each constellation point will vary due to the changing efficiency of the antenna with varying capacitance (Fig. 4.11a). This change is captured in the distortion of the constellation points discussed above. The efficiency simulations show a peak efficiency of 9.3%, which reduces to 3.2% at the extreme constellation points. This is poor expected performance, which could be improved using lower loss substrates, and diodes which operate at lower capacitances and have lower ESR, as discussed above.

The S_{11} with varying capacitance is shown in Fig. 4.11b, showing a best-case match of 5.4dB and a worst-case of 2.6dB at the 0.955pF constellation point. This is a poor match, which contributes to the magnitude distortion of constellation points, and could be improved with a matching network on the antenna input, as mentioned earlier in this Chapter. However, for proof-of-concept, these parameters were considered sufficient to fabricate, measure and test the antenna as a DAM unit.

4.3 Fabrication and characterisation of reconfigurable antenna

The reconfigurable antenna was then fabricated. The FSS was made using standard PCB manufacturing techniques, 1mm diameter holes drilled through the middle of each patch, and 1mm vias inserted and soldered in place to connect the biasing lines to the FSS patches. The diodes were soldered in place by hand, with their cathodes attached to the patch. This ensures that the diodes are reverse biased when a positive voltage is put on these patches, avoiding the signal being pulled to the RF ground when the FSS is in contact with the antenna cavity. An example FSS layer is shown photographed in Fig. 4.12.

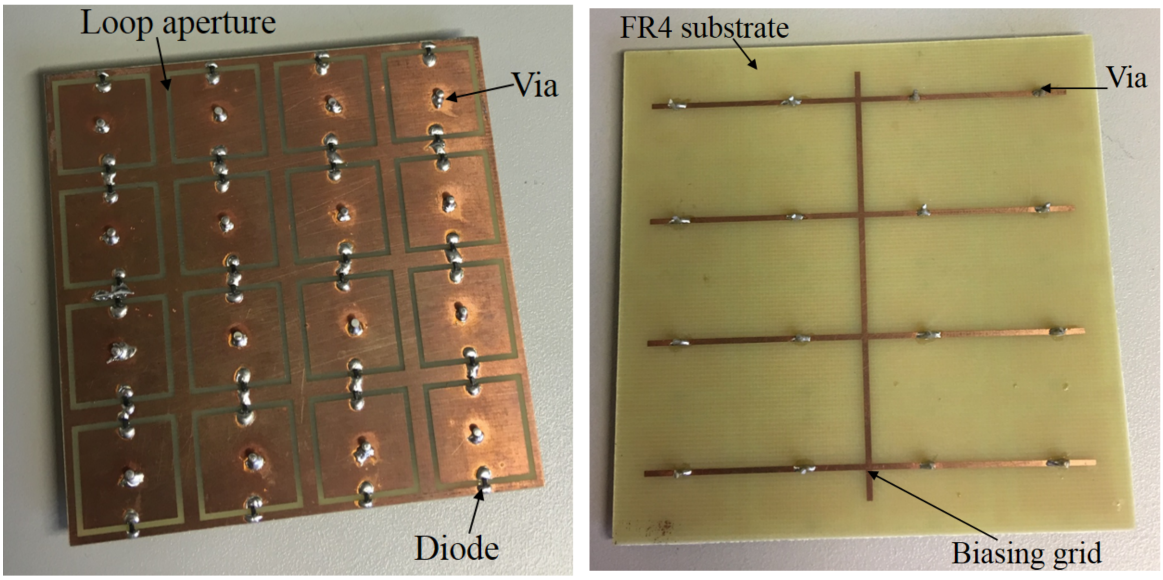

(a) (b)

Figure 4.12: Photograph of constructed FSS for QPSK DAM, (a) front, (b) reverse

The cavity was fabricated from sheet aluminium, and held together by conducting aluminium tape. The monopole probe was made by extending a panel-mount SMA connector to the required l_{probe}=40mm into the cavity. The FSS layers were placed inside the cavity, and held d=40mm apart by blocks of polystyrene, which has a dielectric constant of $\epsilon_r \approxeq 1$, so it appears electromagnetically nearly identical to air. Electrically small holes, 2mm in diameter, were drilled in the side of the cavity to allow twisted pairs of wires to be soldered to the FSS layers inside. The final fabricated reconfigurable antenna for producing QPSK DAM is photographed in Fig. 4.13.

The first antenna characteristic to be measured was the variation in transmitted magnitude and phase with changing bias voltage. This was done by placing the antenna in an anechoic chamber and using an Agilent E5071C network analyser to feed the antenna with a CW signal at 1.8GHz. A DC bias was provided to the varactor diodes in the FSS by a variable voltage supply. A wideband horn antenna was placed 2.5m away at boresight from the antenna, and was connected to the receiving port of the network analyser. The received magnitude and phase was then recorded as the bias voltage was varied. Results are shown in Fig. 4.14, demonstrating that 270^o phase change is produced with distortion of 7.3dB. This is 1dB more magnitude distortion than predicted by simulation, most likely due to larger losses than expected in the fabricated unit. When comparing Fig. 4.14 with Fig. 4.9a, it should be noted that the relationship between bias voltage V and diode capacitance C_v is inverse and non-linear.

When four bias voltages are chosen to give QPSK constellation (2.70V, 2.91V, 3.19V and

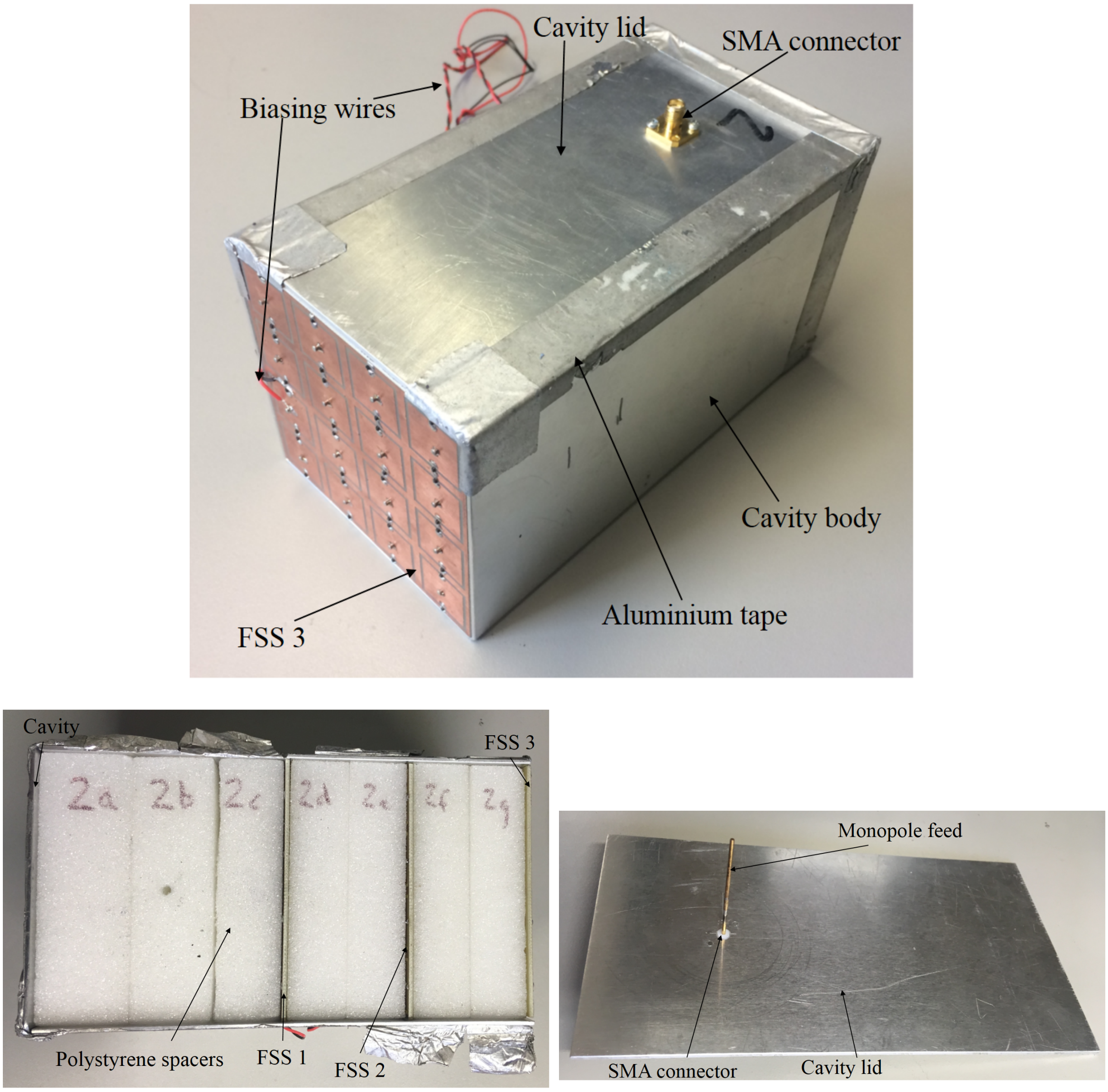

Figure 4.13: Photograph of the fabricated reconfigurable antenna, (a) Complete fabricated antenna, (b) Inside of antenna, (c) Antenna lid with monopole feed

3.74V), the points have a distortion of 6.5dB between the largest two points and the smallest two points. This manifests as two of the constellation points being 0.47 of the amplitude of the other two constellation points (Fig. 4.14b). This impaired constellation has an impact on the BER achieved using this antenna as a DAM modulator, as will be explored later in this chapter.

The radiation pattern of the antenna at these four bias voltages was measured in an anechoic chamber at 1.8GHz, with a receiving pyramidal horn antenna 2.5m away (Fig. 4.15). The bias voltage was again provided using a variable DC voltage source. The patterns were broadly similar for all bias voltages, as previously suggested by simulation. However, as expected, they were all differently attenuated, with a maximum difference of 6.5dB at

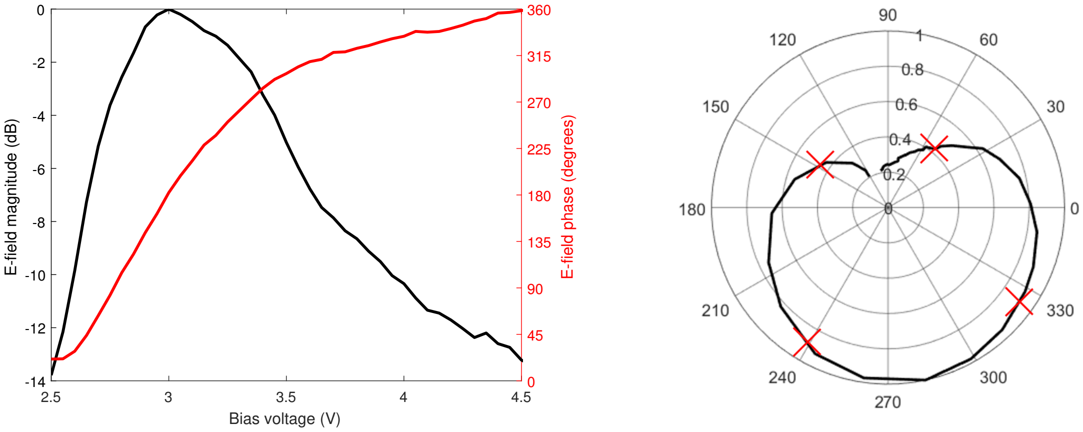

(a) (b)

Figure 4.14: Measured normalised antenna E-field at 1.8GHz with varying bias voltage, (a) magnitude and phase, (b) polar plot

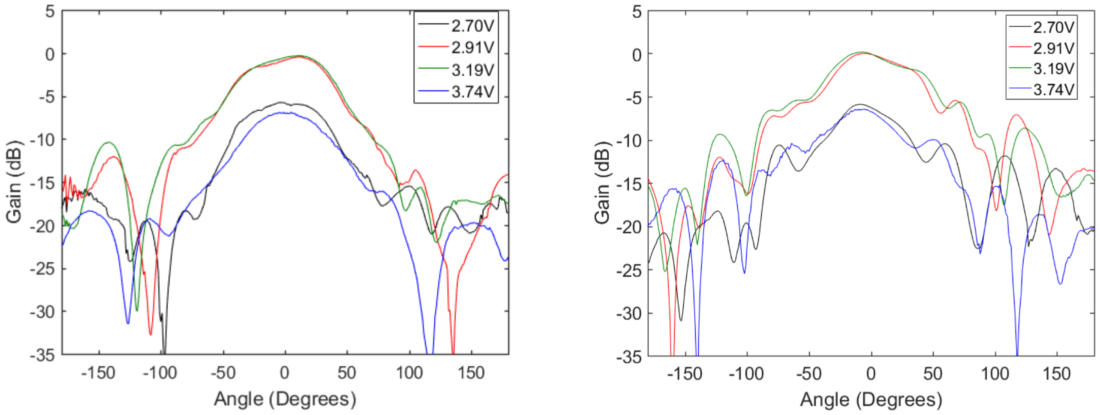

(a) (b)

Figure 4.15: Antenna gain pattern in (a) E-plane and (b) H-plane with different biasing voltages

boresight, corresponding to the magnitude distortion between constellation points. The measured antenna gain varies from 0.15dBi to -6.44dBi, with the low gains arising from a low FSS transmission coefficient and a high varactor diode loss.

Simulation of the antenna gives a range of radiation efficiencies across the QPSK constellation points from -12.8dB to -8.4dB, which reduces to a range from -4.3dB to -0.86dB with lossless diodes. Therefore, 3.44dB of the variation is attributable to the change of the FSS transmission coefficient at each constellation point. Variation of the transmission coefficient can be reduced by having more FSS layers, which increases the FSS bandwidth, but this would reduce the maximum value of the overall transmission coefficient. Designing the FSS with less lossy substrates and tunable components would compensate for the latter.

The antenna S_{11} was also measured at the different constellation points, again in an

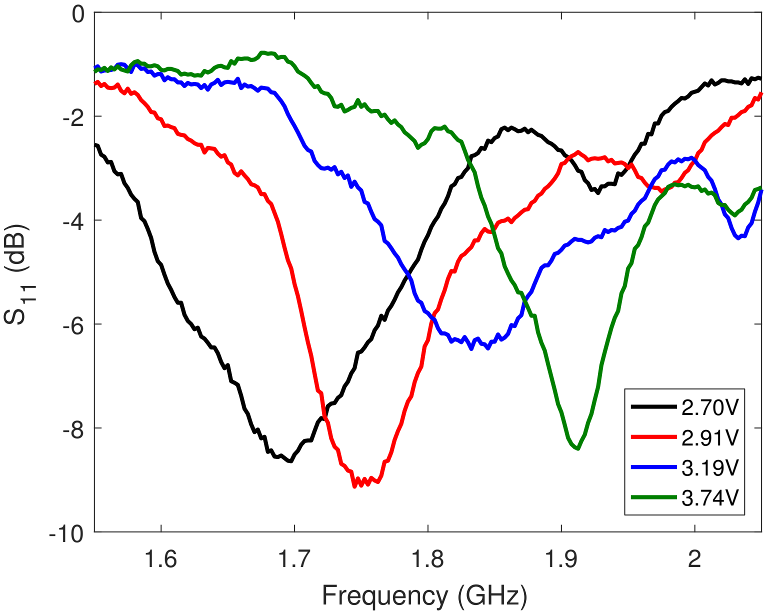

Figure 4.16: Measured S_{11} of reconfigurable antenna against frequency at QPSK bias voltages

anechoic chamber using a network analyser (Fig. 4.16). It shows how the S-parameter of the whole antenna tunes as the FSS inside it tunes. The measured results seem to match well with the simulation shown in Fig. 4.11b, with variation between a match of 6.3dB and 2.4dB at 1.8GHz. This measurement also shows that a broadband matching network would most likely be needed to compensate for the large S_{11}, as the effect of FSS tuning is large.

4.4 QPSK system implementation

In order to characterise its performance as a modulator, and provide a proof-of-principle of FSS DAM, the fabricated reconfigurable antenna was used as a QPSK DAM transmitter in an end-to-end communications system. This section will present a QPSK FSS DAM communications system, and demonstrate how it differs from a conventional QPSK communications system. The construction of the data packets, which will be used to evaluate the FSS DAM system, will also be discussed. A practical testbed design will then be presented, along with the key challenges and limitations of implementation. Finally, experimental results will be given.

4.4.1 A QPSK FSS DAM communications system

A conventional DSSS communications system, as previously discussed in Chapter 2.4, is shown in Fig. 4.17. Binary digital data is mapped to a complex number representing baseband I and Q, then spread by spreading sequence $c(t)$. In the case where a spreading sequence is not used, $c(t)$=1. This string of complex numbers is then modulated onto a radio

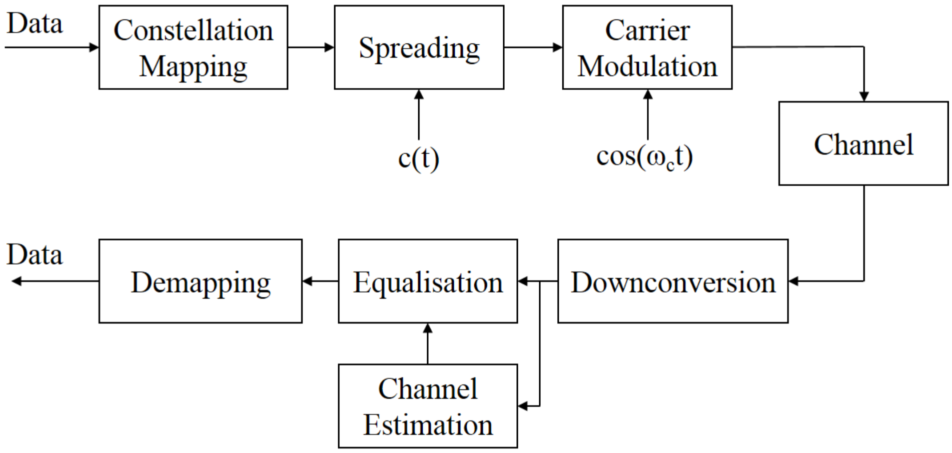

Figure 4.17: System schematic of QPSK DSSS communication system

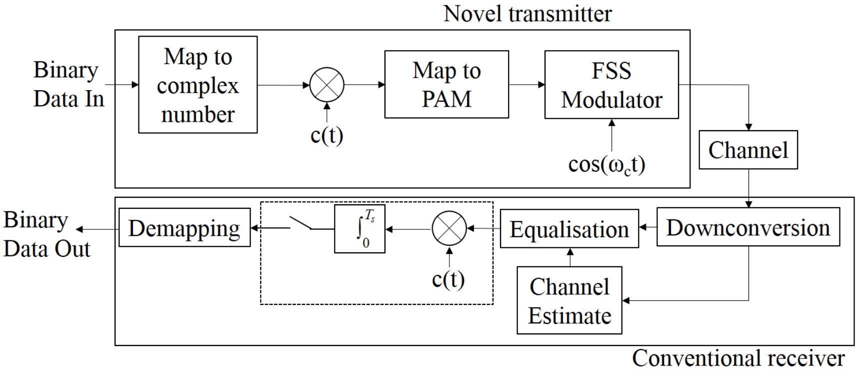

Figure 4.18: System schematic of QPSK DSSS communication system with DAM transmitter

carrier wave at angular frequency ω_c, which passes through a channel with impulse response $h(t)$. At the receiver, the signal is downconverted and sampled, producing a set of complex numbers representing baseband I and Q. It is within this process that noise is added to the signal. A known pilot sequence within each packet of data is used to estimate $h(t)$, and this is used to equalise the received signal. In the line-of-sight case, this is a derotation of the received complex chips. This equalised signal is then multiplied by $c(t)$ again, and a decision is made on the despread baseband signal to demap it into binary digital data.

By contrast, in an FSS DAM transmitter, there is one extra step, as suggested by Fig. 4.18. Once the digital data has been mapped to a complex number and spread, it must then be mapped to a bias voltage signal for the FSS modulator. This signal looks like a pulse amplitude modulation (PAM) signal, and consists of the bias voltage for each desired constellation point. The duration of each voltage level is equivalent to the chip duration T_c, with each spread symbol made of multiple voltage levels in this domain. Feeding this bias voltage to the DAM unit produces the modulated RF signal which passes into the channel. The receiver is identical to a conventional DSSS receiver.

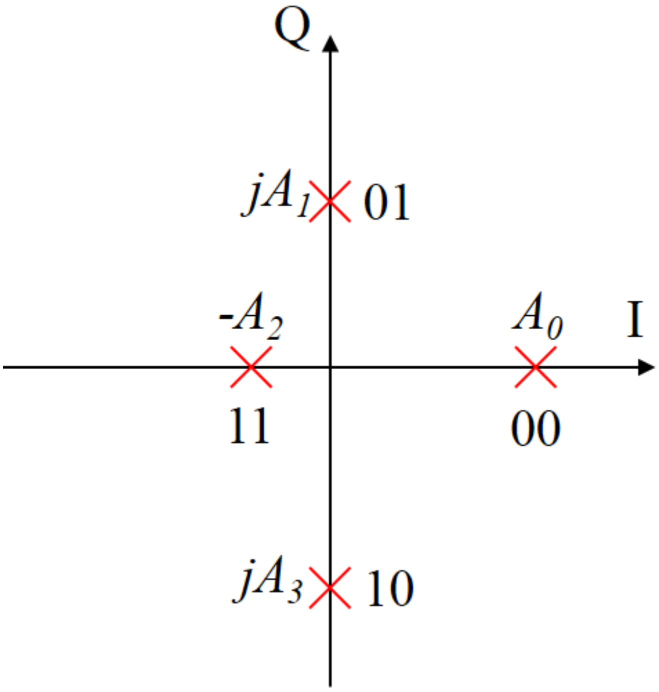

Figure 4.19: Generic Gray-mapped distorted QPSK constellation

For this implementation of QPSK FSS DAM, the pilot sequence was placed at the beginning of the packet, and consisted of a BPSK modulated length 15 m-sequence repeated 222 times. The m-sequence was chosen for its impulse-like autocorrelation, discussed in detail in Chapter 2.4. This is useful for channel estimation and for chip-level receiver synchronisation. The repetition strengthens the mean channel estimation. The effect of channel estimation error on FSS DAM as the amount of repetition is reduced is left for future investigation.

Each packet also contained 888 data bits as a payload, each spread by spreading sequence $c(t)$. DSSS was used because it breaks each data symbol, of duration T_s, into multiple data chips, of duration T_c. Each of these chips, in an FSS DAM system, will be transmitted with the distorted QPSK constellation described in Fig. 4.14b. This distorted constellation has two constellation points which have small amplitude opposite from two which have large amplitude. As such, if $c(t)$ is a balanced sequence, each data bit will be made of an equal number of small and large data chips. At the receiver, these chips are multiplied by the spread sequence and summed over the length of the data bit. As such, the distortion is averaged out, creating a more conventional QPSK constellation and potentially improving the BER.

For example, consider the distorted constellation and mapping shown in Fig. 4.19, with amplitudes A_0 to A_3 at each given phase. A binary spreading sequence $c(t)$ is used with X instances of 1 and Y instances of 0. Taking symbol 00, once it has been mapped and spread, it will be a sequence consisting of X values of A_0 and Y values of $-A_2$. If these values are

Data	Distorted constellation point	Despread constellation point
00	0.47	0.717
01	j1	j0.753
10	-1	-0.753
11	-j0.47	-j0.717

Table 4.3: Table of mappings of binary data to corresponding signal generator output, FSS bias voltage and produced constellation point

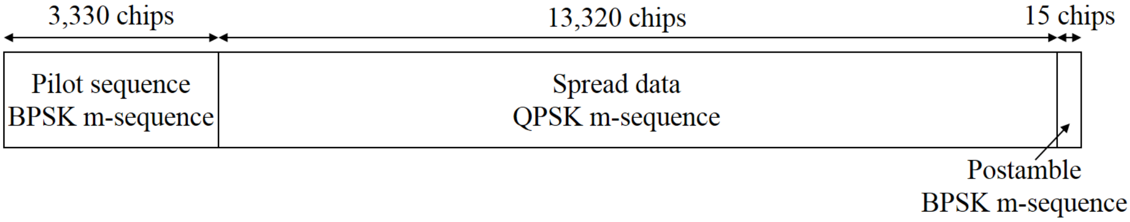

Figure 4.20: Structure of packet under test

then correlated with $c(t)$, the normalised correlator output across this symbol would be

$$x = \frac{XA_0 + YA_2}{X + Y} \tag{4.1}$$

In the special case where $c(t)$ is a perfectly balanced sequence, $X = Y$,

$$x = \frac{X(A_0 + A_2)}{2X} = \frac{A_0 + A_2}{2} \tag{4.2}$$

which is an averaging of A_0 and A_2. Similar effects can be shown for the other three QPSK symbols.

For consistency with the pilot sequence and for its balanced property, the length 15 m-sequence was chosen for the spreading sequence, which has X=8 and Y=7. The effect of this is on the measured distorted constellation produced by the DAM unit is shown in Table 4.3, demonstrating that the final despread constellation should have distortion of only 0.4dB between all four constellation points. The use of the length 15 sequence results in 13,320 data chips being transmitted in each packet.

A short postamble was also included at the end of the packet, of length 15 and consisting of one repetition of the m-sequence, in order to avoid losing data when adjusting for synchronisation error. The final packet construction is shown in Fig. 4.20.

4.4.2 Testbed development

A testbed for transmitting packets of data using DAM was developed to enable this implementation. The requirement for this testbed was to construct a packet from randomly

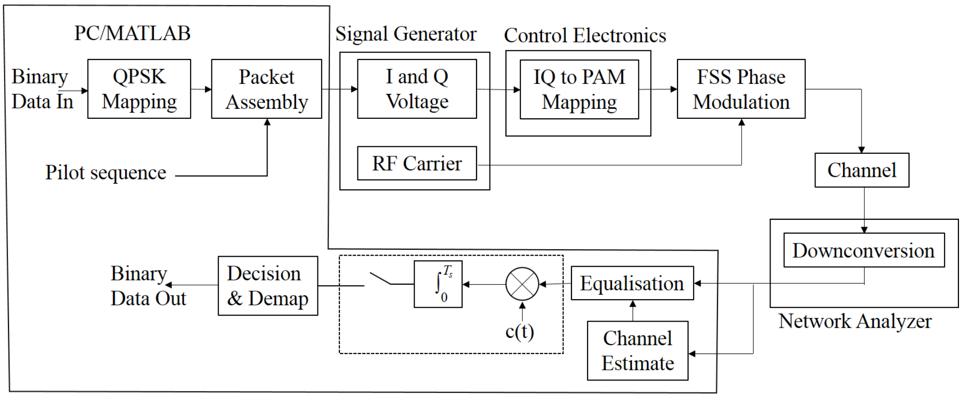

Figure 4.21: Schematic of QPSK FSS DAM communications system

Data	Sig gen output (V)	Voltage output (V)	Ideal constellation point
00	[-0.7,-0.7]	2.7	1
01	[-0.7,+0.7]	2.9	j
10	[+0.7,-0.7]	3.7	-j
11	[+0.7,+0.7]	3.2	-1

Table 4.4: Table of mappings of binary data to corresponding signal generator output, FSS bias voltage and produced constellation point

generated digital data, enact the processes described in Fig. 4.18, compare the output digital data with the original values to determine an error rate for each packet, and repeat this multiple times to obtain a statistically significant result for a given transmit power. The schematic diagram for single iteration of this is shown in Fig. 4.21.

MATLAB code was developed to perform the data generation and packet processing. Binary data representing the complete data packet is sent over general purpose information bus (GPIB) to a Rohde & Schwarz SMBV100A vector signal generator, which maps this data to two voltage signals, representing I and Q, according to a mapping defined by the user. These take values of ±0.707V, as the maximum power of the output constellation must be 1. The signal generator also outputs a CW RF signal at 1.8GHz at power levels between -90dBm and 10dBm, which is fed to the FSS modulator. Control electronics, the design of which will be discussed in depth later in this section, convert the I and Q voltages into the required 4-level PAM signal for the FSS modulator. The required steps of this mapping process are shown in Table 4.4, and were undertaken to allow the available Rohde and Schwarz equipment and its interfaces, which are predominantly baseband or RF inputs and outputs, to produce the signals required for DAM. The design of the mapping electronics for this process is detailed in Appendix B, and the Standard Operating Procedure for the Rohde & Schwarz equipment is found in Appendix C.

A passive, pyramidal horn antenna receives the transmitted signal, which is then down-

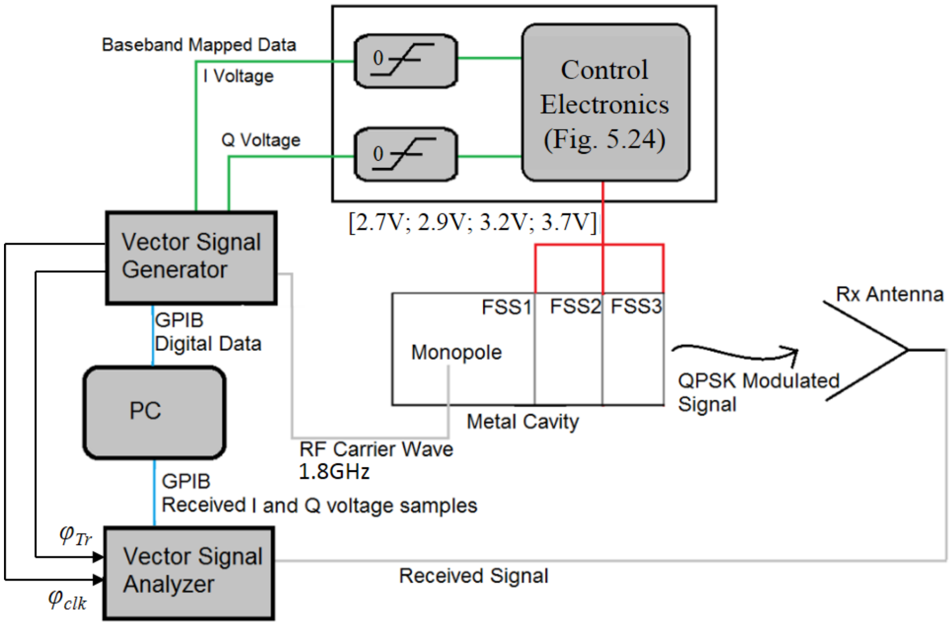

Figure 4.22: Schematic of experimental implementation of QPSK DSSS using DAM transmitter

converted in a Rohde and Schwarz FSV30a vector signal analyser. The sampled signal is then sent over GPIB back to the PC, and is read by MATLAB code, which estimates the channel response, equalises and despreads the signal, before estimating the data using a zero threshold detector. Both Rohde and Schwarz instruments are controlled by MATLAB using the VISA toolkit [151]. They are also connected by a 10MHz signal to support carrier synchronisation, and a trigger voltage is sent from the signal generator to the signal analyser whenever a packet begins to transmit. This instructs the signal analyser to begin measuring the received signal, and ensures synchronisation on the packet level. The complete setup is shown in Fig. 4.22, and the MATLAB code is in Appendix A.

4.4.3 System limitations

One of the key parameters in the implementation of the QPSK FSS DAM transmitter is the symbol rate at which it operates. It has previously been stated that varactor diodes can have switching rates in the order of 10MHz. The SMBV100A signal generator is limited to 40MSymbol/s, and the signal analyser has a front-end bandwidth of 50MHz. As such, with Nyquist sampling at the receiver, the symbol rate in this testbed is theoretically limited to below 25MSymbol/s.

However, the control electronics must be able to produce a clean PAM signal at these rates, and provide this to the DAM unit. As discussed previously and shown in Fig. 4.14a, a small change in bias voltage can lead to a large change in transmitted phase, so small ripple voltages can have a large effect. To investigate this further, the rate-of-change of phase

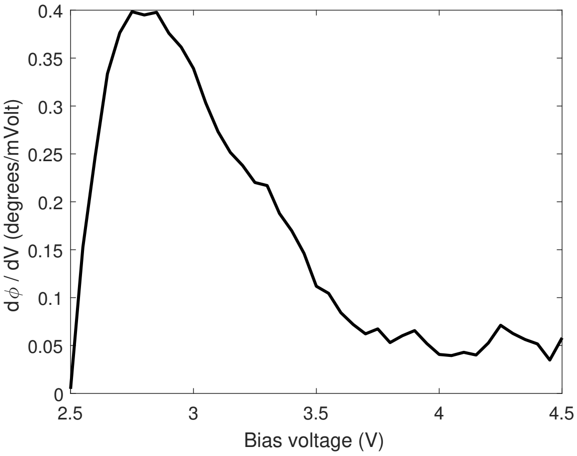

Figure 4.23: Smoothed rate-of-change of E-field phase transmitted by DAM with respect to bias voltage

against voltage, $\frac{d\phi}{dV}$, was calculated from the measured data, and is shown smoothed by a moving average filter with a span of 5 symbols in Fig. 4.23. The peak value is 0.4deg/mV, where V=2.75V, meaning a ripple of 100mV would lead to phase variation of $\pm 20^o$ at that centre voltage.

To try to maximise the switching rate, high speed components were chosen, with the LT1711 comparators having a rise time of 2ns and the OPA254 op-amp having a gain bandwidth product of 250MHz. Bypass capacitors were placed on the supply-lines of all the components to minimise the effects of noise feedback. The output of these electronics in response to a repeating 2-value data signal of [01, 10] at various rates was measured using an oscilloscope and is shown in Fig. 4.24. This is expected from simulation to produce a voltage signal of [2.9, 3.7V], but falls short due to variable tolerances of the resistors in the ladder network. The electronics show a rise time of 11ns and fall time of 19ns, with 4.2% overshoot at 1MSymbol/s and no overshoot at 10MSymbol/s. The ripple on the output voltage is consistent at around 60mV, which at the constellation points with the highest $\frac{d\phi}{dV}$, namely 2.7V and 2.9V with $\frac{d\phi}{dV}$=0.38deg/mV, would lead to $\pm 11^o$ phase variation. This was deemed acceptable for proof-of-principle operation, though the added distortion will affect the DAM modulator's EVM.

The operation of the electronics is complicated by the feeding of signals to the DAM unit, which has a capacitive impedance due to the network of varactor diodes. The output of the electronics, when connected to the antenna, is shown in Fig. 4.25. At 1MSymbol/s, this removes the overshoot, due to an increased rise time of 50ns and fall time of 66ns, while the voltage ripple remains constant. Note also the drop of 0.1V in output voltage, which can be compensated for by raising the feed voltages of the comparators. However, at 10MSymbol/s, the rise times are large enough to prevent the output from reaching peak voltage until halfway through the desired symbol, providing a distorted PAM output. The

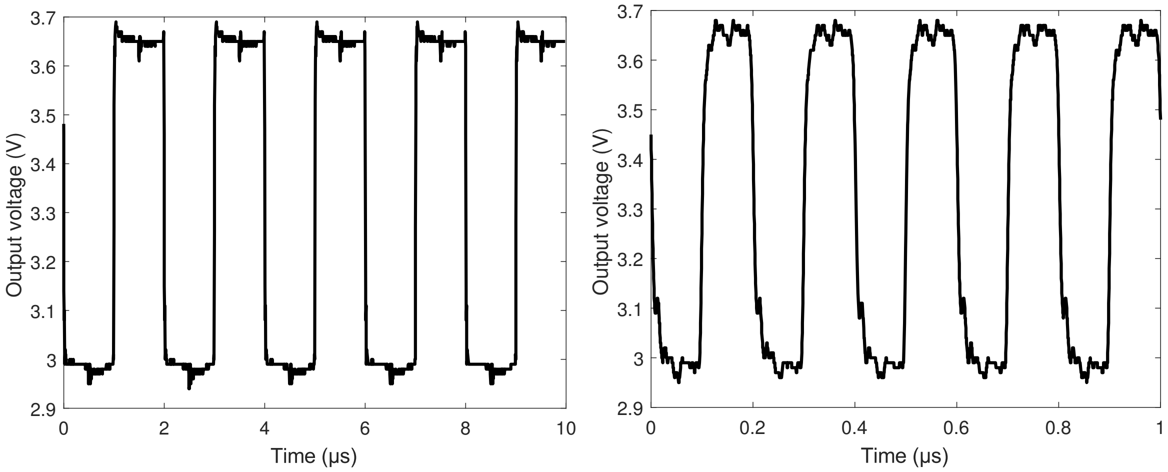

(a) (b)

Figure 4.24: Measured output of control electronics not connected to DAM in response to repeated data sequence 0110 at (a) 1MSymbol/s, (b) 10MSymbol/s

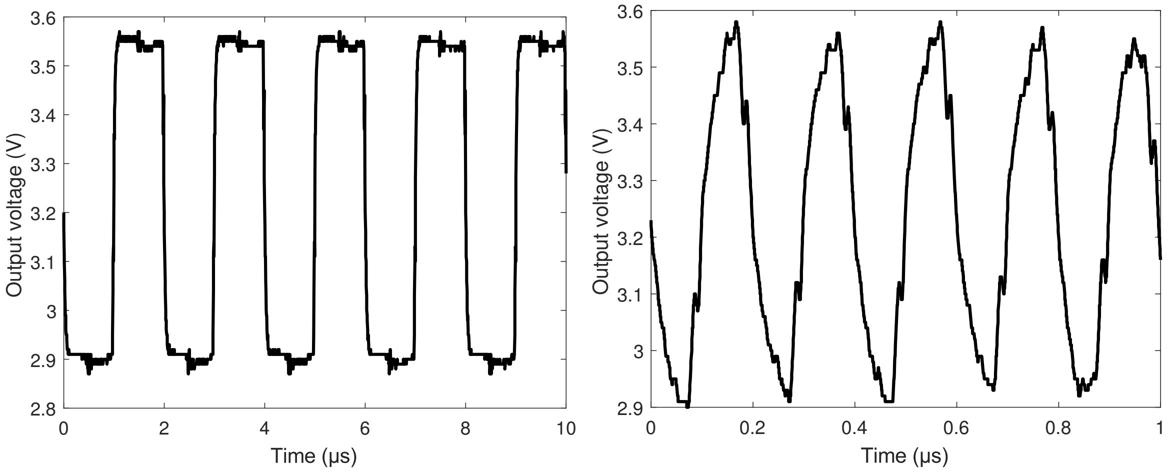

(a) (b)

Figure 4.25: Measured output of control electronics connected to DAM unit in response to repeated data sequence 0110 at (a) 1MSymbol/s, (b) 10MSymbol/s

effect of these output voltages on the QPSK constellations produced will be explored later in this chapter.

4.4.4 Experimental results

The designed QPSK FSS DAM communications system was then implemented and tested experimentally. The receiving antenna was placed 0.41m away from the DAM unit, which is considered to be the farfield as it is greater than $2\frac{(Kp)^2}{\lambda_0} = 0.093$m away, with the DAM unit having $K = 4$ unit cells with periodicity $p = 22$mm. A short distance was chosen to minimise the effects of reflections in the laboratory test environment used. The complete

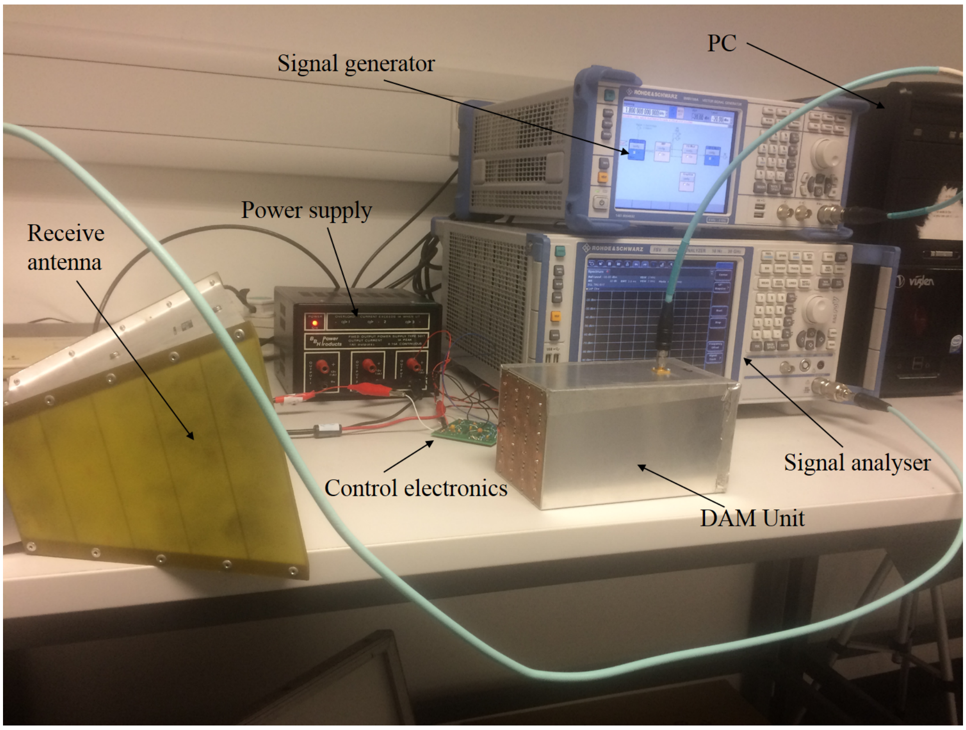

Figure 4.26: Photograph of the experimental setup for measuring the performance of QPSK FSS DAM

setup is shown photographed in Fig. 4.26.

Fig. 4.27a shows the equalised chips before correlation and the symbols after correlation for a single packet transmitted at 1MSymbol/s. There is a systematic phase offset of up to 18.1^o in the M-sequence chips compared to ideal QPSK constellation points. This is mainly caused by the difference between the measured and desired voltages in Table B.1, attributed attributed to the tolerance of resistor values and the limitations of the non-linear ladder network DAC, as well as the large rate of change of phase with respect to changes in bias voltage in some regions of the reconfigurable FSS response. There is also the expected magnitude distortion present, which is inherent in using an FSS as a modulator. At maximum, this is 6.5dB, as discussed previously. However, these distortions are reduced when the balanced spreading sequence is correlated, with maximum phase distortion of 6.6^o and maximum magnitude distortion of 1.3dB. This reduction in distortion is due to each I and Q symbol consisting of an almost equal number of less attenuated and heavily attenuated chips, thereby averaging out the magnitude and phase distortion.

The constellation produced at 10MSymbol/s is shown in Fig. 4.27b. The constellation is heavily distorted, though the response of the m-sequence is able to retrieve a recognisable QPSK constellation. However, it has a high EVM of 11%, as opposed to the 1% EVM of the despread constellation at 1MSymbol/s. This, in itself, is a large improvement over the EVM of the QPSK chips produced by the DAM unit at 1MSymbol/s, which is 8%. As such, for BER measurements, only the 1MSymbol/s setup using the spreading sequence was used.

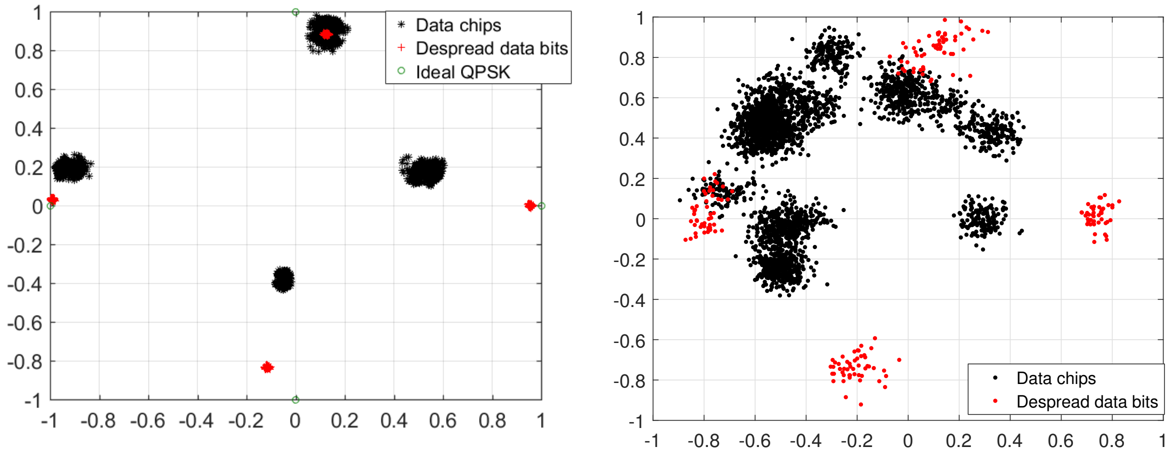

(a) (b)

Figure 4.27: Normalised constellation diagram of received chips from DAM implementation and data bits after despreading with DSSS, at (a) 1MSymbol/s, (b) 10MSymbol/s

To evaluate the BER, 1,127 packets, containing over 10^6 data bits in total, were transmitted at a range of power levels, and the error rate was calculated at each. Fig. 4.29 plots system bit error rate (BER) versus received signal power for the DAM, DSSS QPSK system. For comparison, the BER performance of instrument grade DSSS QPSK is also shown. The latter is generated by the SMBV100A generator and transmitted through the FSS which is fix biased at 3.3V to achieve maximum transmission (Fig. 4.28). This was done to preserve as much as possible the channel conditions used when measuring the BER performance of FSS DAM, such as radiation pattern and reflections in the lab environment.

The DAM curve follows the expected shape for a line-of-sight AWGN channel, but the FSS transmitter power must be increased by 4dB compared with instrument grade modulation to achieve a BER of 10^{-4}. This is due to the phase error still present on the DSSS plots, which could be mitigated by using more accurately calibrated components or by adjusting the decision levels of the threshold detector to ensure the decision is true maximum likelihood.

4.5 Discussion

In this chapter, the concept of using FSS to phase modulate was introduced, explored and implemented. The potential benefits of FSS DAM, especially for the energy efficiency of the PA in the transmitter, were discussed, and the principle of operation detailed. Then, the first experimental implementation of FSS DAM was described. An FSS for QPSK modulation was designed, using three layers to achieve the required 270^o phase variation, and using varactor diodes as the reconfigurable device. An antenna incorporating this FSS was then

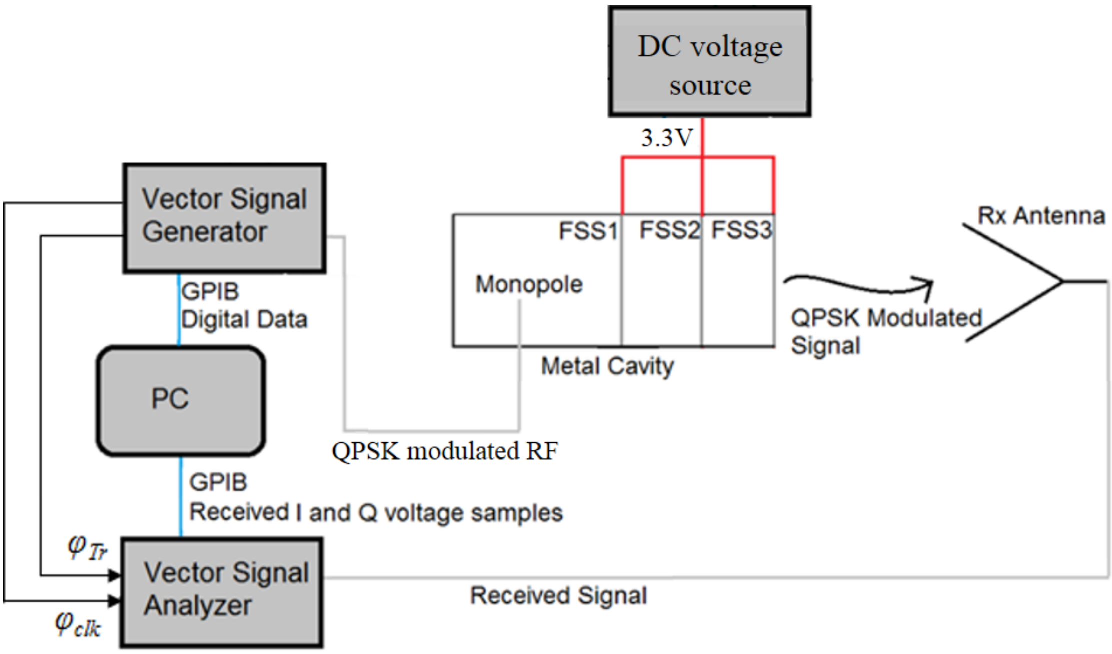

Figure 4.28: Schematic of experimental implementation for producing instrument grade modulation with equivalent channel conditions

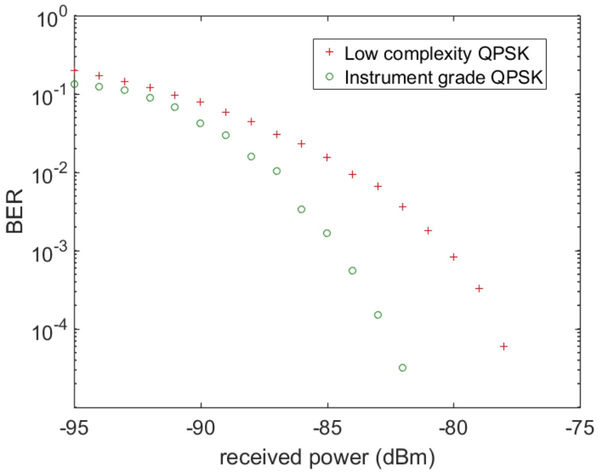

Figure 4.29: Bit Error Rate of DAM QPSK (red markers) and instrument grade QPSK (green markers) through reconfigurable antenna at static bias voltage

designed, using a waveguide-style structure to ensure all fields passed through all layers of the FSS. Simulation suggested a maximum 4.2dB distortion between constellation points, though due to additional losses this grew to 6.5dB in the measured, fabricated DAM unit.

This large distortion was mitigated by using a DSSS system, with a length 15 m-sequence reducing the magnitude distortion in the final symbols to 1.3dB. However, due to error introduced by the control system, there was still 6.6^o phase error in the despread constellation. This lead to a degradation of 4dB in the BER performance of the DAM transmitter com-

DAM technique	Modulation format	Symbol rate (MSymbol/s)	Operating frequency (GHz)	Physical size (λ_0^3)
FSS DAM (1st iteration)	QPSK	1	1.8	0.53×0.53×0.96
Integrated switches [42]	OOK	5	1	0.32×0.39×0.01
Reflective metasurface [59]	8PSK	2.048	4.25	5.44×1.36×0.07

Table 4.5: Comparison of key metrics for IoT 1st iteration of FSS DAM with experimentally implemented state-of-the-art DAM techniques

pared with instrument grade modulation from the signal generator. As a proof of concept, however, this shows that linearly polarised QPSK modulation can be produced using a transmissive, reconfigurable bandpass FSS, meeting the key requirement of the design parameters (Table 4.1). It also shows that simple systems solutions, such as DSSS, can ameliorate the magnitude distortion of constellation points inherent in FSS DAM as a technique. While the final efficiency simulations show a loss over traditional modulation techniques, due to the inefficiency of the DAM transmitter, this could be overcome using less lossy components and materials. The effect of these changes will be explored in future chapters.

The suitability of the DAM technique designed in this Chapter for acting as transmitters at IoT wireless access points, compared with existing DAM technologies, can be drawn from Table 4.5. Only DAM techniques using single transmit antennas are considered, as only LTE-M makes use of multiple antenna transmitters of all the IoT schemes considered [136]. This leaves the state-of-the-art in integrated switch DAM [42], and in reflective metasurface DAM [59], as comparisons.

The FSS DAM technique developed here operates at 1.8GHz, meeting the requirement, which is one of the frequencies used for EC-GSM-IoT communications [135]. It should scale without complication or major changes in losses to both 2.4GHz, where Ingenu operates, and down to the sub-GHz frequencies used for the majority of LP-WAN technologies (Table 2.3). This is similar to the operating frequencies of the two comparison devices, which would also most likely scale to these operating frequencies.

Further, the symbol rates used by all three DAM techniques are similar, allowing both the wideband Ingenu and LoRa bandwidths, and the narrowband Sigfox and Weightless-P symbol rates, to be produced by all of them. However, NB-IoT and LTE-M both require OFDMA signalling, which is too complex for any of the above examples to produce, requiring high rate control of both amplitude and phase. The OOK modulation produced by integrated switch DAM limits its use significantly, with no wide-area IoT standard using this modulation. Both the work presented in this Chapter and relective metasurface DAM, however, are capable of producing the DBPSK and QPSK modulation required for Sigfox, Weightless-P and Ingenu modulation. The work in this Chapter also suggests that the spread spectrum of Ingenu lends itself to transmissive FSS DAM. The CSS waveform of LoRaWAN, however, may be possible to achieve with the two presented phase modulating

DAM techniques, but no investigation has been undertaken.

The physical size of each DAM unit should also be considered. Integrated switch DAM is small in all dimensions and is low profile, making it suitable for mounting on small, street furniture style base stations. The reflective metasurface, meanwhile, is electrically large, though its low thickness should allow it to be mounted on street furniture and rooftops, though it will be significantly more intrusive than the integrated switch unit. Further, the metasurface must be fed by an active antenna in the surface's farfield, increasing the overall size of the transmitter significantly and so restricting its use in a dense network. This is not an issue faced by FSS DAM, where the feed is within the enclosed unit, though at the cost of the modulator itself being significantly deeper than its competitors. The unit is still of volume $0.27\lambda^3$, and consists mostly of empty space inside the cavity, so it is still suitable for mounting on street furniture and rooftops for network densification.

However, the FSS DAM unit presented in this Chapter does not meet one of the key requirements of a transmitter for dense IoT wireless access points, as it is simulated as having peak efficiency of 9.3%, significantly below the 30% benchmark described in Table 4.1. This is worse than the performance of conventional transmitters. Further, the impaired modulation means 4dB extra power is required to reach the same BER performance as an instrument grade transmitter, and only when a spreading sequence is used. While a dense IoT network would not use transmitters with instrument grade quality modulation, the DAM unit should be improved to ensure it is an improvement over conventional technology.

4.6 Conclusion

A proof-of-principle FSS DAM unit has been designed, fabricated, measured and implemented in an end-to-end communications system in this Chapter. By producing modulation within the antenna, it replaces much of the RF electronics usually required in a transmitter with simple electronics operating at the baseband rate. It is capable of producing some existing IoT waveforms, in particular that of Ingenu, and is suitable for installation in a variety of locations for dense IoT networks. However, the unit has poor simulated efficiency and non-ideal modulation quality. Importantly, this Chapter has demonstrated that PSK modulation can be produced using FSS DAM, and can reliably transmit information over a LoS channel. The following Chapter will look to improve on this design, increasing the efficiency and extending modulation to higher order PSK.

Chapter 5

Continuous phase DAM

5.1 Introduction

In the previous chapter, a proof-of-concept frequency selective surface (FSS) direct antenna modulation (DAM) transmitter was designed, fabricated, measured and tested in an end-to-end communications system. It used a 3-layer FSS, which was able to produce QPSK, but with significant distortion of the constellation. It was also only 10% efficient on average due to losses in the varactor diodes and FR4 substrate used, and as such is currently unsuitable for use as a transmitter in dense Internet of Things (IoT) networks, though it may have other applications.

To improve the performance of the FSS DAM transmitter, a full analysis of the design process was undertaken, and is detailed in this chapter. In particular, the combined effects of the number of layers used and loss in the variable capacitors and in the FSS substrate are explored. A DAM transmitter capable of producing continuous phase modulation was then designed, simulated, fabricated and measured, with a focus on its characteristics as an antenna. The key design requirements are shown in Table 5.1. Again the frequency of operation will be 1.8GHz, the symbol rate at least 1MSymbol/s and the polarisation linear. The unit should be able to produce BPSK, QPSK and 8PSK modulation, with efficiency greater than the basestation PA benchmark of 30%. Finally, the unit size should again have an aperture area of as close to $(\lambda_0/2)^2$ as possible, though the depth requirement has been relaxed to 1.5λ to allow further FSS layers and so better modulation performance.

The designed unit was then implemented in an end-to-end communications system over a line-of-sight channel, demonstrating BPSK, QPSK and 8PSK modulation. BER and PER measurements were taken for each case, using both uncoded and Manchester coded transmission, rather than the DSSS approach taken in the previous chapter. The prototype continuous phase DAM transmitter showed a degradation in performance of only 1.5dB for balanced 8PSK modulation when compared with an instrument grade transmitter. This

Parameter	Requirement
Modulation format	BPSK, QPSK, 8PSK
Frequency of operation	1.8GHz
Efficiency	¿30%
Symbol rate	> 1MSymbol/s
Polarisation	Linear
Size	$\frac{\lambda_0}{2} \times \frac{\lambda_0}{2} \times 1.5\lambda_0$

Table 5.1: Key design requirements for continuous phase FSS DAM

performance will be evaluated as a potential low complexity, energy efficient transmitter at IoT wireless access points. Some of this work has previously been published in [152], and some is currently under review by the IEEE Transactions on Antennas and Propagation.

5.2 Design of a phase modulating antenna

In this section, the design process of a FSS-based modulating antenna is discussed. For demonstration, the antenna will be capable of a single linear polarisation and operate at 1.8 GHz.

5.2.1 Frequency selective surface design for continuous phase DAM

In order to produce arbitrary PSK modulation, the FSS must be able to produce 360^o phase change with a minimum of variation in magnitude. Also, as discussed previously, the FSS may have to modulate signals with an oblique angle of incidence and operate effectively in a limited space. Once again, the square-loop aperture unit cell was chosen. The unit cell geometry was again designed using Langley and Parker's equivalent circuit equations, described in Chapter 2.3 [74]. Here, the FSS unit cell was designed to have a static resonant frequency of around 3GHz higher than the frequency of interest. This was to ensure that low values of variable capacitance could be used, resulting in reduced loss from I^2R losses. The gap g was fixed at 1mm, for ease of fabrication and to allow the variable capacitors to sit across the gap easily. The ratio s/p was chosen to be $\frac{2}{3}$ to reduce loss, as discussed in Chapter 3, and also to allow space for soldering on the variable capacitors. As such, final dimensions of p=22.5mm, s=15mm and g=1mm were chosen (Fig. 5.1a). Using Langley and Parker's equations, this gives an intrinsic inductance L_{FSS}=17.1pH and capacitance C_{FSS}=57.1pF, resulting in a static resonant frequency of 5.1GHz. This is confirmed through simulation in Fig. 5.1b.

The choice of substrate material for the FSS was investigated. Previously in this thesis,

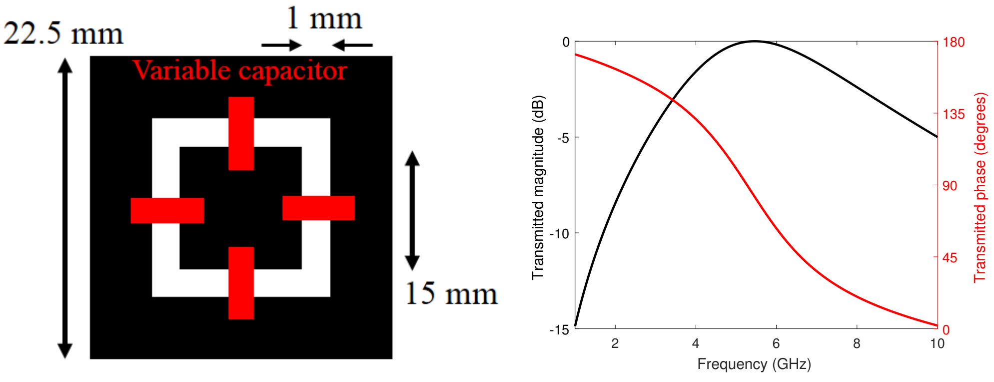

(a)

(b)

Figure 5.1: (a) Schematic of designed reconfigurable FSS unit cell, (b) Free-space simulation of lossless, static FSS S_{21} against frequency

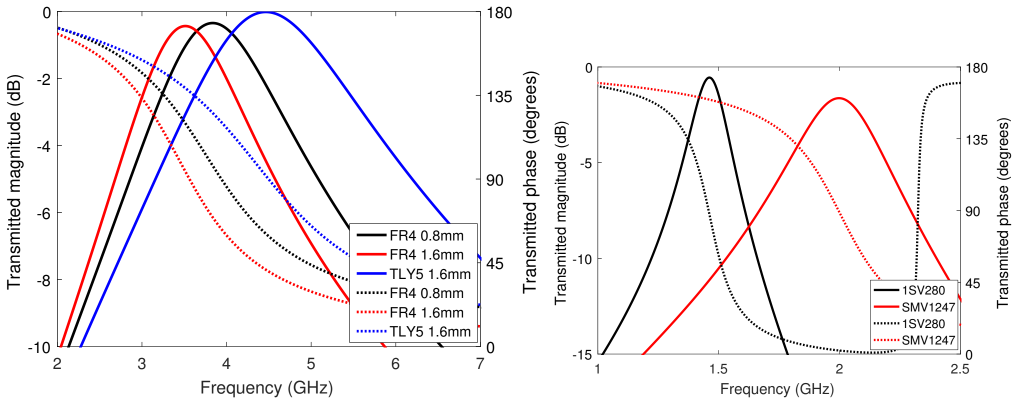

(a)

(b)

Figure 5.2: Simulated S_{21} of single layer FSS, (a) static with different substrates, (b) reconfigurable with different varactor diode models at minimum capacitances

FR4, with loss tangent $\tan\delta = 0.025$ and dielectric constant $\epsilon_r = 4.3$ has been used, with a thickness of t_{sub}=0.8mm. Due to a change in supplier of PCBs, the minimum thickness of FR4 available increased to 1.6mm. The effect of this increase on the static FSS is shown in Fig. 5.2a, with 0.1dB more loss added per layer, and a 340MHz shift downward in resonant frequency. The effects of lower loss dielectrics were also explored, and are also shown in Fig. 5.2a. Taconic's TLY5 was investigated for its low loss tangent, $\tan\delta a = 0.0009$, and has a relative permittivity of $\epsilon_r = 2.2$. Again, the thinnest available product was 1.6mm. Simulations suggest the loss through a single static FSS layer would be only 0.01dB, 0.42dB less than with a FR4 substrate of the same thickness. However, the reduced ϵ_r of TLY5 introduces a 1GHz upwards shift in resonant frequency compared with the FR4 case, which will then require a larger capacitance to tune the FSS to the desired frequency, increasing loss in the variable capacitors. For reasons of cost and ease of fabrication, the FR4 substrate was chosen for this design.

The choice of variable capacitor was also revisited for this design. Varactor diodes were

Diode	C_v range (pF)	Typical R_v (Ω)	L_v (nH)	Tuning voltages (V)
SMV1247	0.6 - 7	4.9	0.7	0.3 - 4.7
1SV280	1.2 - 5	0.44	0.5	1 - 30

Table 5.2: Comparison of possible varactor diode characteristics

chosen again, for their high switching rates and low variable capacitance. However, the requirement for low bias voltages was relaxed, allowing consideration of diodes requiring voltages of up to 30V rather than 5V. This was allowed by an update to the control electronics design, which will be discussed in depth later in this chapter, and the recognition that only small amounts of capacitance change, and so relatively small voltage swings, were required to produce full tuning in a multilayer reconfigurable FSS (Chapter 4.3). As such, the 1SV280 diode from Toshiba was investigated, with ESR R_v=0.44Ω, inductance L_v=0.5nH, and capacitative tuning range C_v=1.2-5pF. The effect of this diode at minimum capacitance, 1.2pF, versus the SMV1247 diode used in the previous design at its minimum capacitance of 0.6pF, demonstrates 1.1dB less loss per layer- 0.563dB rather than 1.63dB (Fig. 5.2b). The details of both diodes are described in Table 5.2. As such, 1SV280 diodes were used going forward in this design.

The final design choice for the FSS is the number of layers required. It has been shown theoretically that 3 layers or less can give 360^o phase change only with at least 3dB magnitude variation, as discussed in Chapter 2.3 [112]. As such, only 4 and 5 layers are explored here, through simulation of the multilayer reconfigurable FSS with varying capacitance (Fig. 5.3a). Note that the frequency point taken is 1.68GHz, which is below the desired frequency of operation, as the FSS will resonate at a higher frequency in a waveguide solution due to the electrical length of the dielectric substrate being different, as discussed in detail in Section 3.4.2. For a 4-layer FSS, 360^o phase change is achieved over 0.3pF and for 5.7dB magnitude variation. This is improved on with 5 layers, with only 2.7dB magnitude variation, with similar capacitance change required. However, the minimum loss through the FSS increases from 2.6dB to 3dB when the number of layers increases from 4 to 5. It should also be noted that for an 8-PSK constellation, with total required phase change of 315^o, the magnitude variation would be 4.6dB for 4 layers and 2.1dB for 5 layers. As such, the variation expected with a 4-layer FSS was deemed acceptable in trade-off with the total loss and the final antenna form factor, which would increase in length $\lambda_c/4$ with an added layer. The final FSS design is shown tuning over a range of capacitances in Fig. 5.3b.

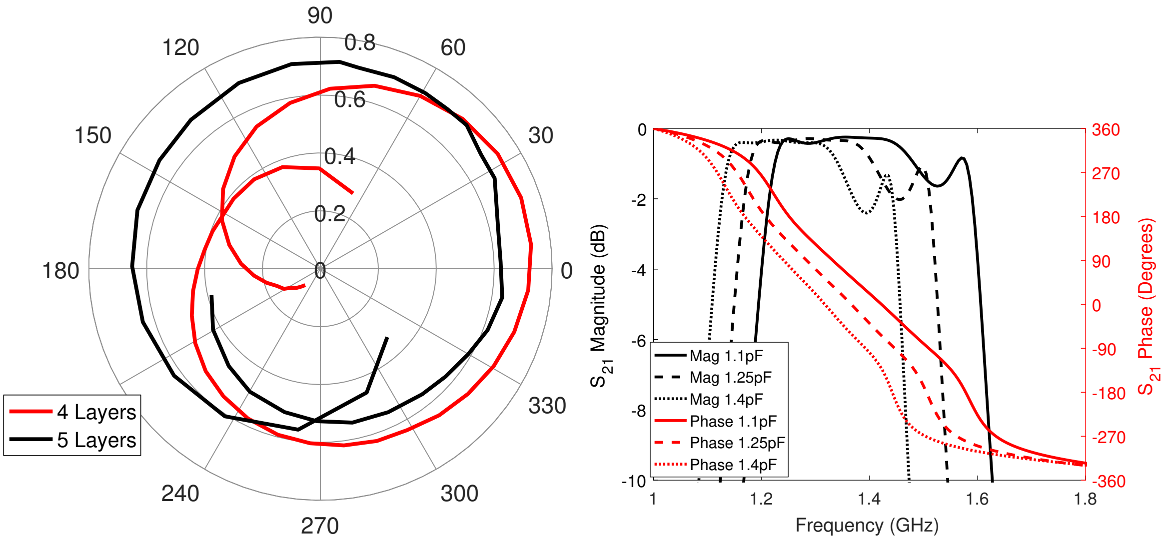

(a) (b)

Figure 5.3: Simulated S_{21} of multilayer reconfigurable FSS, (a) polar plot with changing capacitance at 1.68GHz, (b) magnitude and phase against frequency at different diode capacitances

5.2.2 Antenna design

In order to operate in a practical transmitter, the modulating FSS must again be integrated with an antenna. The generic design of the modulating antenna is provided again in Fig. 5.4, here showing that a 4 layer FSS is being used. The appropriate values of M and K are evaluated by simulating antennas of varying aperture size, containing FSS of different numbers of unit cells, while maintaining the fundamental unit cell geometry (Fig. 5.5a). As in the previous design, a square configuration, with $M = K$, was chosen for symmetry. A 3x3 FSS has potential variation of 4.8dB across 360^o, which is larger than expected due to the FSS being spatially undersampled. However, for 4x4 and 5x5 configurations, the performance is consistent, with 2.9dB variation. Using smaller numbers of unit cells reduces the number of diodes required for operation. However, it was found that for operation at 1.8GHz while maintaining an acceptable antenna width of approximately 0.6λ, a 5x5 arrangement was required to have tuning capacitances in the low loss, low capacitance end of the chosen 1SV280 diode's tuning range.

The optimal spacing between layers of the FSS was also explored. Using the equivalent circuit analogy, to provide the flattest filter response a transmission line of a quarter of a wavelength is required between each LC combination. However, within the cavity a quarter of a wavelength at transmit frequency is neither what it would be in free space, $\lambda_0/4$, nor the theoretical wavelength in an infinitely long square waveguide of size W, $\lambda_g = \lambda_0/\sqrt{1-(\frac{\lambda_0}{2W})^2}$. Instead, it will be somewhere in between. In order to find this cavity wavelength λ_c, the full antenna structure was simulated with varying spacings at a fixed capacitance. Results for a waveguide of $W = 112.5$mm and length $L_{cav} = 5\lambda_c$ is shown in Fig. 5.5b, with the flattest

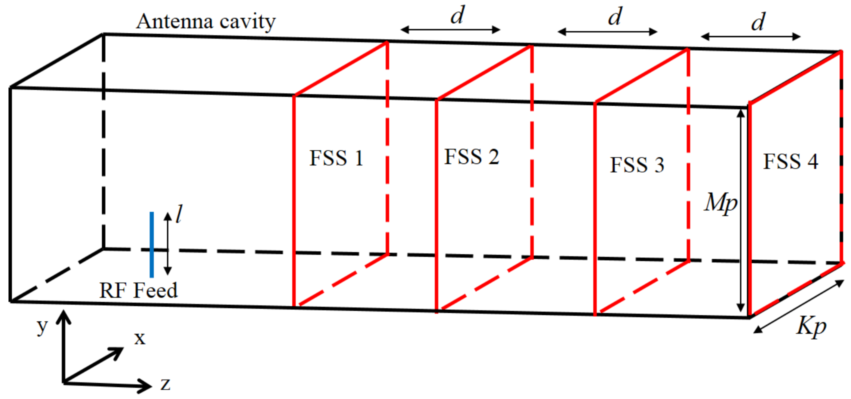

(a)

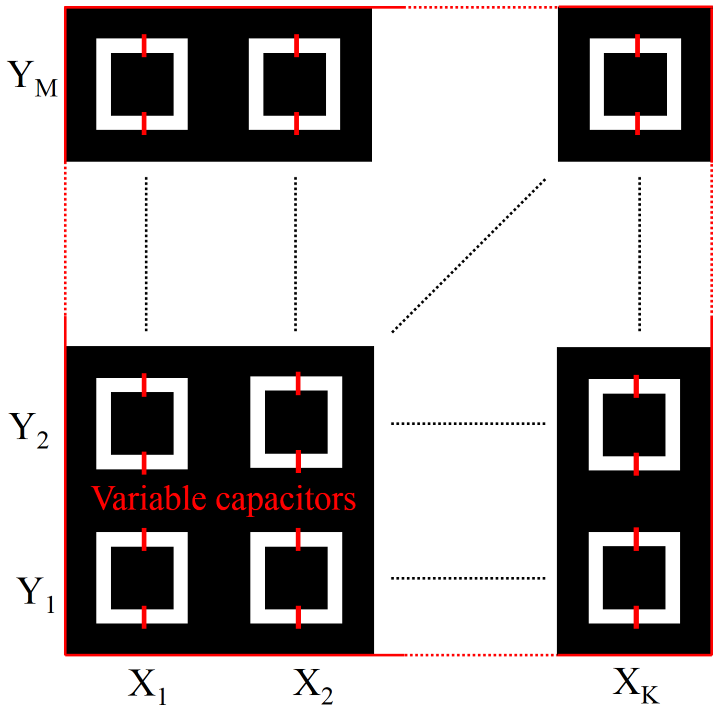

(b)

Figure 5.4: Diagrams of modulating antenna concept. (a) 3D antenna structure, (b) FSS structure in antenna

response being the optimum, here $\lambda_c/4 = 57$mm. Combinations of different spacings between FSS layers were also explored, but did not show any improvement in passband flatness.

The final variable in the antenna design is the length of the monopole probe, l_{probe}, injecting energy into the cavity. This should be optimised to produce the best match to the antenna, and as such the antenna S_{11} is simulated with varying l (Fig. 5.6a). The best match at 1.8GHz is -14dB, when l=35mm. This is considered a good match as it is less than -10dB, and the bandwidth of the antenna using this criterion is 83MHz, 44MHz greater than the bandwidth where l_{probe}=40mm. As such, l was chosen to be 35mm. Note that the S_{11} will also vary with bias capacitance C_v, as will be explored later in this section.

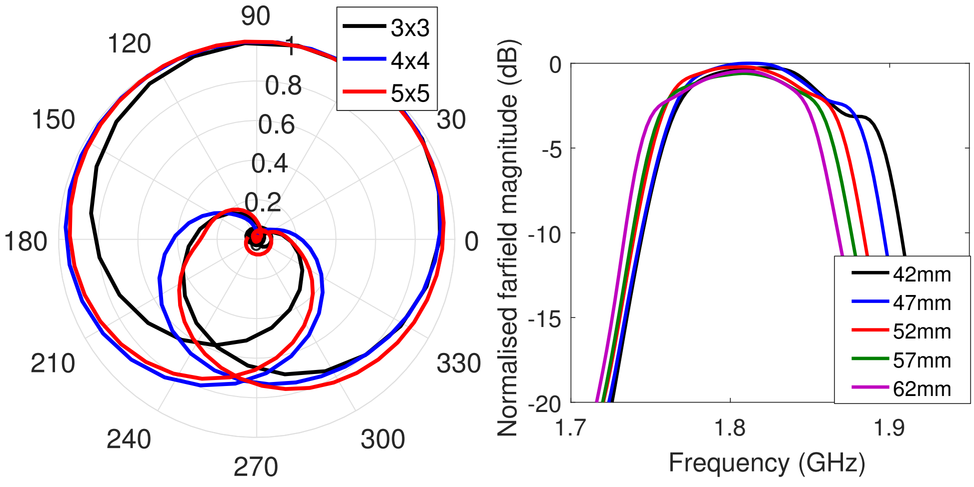

(a) (b)

Figure 5.5: Simulated antenna at 1.42pF against frequency, (a) polar farfield at boresight with different $M \times K$ numbers of unit cells as a parameter, (b) farfield magnitude with different spacings between FSS layers as a parameter

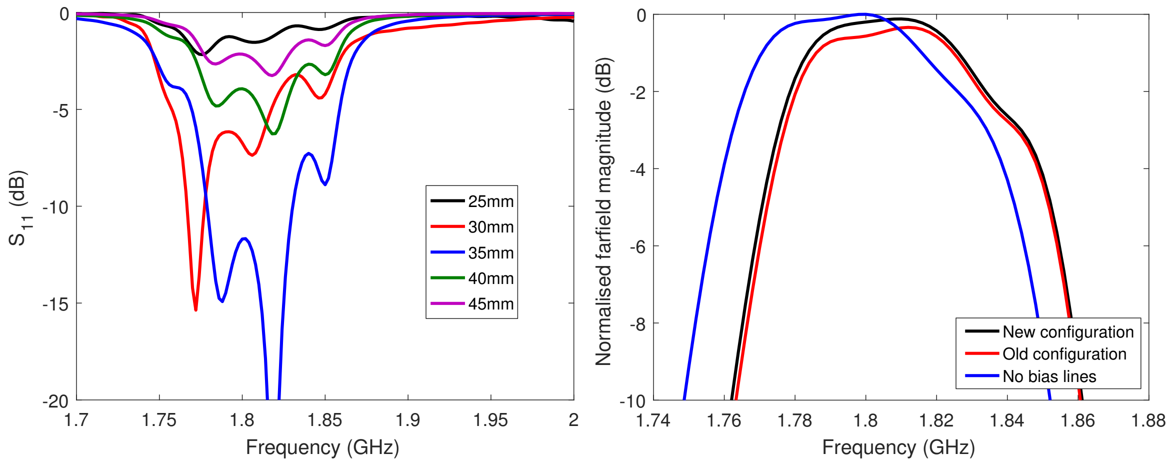

(a) (b)

Figure 5.6: (a) Simulated antenna S_{11} with different probe lengths l_{probe} when C_v=1.5pF, (b) Magnitude and phase in the farfield for different bias line configurations, C_v=1.5pF

The antenna also requires a biasing network on each FSS layer to ensure all diodes are biased at the same time by the same voltage. However, this network should be designed to minimise the impact on the transmitted wave. The previous design, discussed in Chapter 4, used bias lines which were largely orthogonal to the incident E-field, and one line down the middle of the FSS connecting them all (Fig. 4.6a). However, as the E-field is strongest in the middle of the cavity, where this vertical line is present, it was theorised that this line has more influence than it could do. As such, the design shown in Fig. 5.7c was explored, where two vertical connecting lines are moved to the edges of the cavity, where the E-field is at its weakest. The effect of this is explored in Fig. 5.6b, which shows no change in resonant

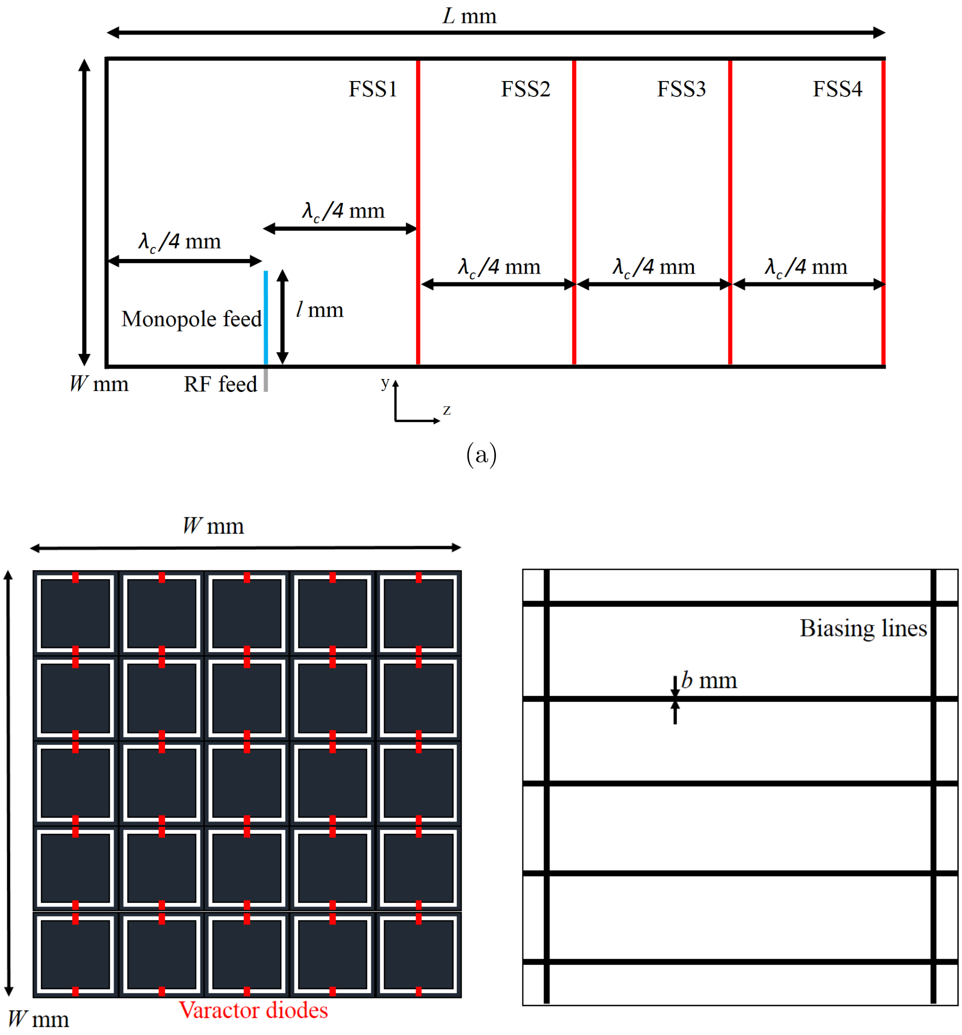

(a)

(b)

(c)

Figure 5.7: Diagrams of antenna design. (a) Side view, (b) Front view, (c) Bias lines on reverse of FSS

frequency with the new biasing configuration, but a 0.21dB reduction in loss. As such, the new design in Fig. 5.7c was used. Compared with no biasing on the FSS layers, there is a 0.13dB increase in loss and a 12MHz shift in resonant frequency when the biasing network shown in Fig. 5.7c is used.

The final antenna design is shown in Fig. 5.7, with its key parameters shown in Table 5.3. The antenna is designed to operate in the licensed mobile band at 1.8GHz, as with the previous iteration. A 5 × 5 FSS was chosen with p = 22.5mm, s = 15mm, and g = 1mm, with the latter chosen to fit the diode footprint (Fig. 5.7b). This gives a cavity size $W = 0.675\lambda$ = 112.5mm and so optimum spacing $\lambda_c/4$ = 57mm and probe length 35mm. This is then simulated in CST with varying capacitance, with the diode assumptions given in Section 5.2.2 (Fig. 5.8a). The capacitance range of the passband is between 1.2pF and 1.5pF at the low tuning end of the 1SV280, minimising loss in the varactor diodes. Note

W (mm)	L_{cav} (mm)	$\lambda_c/4$ (mm)	d (mm)	b (mm)
112.5	285	57	25	1

Table 5.3: Final antenna design parameters

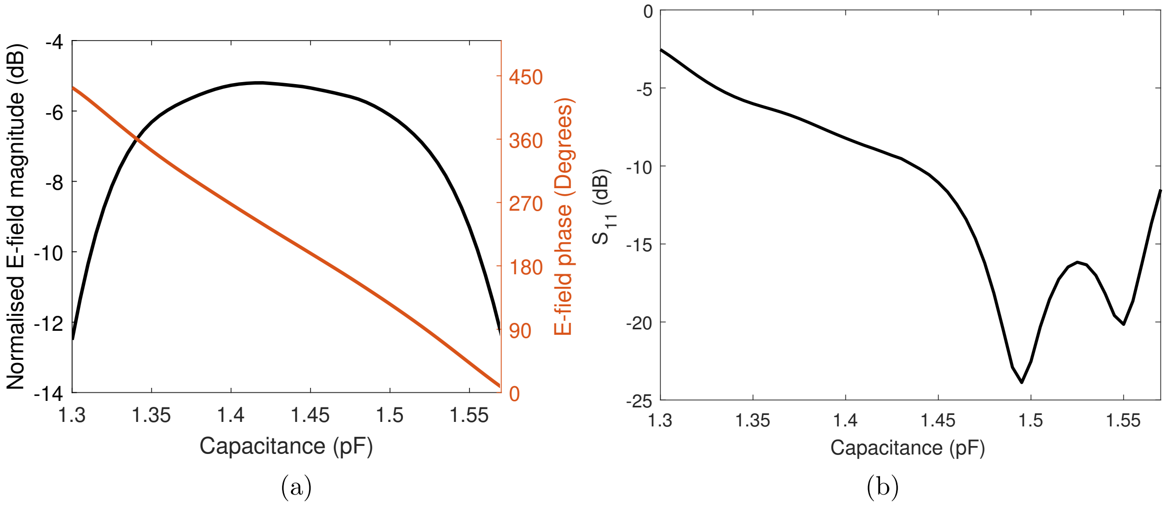

(a) (b)

Figure 5.8: Simulated antenna with varying capacitance, (a) farfield magnitude and phase, (b) S_{11}

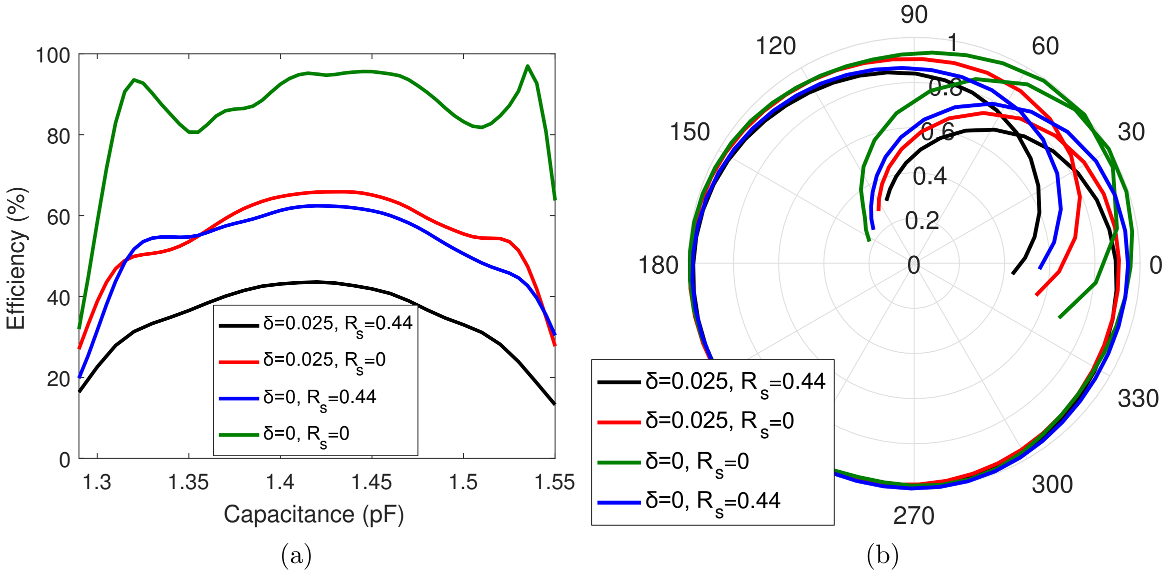

(a) (b)

Figure 5.9: Simulated antenna against varying capacitance with substrate loss tanδ and diode resistance R_v as parameters, (a) total efficiency, (b) polar plot of antenna E-field at boresight

the 5dB loss through adding the FSS compared with an empty cavity. However, the phase change in the pass band is greater than 360^o, and the expected magnitude variation across this is 2.7dB. 1.3dB of the variation can be attributed to the diodes' ESR, while 0.3dB is due to losses in the FSS substrate (see Fig. 5.9b).

The simulated S_{11} is shown in Fig. 5.8b, showing less than -10dB match over the

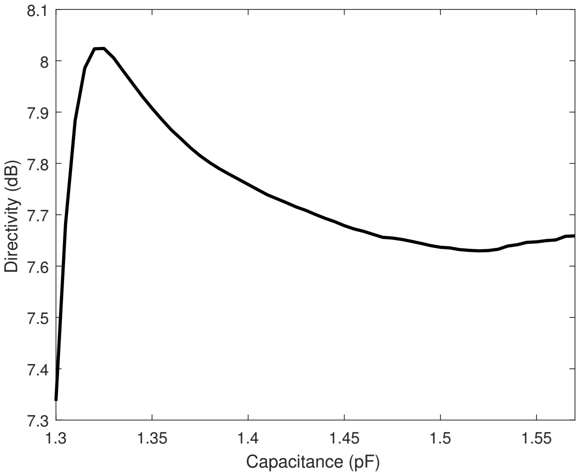

(a)

Figure 5.10: Simulated antenna directivity against varying capacitance

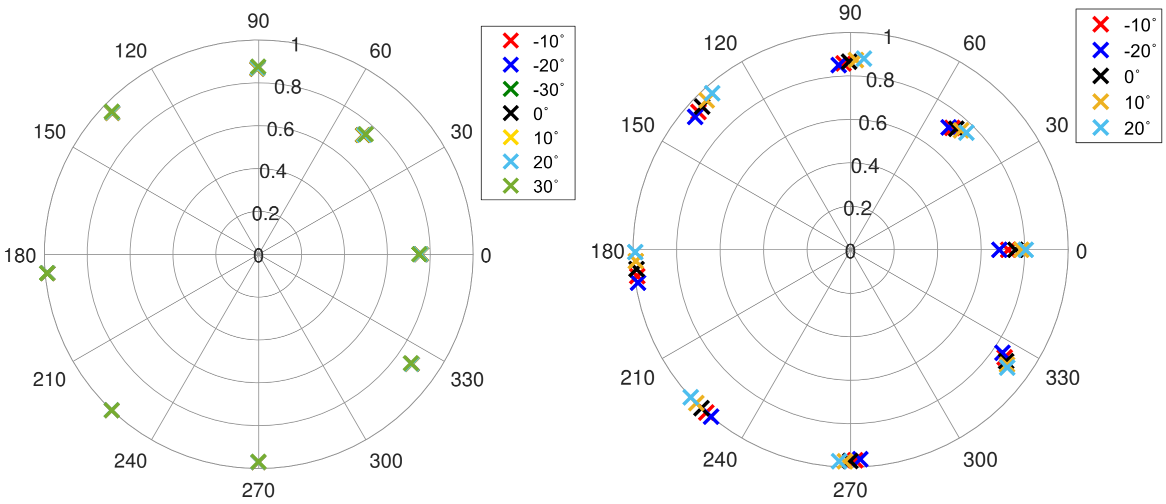

(a) (b)

Figure 5.11: Simulated 8PSK constellation produced by DAM unit at 1.8GHz with different viewing angles as a parameter, in (a) H-plane (x-z), (b) E-plane (y-z)

majority of the pass band, and -6dB match for the whole of it, from 1.23pF to 1.49pF. This could be improved by using a matching network, but for demonstration purposes this was deemed acceptable. The simulated total efficiency is shown in Fig. 5.9a, showing a maximum 46% efficiency. 1.8dB of the loss in the antenna at peak efficiency is due to the diodes, 1.6dB is due to the substrate, while the other 0.2dB is due to matching differences between the feed and the cavity interior and reflections from the FSS. Some variation in the magnitude received at boresight is due to a slight change in the antenna pattern, as shown by the simulated boresight directivity in Fig. 5.10a. It is mostly stable at 7.6dB within the passband, but has a peak to 8dB at 1.26pF. This raises the received magnitude at boresight compared with the overall efficiency of the antenna at this capacitance.

An 8PSK constellation can be drawn from the simulated results, with maximum magnitude variation of 2.5dB (Fig. 5.11). However, the magnitude and phase produced by the DAM unit may vary in different directions, and is shown simulated in Fig. 5.11. Within the H-plane 3dB beamwidth of 60^o, there is almost no variation in either transmitted magnitude or phase, suggesting the constellation will be identical across this plane. However, in the E-plane 40^o beamwidth there is some slight variation in phase and magnitude. This becomes more pronounced towards the edge of the beam, with maximum 7.7^o variation between the same constellation points at $\pm 20^o$ viewing angles. Further, at a viewing angle of -20^o, the magnitude variation across the constellation increases to 3.3dB. This suggests a slight distortion in received constellation across the beamwidth, though not enough to cause significant degradation in performance. The variation in the E-plane is due to the lack of symmetry of the DAM unit in the y-z plane, with the monopole feed being at the base. This could be mitigated by using a more symmetrical feed for injecting energy into the cavity.

The simulated E-field distribution within the antenna at 1.42pF is shown in Fig. 5.12a. This shows the fields being injected into the cavity by the monopole and passing through each FSS layer. Note that at the cavity backing, the E-field is nearly zero, showing deconstructive interference of the incident and reflected waves and suggesting that the spacing is near-optimal for ensuring constructive interference in the positive z-direction from the monopole. The strong fields around the resonating FSS unit cells can also be seen, with nearly equal distribution between unit cells in the y-direction. There is some unevenness of field distribution in the y-direction between FSS, due to the monopole feed being at the bottom of the cavity, but this evens out after the third FSS layer. The loss through each layer can be seen with the progressive weakening of the E-field amplitude.

Fig. 5.12b shows the E-field at the front of the antenna, demonstrating again that the field strength is strongest at the centre of the FSS in the x-direction. It can be seen that peak E-fields occur across the apertures bridged by the diodes, showing that the field is linearly polarised in the y-direction. This is further demonstrated by the surface currents, shown in Fig. 5.12c, which are induced predominantly in the y-direction, and are again strongest at the centre of the FSS in the x-direction.

5.3 Experimental results

5.3.1 Antenna fabrication

The FSS was fabricated with standard PCB etching techniques, with copper conductor on 1.6mm thick FR4 board. Through-hole vias, of the electrically small diameter 1mm, were included in the centre of each FSS layer to allow biasing of the variable capacitors. 1SV280 varactor diodes were then soldered by hand across the gaps of each FSS unit cell, all placed

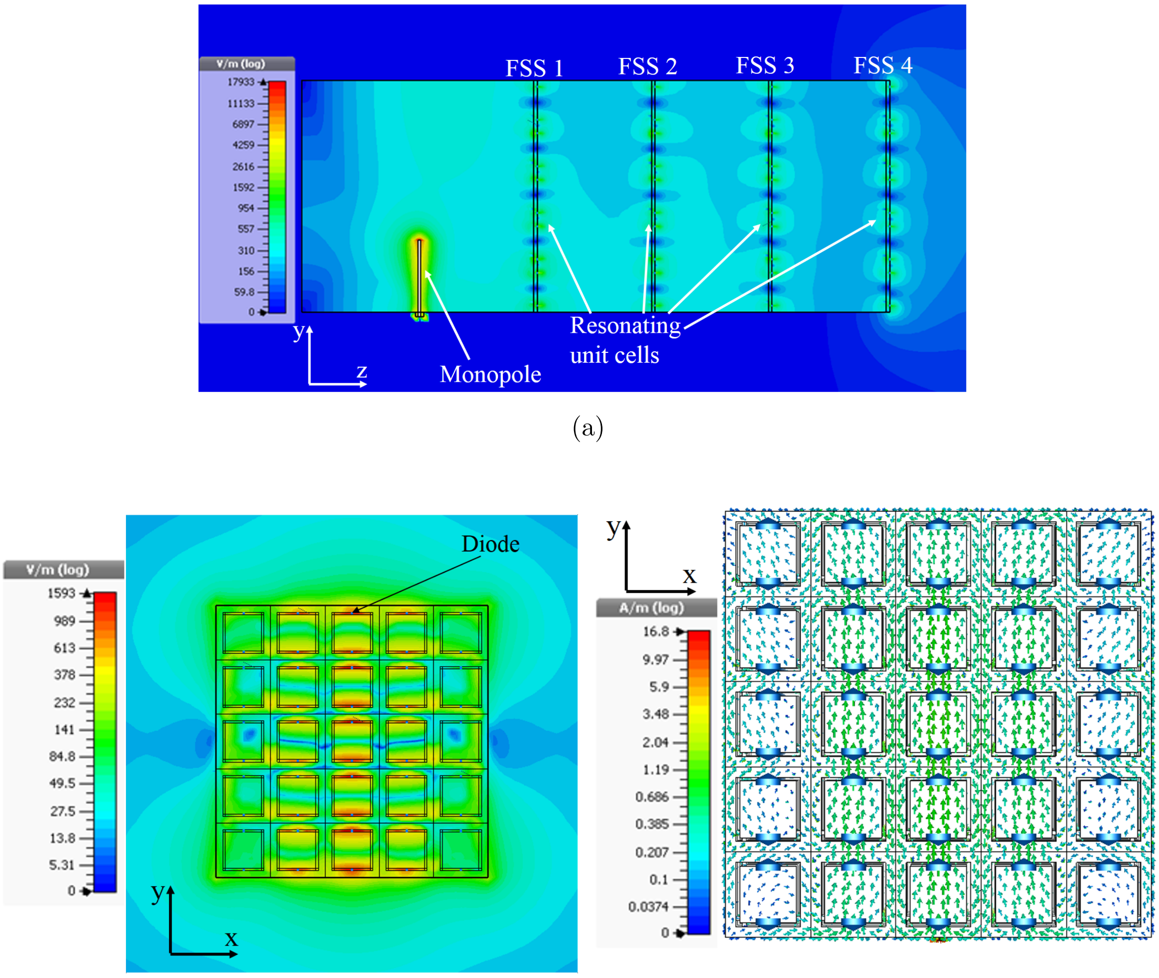

(a)

(b)

(c)

Figure 5.12: Simulated fields and currents of final antenna at 1.8GHz with C_v=1.42pF, (a) E-field side profile, (b) E-field antenna front, (c) Surface currents of final FSS layer

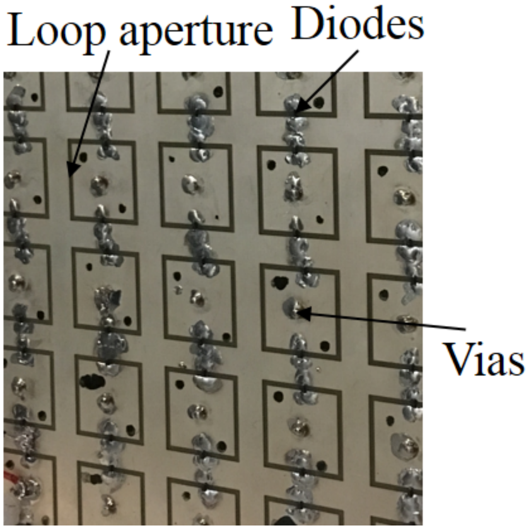

Figure 5.13: Photograph of fabricated DAM unit

in line with the expected E-field. As before, the cathodes of each diode were soldered to the FSS patches to ensure the positive bias voltage wasn't pulled to the radio frequency (RF) ground by contact with the cavity walls. The constructed FSS is shown photographed in Fig. 5.13.

In the previous design, sections of polystyrene were placed inside the cavity to control the spacing of the FSS layers. However, this was less accurate than desired, due to the softness and malleability of polystyrene. In this design, holes were drilled in the corners of each FSS layer and a teflon threaded rod passed through, with teflon nuts holding each layer 57mm from the next. This allowed finer control of the FSS layer spacing. The 4mm diameter holes were drilled in the extreme corners of the FSS to limit their impact on the FSS performance, as the E-field is weakest toward the edges of the cavity.

The antenna cavity was fabricated from sheet aluminium, with a hole drilled for a panel-mount SMA connector with its centre extended to 35mm. 2mm diameter holes were also drilled in the antenna side near where each FSS was to be placed to allow the biasing lines to be connected to wires, then to a single coaxial cable for carrying the biasing signal. The cavity walls are held in place with conducting aluminium tape, and the final antenna is shown photographed in Fig. 5.14.

5.3.2 Antenna measurement

The salient characteristics of the antenna were then measured, using a controllable voltage source to provide biasing. The antenna S_{11} was measured using an Agilent E5071C network analyzer in an anechoic chamber, and gives below 10dB match for the majority of the antenna passband, though this is at some points reduced to 4dB (Fig. 5.15a). The farfield magnitude

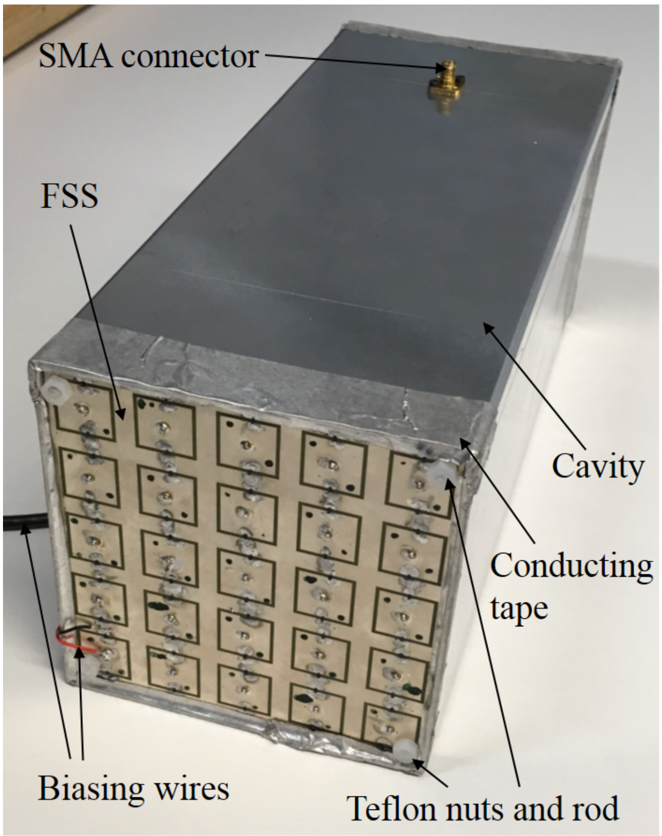

Figure 5.14: Photograph of fabricated DAM unit

and phase variation were measured with the network analyzer with a wideband horn antenna receiving the transmitted signals (Fig. 5.15b). They show within the passband a drop in magnitude as bias voltage increases. Note that voltage is non-linearly proportional to diode capacitance, accounting for the non-linear change in phase across the passband. There is 10.6dB variation for 360^o phase change, between 13.3V and 26.6V, which is significantly larger than the 5.7dB expected, but most of this occurs in the final 29^o, partly because of the greater than expected increase in S_{11} at low voltages.

An 8-PSK constellation can be created from this response, requiring 315^o phase change, with 5.3dB variation, which is only 0.7dB greater than expected from simulation. This constellation is shown in Fig. 5.16 observed over a range of viewing angles in both the E and H planes, showing a maximum of 15.6% variation in magnitude and 5.6^o in phase for the H-plane over a 60^o viewing angle. The E-plane beamwidth is smaller at 40^o, and within this has a maximum of 12.1% variation in magnitude and 22^o in phase. The variation is larger in the E-plane due to the asymmetry of the monopole feed in this plane, and could be reduced by using a symmetrical feed element such as a planar dipole in the centre of the cavity.

The simulated and measured antenna radiation patterns are shown in Fig. 5.17 for the most and least transmissive constellation points measured. The peak gains differ between

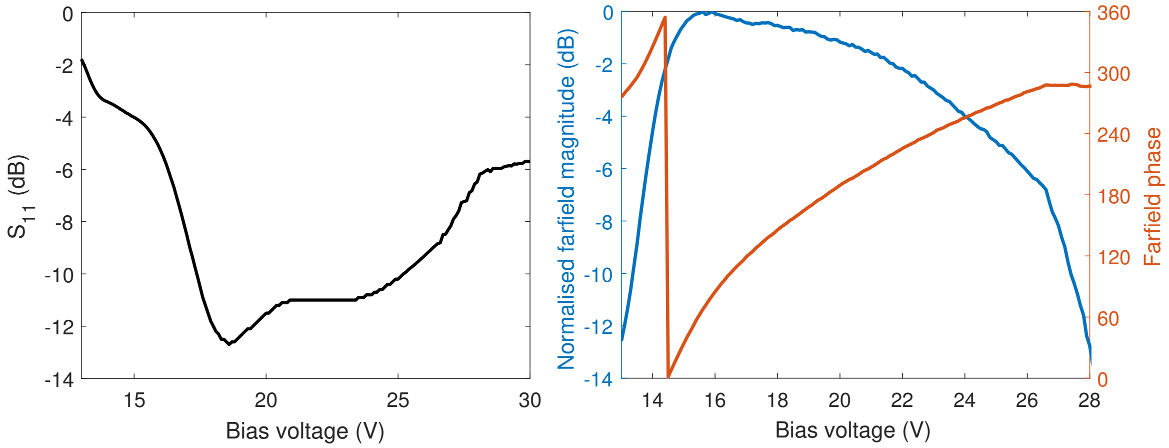

(a) (b)

Figure 5.15: Measured antenna with changing bias voltage, (a) reflection coefficient at 1.8GHz, (b) Normalised farfield magnitude and phase

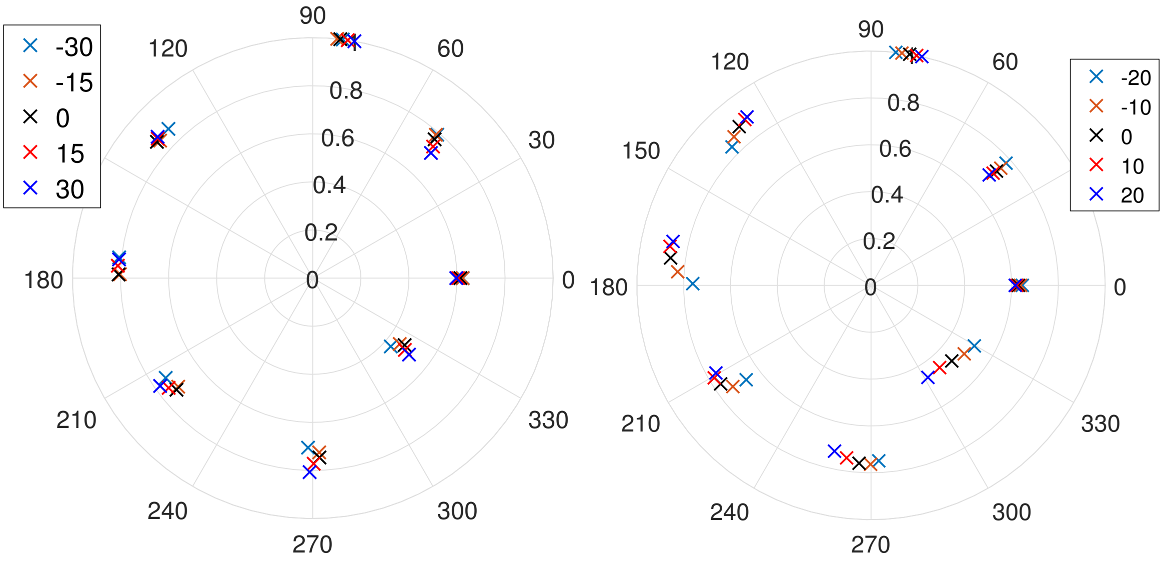

(a) (b)

Figure 5.16: 8-PSK constellation produced by antenna with the viewing angle as a parameter, (a) H-plane, (b) E-plane

simulated and measured by 1.7dB at maximum transmission (black curves) and 4.1dB at minimum (red curves), showing a much steeper drop-off in magnitude at the edges of the response than expected. The measured beamwidth also decreases at extreme bias, from with a peak gain of 2.3dB and 3dB beamwidths of between 80^o and 92^o in the H-plane and 67^o and 86^o in the E-plane. This is due to the known deficiency in diode modelling for FSS applications, as manufacturer models are based on diodes being applied in microstrip transmission lines, rather than being embedded in an FSS orthogonal to the direction of power flow. Similar effects can be seen in [114]. All the cross-polar components produced

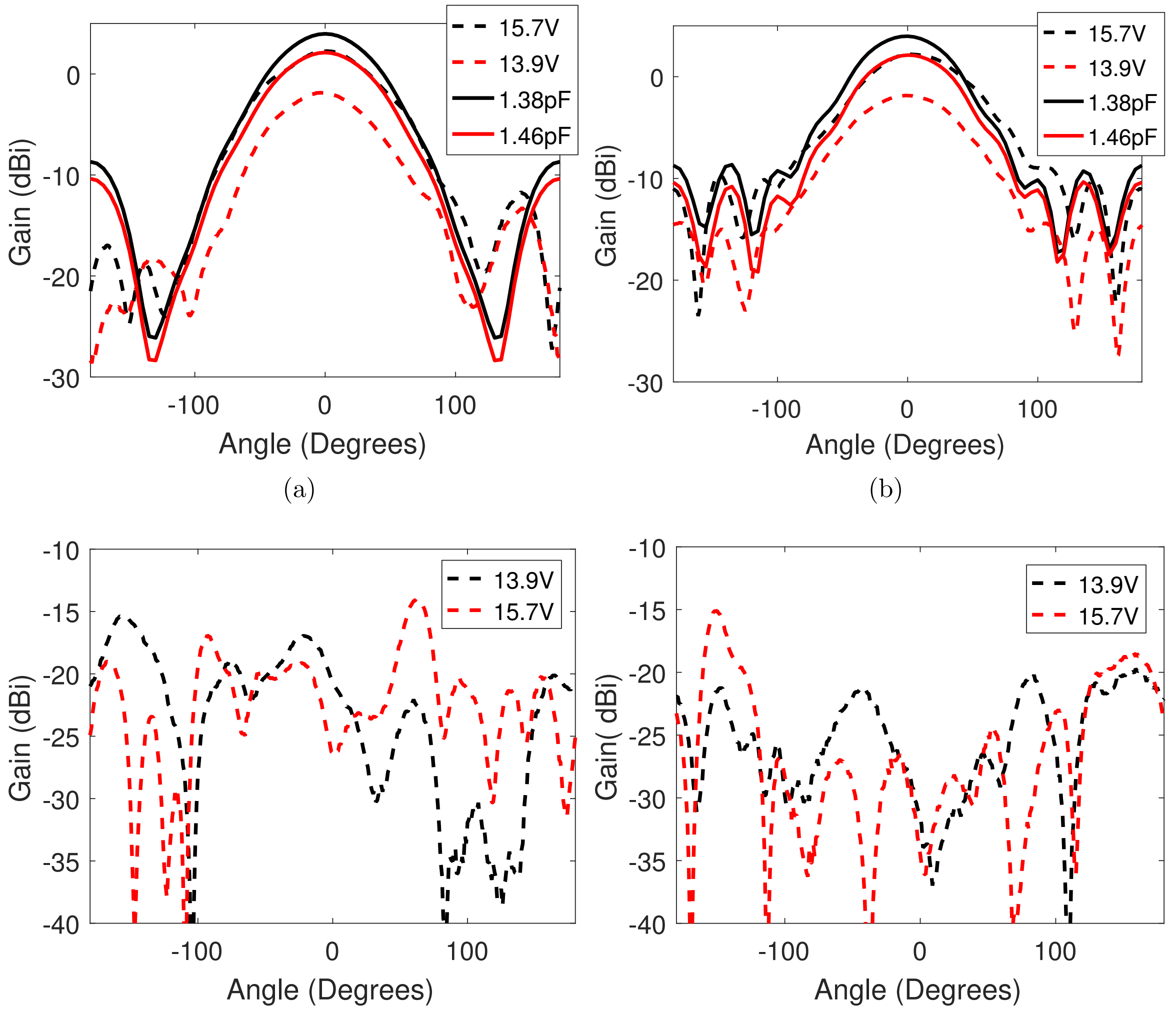

(a) (b) (c) (d)

Figure 5.17: Measured (voltage, dashed lines) and simulated (capacitance, solid lines) pattern of antenna at 1.8GHz at peak and minimum transmission, (a) H-plane co-polar, (b) E-plane co-polar, (c) H-plane measured cross-polar, (d) E-plane measured cross-polar

within these beamwidths are at least 14.2dB below the co-polar magnitude at that angle.

Measurements of the DAM unit's non-linear effects were then made. As varactor diodes are voltage-controlled devices, high power RF inputs may cause currents in the FSS large enough to create voltages across the devices capable of changing their capacitance notably. This non-linearity causes intermodulation products when multiple frequencies pass through the FSS, as will happen during the desired modulation inside the antenna. Also, discontinuities in antenna fabrication may add further non-linearity, such as solder on the FSS and the aluminium tape joints between the cavity walls.

To investigate this, a spectrum analyzer injected two sine-waves, with frequencies f_1 and f_2 equally spaced some Δf either side of 1.8GHz, into the RF port of the DAM unit, which was biased by a static DC voltage of 18.5V. A passive horn antenna was placed 0.5m away at

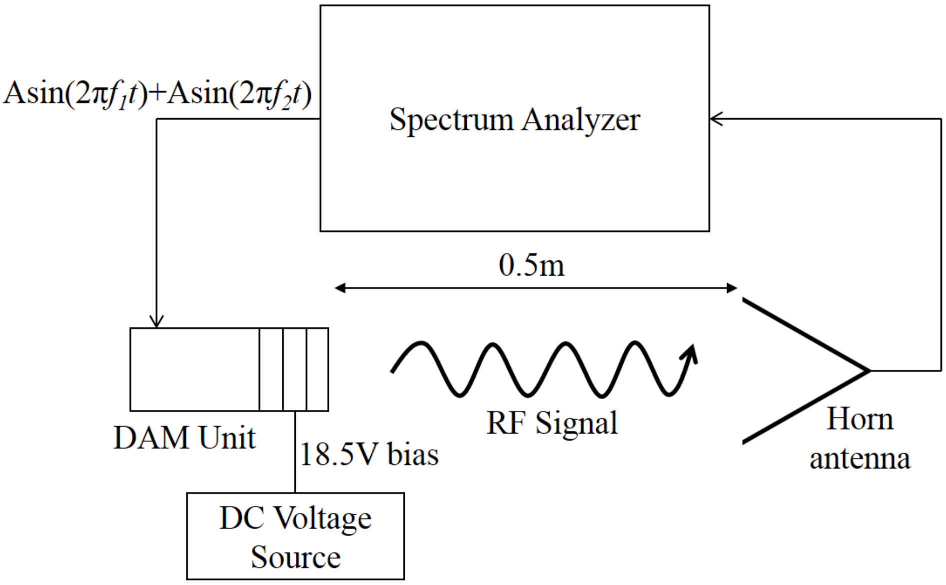

Figure 5.18: Experimental setup for investigating DAM unit intermodulation products

boresight, and connected to the receive port of the spectrum analyzer. The complete setup is shown in Fig. 5.18. In Fig. 5.19a, the average power of the received fundamental and third-order harmonic frequencies is shown as Δf is varied between 1MHz and 50MHz. The input RF power to the DAM unit is 5dBm, the maximum output power from the analyzer. Fig. 5.19a shows that there is intermodulation occurring within the DAM unit, 50dB below the fundamental power transmitted. This decreases as the inserted tones become further apart, due to the filter response of the FSS having an increased effect as the third harmonic moves further from the fundamental. It should also be noted that the two input frequency tones have slightly different powers when transmitted, again due to the filter response of the FSS at different frequencies.

To find the DAM unit's third order intercept point, two sine waves with frequencies f_1=1.795GHz and f_2=1.805GHz, giving Δf=10MHz, were injected at powers varying from -5dBm to 5dBm. -5dBm was the lower limit as below this, the third harmonic was lost in the noise in the analyzer. Fig. 5.19b shows the received powers of the fundamental and third harmonic, which reach -12dBm and -73dBm respectively at transmit power 0dBm. These trends were then extended to find the third order intercept point, which is at the transmit power 31dBm. Note that the DAM unit's output power for the third order intercept would be slightly lower due to losses in the unit.

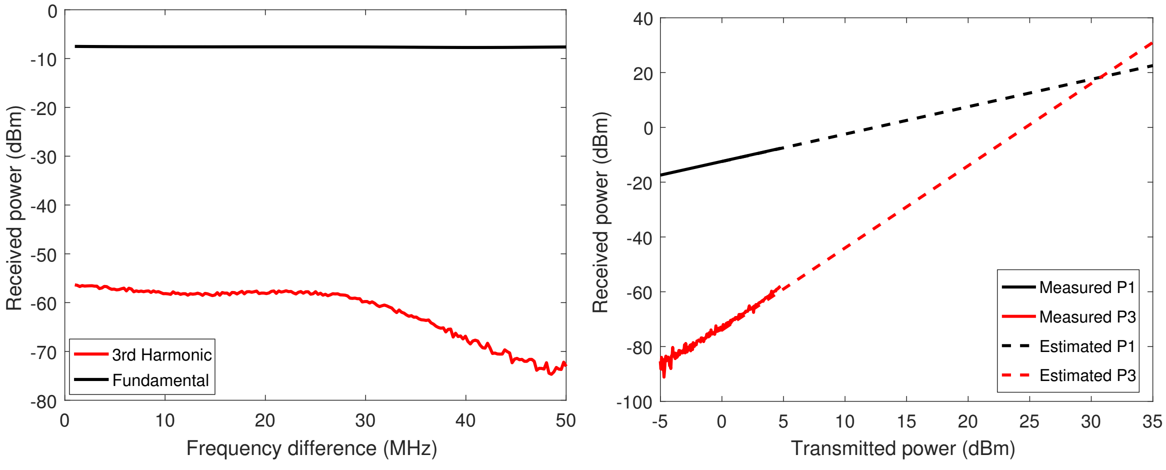

(a) (b)

Figure 5.19: Power of fundamental and third harmonic produced by DAM unit, (a) Changing Δf where P_{in}=5dBm, (b) Changing P_{in} where Δf=10MHz

5.4 System implementation of DAM

In order to demonstrate the functionality of the fabricated modulating antenna, it was integrated into an end-to-end communications system. Bit Error Rate (BER) and Error Vector Magnitude (EVM) measurements were taken for BPSK, QPSK and 8PSK modulation using two possible pulse-shaping waveforms.

5.4.1 Design of end-to-end communications system with DAM

The overall structure of this DAM communications system is identical to that designed and tested in Chapter 4.4.1, and the overview is shown again here for convenience (Fig. 5.20). Digital data must be mapped to a complex number, spread by some spreading sequence $c(t)$, which may also be considered as a pulse-shaping signal. This shaped signal is then mapped to a PAM signal consisting of the required bias voltages and sent to the DAM unit, which modulated the RF carrier wave accordingly. The receiver is again a conventional DSSS PSK receiver, with downconversion, equalisation based on some known pilot sequence, correlation with $c(t)$ and finally a demapping of the processed signal back into digital data.

The key difference between the system designed in Chapter 4.4.1 and the one required for this implementation of DAM is the flexibility in modulation types. Instead of the complex number mapping always resulting in a QPSK constellation, at times a BPSK and 8PSK constellation will be required. This adds the further requirement that the PAM signal must have 2, 4 and 8 different possible levels. It is also not given that the optimum DAM QPSK constellation will be produced with any of the same voltage levels as the optimum DAM 8PSK constellation, and similarly with BPSK. This will be explored in depth later in this

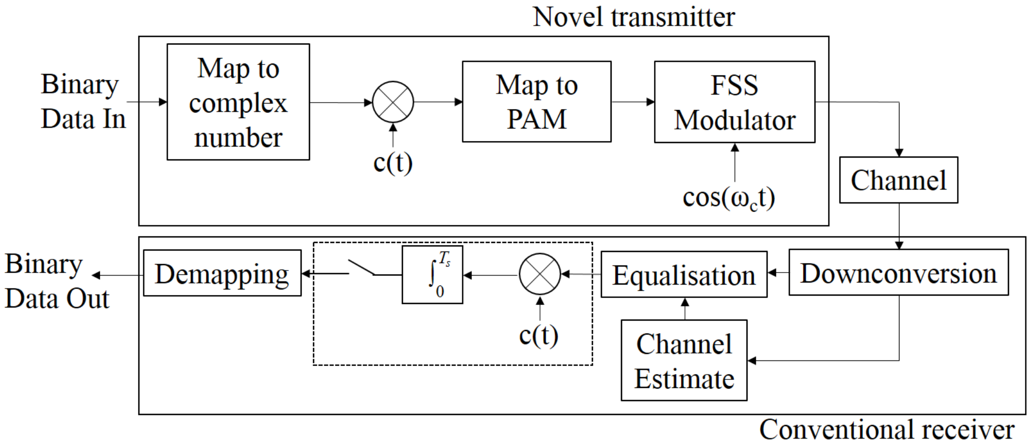

Figure 5.20: System schematic of communications system with DAM transmitter

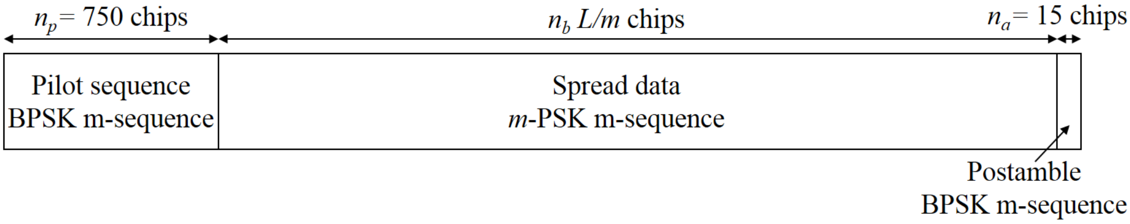

Figure 5.21: Construction of data packet for investigating FSS DAM performance

Chapter.

In order to evaluate the performance of FSS DAM across a number of formats, a generic data packet was designed. The number of data bits transmitted per packet was always approximately $n_b = 8000$ bits, or 1000 Bytes of data. As such, the length of the packet varies with different modulation orders m, and with the length of the pulse-shaping waveform N, such that the number of data chips $n_c = \dfrac{n_b \times N}{m}$. Note that when m=3, in order to ensure a whole number of chips, n_b was set to 8001 bits.

A pilot sequence is placed at the start of the packet, always using two constellation points from the modulation order of choice, which are opposite each other on the complex plane, approximating a BPSK signal. The choice of which constellation points to use as the pilot sequence depends on maximising the strength of the received pilot signal, so uses two relatively unimpaired constellation points. The length 15 m-sequence is again used as the pilot sequence, for its impulse-like autocorrelation function, and is repeated 50 times. This was chosen such that the number of pilot chips was 10% the number of data chips in BPSK. A short postamble of 15 chips, consisting of the BPSK m-sequence, was appended to the packet to allow some compensation for synchronisation error. The final generic packet construction is shown in Fig. 5.21.

In Chapter 4.4.1, the only $c(t)$ fully investigated was the length 15 m-sequence. This was

	BPSK	QPSK	8PSK
Rectangular pulse	8000	4000	2667
Manchester code	16000	8000	5334

Table 5.4: Number of data chips for each packet combination

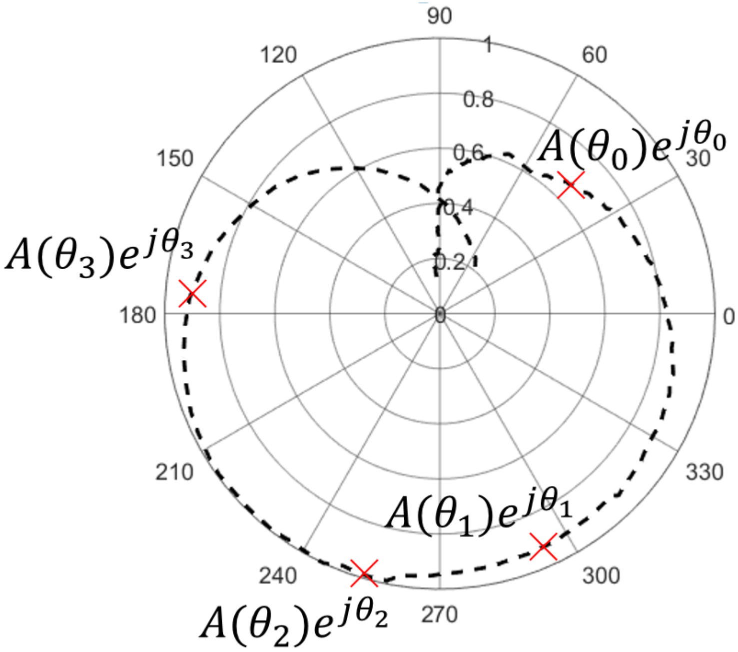

Figure 5.22: Polar plot of possible DAM antenna outputs, with arbitrary 4-PSK constellation marked on

to keep compatibility with the pilot sequence and to attempt to maximise the ameliorating effect of despreading the distorted constellation. However, due to its length the data rate is reduced by 1/15, such that at 1MSymbol/s the data rate, without considering signalling overheads, is 66.7kbit/s. Also, as the sequence is of an odd length, it is only pseudo-balanced. As such, shorter sequences, which may be considered as pulse-shaping waveforms, are examined here.

To investigate the effects of these pulse-shaping waveforms on the constellations produced using DAM, the analysis in Chapter 4.21 can be extended to a DAM PSK modulation scheme of order m and any pulse-shaping waveform $c(t)$ operating along the line in signal space produced by FSS DAM. For a given desired constellation point $a_n, n = 0, 1, \ldots, m-1$ with phase θ_n, the normalised transmitted signal over the symbol duration is

$$s(t, a_n) = A(\phi(t, \theta_n)) \cos(\omega_c t + \phi(t, \theta_n)) \tag{5.1}$$

where $A(\phi(t, a_n))$ is the amplitude produced by the DAM FSS transmitter at phase

$$\phi(t, a_n) = \theta_n + \theta_c(t), \qquad 0 < t < T_s \tag{5.2}$$

where T_s is the symbol duration and $\theta_c(t)$ is the phase of the pulse-shaping waveform $c(t) = e^{j\theta_c(t)}$. Note that θ_n is constant for the duration of the symbol, but may then be different for the next symbol duration. All variations in ϕ during the symbol period is due to $c(t)$. The transmitted complex baseband across one symbol can be represented as

$$u(t, a_n) = A(\phi(t, \theta_n))e^{j\phi(t,\theta_n)} \tag{5.3}$$

The line $A(\phi)e^{j\phi}$ for all possible values of ϕ is shown in Fig. 5.22, with an arbitrary 4-PSK constellation marked on. Note that this line is determined through measurement of the DAM unit being used, and will vary between different designs.

At the receiver, after downconversion, equalisation and correlation with the conjugated pulse-shaping signal (Fig. 5.20), the normalised resultant complex baseband ignoring noise is

$$\begin{aligned} y(T_s, a_n) &= \int_0^{T_s} A(\phi(t, \theta_n))e^{j(\theta_n+\theta_c(t))} \cdot e^{-j\theta_c(t)}dt \\ &= \int_0^{T_s} A(\phi(t, \theta_n))e^{j\theta_n}dt \end{aligned} \tag{5.4}$$

As such, the effect of the pulse-shaping sequence $c(t)$ is an averaging effect of the amplitude produced at the phases $\phi(t, a_n)$ traverses during T_s. For mitigation of distortion in amplitude due to FSS DAM, $c(t)$ should be chosen to produce the same average amplitude for all constellation points a_n. From the shape of $A(\phi)$ (Fig. 5.22), where the largest values of $A(\phi)$ are in general roughly an angle of π away from the smallest values $A(\phi+\pi)$, intuitively a waveform providing phase balance should produce a constellation with approximately equal amplitude at the receiver output.

This will be tested numerically using the above analysis. The baseline for comparison will be a rectangular pulse, represented by $c(t) = \dfrac{\mathrm{rect}(t)}{T_c}$, where $\mathrm{rect}(x)$ is the rectangular function and T_c is the chip period. For this pulse $T_s = T_c$, maximising the data rate, but the static and unbalanced nature of the waveform is expected to provide no ameliorating effect on the constellation, potentially sacrificing the error rate. The alternative waveform explored is a Manchester code pulse, where $c(t) = [1, -1] \cdot \dfrac{\mathrm{rect}(t)}{T_c}$. This represents a value of $\dfrac{1}{T_c}$ for one chip period followed immediately by a value of $\dfrac{-1}{T_c}$ for one further chip period. The notation is equivalent to $\theta_c(t) = 0$ for $0 < t < T_c$ and $\theta_c(t) = \pi$ for $T_c < t < 2T_c$. Using this balanced code halves the throughput of the system as here $T_s = 2T_c$, and extends the length of the packet. The number of data chips per packet for each combination of modulation order and pulse waveform are presented in Fig. 5.4.

Data	Opposite point	Assigned phase	Point amplitude with rectangular pulse	Point amplitude with Manchester code pulse
0	1	0	0.90	0.95
1	0	π	1	0.95

Table 5.5: Normalised BPSK constellation points received using DAM with pulse-shaping

In the case of using a rectangular pulse $c(t) = \dfrac{\text{rect}(t)}{T_c}$ (i.e. $\theta_c(t) = 0$), $\phi(t, \theta_n) = \theta_n \dfrac{\text{rect}(t)}{T_c}$ and so $A(t, \phi)$ is static over T_s. As such there is no averaging effect, and so no amelioration of the distorted DAM constellation occurs. However, when the Manchester code is used, $\theta_c = [0, \pi] \cdot \dfrac{\text{rect}(t)}{T_c}$ so $A(\phi)$ takes on two values. The first of these is $A(\theta_n)$, the amplitude of the original constellation point. The second is $A(\theta_n + \pi)$, which is the amplitude produced by the DAM modulator directly opposite the original constellation point. The final complex baseband value at the receiver output will have the amplitude of the average of the two,

$$y(T_s) = \frac{A(\theta_n) + A(\theta_n + \pi)}{2} e^{j\theta_n} \tag{5.5}$$

In conventional PSK modulation, in order to maximise Euclidean distance, the constellation points are placed $\frac{2\pi}{m}$ radians apart. Where M_{mod} is even, which in conventional PSK it always is, each constellation point will have another constellation point directly opposite it (π radians away). As such, a conventional PSK constellation point shaped by a Manchester code pulse will consist of two PSK constellation points. The values of these points is shown in Table 5.5 for BPSK, Table 5.6 for QPSK and Table 5.7 for 8PSK. The location of each set of constellation points on the line $A(\phi)e^{j\phi}$ was chosen to ensure $\frac{2\pi}{m}$ radians of phase separation between each constellation point whilst maximising the amplitude of all constellation points. As such the sets of constellation points have a different reference 0 phase in order to simplify their representation. Gray mappings were also used. The voltages used to achieve these constellation points will be discussed in detail later in this chapter. The tables also show the values of each constellation point after correlation for the DAM unit measured earlier in this Chapter, using both rectangular and Manchester code pulse-shaping. The distortion of constellation points reduces from maxima of 0.9dB, 4.1dB and 6.9dB for BPSK, QPSK and 8PSK respectively when the rectangular pulse is used, to 0dB, 0.2dB and 1.5dB when a Manchester code is used. This will result in significant performance improvements in BER, as will be shown later in this Chapter. It should, however, be noted that doubling the bandwidth of the system by using the Manchester code doubles the noise power at the receiver, introducing a 3dB penalty in performance against signal to noise ratio (SNR).

Data	Opposite point	Assigned phase	Point amplitude with rectangular pulse	Point amplitude with Manchester code pulse
00	11	$-3\pi/4$	0.62	0.81
01	10	$3\pi/4$	0.72	0.79
10	01	$-\pi/4$	1	0.79
11	00	$\pi/4$	0.85	0.81

Table 5.6: Normalised QPSK constellation points received using DAM with pulse-shaping

Data	Opposite point	Assigned phase	Point amplitude with rectangular pulse	Point amplitude with Manchester code pulse
000	110	0	0.80	0.83
001	111	$\pi/4$	0.63	0.82
010	100	$3\pi/4$	0.66	0.73
011	101	$\pi/2$	0.45	0.70
100	010	$-\pi/4$	0.80	0.73
101	011	$-\pi/2$	0.95	0.70
110	000	π	0.86	0.83
111	001	$-3\pi/4$	1.0	0.82

Table 5.7: Normalised 8PSK constellation points received using DAM with pulse-shaping

5.4.2 Testbed implementation

The communications system designed above is now implemented into a testbed, in order to measure the BER performance of the DAM transmitter. The testbed must be able to generate random binary data, construct the packet described in Fig. 5.21, convert the baseband data for this packet into an appropriate bias voltage for the DAM unit to produce a BPSK, QPSK or 8PSK signal. This signal must then be received, downconverted, equalised using an estimate of the channel state information (CSI), correlated with the pulse-shaping waveform, and finally a decision must be made on the sampled signal to recover the data (Fig. 5.23).

As in Chapter 4.4.1, the data is generated, multiplied by the pulse-shaping waveform and formatted into a packet in MATLAB on a PC. The whole packet data is then sent to a Rohde & Schwarz SMBV100a signal generator over GPIB, as before, and the signal generator also supplies the 1.8GHz RF carrier wave. Downconversion of the received signal to digital baseband I and Q is again performed in a Rohde & Schwarz FSV Spectrum Analyzer, which samples the signal and sends digitised I/Q baseband signals to MATLAB in the PC. Again, the operating procedure for this equipment can be found in Appendix C. The received pilot sequence is correlated with the m-sequence to estimate a complex number defining the channel [27]. The conjugate of this channel estimate is multiplied with the received data

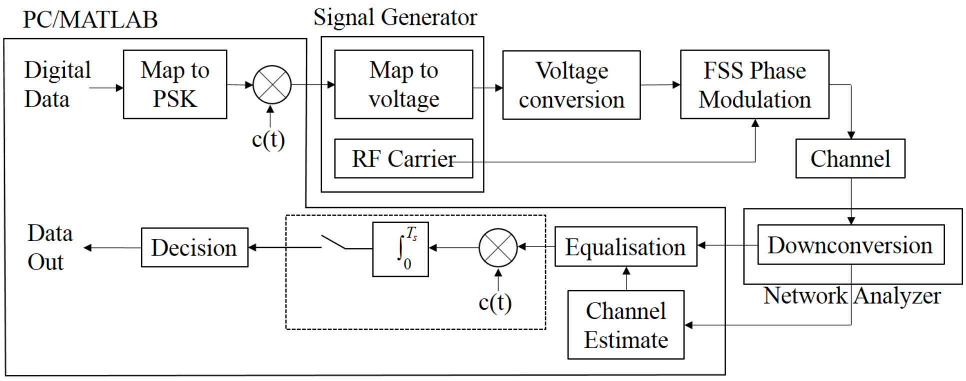

Figure 5.23: System diagram for implementation of modulating antenna

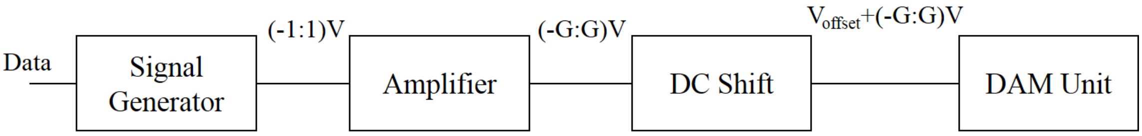

Figure 5.24: Overview of PAM signal production from processed data

chips to equalise the channel effects, and these equalised chips are then multiplied by the pulse-shaping waveform $c(t)$ and integrated over the symbol period T_s to recover the data symbols. A minimum distance detector was used to demap the symbols into binary data.

The key difference in requirements between this experiment and the equivalent QPSK DAM experiment is the requirement for different orders of modulation to be achieved, including 8PSK. This requires a PAM mapping capable of producing up to 8 different levels, which is not possible using the previous implementation of separate I and Q lines carrying binary signals. It was found that the Rohde & Schwarz SMBV100a signal generator can be programmed with any generic mapping, as long as the maximum combined magnitude of the I and Q is 1. As such, if a mapping is designed where the value of Q is always 0V, the I can take any value as long as the minimum is -1V and the maximum is 1V. This can be used to create a non-linear PAM mapping, and is described by the 'Map to voltage' block in Fig. 5.23. To then convert this to the required bias voltages for the DAM to produce the desired constellation, which are all in the range 13.8V to 26V as described in Fig. 5.15b, the signal must be amplified and a DC shift added. This is the 'Voltage Conversion' block in Fig. 5.23, and is further described in Fig. 5.24.

The circuit designed to achieve this is shown in Fig. 5.25. The input value v_{in} is the non-linear PAM signal between -1V and 1V, from the I output of the signal generator. This is first put through a THS4271 unity gain op amp, which acts as a high-speed buffer. The THS4271 was chosen due to its stability at unity gain, its 1.4GHz bandwidth and its bipolar feed allowing amplification of both negative and positive voltages. The buffer increases the possible rate of operation by minimising the amount of current draw from the signal

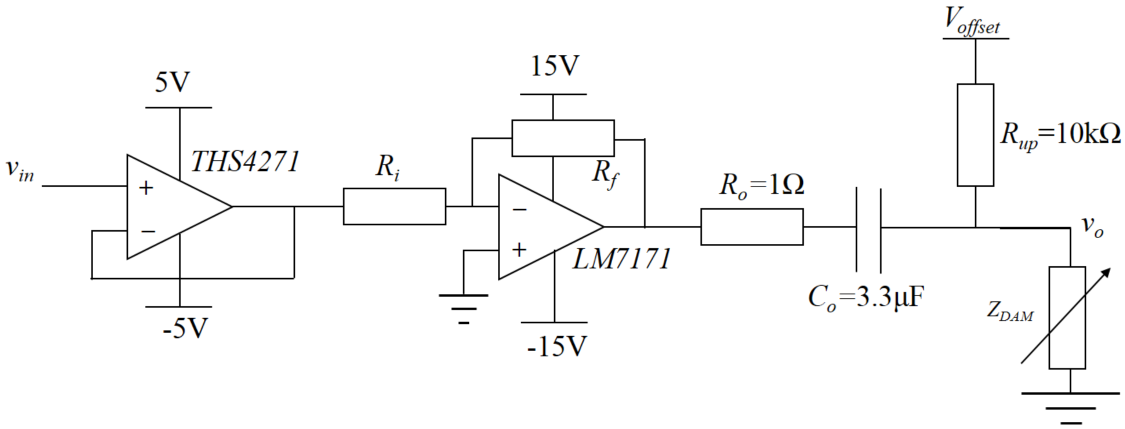

Figure 5.25: Circuit diagram for producing PAM from signal generator input with unmarked component values shown in Table 5.11

generator. There is then a LM7171 op amp in an inverting amplifier configuration. The gain is determined by $G = \frac{-R_f}{R_i}$ and the LM7171 op amp was chosen for its 200MHz bandwidth, 4100V/μs slew rate and higher voltage operation, being specified for operation at ±15V. This stage amplifies the PAM signal such that the spacing between voltage levels is at the desired values.

An output resistor R_0 controls the current output required of the LM7171 op amp. Finally, a DC blocking capacitor C_0 is used to decouple the LM7171 op amp from pull-up resistor R_{up}, which provides the desired average DC offset V_{offset}. C_0 must be chosen to give a large enough time constant $\tau \approxeq C_0 R_0$ to minimise drift in the centre voltage over the packet, as different PAM levels are transmitted, which may not have a consistent average, while minimising the rise time of signals and so the maximum achievable modulation rate. The pilot sequence, consisting of only two voltages rather than all possible values, gives a particular time period over which to ensure there is minimal drift in output voltage. For an input signal v_i with average V_{av}, the output signal is given by

$$v_0 = V_{offset} + G(v_i - V_{av}) \tag{5.6}$$

Using this equation, the required input voltage signal, offset voltage and gain can be calculated. The voltage mappings are shown in Tables 5.8, 5.9 and 5.10 for BPSK, QPSK and 8PSK respectively, while the gain, offset voltage required and chosen resistor values are shown in Table 5.11. R_f was held constant at 224Ω for all modulation orders to maximise the rate achievable by the LM7171 op amp, in agreement with the Texas Instruments data sheet [153].

The measured output of the control electronics for QPSK, when disconnected from the load, is shown in Fig. 5.26. Note that the gain is larger than expected, due to the absence of the load, producing a signal with voltage points up to 0.5V away from those described in

Data	Constellation point	Bias voltage (V)	Input voltage (V)
0	-1	14.7	-1
1	1	20.3	1

Table 5.8: Mappings for BPSK constellation using DAM

Data	Constellation point	Bias voltage (V)	Input voltage (V)
00	$1e^{-j3\pi/4}$	14.2	-1
01	$1e^{j3\pi/4}$	23.5	1
10	$1e^{j\pi/4}$	15.7	-0.67
11	$1e^{-j\pi/4}$	18.6	-0.04

Table 5.9: Mappings for QPSK constellation using DAM

Data	Constellation point	Bias voltage (V)	Input voltage (V)
000	1	22.1	0.44
001	$1e^{j\pi/4}$	25.3	1
010	$1e^{j3\pi/4}$	14.5	-0.89
011	$1e^{j\pi/2}$	13.9	-1
100	$1e^{-j\pi/4}$	19.7	0.02
101	$1e^{-j\pi/2}$	17.7	-0.03
110	$1e^{j\pi}$	15.2	-0.77
111	$1e^{-j3\pi/4}$	16.2	-0.60

Table 5.10: Mappings for 8PSK constellation using DAM

Modulation	Gain	V_{offset} (V)	R_i (Ω)	R_f (Ω)
BPSK	2.8	17.2	80	224
QPSK	4.6	18.1	48.7	224
8PSK	5.7	18.3	39	224

Table 5.11: Normalised BPSK constellation points received using DAM with pulse-shaping

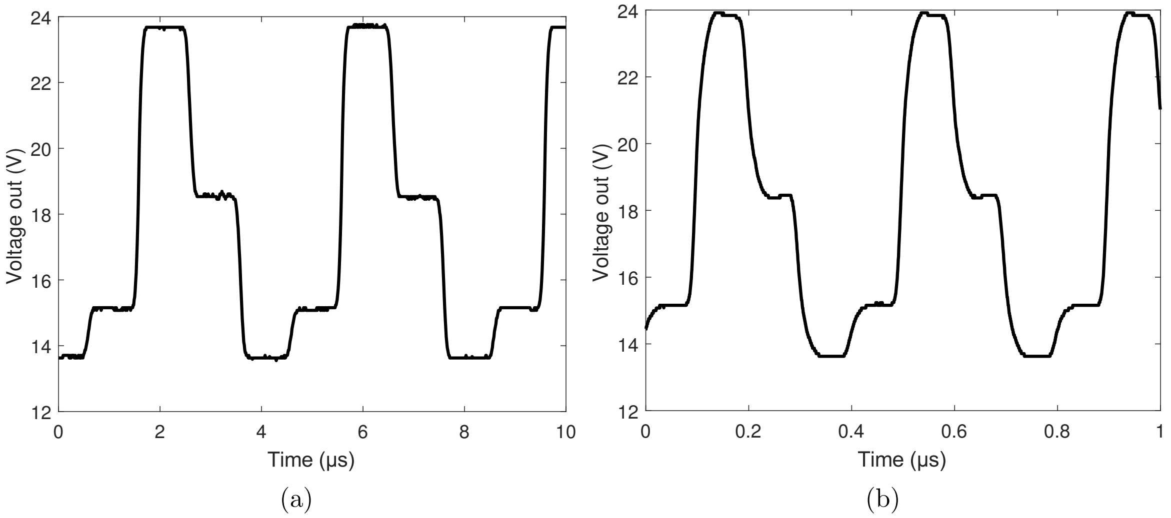

Figure 5.26: Measured output of QPSK control electronics not connected to DAM in response to repeated data sequence 00100111 at (a) 1MSymbol/s, (b) 10MSymbol/s

Table 5.9. Despite this, the signal is clean, producing only 50mV ripple, and has a rise time of 40ns, comfortably allowing operation at 10MSymbol/s (Fig. 5.26b).

Once the electronics are connected to the DAM unit, the desired voltages for each constellation point are correctly produced, as shown measured with an oscilloscope in Fig. 5.27a. However, this also increases the ripple voltage to 100mV, and increases the signal rise time to approximately 150ns. This means that at 10MSymbol/s, the desired voltage values do not settle before the symbol changes, producing a distorted signal (Fig. 5.27b). The increased rise time is due to the interplay between the impedance of the load, which is largely capacitive, and the resistive and capacitive circuit elements R_0 and C_0 at the output of the control electronics circuit (Fig. 5.25).

In the above experiments, R_0 was chosen as 1Ω to provide some damping while minimising the RC time constant of the output. C_0 was chosen as 33μF as it produced a large enough time constant to maintain the average output voltage across the whole data packet, without varying while the 750 chip pilot sequence was output, at 1MSymbol/s. As such, this setup was optimised for operation at 1MSymbol/s. Correct choices of C_0 and R_0 may allow the driving of the DAM unit at over 10MSymbol/s, but without accurate modelling of the load impedance, which is non-trivial, trial-and-error approaches were unable to produce such an arrangement.

In order to investigate the effect of this voltage ripple on the antenna output, the phase change per volt ($\frac{d\phi}{dV}$) was examined (Fig. 5.28). Again, this relates to both the relationship between bias voltage and diode capacitance, and the link between diode capacitance and the phase change produced. Due to the higher voltages required for tuning compared with the SMV1247 diodes used in the previous Chapter, the maximum value of $\frac{d\phi}{dV}$ is only

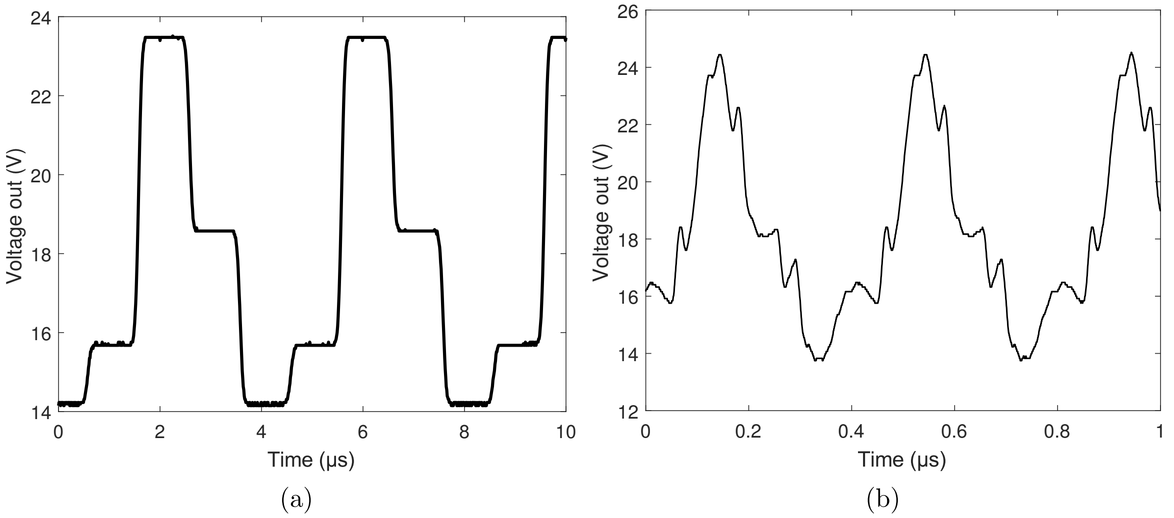

(a) (b)

Figure 5.27: Measured output of QPSK control electronics connected to DAM unit in response to repeated data sequence 00100111 at (a) 1MSymbol/s, (b) 10MSymbol/s

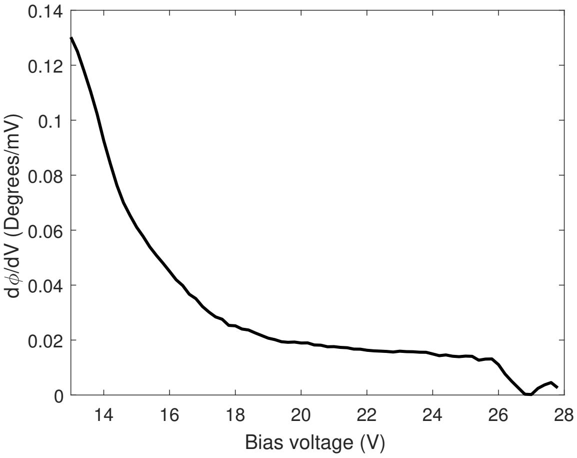

Figure 5.28: Rate of change of E-field phase produced by DAM unit at boresight with voltage, against total bias voltage

0.13deg/mV compared with 0.4deg/mV with the previous design. This suggests that a ripple of 100mV would produce 13^o phase variation even at this worst point. However, as a percentage of the bias voltage, phase variation is similar, with a 1% ripple producing up to 14^o phase variation at 13.9V, compared with 11^o at 2.75V in the previous design. Note also that $\dfrac{d\phi}{dV}$ reduces to approximately 0.02deg/mV for bias voltages higher than 18V. From this analysis, the maximum phase distortion due to voltage ripple at 1MSymbol/s in QPSK would be 8.4^o, due to 100mV ripple at 14.2V.

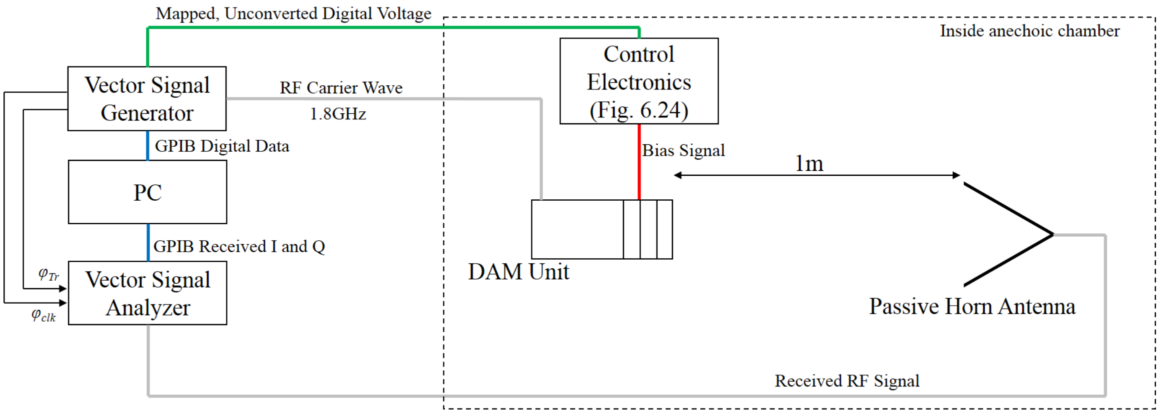

Figure 5.29: Diagram of measurement setup in anechoic chamber for DAM

5.4.3 Measurement of system in AWGN

The system measurements were performed in an anechoic chamber to minimise reflections and interference. The PC, signal generator and signal analyzer were all placed outside the chamber, with long coaxial cables used to supply the RF carrier wave to the DAM unit and initial unconverted voltage signal to the electronics, which were both placed inside the chamber (Fig. 5.29). DC power supplies were used to provide the voltages for the control electronics, and were also placed inside the chamber, surrounded by RF absorber to minimise reflections. A passive receiving horn antenna was placed 1m away from the DAM unit at boresight, and a long coaxial cable connected this to the signal analyzer. The antennas were placed on polystyrene blocks to hold them above the RF absorber while minimising any reflections or dielectric effects. A photograph of this equipment is shown in Fig. 5.30.

The constellations produced are shown in Fig. 5.31, with $c(t)$ as a rectangular pulse and as a Manchester code. The constellations shown are for BPSK, QPSK and 8-PSK, with transmission at 1MSymbol/s and a constant E_b/N_0 of 52dB. The amplitude variation between constellation points is 1.1dB for BPSK, 4.4dB for QPSK and 8.5dB for 8-PSK. When a Manchester code is used, these reduce to 0.03dB for BPSK, 1.8dB for QPSK and 2.0dB for 8-PSK, due to the averaging of the magnitude variation. It should also be noted that the EVM of the DAM constellation is noticeably larger than expected, with values of 7.4%, 8.3% and 8.2% for BPSK, QPSK and 8-PSK, respectively. However, this reduces significantly when the Manchester code is used, to 2.3%, 4.0% and 2.4%. This suggests the variation is deterministic, and most likely caused by imperfections in the biasing signal sent to the direct antenna modulator. As such, improved driving of the antenna may improve the EVM further.

BER measurements are taken for each modulation scheme, with and without using a Manchester code, and compared against instrument grade modulation from the SMBV1000a signal generator. This was transmitted through the DAM unit biased at 18.5V in order to

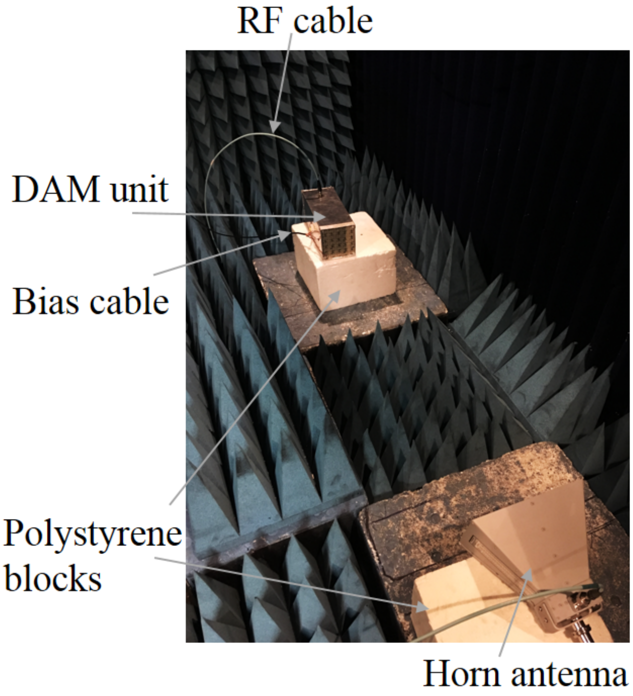

Figure 5.30: Photograph of DAM measurement setup in anechoic chamber

maintain the same channel (Fig. 5.32). For demonstration, the transmitter sample rate in each case is 1MSymbol/s. At each transmit power level, measurements were taken until 200 bit errors were observed and at least 10 packet errors were detected. The E_b/N_0 was calculated by comparing the noise power to the average signal power across 100 different packets at the signal generator's maximum transmit power to find a baseline.

For BPSK, without balancing the DAM transmitter requires 2dB more transmit power to achieve a BER of 10^{-5} compared with instrument grade modulation, whereas using a balancing sequence reduces this to nearly 0dB. For QPSK, the difference is approximately 1.5dB without balance, and 0.5dB with balance. Unbalanced 8PSK has an error rate which is only reducible to 10^{-4} due to the distortion of the constellation. However, using a balancing sequence allows performance only 1.5dB worse at a BER of 10^{-5}. Across all modulation orders, the instrument grade modulation follows the theoretical BER curve, showing the quality of this modulation, compared with the prototype DAM transmitter, which has some degradation, which increases with the modulation order.

The packet error rate (PER) of each experiment were also measured (Fig. 5.34). This was to examine whether DAM suffers from errors in a different way from conventional modulators. This could be so in two ways- either bit errors are rare but happen consistently across different packets, in which case the differences between the PER performance with DAM and conventional modulation would be greater than the differences in the BER performance. Alternatively, DAM may be susceptible to burst errors where, when a packet

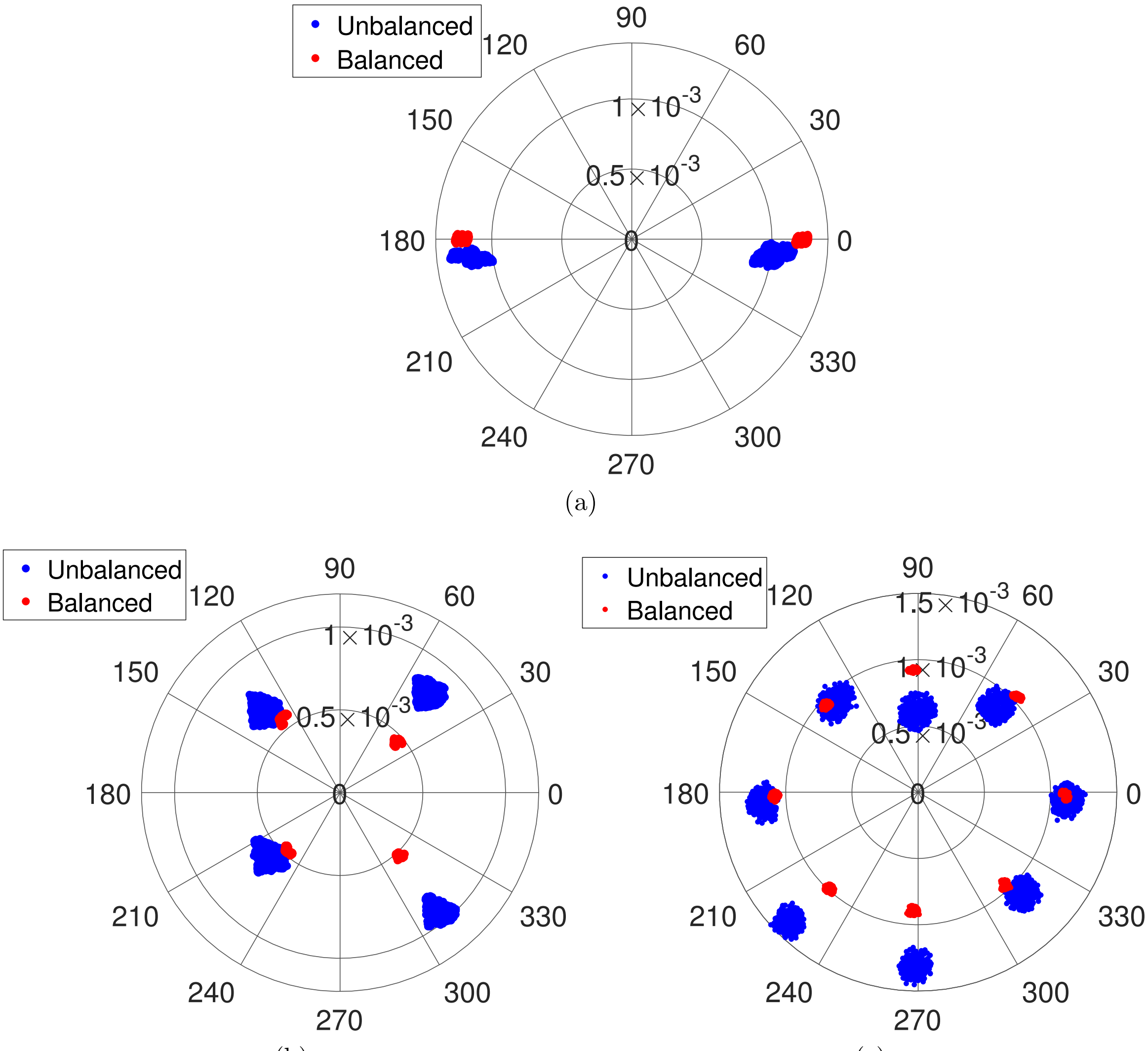

(a)

(b)

(c)

Figure 5.31: Measured constellations produced by DAM in AWGN, Eb/N0=52dB, balanced and unbalanced. (a) BPSK, (b) QPSK, (c) 8PSK

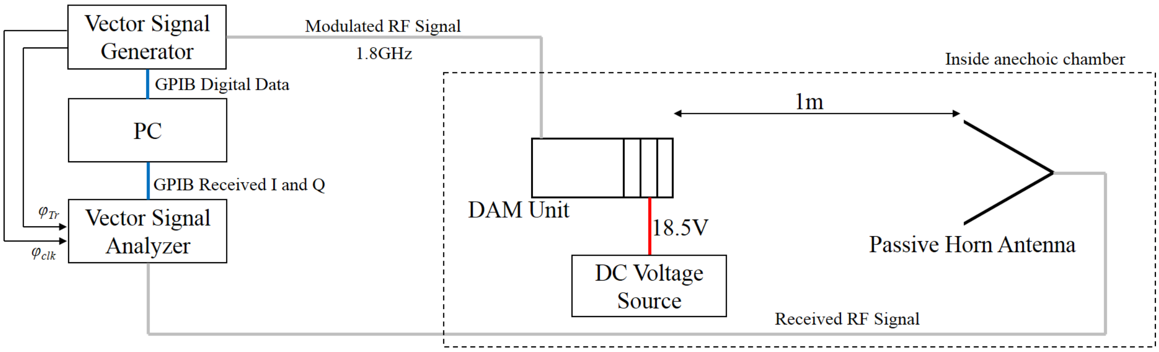

Figure 5.32: Diagram of measurement setup for instrument grade conventional modulation comparison

fails, many errors are present. This would lead to the difference in PER between DAM and conventional modulation being smaller than the difference between BER performances. In the measurement DAM performs as expected, with equivalent differences between DAM and conventional modulation performance for both BER and PER, with approximately 1.5dB difference at PER of 10^-2 with unbalanced QPSK, and similar for balanced 8PSK at the same PER. This suggests that DAM behaves similarly to conventional transmitters.

In order to gain an understanding of how this DAM transmitter may be used in real conditions, the throughput S of the different approaches can be calculated. Note that for comparison, it will be assumed that the waveform for the rectangular pulse is the same length T_s as the Manchester pulse. This is not how the measurements above were taken, where the period of the Manchester pulse was twice that of the rectangular pulse. However, it is safe to assume that the SNR remains constant between these two cases. From the measured PER P_{ep} at each given SNR, throughput S of the measured system can be calculated as follows:

$$S = (1 - P_{eP}) \cdot \frac{\frac{n_b N}{m}}{n_p + n_a + \frac{n_b N}{m}} \cdot \frac{m}{T_s} \tag{5.7}$$

where n_p and n_a are the number of pilot chips and postamble chips respectively, and as discussed previously $\frac{n_b N}{m}$ gives the number of data chips in the packet. Note that $SNR = \frac{m \cdot E_b}{N_0}$. In the above experiments, a large pilot sequence and a short postamble were used to ensure reliable synchronisation between transmitter and receiver, with data occupying 91%, 84% and 78% of the packet length for BPSK, QPSK and 8PSK, respectively. However, in a practical implementation this factor $\frac{T_{data}}{T_{packet}}$ would tend to 100% by using a significantly shorter pilot sequence. Any effects on the performance of DAM with channel estimation errors due to reducing the pilot sequence length is left for future work. As such, in the following calculations it will be assumed that $\frac{\frac{n_b N}{m}}{n_p + n_a + \frac{n_b N}{m}} = 1$.

The throughputs calculated with the above assumptions are shown in Fig. 5.35, and suggest the situations in which different pulse-shaping waveforms and modulation orders may

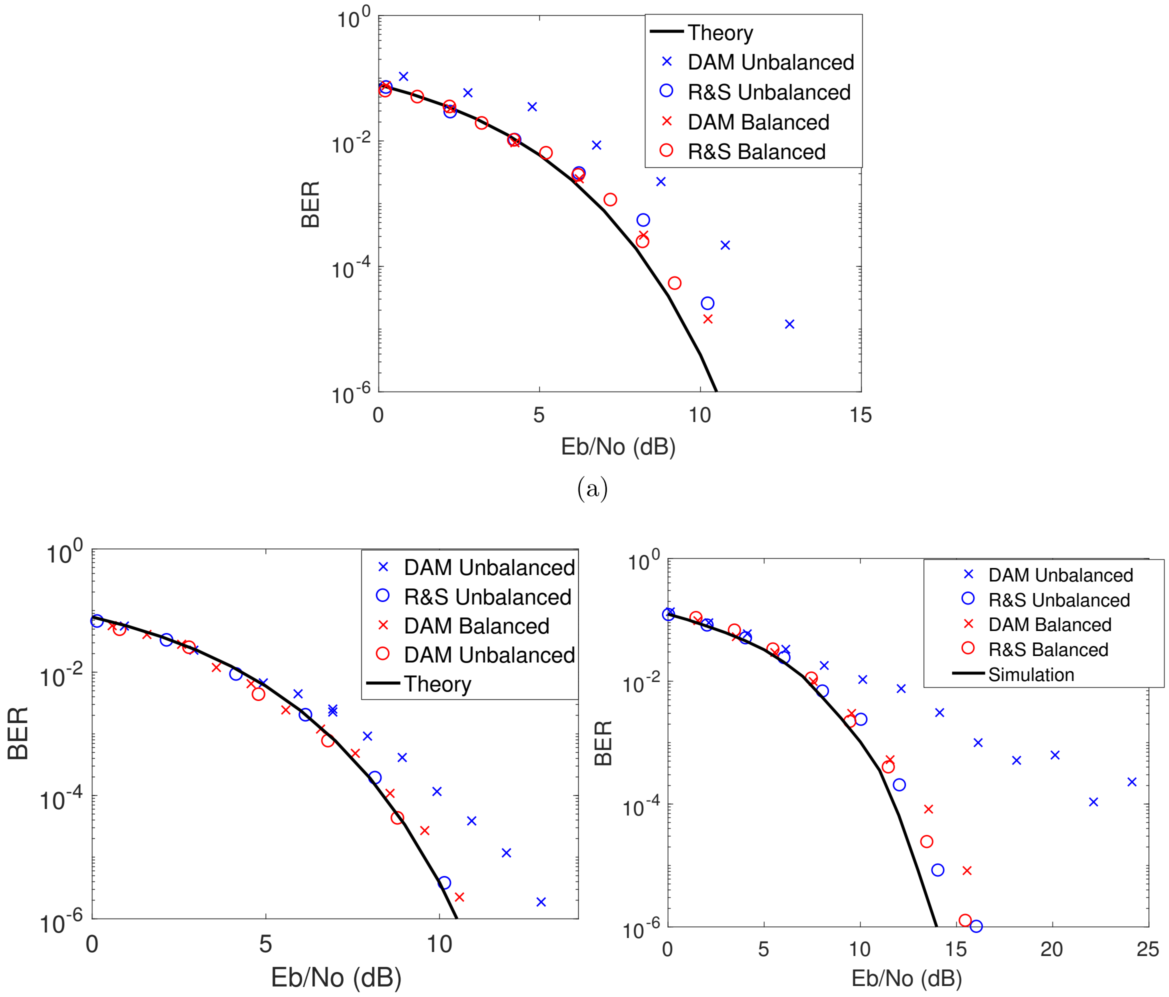

(a)

(b)

(c)

Figure 5.33: Measured bit error rates for DAM and instrument grade modulation in AWGN, balanced and unbalanced. (a) BPSK, (b) QPSK, (c) 8PSK

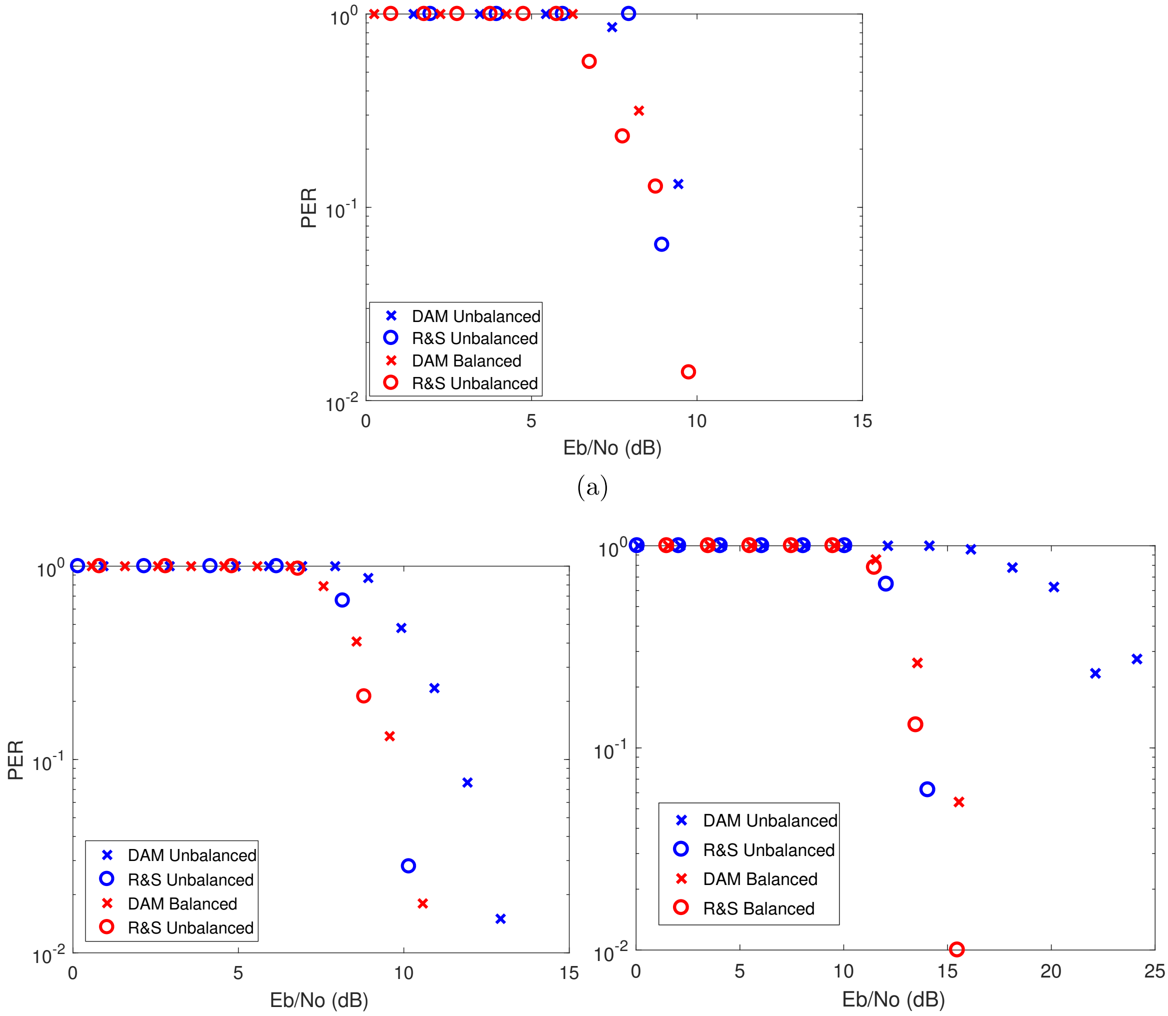

(a)

(b)

(c)

Figure 5.34: Measured packet error rates for DAM and instrument grade modulation in AWGN, balanced and unbalanced. (a) BPSK, (b) QPSK, (c) 8PSK

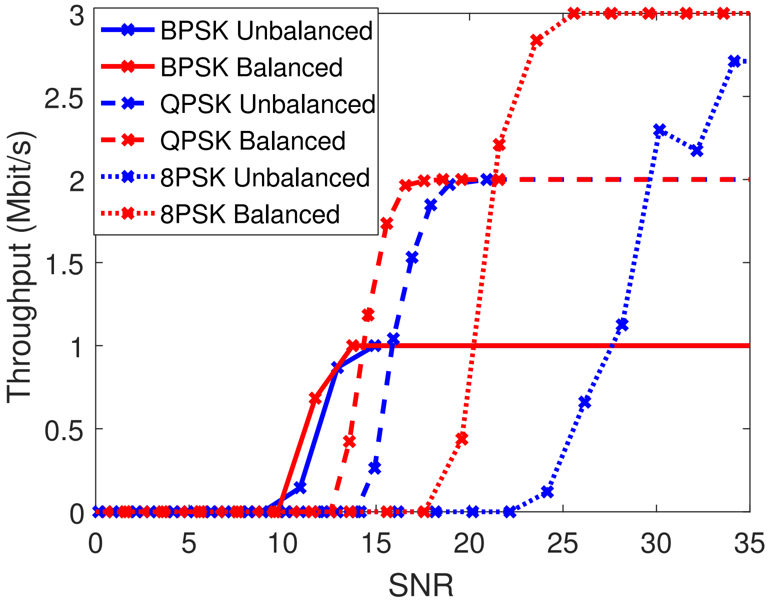

Figure 5.35: Calculated throughputs of DAM transmission for different modulation orders and pulse-shaping waveforms with changing SNR

be used. Using a balanced waveform gives best-case performance at SNRs of 14dB and 18dB for BPSK and QPSK, respectively; 1dB and 2dB lower than when the rectangular pulse is used. This suggests that a balancing sequence is particularly important when received powers are low, providing improved throughput at the cost of greater bandwidth occupancy. For 8PSK, the peak throughput of 3Mbit/s is only reached when using a Manchester pulse, with the unbalanced case peaking at 2.71Mbit/s due to the irreducible PER. However, where the SNR is greater the 35dB, which is not uncommon in real channels, it may be that unbalanced 8PSK would be used to achieve throughput with only a small degradation in performance compared with balanced 8PSK while maximising the spectral efficiency of the waveform.

5.5 Discussion

In this Chapter, the first FSS-based direct antenna modulator capable of producing phase modulation up to 8-PSK has been presented, designed, characterised, and tested in an end-to-end communications system. The designed antenna was simulated to have a peak efficiency of 46%, which compares favourably with other DAM techniques (Table 5.12). There is also potential efficiency improvement from using lower loss materials as substrates. Simulation also suggested magnitude variation of 2.7dB over 360^o of phase change could be produced. Measurement found a peak gain of 2.3dB, and 6dB variation for 315^o of phase change. The transmitted constellation was consistent in magnitude and phase within the antenna 3dB beamwidth of 60^o in the H-plane and 40^o in the E-plane.

The communications system used in this Chapter has also developed from that used in

DAM technique	Modulation format	Symbol rate (MSymbol/s)	Operating frequency (GHz)	Physical size (λ_0^3)
FSS DAM (2nd iteration)	BPSK, QPSK, 8PSK	1	1.8	0.68×0.68×1.71
FSS DAM (1st iteration)	QPSK	1	1.8	0.53×0.53×0.96
Integrated switches [42]	OOK	5	1	0.32×0.39×0.01
Reflective metasurface [59]	8PSK	2.048	4.25	5.44×1.36×0.07

Table 5.12: Comparison of key metrics for FSS DAM with experimentally implemented state-of-the-art DAM techniques

Chapter 4. Previously, a spreading sequence was used to provide mitigation of the distortion caused by FSS DAM, which achieved this at the cost of reduced data rates. Here, the spreading sequence was replaced with a pulse-shaping waveform, which could be designed to achieve the same amelioration with improved data rates. One waveform used was a rectangular pulse, which provides no reduction of distortion but maximises data rate. This gave EVM measurements in the order of 8%, and in comparison to instrument grade modulation caused a degradation of BER performance of 2dB and 1.5dB for BPSK and QPSK modulation, respectively. For 8PSK, the error rate became irreducible at 10^{-4} due to the systematic distortion of the constellation and the high EVM. The alternative pulse-shaping waveform considered was a Manchester pulse, which halves the data rate but provides amelioration of the constellations. Using this waveform, the DAM transmitter produces constellations with EVM of the order of 2%. The BER performance of the DAM transmitter using this balanced waveform, when compared with instrument grade modulation, is impaired by 0dB, 0.5dB and 1.5dB for binary, quaternary and 8PSK, respectively. As such, it can be said that the requirement of achieving up to 8PSK modulation has been met (Table 5.1).

As it is based on the same general design as the previous Chapter, in most key metrics the DAM unit produced here is similar to the previous one (Table 5.12). It operates at the same frequency of 1.8GHz and the same symbol rate of 1MSymbol/s as intended in the design parameters, and broadly similar to the frequencies of operation and symbol rates of both integrated switch DAM and reflective metasurface DAM. However, the work of this Chapter has increased the size of the unit, in particular its depth to $1.71\lambda_0$, in order to accommodate an extra FSS layer, increasing the modulation order to 8PSK. This is slightly larger than the design requirement, making the unit less suitable for street furniture mounting, though it is still lightweight due to mostly being free space. The size could be reduced by loading the unit with a dielectric, but this is beyond the scope of this thesis.

The FSS DAM unit produced here is, however, still more suited for dense deployment than reflective metasurface DAM, which, despite being an electrically thin surface, requires a feed placed in its farfield, increasing the size of the whole system. Further, this Chapter has now demonstrated 8PSK modulation, equal to that achieved by reflective metasurface

DAM, and reduced its BER performance below 10^{-6}, significantly lower than the 10^{-3} BER demonstrated by [59]. As such, as well as the low power wide area network (LP-WAN) waveforms discussed in the previous chapter such as Sigfox, Weightless-P and Ingenu (Table 2.3), this DAM unit could also reliably transmit EC-GSM-IoT modulation (Table 2.2). The continuous phase nature of the designed unit may also lend itself to producing chirp spread spectrum (CSS) modulation for LoRaWAN communications, though this is uninvestigated.

The greatest improvement of this Chapter over the previous work is the increase in simulated peak efficiency from less than 10% to 46%, with potential to increase to 60% with the use of low loss substrates. This is greater than the typical modelled 30% efficiency of a communications power amplifier (PA), which would likely be even lower in the low complexity, low cost transmitters required for dense deployment of IoT wireless access points, and so this design requirement is met. There is also minimal performance loss over instrument grade conventional modulation, especially when balanced waveforms are used. This improvement in systems using balanced waveforms suggests Ingenu may be the ideal existing IoT standard for deployment of FSS DAM, though it does not lend itself to dense networks.

However, one key requirement of practical wireless transmitters has not yet been demonstrated. Due to spectrum being a limited resource, there are strict limits defined in IoT standards for the amount of bandwidth each frequency channel occupies [154]. These are usually met by passing baseband signals through pulse shaping filters before modulation onto the carrier, removing the discontinuities and sharp transitions which lead to the production of spectral emissions outside the defined channel bandwidth. In this Chapter, the pulse shaping has in effect been provided by the baseband electronics, but they have been designed to produce as close to a square wave representation of the baseband as possible to minimise transmitted EVM. As such, the spectral output is similar to the spectrum of a rectangular function, which is a sinc function, centred at the carrier frequency. Due to the slow decay in the power of a sinc function as the frequency moves away from the carrier frequency, this would not meet the spectral masks of any of the standards discussed here [25, 26]. This could be improved by adding a filter to the control electronics to reduce discontinuities in the bias voltage signal to the DAM unit and so reduce spurious emissions. However, without an equivalent filter at the receiver, this would increase the EVM and so effect the BER performance of the system. As such, future work should evaluate how a filtered control signal to a DAM unit affects the modulated signal in terms of baseband I and Q at the receiver, so some matched filter can be applied there.

5.6 Conclusion

This Chapter has produced a FSS DAM unit capable of producing phase modulation with demonstration up to 8PSK, with only some degradation compared with instrument grade modulation. This allows the production of many IoT waveforms more efficiently than conventional modulation, while using less complex equipment such as a non-linear PA and electronics operating at the symbol rate rather than RF. However, no demonstration of transmitting these IoT signals in non-line-of-sight channels has been presented, and there is some degradation in performance when transmitting non-balanced waveforms. These could be overcome simultaneously by designing a new IoT waveform which makes use of the advantages of FSS DAM while mitigating the disadvantages. This co-design of transmitter technology and communications system could produce a viable solution to providing dense IoT networks, and will be investigated fully in the following Chapter.

Chapter 6

Cyclic Direct Sequence Spread Spectrum for DAM in wideband fading channels

6.1 Introduction

This thesis has so far focussed on the development of frequency selective surface direct antenna modulation (FSS DAM) as a new transmitter technology for the Internet of Things (IoT), and compared it against standard SISO, single-user transmission schemes in line-of-sight channels using PSK modulation. While the FSS DAM units designed and tested are likely capable of reproducing some existing IoT waveforms, it may be that designing a new scheme, which utilises the advantages of FSS DAM and mitigates some of its disadvantages, may produce a more effective solution to the problem of affordable densification of IoT networks. This Chapter will introduce a new transmission scheme for IoT communications capable of operating in broadband fading channels, specifically designed to leverage the advantages of FSS DAM.

The new scheme is based on direct sequence spread spectrum (DSSS), because it has been shown that DAM gains some advantage from using spreading sequences due to the averaging effect of correlating the received signal with the sequence mitigating the distortion of the constellation produced by DAM. To overcome the problem of intersymbol interference (InterSI), where neighbouring spread symbols interfere with each other in broadband channels, a cyclic prefix (CP) is added at the start of each spread symbol. This consists of the final few chips of the spread symbol repeated at the start, in analogy with the CP format used in OFDM [155]. At the receiver, this CP is discarded, leaving spread symbols that have been subject only to intrasymbol interference (IntraSI) from within the spread symbol. This leverages the trend in spreading codes to have better periodic autocorrelation than aperiodic autocorrelation, in addition to eliminating InterSI, at the cost of reduced signal energy due to discarding the CP. When codes with perfect autocorrelation properties are used, and the CP is one less than the length of the channel, InterSI and IntraSI are completely eliminated, improving BER performance considerably.

The new transmission scheme has been named cyclic prefix direct sequence spread spectrum (CPDSSS). While the analysis and experiments here will be single user in order to characterise the new waveform, it could be used for transmitting data to and from large numbers of IoT devices. In this, devices transmit large amounts of stored data to a base station in a small time window, rather than consistent, low data rate communication. This is a high-energy but low-power solution. A contention-based random multiple access system, where devices transmit packets at any time and are informed by the base station whether they have been successfully received or should be retransmitted, could support large numbers of devices proportional to the length of time between packet transmission being required. A downlink transmitter would be required to send these messages, which could use FSS DAM as the modulator to reduce power consumption at this base station. As such, it should be shown that FSS DAM is capable of successfully transmitting data using the CPDSSS waveform.

In the following sections, the CPDSSS system model will be introduced in detail, and an analytical BER performance will be derived. This analysis makes use of established methods for analysing the performance of DSSS systems, but is able to apply the assumptions often used in systems with long spreading codes, of near-perfect InterSI elimination, to spreading codes of similar length to the channel, due to the deterministic nature of the periodic autocorrelation produced by this technique. Simulations will then verify the analysis for binary and polyphase sequences. In particular, the binary codes of the length 4 Barker sequence and the length 7 m-sequence will be considered. These will then be verified experimentally using instrument grade modulation, and finally implemented with a FSS DAM transmitter. This will demonstrate FSS DAM is capable of transmitting information in wideband channels, and contend that dense networks of wireless access points utilising FSS DAM transmitters and CPDSSS modulation is a viable and cost effective solution to supporting increasing numbers of IoT devices.

6.2 System overview

A diagram presenting the basic concept for CPDSSS is shown in Fig. 6.1. A stream of binary data is mapped to complex baseband symbols

$$b(t) = \sum_{i=-\infty}^{\infty} b_k P_{T_b}(t - iT_b) \tag{6.1}$$

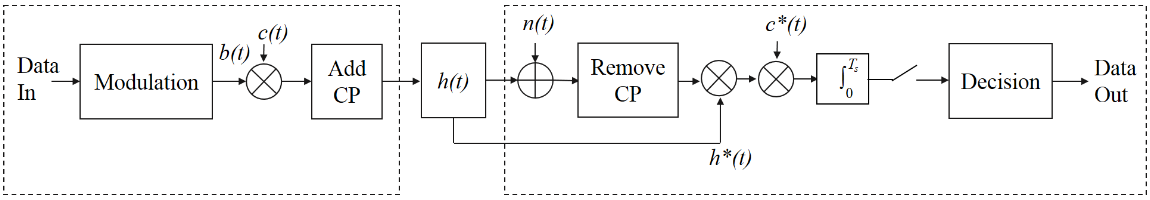

Figure 6.1: Schematic of CPDSSS communications system

where b_k is the kth symbol and $P_{T_b}(.)$ is the symbol pulse shaping function. Here it is assumed that unit rectangular pulses are used. The spreading sequence stream is given by

$$c(t) = \sum_{i=-\infty}^{\infty} c_{i(modN)} P_{T_c}(t - iT_c) \tag{6.2}$$

where c_k is from the length N spreading sequence vector $\mathbf{c} = [c_0, c_1, ..., c_{N-1}]$, which in this thesis may be binary or polyphase, and the chip pulse shaping factor $P_{T_c}(.)$ is again rectangular. After addition of a CP of length Q, the baseband transmitted signal is given by

$$s(t) = \sqrt{2P} b(t) c'(t) \tag{6.3}$$

where P is the transmit power, and the effective cyclic spreading sequence

$$c'(t) = \sum_{i=-\infty}^{\infty} c'_{i(modN+Q)} P_{T_c}(t - iT_c) \tag{6.4}$$

with its values taken from the cyclic spreading code vector

$$\mathbf{c}' = [c_{N-Q}, c_{N-Q+1}, ..., c_{N-1}, c_0, c_1, ..., c_{N-1}] \tag{6.5}$$

of length $N + Q$. The symbol period is $T_s = (N + Q)T_c$ where T_c is the chip period.

The frequency selective channel is modelled as an L-path wideband channel, where all paths are of equal average power and are faded with Rayleigh distribution:

$$h = \sum_{l=0}^{L-1} \alpha_l e^{j\phi_l} \delta(t - \tau_l) \tag{6.6}$$

where α_l describes the Rayleigh distributed amplitude of the lth fading path, ϕ_l describes the phase of the lth path uniformly distributed over $[0, 2\pi)$, and τ_l describes the lth path delay. In this model and commensurate with $P_{T_c}(t)$, the fading paths are assumed to resolve to the chip rate, so τ_l=lT_c. Slow fading is assumed, such that L is constant for all values, and $h(t)$ can be represented by one static vector across each spread symbol, $\boldsymbol{h}$. At the receiver, $n(t)$ is added to the signal to describe the random AWGN process within the receiver, which

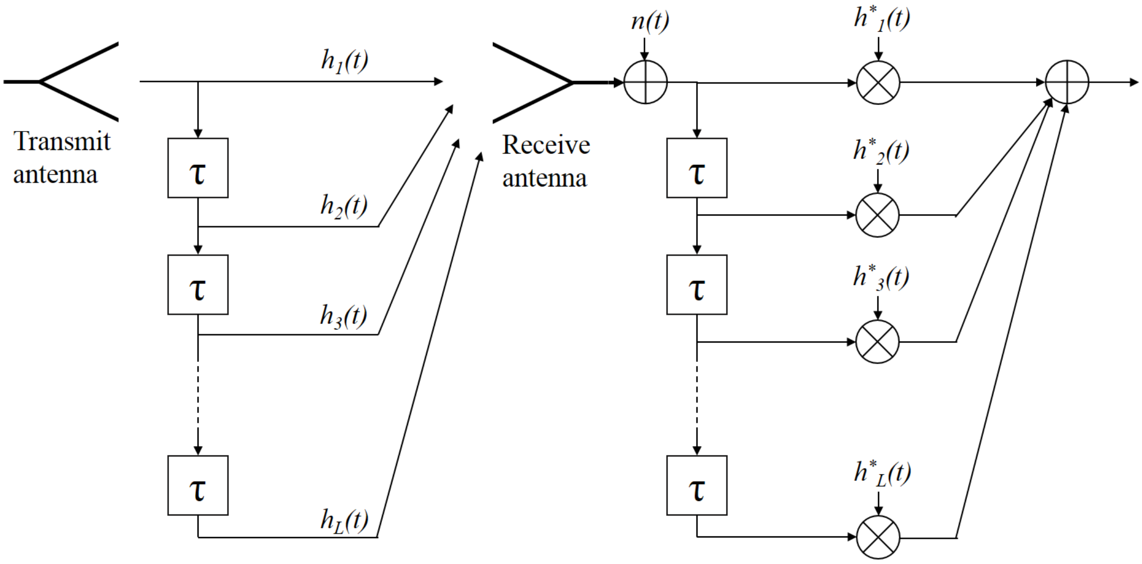

Figure 6.2: Delay profile representation of wideband channel and RAKE receiver

has single-sided spectral density N_0, giving the received signal

$$y(t) = h(t) * s(t) + n(t) \tag{6.7}$$

where $*$ denotes convolution.

This received signal then has the first Q chips, which make up the CP of the system, removed. This has two effects. First, where $Q \geq L$, this removes all InterSI, reducing wideband fading effects to the IntraSI of the self-interfering code. Second, the combination of delays to the signal and the cyclic nature of the CP means each delayed path is effectively a circularly shifted version of the first received path, scaled and rotated in phase by the differing $h_l(t)$. This means the IntraSI- and as such, apart from AWGN, the total interference experienced by single-user CPDSSS- is determined by the periodic autocorrelation function of $\mathbf{c}$. This allows control of the BER performance of CPDSSS through choice of $\mathbf{c}$, and suggests that codes with good periodic autocorrelation properties will perform well in this system.

A RAKE receiver is then used to extract useful energy from each delayed version of the signal, as in Figs. 6.1 and 6.2 (Chapter 2.4). Note that this can be represented in two different ways: as either a multiplication of the received signal vector by the conjugated channel vector $\underline{h}^*(t)$ (Fig. 6.1); or as a set of delayed copies of the signal being multiplied by the appropriate channel delay tap $h_l(t)$, which are then summed together (Fig. 6.2). The equalised chips are then correlated with the length N spreading sequence $c(t)$ to produce a single output symbol, and a decision is made demapping this symbol to digital data.

6.3 BER analysis

In the conventional BER analysis of DSSS systems, it is assumed that sequences are used which are much longer than the length of the channel, such that with reasonable merit factors (MFs) the self-interference produced by wideband channels can be ignored [156]. This is assumed for both IntraSI and InterSI. However, this Chapter is exploring the use of short codes with the protection of a CP. As long as the CP is of length $Q \geq L-1$, it removes all InterSI, and translates the IntraSI from being dependent on the aperiodic autocorrelation to dependence on the periodic autocorrelation. This change allows the use of codes with perfect periodic autocorrelation, such as the length $N=4$ Barker code or polyphase Frank Zadoff Chu sequences, which eliminate all IntraSI. In these situations, the conventional DSSS analysis can be applied accurately to CPDSSS with short, "ideal codes", with a small adjustment in the energy in each symbol due to the discarding of the CP.

Assuming all transmitted symbols are binary, such that $b_k \in \{-1, 1\}$, the transmitted signal can be written as

$$s(t) = \sqrt{2P}x(t) \tag{6.8}$$

where $x(t) = \pm c'(t)$. At the receiver, once the CP has been removed, the signal

$$y(t) = \frac{\sqrt{2P}N}{N+Q}h(t) * x(t) + n(t) \tag{6.9}$$

The factor $\frac{N}{N+Q}$ represents the reduction in power of the received signal due to the discarding of the CP. Note that $Q \geq L-1$ to ensure removal of InterSI and to make the autocorrelation behaviour completely periodic. Once sampled, this signal can be written in vector form for a single spread symbol as

$$\boldsymbol{r} = \frac{\sqrt{2P}N}{N+Q}\boldsymbol{C} \cdot \boldsymbol{h} \cdot b + \boldsymbol{n} \tag{6.10}$$

where $\boldsymbol{h}$ is the column vector of channel taps at time t, $\boldsymbol{n}$ is the noise vector, and $\boldsymbol{C}$ is the circularised code matrix

$$\boldsymbol{C} = \begin{bmatrix} C_1 & C_N & C_{N-1} & \cdots & C_{N-L+2} \\ C_2 & C_1 & C_N & \cdots & C_{N-L+3} \\ C_3 & C_2 & C_1 & \cdots & C_{N-L+4} \\ \vdots & \vdots & \vdots & \ddots & \vdots \\ C_N & C_{N-1} & C_{N-2} & \cdots & C_{N-L+1} \end{bmatrix} \tag{6.11}$$

of size $N \times L$. This matrix captures both the spreading sequence and the circular nature of the delayed channel once the CP has been removed.

Equalisation by multiplication by the channel vector $\boldsymbol{h}$ and correlation with the code $\boldsymbol{c}$ must be represented simultaneously to ensure the cyclic nature of the channel is not ignored, giving the decision variable z

$$z = \frac{\sqrt{2P}N}{N+Q}\boldsymbol{h}^H \cdot \boldsymbol{C}^H \cdot \boldsymbol{C} \cdot \boldsymbol{h} \cdot b + \eta \tag{6.12}$$

where $[\cdot]^H$ is the Hermitian transpose, and η is the noise random variable coloured by equalisation and despreading. Note that multiplying by all of $\boldsymbol{h}$ is equivalent to using a RAKE receiver, as all paths will be taken and summed. Choosing the largest value of $\boldsymbol{h}$ could be examined for evaluating single-path receivers, but this is not done here. The decision variable can be rewritten as

$$z = \frac{\sqrt{2P}N}{N+Q}\boldsymbol{h}^H \cdot \boldsymbol{W} \cdot \boldsymbol{h} \cdot b + \eta \tag{6.13}$$

where $\boldsymbol{W}$

$$\boldsymbol{W} = \begin{bmatrix} W(0) & W(1) & \cdots & W(L-1) \\ W(-1) & W(0) & \cdots & W(L-2) \\ \vdots & \vdots & \ddots & \vdots \\ W(-L-1) & W(-L-2) & \cdots & W(0) \end{bmatrix} \tag{6.14}$$

is the periodic autocorrelation matrix of $\boldsymbol{C}$, with elements $W(\Lambda)$ as defined previously in Chapter 2.4. This can be written in summation form as

$$z = \frac{\sqrt{2P}N}{N+Q} \cdot b \cdot \sum_{l=1}^{L}\sum_{k=1}^{L} h_l^* h_k W(k-l) + \eta \tag{6.15}$$

allowing the desired signal and interference terms to be separated out as

$$z = \frac{\sqrt{2P}N}{N+Q} \cdot \left[N\sum_{l=1}^{L} |h_l|^2 + \sum_{l=1}^{L}\sum_{k=1,k\neq l}^{L} h_l^* h_k W(k-l) \right] \cdot b + \eta \tag{6.16}$$

This shows that the desired signal consists of the sum of the magnitude of the power in all channel paths, scaled by the total signal power and the length of the CP Q relative to the length of the code N. Note also the extra factor N in the desired signal term, which arises from using unit magnitude values of $\boldsymbol{C}$, and so non-normalised autocorrelation values in $\boldsymbol{W}$. The interference, meanwhile, is primarily determined by the periodic autocorrelation function of the code used, scaled by the correlation between two random variables. This means the IntraSI experienced by CPDSSS will be random, but controllable through the choice of spreading sequence. As such, codes with low autocorrelation values over the desired length of the CP should be used to obtain good BER performance in multipath channels. It should also be noted that the interference scales with signal power P, meaning increasing the SNR beyond a certain point will not further reduce the error rate.

When a code with a perfect periodic autocorrelation function is used, this interference term reduces to zero, as

$$W(\Lambda) = \begin{cases} N, & \Lambda = 0 \\ 0, & \Lambda \neq 0 \end{cases} \tag{6.17}$$

for such codes. This reduces the decision variable to

$$z = \frac{\sqrt{2P}N^2}{N+Q} \cdot \sum_{l=1}^{L} |h_l|^2 \cdot b + \eta \tag{6.18}$$

This is equivalent to maximum ratio combining of L diversity branches, and so gives an error probability [157]

$$p_e = \mathbb{E}\left[Q\Big(\frac{2PN^2}{N+Q}\frac{1}{N_0}\sum_{l=1}^{L}|h_l|^2\Big)\right] \tag{6.19}$$

where $Q(\cdot)$ is the Q-function and $\mathbb{E}$ gives the expectation. When the elements of $\boldsymbol{h}$ are independent Rayleigh variables with equal average power $1/L$, this can be written [157]

$$p_e = \Big(\frac{1-\mu}{2}\Big)\sum_{l=0}^{L-1}\binom{L-1+l}{l}\Big(\frac{1+\mu}{2}\Big)^l \tag{6.20}$$

where $\mu = \sqrt{\dfrac{SNR}{1+SNR}}$, where the signal-to-noise ratio SNR is given by

$$\begin{aligned} SNR &= \frac{2PN^2}{L(N+Q)} \cdot \frac{1}{N_0} \\ &= \frac{E_b}{N_0} \cdot \frac{N}{L(N+Q)} \end{aligned} \tag{6.21}$$

Note that this includes both an offset in SNR for the removal of the CP of $\dfrac{N}{N+Q}$, and shows that the received energy is split equally over all channels with the factor $1/L$.

The final calculated BER for binary CPDSSS signalling in various length channels using a code of $N = 4$ with perfect autocorrelation properties, namely the length 4 Barker code $[1, 1, 1, -1]$, are shown in Fig. 6.3. The BER where $L = 1$ is equivalent to the BER of binary signalling in Rayleigh fading, as is expected. As the number of paths increases, the error rate improves. This is due to the increase in receive diversity: as the different paths are equal power but varying independently, as the number of paths increases the chance of all paths

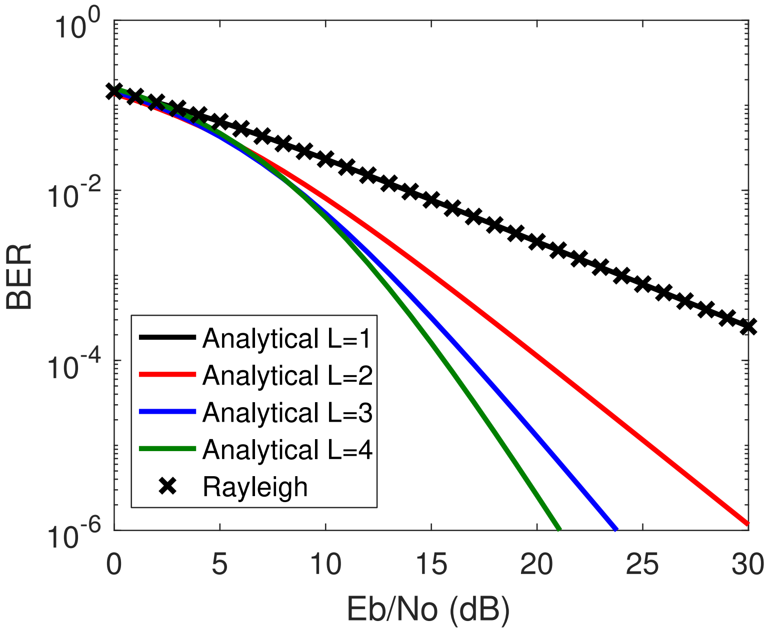

Figure 6.3: Analytical BER of binary CPDSSS with an ideal code $N = 4$ with for different channel lengths L

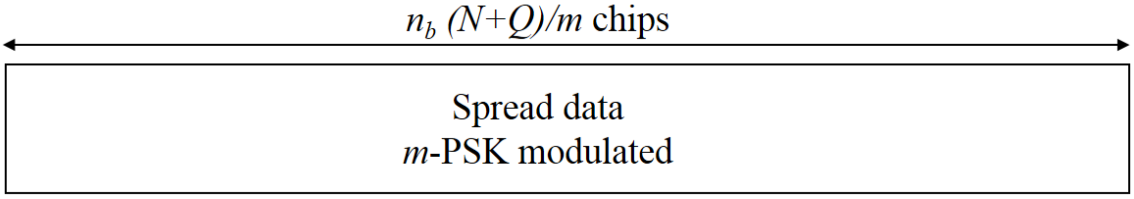

Figure 6.4: Structure of data packet under test in simulated CPDSSS system

having low power decreases, so reducing the chance of an error. However, the amount of improvement from increasing L decreases as L decreases. The RAKE receiver also aids the diversity gain by ensuring that all of the signal energy arriving at the receiver contributes to the final symbol. Due to the elimination of self-interference from the wideband channel, this is analogous to having L receive antennas using maximum ratio combining techniques in a narrowband channel, but with an $\frac{L}{L+Q}$ penalty on the $\frac{E_b}{N_0}$ due to the discarding of the CP. This analysis can be extended to longer perfect sequences, though this requires polyphase sequences, such as the Frank Zadoff Chu sequences, to be used. As such, this extension is left to further work.

6.4 Simulations

Simulation of the above CPDSSS system was performed in MATLAB using the script in Appendix E. The channel $\underline{h}(t)$ is simulated as a length L vector of complex Gaussian values

Type	Length	Values
Barker	4	$[1, 1, 1, -1]$
m-sequence	7	$[1, 1, 1, -1, -1, 1, -1]$
Barker	11	$[1, 1, 1, -1, -1, -1, 1, -1, -1, 1, -1]$

Table 6.1: Table of spreading sequences used in this Chapter

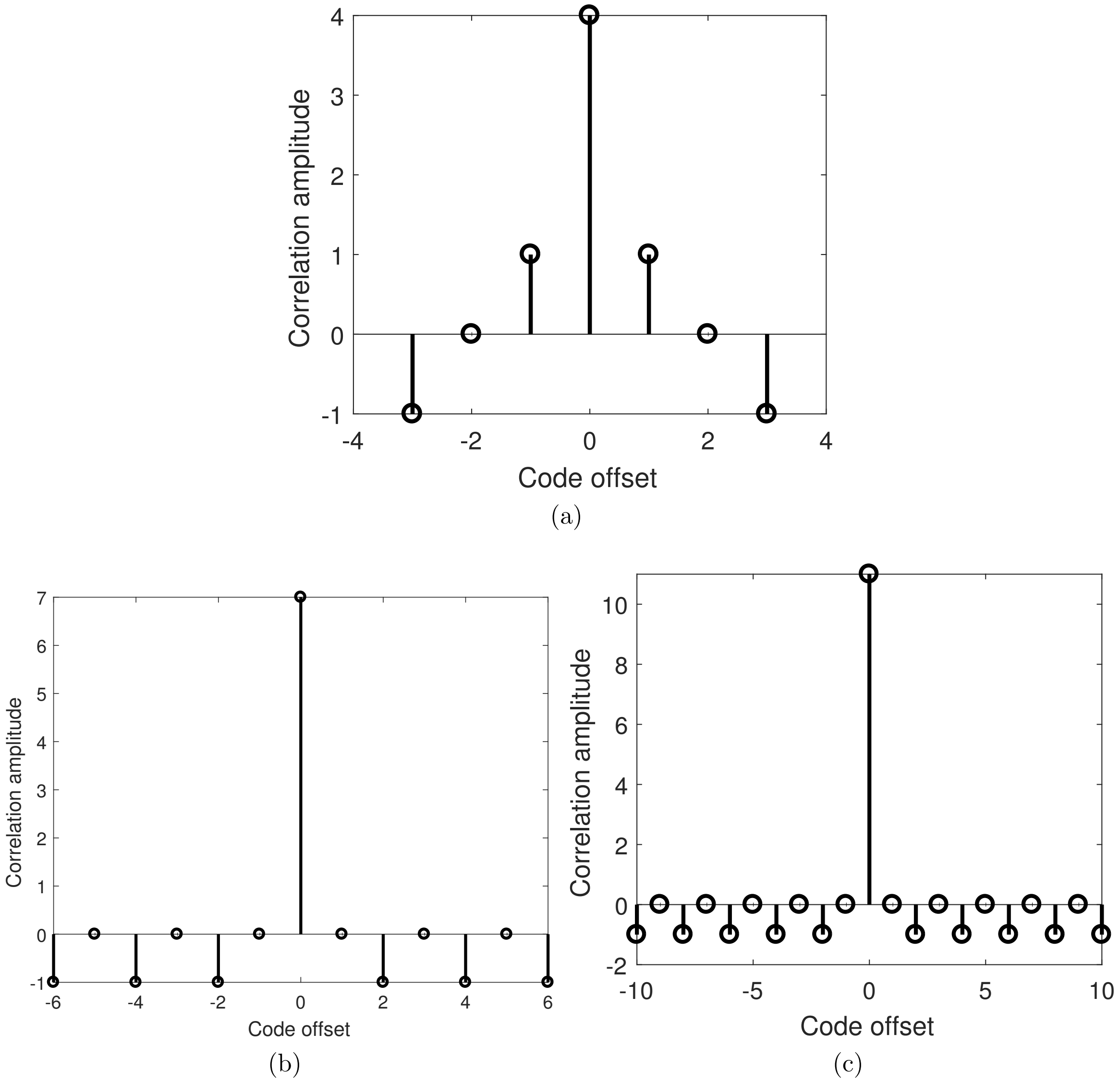

(a)

(b)

(c)

Figure 6.5: Aperiodic autocorrelation functions of sequences under test in this Chapter

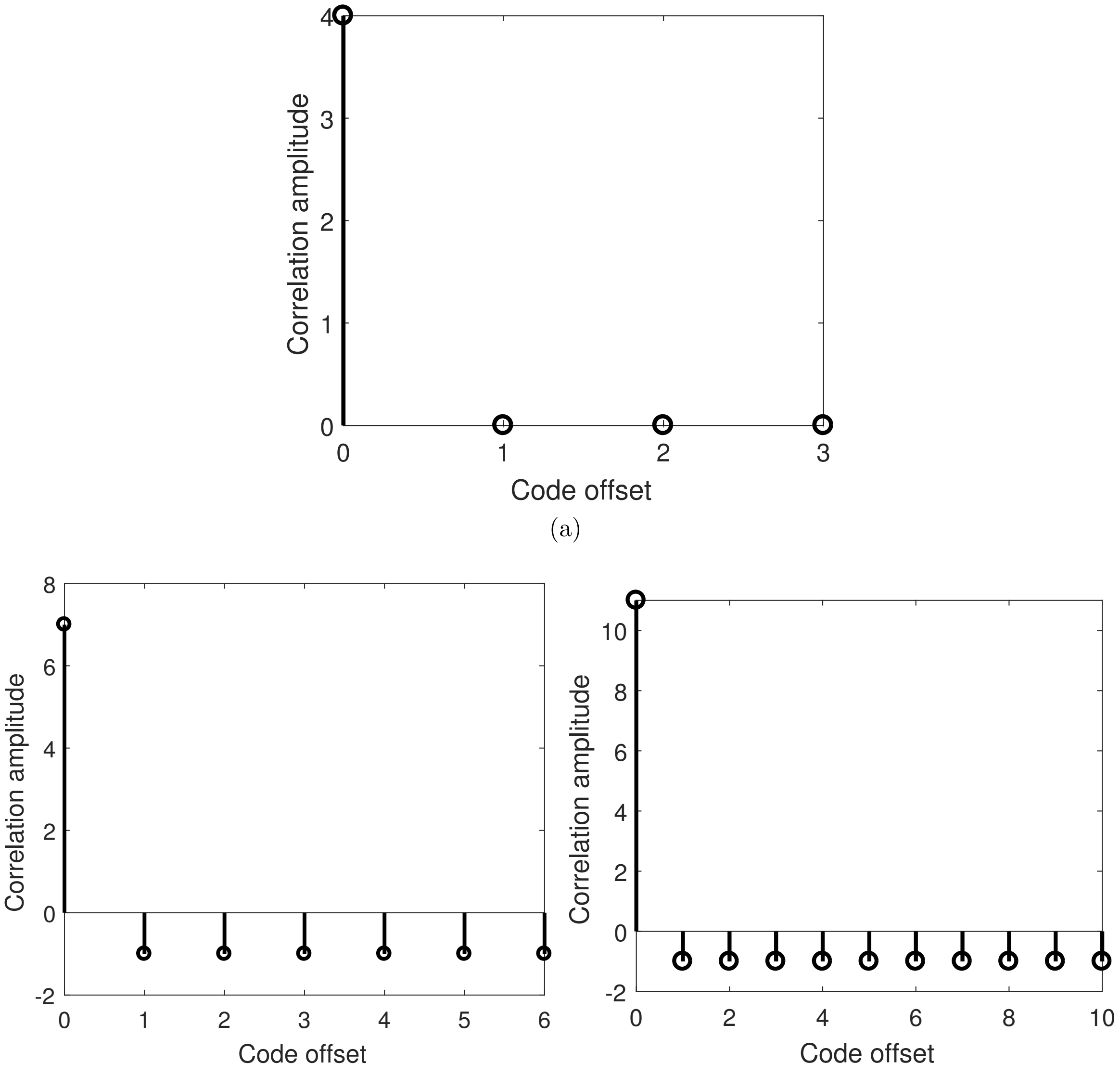

(a)

(b)

(c)

Figure 6.6: Periodic autocorrelation functions of sequences under test in this Chapter

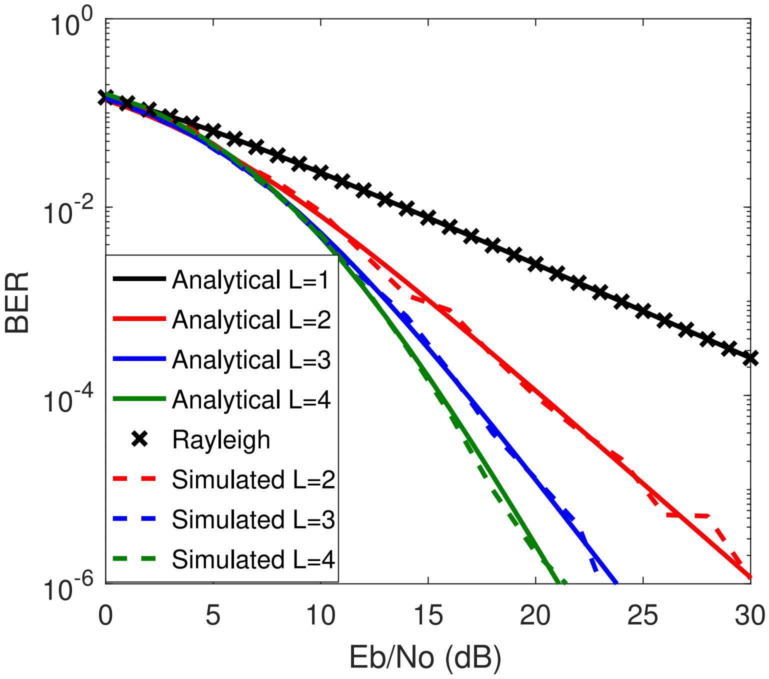

Figure 6.7: Analytical and simulated BER of binary CPDSSS with a Barker code $N = 4$ for different channel lengths L

varying independently, though static over the length of a packet. The channel values are randomly assigned for each transmitted packet, and perfect knowledge of the channel at the receiver is assumed. For consistency with modulation orders that can be achieved with FSS DAM, BPSK, QPSK and 8PSK modulation are considered in this Chapter. Each packet consists of $n_b = 1002$ bits of data spread by the length N sequence (Fig. 6.4). For reference, the spreading sequences used are presented in Table 6.1, and their aperiodic autocorrelation functions are plotted in Fig. 6.5, while their periodic autocorrelation functions are plotted in Fig. 6.6.

6.4.1 CPDSSS with binary sequences

The perfect binary sequence

As mentioned previously, only one binary sequence with perfect periodic autocorrelation properties exists- the length $N = 4$ Barker code (Table 6.1). As such, this code will be the first examined through simulation. First, for comparison with the above analysis, the effect of different length channels on binary CPDSSS (BPSK), where $Q = L - 1$, is explored (Fig. 6.7). This shows good agreement with the analysis, validating the simulation for the case of ideal sequences.

Simulation is then used to explore the effects of using CPDSSS in comparison with conventional DSSS with longer codes. First, a CPDSSS system using a Barker code of

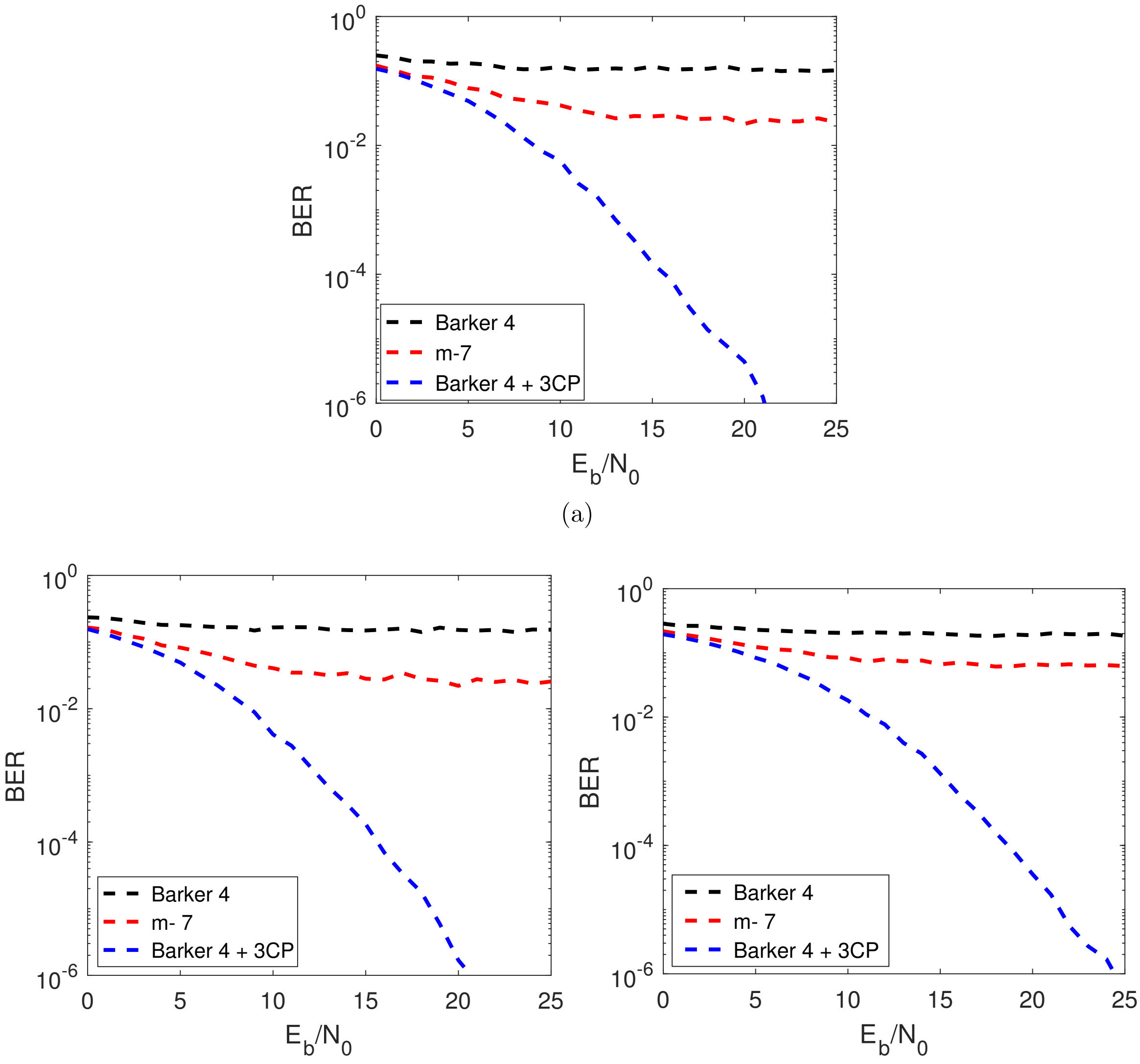

(a)

(b)

(c)

Figure 6.8: Simulated bit error rates for conventional DSSS system with RAKE receiver in wideband channel $L = 4$ versus equivalent length CPDSSS system in same channel. (a) BPSK, (b) QPSK, (c) 8PSK

length $N = 4$ in a length $L = 4$ channel is explored. As the CP length $Q = L - 1 = 3$, the CPDSSS transmitted signal can also be thought of as having been spread by a length 7 sequence. For comparison a length $N = 7$ m-sequence, which also has the properties of a Barker sequence when in its least sidelobe energy phase, is used, with simulated BER curves shown in Fig. 6.8. Note that here a RAKE receiver with the same number of fingers as the channel length $L = 4$ is used. For all modulation orders, the conventional DSSS system encounters an error floor at around 10^{-1} for the length 4 Barker sequence and between 10^{-2} and 10^{-1} for the length 7 m-sequence. However, when a CP of length 3 is added to the length 4 sequence, the BER becomes reducible to below 10^{-6}. Note also that the reduction in error rate requires a lower average $\frac{E_b}{N_0}$ than in the Rayleigh case (Fig. 6.3), suggesting that increasing a system's symbol rate to obtain wideband fading and so exploit time diversity effects with CPDSSS is advantageous.

In IoT schemes, another important factor is the PER, which will determine the throughput of the system. The simulated results for this are shown in Fig. 6.9, using the packet design in Fig. 6.4. The increase in code length for conventional DSSS improves the PER notably, but CPDSSS is required in order to bring the PER below 10^{-2} with short codes. This means an IoT CPDSSS system would only rarely have to retransmit a failed packet when a reasonable average SNR is achieved.

This work demonstrates that for wideband fading channels of $L \leq 4$, the length 4 Barker sequence in a CPDSSS system can provide reliable transmission of data at reasonable values of $\frac{E_b}{N_0}$. Extension of this concept to polyphase perfect sequences is left for future work.

Imperfect binary sequences

However, other than the length 4 Barker sequence, all other binary sequences have periodic autocorrelations with non-zero sidelobes. This means that for any path lengths $L > 4$ these longer, imperfect sequences must be used. In these cases, while the CP removes any InterSI, IntraSI still occurs within each spread symbol. This interference is determined by the periodic autocorrelation of the sequence used, and the channel response of each path. In order to investigate the effect of this IntraSI on the performance of CPDSSS, simulation was performed using a length $L = 5$ channel with equal average power in each path and independent Rayleigh fading on each path. A CPDSSS system using the length $N = 7$ m-sequence and a CP of length $Q = L - 1 = 4$ is compared against a conventional DSSS system using the $N = 11$ Barker sequence and the $N = 7$ m-sequence.

Fig. 6.10 shows the simulated BER performance of this setup. Fig. 6.10a shows the robustness of BPSK in reducing the BER of conventional DSSS with $N = 11$ to 4×10^{-6}. However, CPDSSS of equivalent length performs even better, reaching this BER with an $\frac{E_b}{N_0}$

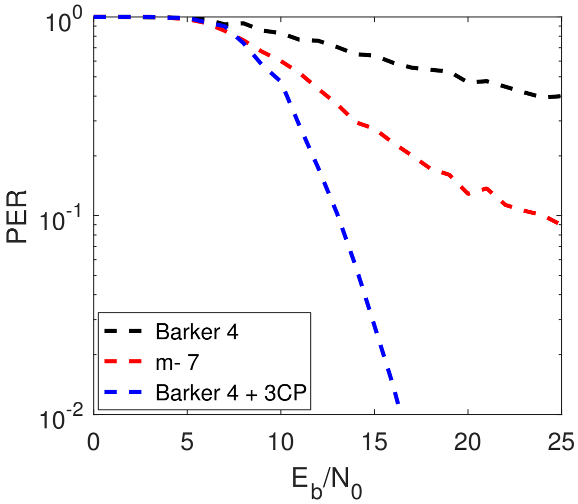

(a)

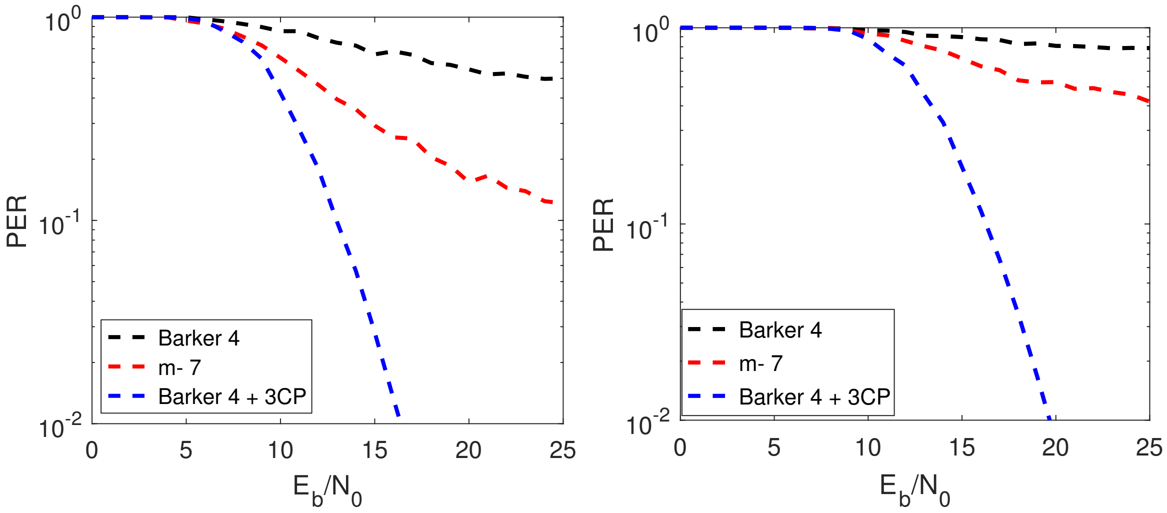

(b)

(c)

Figure 6.9: Simulated packet error rates for conventional DSSS system in wideband channel $L = 4$ versus equivalent length CPDSSS system in same channel. (a) BPSK, (b) QPSK, (c) 8PSK

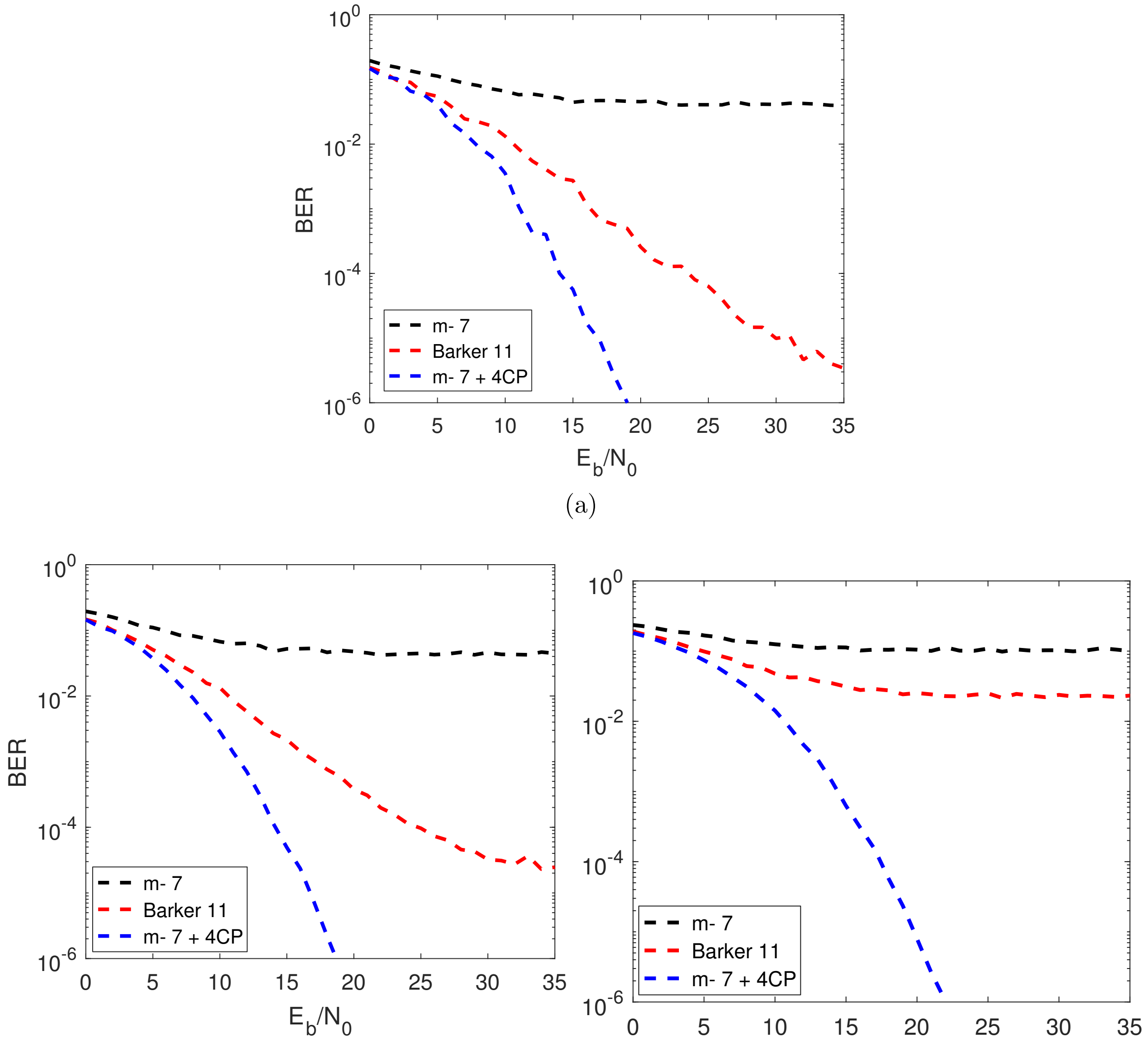

(a)

(b)

(c)

Figure 6.10: Simulated bit error rates for conventional DSSS system in wideband channel $L = 5$ versus equivalent length CPDSSS system in same channel. (a) BPSK, (b) QPSK, (c) 8PSK

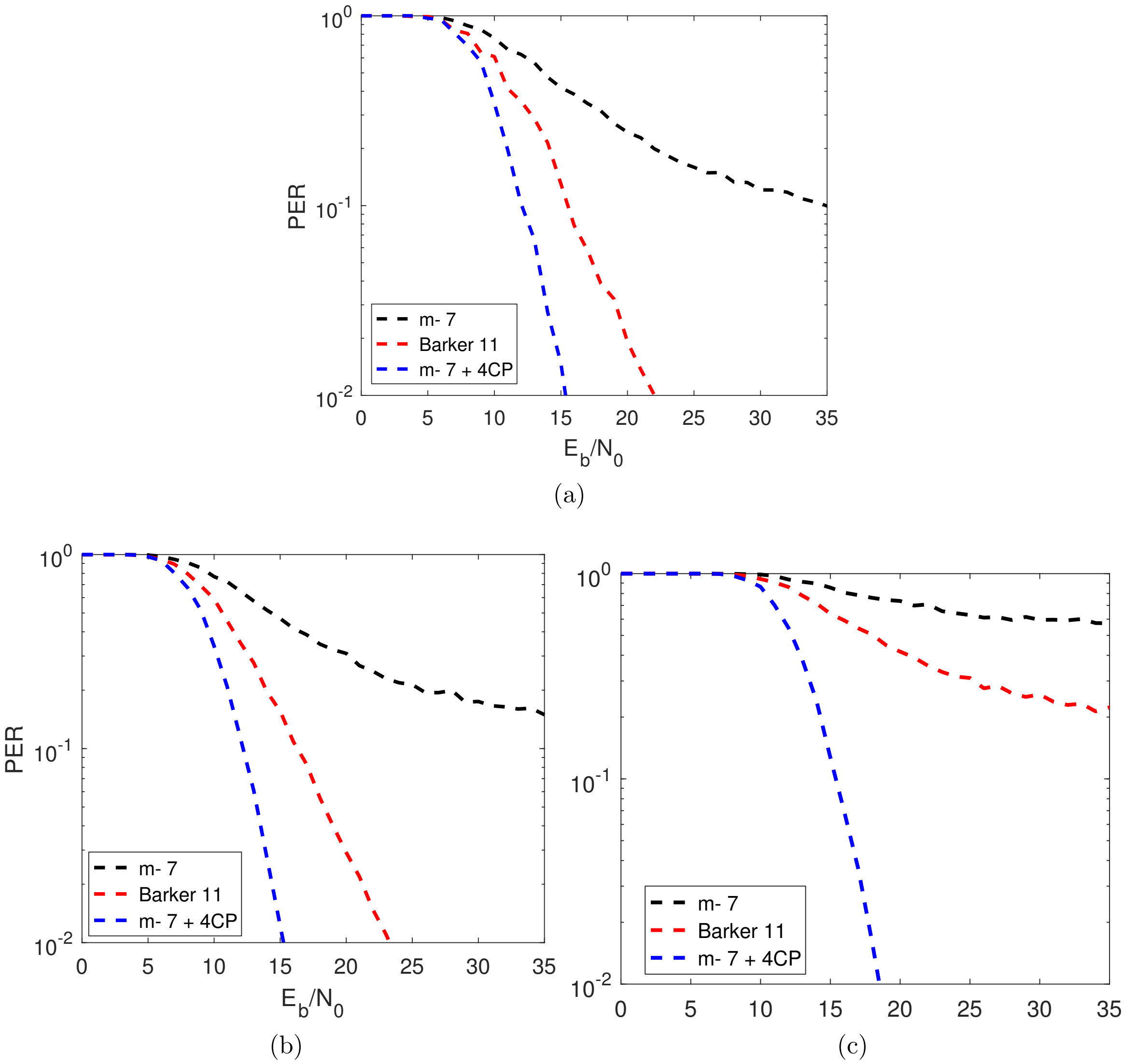

(a)

(b)

(c)

Figure 6.11: Simulated packet error rates for conventional DSSS systemin wideband channel $L = 5$ versus equivalent length CPDSSS system in same channel. (a) BPSK, (b) QPSK, (c) 8PSK

16dB lower. This effect is shown for QPSK (Fig. 6.10b) and 8PSK (Fig. 6.10c), though in these cases the BER of conventional DSSS do not go below 10^{-5} and 10^{-2} respectively. This shows that despite the introduction of intrasymbol interference from non-ideal spreading sequences, CPDSSS is still able to reduce the BER performance below 10^{-6} reliably with short spreading codes in wideband channels, even with higher order modulation. This is further confirmed with the PER simulated results in Fig. 6.11.

6.5 Experimental implementation of conventional CPDSSS

In order to further evaluate the performance of CPDSSS, it was implemented in an end-to-end quasi-real-time communications system. The principle aim was to validate the simulation

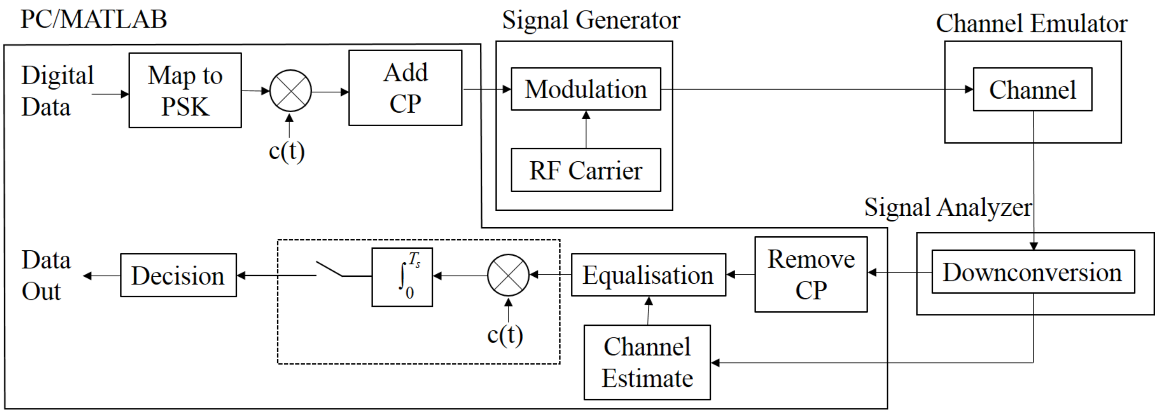

Figure 6.12: Schematic of experimental testbed for evaluating CPDSSS in multipath channels using conventional modulation

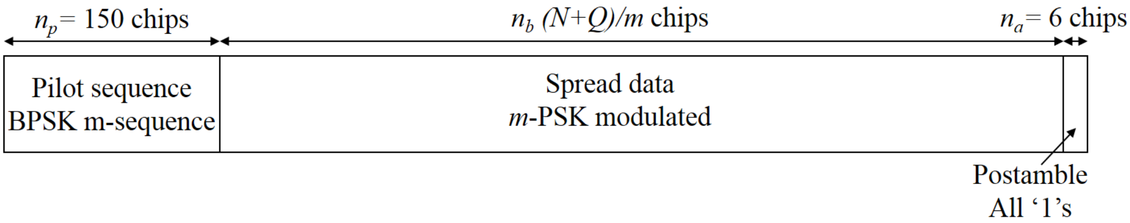

Figure 6.13: Packet construction for experimentally evaluating CPDSSS

results, and also to provide a benchmark for CPDSSS with instrument grade modulation for comparison with the system using FSS DAM. As such, the carrier frequency used for the below experiments was 1.8GHz.

6.5.1 Testbed development

The CPDSSS communications system described previously in Fig. 6.1 was developed into an experimental testbed (Fig. 6.12). A PC running MATLAB was used to generate $n_b = 1002$ bits binary data, map it to PSK symbols as complex numbers, spread the symbols with spreading sequence $c(t)$ of length N, add a CP of length Q and assemble a packet. The value of n_b was chosen as a small packet as with many IoT protocols, while being divisible by the different modulation orders used, $m = 1, 2, 3$. The pilot sequence was a length 15 m-sequence repeated 10 times to ensure good channel estimation, providing $n_p = 150$ chips to the packet. Finally, a postamble of $n_a = 6$ chips, all symbols of value all 1s, was added to the end of the packet to allow for some propagation delay through the system. The packet construction is shown in Fig. 6.13, and the MATLAB code used for these processes is found in Appendix E.

This packet was then sent digitally via a GPIB link to a Rohde & Schwarz SMBV100a Signal Generator, which modulates the data onto a radio carrier wave with frequency 1.8GHz

Bandwidth	26MHz
Carrier range	400 - 2700MHz
Output power range	-110 - -30dBm
Noise floor	-167dBm
Delay resolution	0.1ns
Power resolution	0.01dB
Phase resolution	0.1^o

Table 6.2: Key RF specifications of Spirent 5500 Channel Emulator

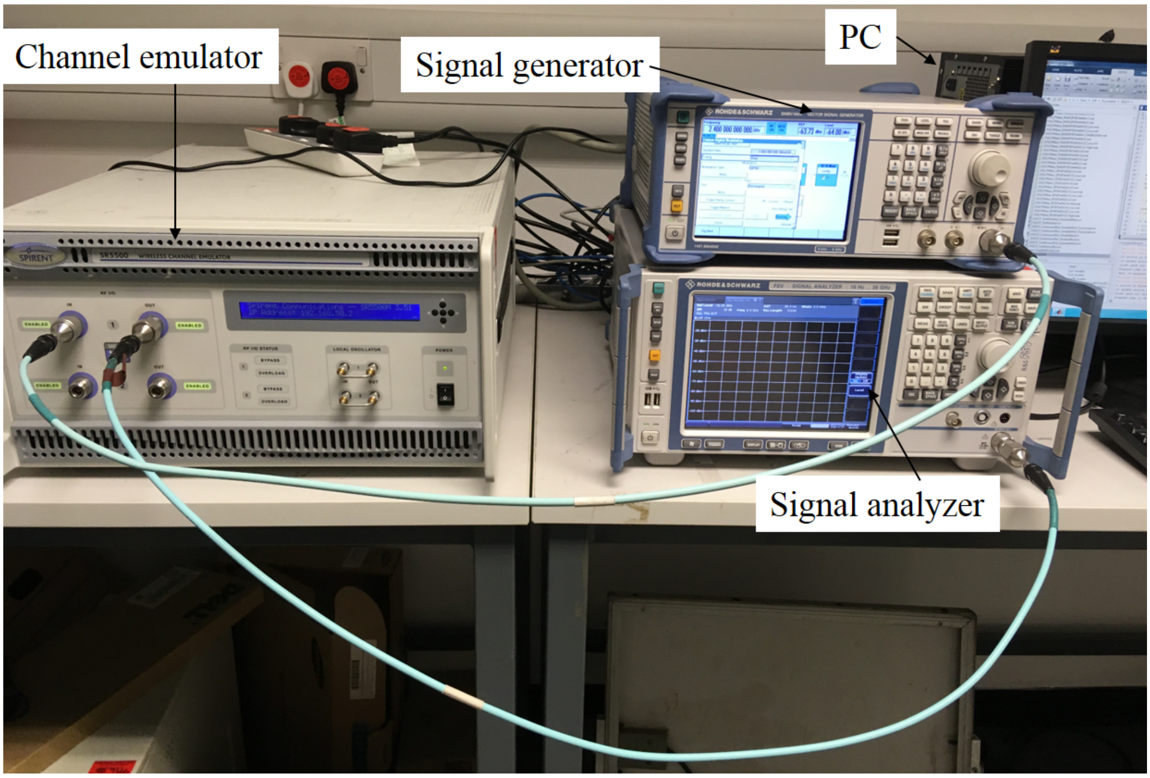

Figure 6.14: Photograph of experimental setup for CPDSSS with conventional modulation

at a chip rate of 1Mchip/s. This modulated signal passes along a coaxial cable to a Spirent 5500 Channel Emulator (Table 6.2). Following procedures outlined in Appendix F, this was set up to provide a multipath channel with L paths, with a delay of $l\mu$s to provide a single chip delay for each path. Each path was an independently varying Rayleigh channel with equal gain $1/L$, and the minimum allowed Doppler variation, of 0.1Hz, chosen to avoid fast-fading effects in the channel. As each packet takes between 6s and 14s to process and transmit fully, even this slow variation leads to a thorough sampling of a slow Rayleigh channel.

The output of the Channel Emulator is connected by coaxial cable to a Rohde & Schwarz FSV Spectrum Analyzer, which downconverts and samples the incoming signal at twice the chip rate. It should be noted that there is a variable propagation delay of between 3μs and

Code type	Code length N	CP length Q	Code
Barker	4	0	1, 1, 1, -1
m-sequence	7	0	1, 1, 1, -1, -1, 1, -1
Barker	4	3	1, 1, -1, 1, 1, 1, -1

Table 6.3: Combinations of code

4μs through the Channel Emulator, so as such the Spectrum Analyzer is only triggered by the Signal Generator to start sampling the incoming signal 3 chips into the packet. This sampled baseband IQ is then sent digitally via GPIB to the PC, where MATLAB processes the received signal to achieve chip-level synchronisation and estimate the channel using the pilot sequence, equalise the packet, remove the CP, correlate the signal with $c(t)$ and finally demap the signal to a stream of binary data, which is checked against the original data stream for errors. The transmit power is varied to control the E_b/N_0, and a successful measurement at each transmit power is only accepted after at least 60 packet errors have been found. This ensures fair sampling of the multipath channel for each E_b/N_0. A photograph of the experimental setup is shown in Fig. 6.14, and operating procedures for the Rohde & Schwarz equipment are found in Appendix C.

6.5.2 The perfect binary sequence

The first scenario examined by this experimental setup was that explored through simulation in Section 6.4.1. Here, the only binary sequence with perfect periodic autocorrelation properties, the $N = 4$ Barker sequence, was used in a length $L = 4$ channel, both with and without a CP of length $Q = L - 1 = 3$. For comparison, the $N = 7$ Barker or m-sequence was used with no CP added (Table 6.3). Note that E_b/N_0 in the measured case was calculated through measuring the average received signal strength for each packet construction at a transmit power of -30dBm, the maximum input power accepted by the Channel Emulator, over 100 packets; compared with the measured average received power over 100 packets when no signal was input into the Channel Emulator while the receiver is expecting the same packet construction.

In the case where $m = 1$ and the CP is used, direct comparison can be made between measured, simulated and analytical BER performance (Fig. 6.15a). This shows good agreement between all three, with negligible difference between analytical and simulated performance at all E_b/N_0 values under test, and a maximum deviation of 0.8dB between measured BER and the other two rates up to 10^{-4}. This small deviation varies either side of the simulated and analytical BER curves, so can be assumed to be largely due to statistical effects, with only 60 packet errors required for a BER measurement to be valid as opposed to 500 packet errors

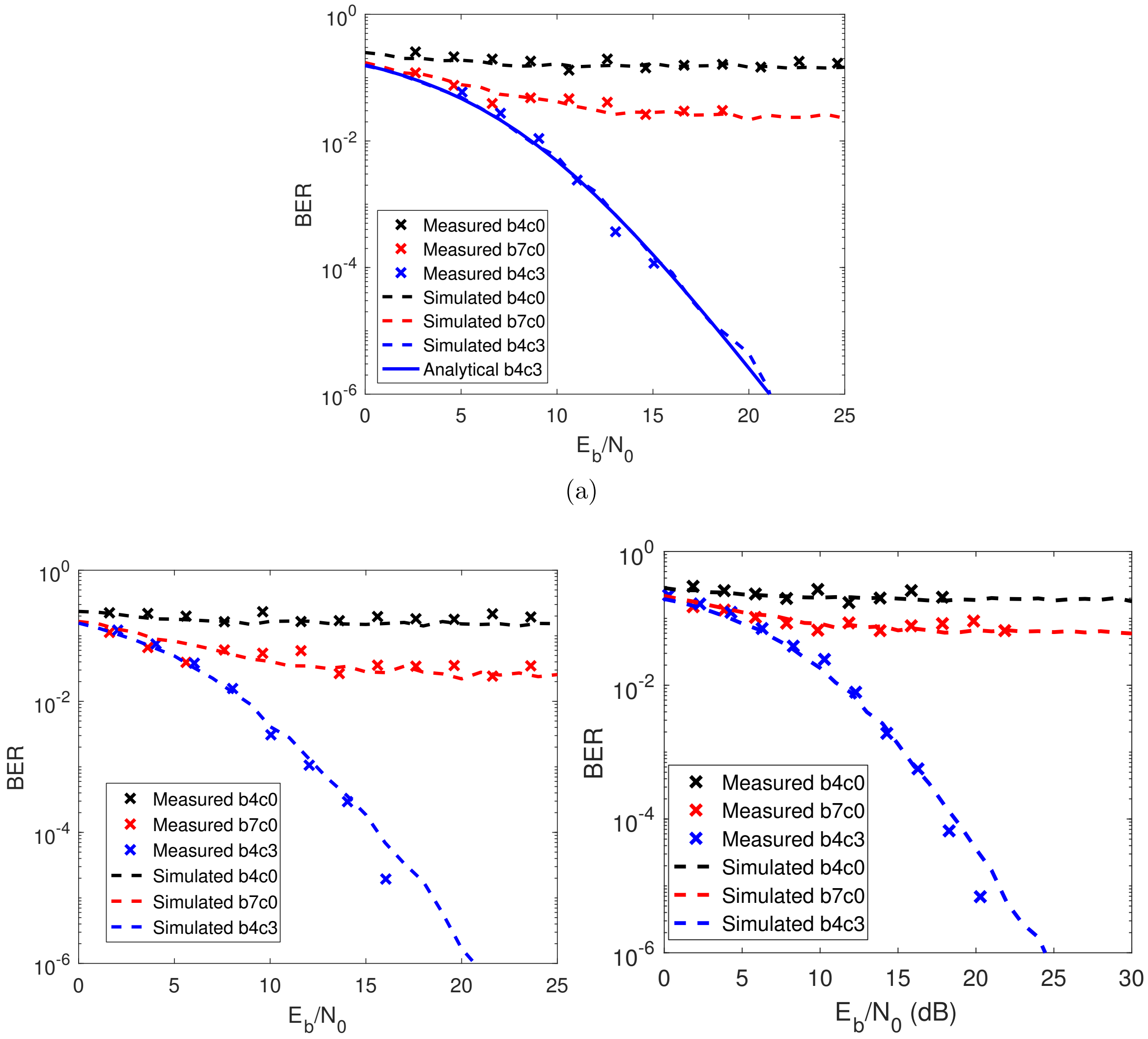

(a)

(b)

(c)

Figure 6.15: Measured (crosses), simulated (dashed lines) and analytical (solid lines, BPSK only) bit error rates for conventional DSSS system in wideband channel $L = 4$ versus equivalent length CPDSSS system in same channel. (a) BPSK, (b) QPSK, (c) 8PSK

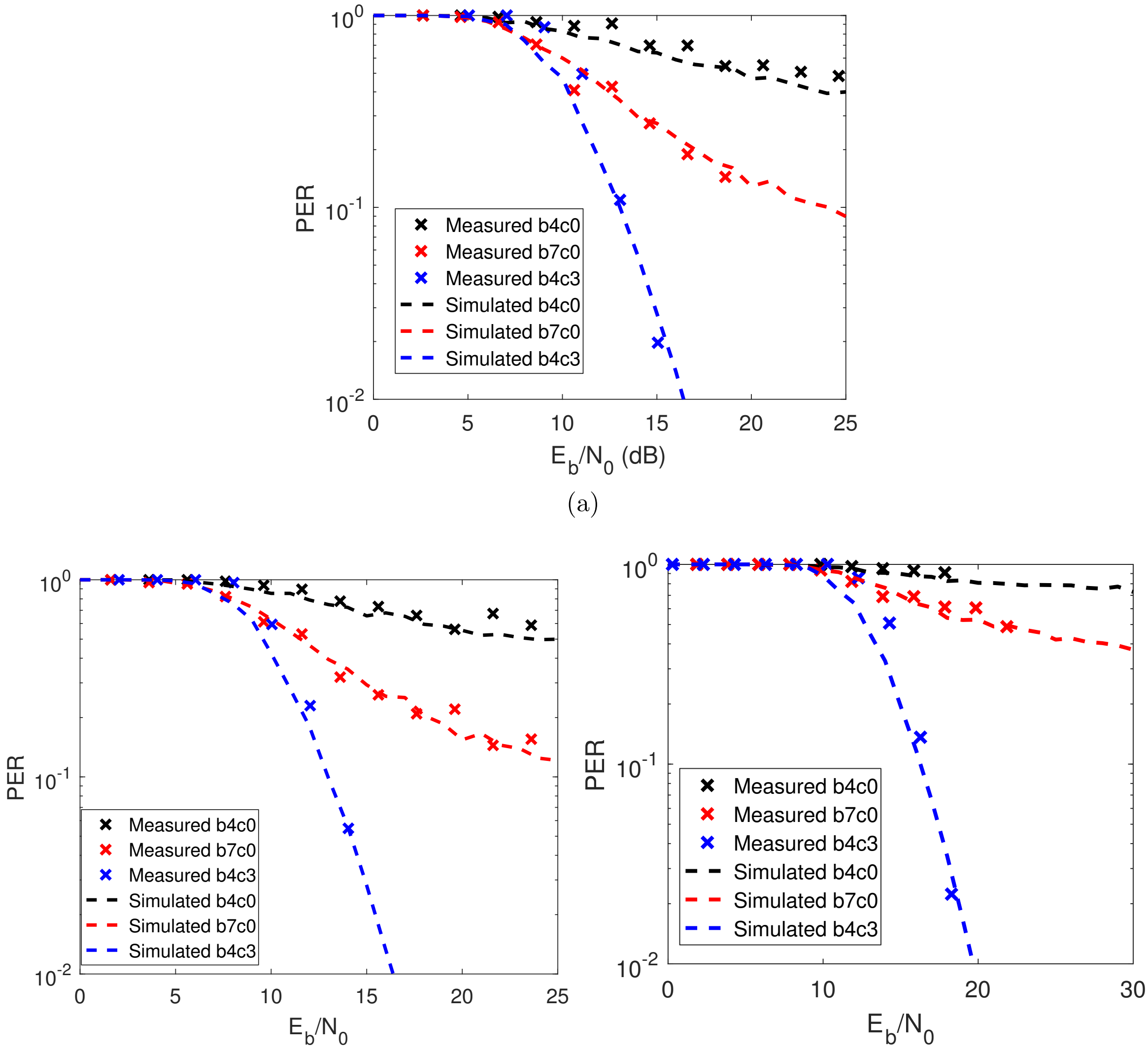

(a)

(b)

(c)

Figure 6.16: Measured (crosses), simulated (dashed lines) and analytical (solid lines, BPSK only) packet error rates for conventional DSSS system in wideband channel $L = 4$ versus equivalent length CPDSSS system in same channel. (a) BPSK, (b) QPSK, (c) 8PSK

in simulation and a perfectly known distribution in the analysis. Measurement of BER for the other modulation orders and comparison experiments is also consistent with simulation (Fig. 6.15), with a maximum deviation of 1.5dB between the BER measurement at 7×10^{-6} and the simulated equivalent. The largest deviation in the QPSK BER measurement was also at low BER, suggesting it may be due to statistically less significant results causing deviation in the measured error rate. Confirmation of this through transmitting in the order of 10^4 packets at these high E_b/N_0 values is left for future work.

This inaccuracy at low BER does not seem to extend to the PER measurements (Fig. 6.16), though this may be because the offending points are below the 1% threshold examined here. As such, in practical schemes the difference between such small BERs will have only a slight effect on performance. The greatest deviation from the simulated performance is

Code type	Code length N	CP length Q	Code
m-sequence	7	0	1, 1, 1, -1, -1, 1, -1
Barker	11	0	1, 1, 1, -1, -1, -1, 1, -1, -1, 1, -1
m-sequence	7	4	-1, -1, 1, -1, 1, 1, 1, -1, -1, 1, -1

Table 6.4: Combinations of code

1dB in 8PSK at a PER of 0.47, but this then reduces to 0.5dB in the other direction at 0.02 PER, suggesting this is probably a statistical blip. As such, the performance improvement of using a CP with the perfect binary sequence in relatively long, strong wideband channels has been validated through experiment, showing that BER can be reduced below 10^{-4} and PERs below 10^{-2} for a variety of PSK modulation orders.

6.5.3 Imperfect binary sequences

The performance of imperfect binary sequences in CPDSSS systems in wideband multipath channels should also be validated through experiment. Using the same testbed as in the previous Subsection, a channel with $L = 5$ taps, each with equal gain, was implemented by the Channel Emulator. The sequence used was the $N = 7$ m-sequence, which, as mentioned previously, is also a Barker sequence, and a CP of $Q = 4$ was used. This was compared with conventional DSSS systems with the $N = 7$ m-sequence, and with the $N = 11$ Barker sequence, which has the same length as CPDSSS with $N = 7$ and $Q = 4$ (Table 6.4).

The measured BER performance of these systems is shown in Fig. 6.17 for BPSK, QPSK and 8PSK modulation, compared with the expected performance through simulation. Good agreement is shown between measured and simulated performance in all cases. Using DSSS with $N = 11$, BPSK and QPSK are shown to reach a BER of 10^{-4}, though from simulation this is expected to reach error floors soon after. There is also clear improvement over DSSS with $N = 11$ in these cases, by 6dB and 10dB for a BER of 10^{-4} for BPSK and QPSK, respectively. For 8PSK, as with simulation the error floor for conventional DSSS in this channel is 9.5×10^{-2} and 1.9×10^{-2} for $N = 7$ and $N = 11$ respectively, while CPDSSS is shown to allow reduction below 10^{-4} BER. The maximum deviation was 1.7dB, in the 8PSK case at a BER of 2.5×10^{-5}, which can reasonably be said to be due to statistical variation in the sampling of the channel by the experiment.

This relationship is consistent when the PER measurements are considered. Again agreement is good in the majority of cases, though drift of up to 1dB occurs in the BPSK DSSS measurement with $N = 11$. For measurement of CPDSSS, the points of crossing the 1% PER are very closely aligned with simulation, with maximum deviation of 1dB. Further, for all modulation orders measurements were taken below this threshold, suggesting it is a

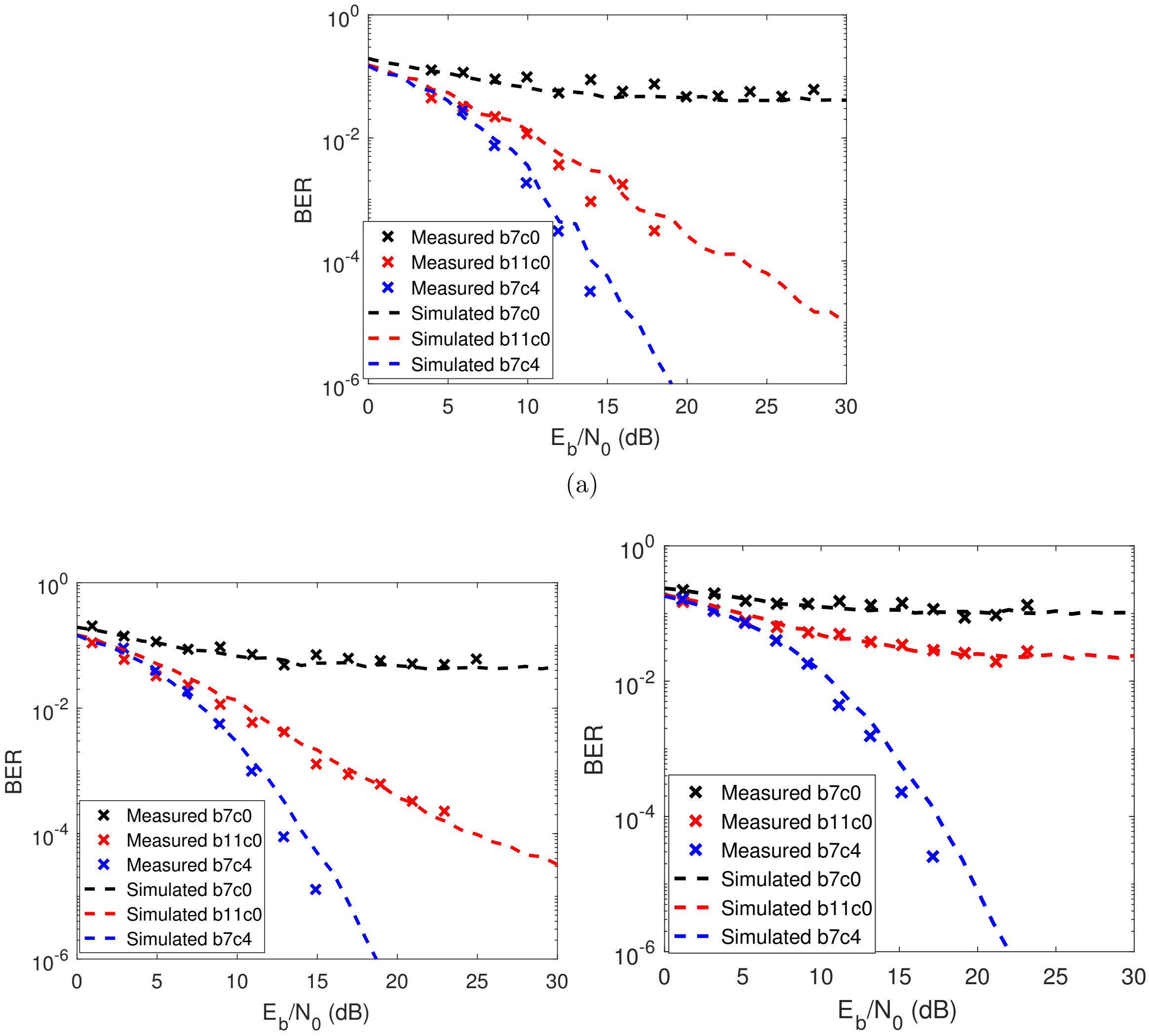

(a)

(b)

(c)

Figure 6.17: Measured (crosses) and simulated (dashed lines) bit error rates for conventional DSSS system in wideband channel $L = 5$ versus equivalent length CPDSSS system in same channel. (a) BPSK, (b) QPSK, (c) 8PSK

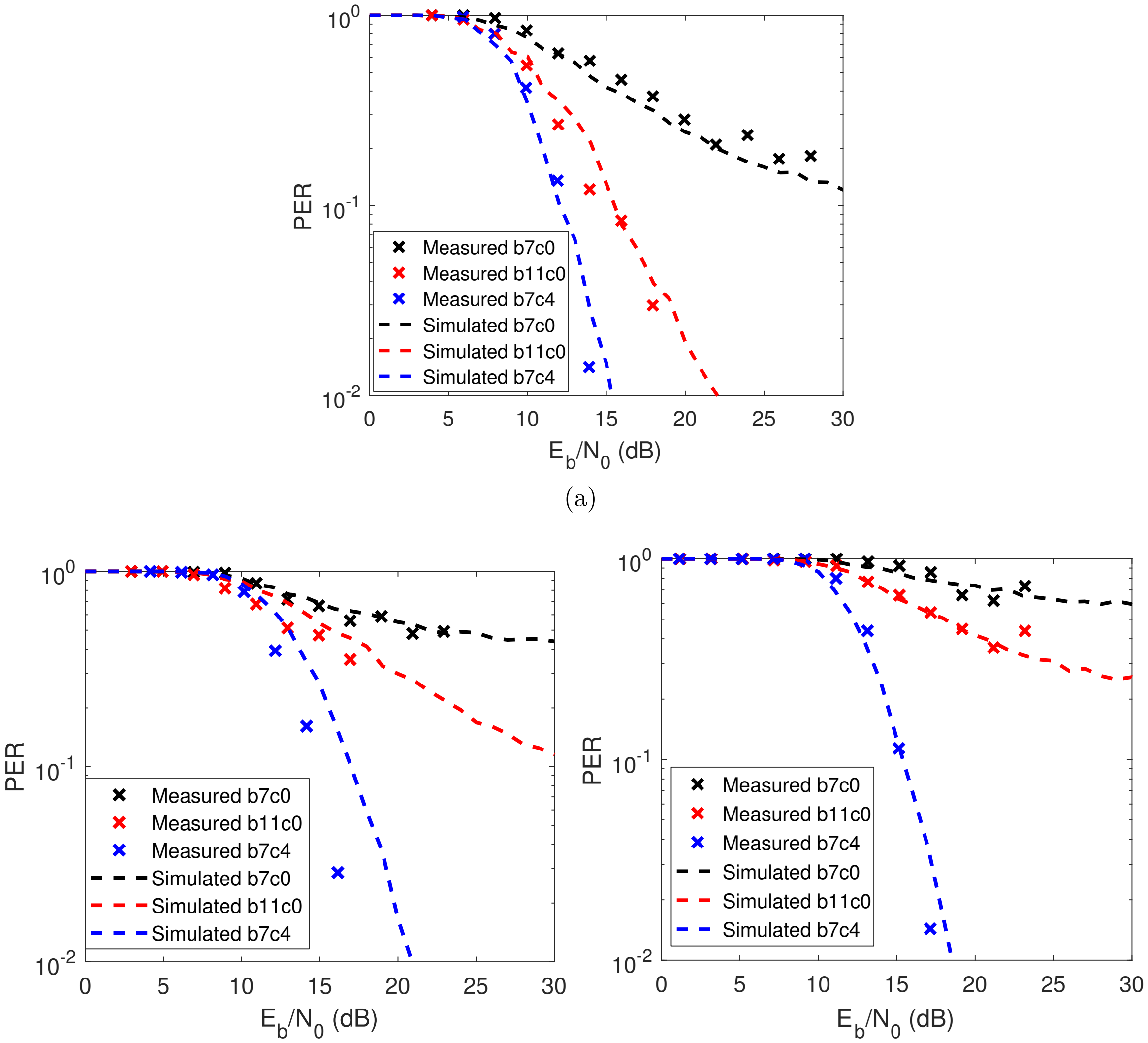

(a)

(b)

(c)

Figure 6.18: Measured (crosses) and simulated (dashed lines) packet error rates for conventional DSSS system in wideband channel $L = 5$ versus equivalent length CPDSSS system in same channel. (a) BPSK, (b) QPSK, (c) 8PSK

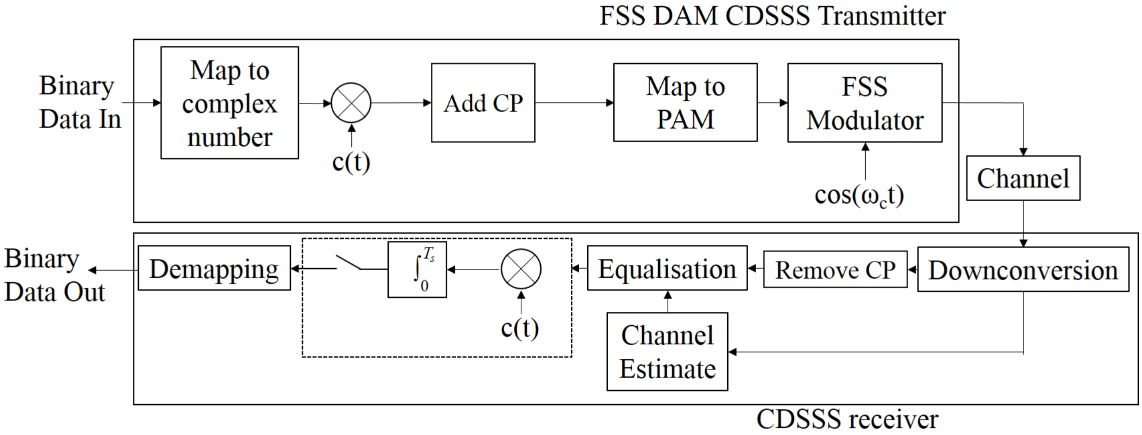

Figure 6.19: Schematic of CPDSSS communications system with a DAM transmitter

suitable transmission scheme for wideband IoT channels.

This Section has experimentally implemented a CPDSSS communications in a quasi-real-time testbed, using BPSK, QPSK and 8PSK modulation. Good agreement has been shown between simulated and experimental results, with CPDSSS reducing the PER below 10^{-2} with both perfect and imperfect binary sequences in the situations examined. The BER was found to reduce comfortably below 10^{-4}, in all cases. This may not hold for higher-order modulation schemes, where the Euclidean distances between constellation points are smaller, though this is left for future work to examine.

6.6 CPDSSS with DAM

The viability of CPDSSS as a potential solution to signalling with short spreading sequences in wideband channels has been demonstrated experimentally. However, it must now be shown that this system is a suitable solution for using FSS DAM in these wideband channels. As such, this Section will experimentally implement a quasi-real-time CPDSSS communications system using a FSS DAM transmitter. BER and PER measurements will be taken and compared with the measured performance of CPDSSS with instrument grade modulation, as carried out in the previous Section.

6.6.1 Testbed design and implementation

Fig. 6.19 shows the system diagram for a CPDSSS communications system using FSS DAM as a transmitter technology. It is broadly identical to the CPDSSS system described earlier in this Chapter (Fig. 6.1), and uses exactly the same packet structure, but has the intermediate stage of mapping the modulated, spread waveform with added CP to a PAM waveform, which causes the FSS DAM modulator to produce the desired modulated

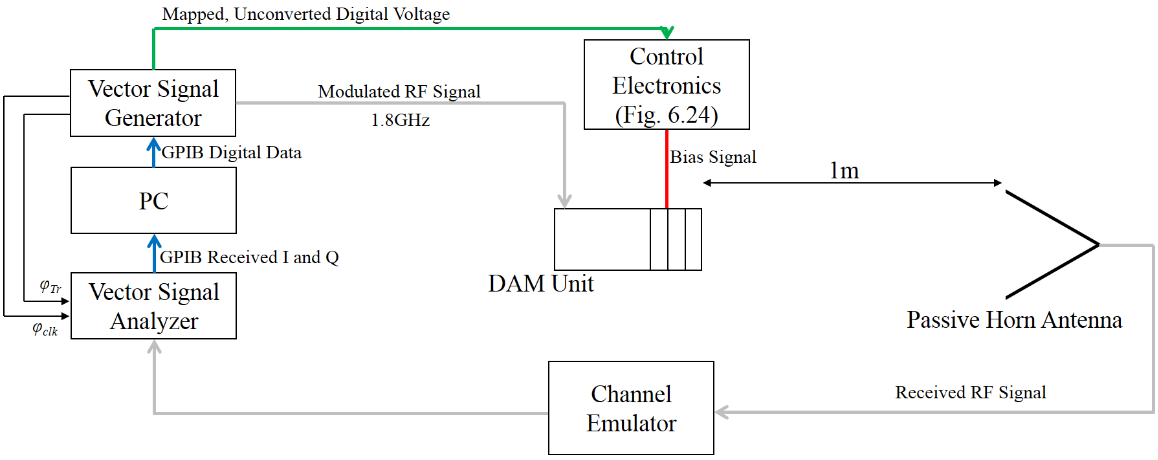

Figure 6.20: Implementation of CPDSSS communications system with a DAM transmitter

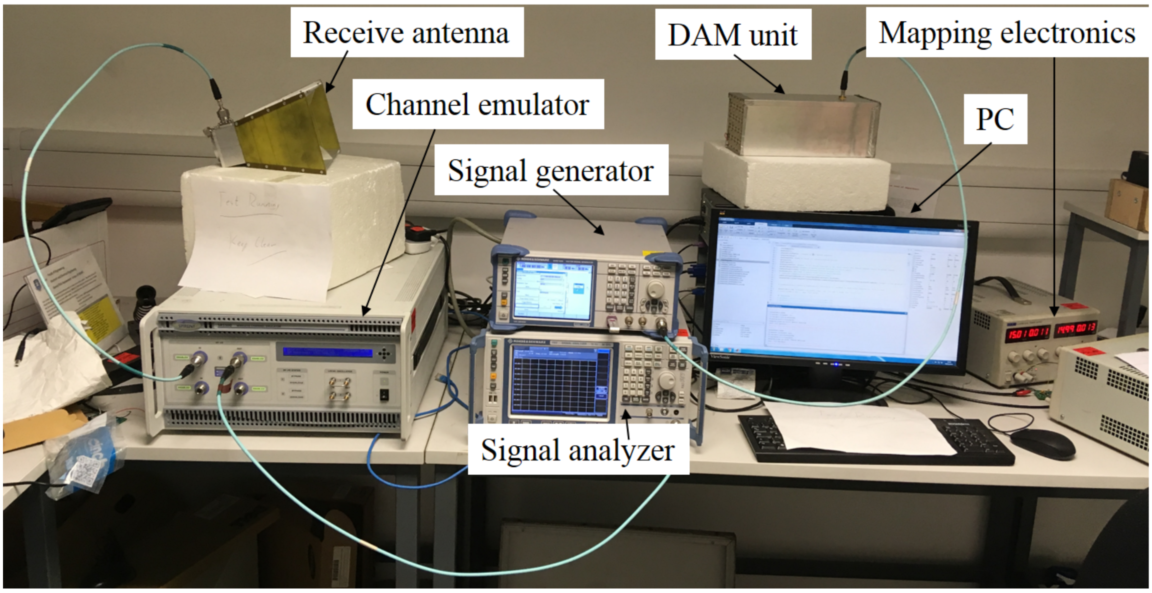

Figure 6.21: Photograph of the experimental setup for CPDSSS with FSS DAM

radio frequency (RF) signal. The DAM unit and control electronics used in this Section are the ones under test in Chapter 5, allowing production of phase modulation up to 8PSK at 1MSymbol/s also at a carrier frequency of 1.8GHz.

The implementation of this experiment is shown in Fig. 6.20. As in Chapter 5, the data generation and packet construction were performed in MATLAB, using the same script as earlier in this chapter (Appendix E). Digital data representing the processed packet is then sent to the Rohde & Schwarz Signal Generator, which maps this to a non-linear PAM signal. This signal is then amplified and offset to produce the required voltage signal for the FSS Modulator to produce the desired RF waveform.

In order to create a multipath channel, the DAM unit was placed in a laboratory environment 1m away from a passive horn antenna attached to the input port of the Spirent

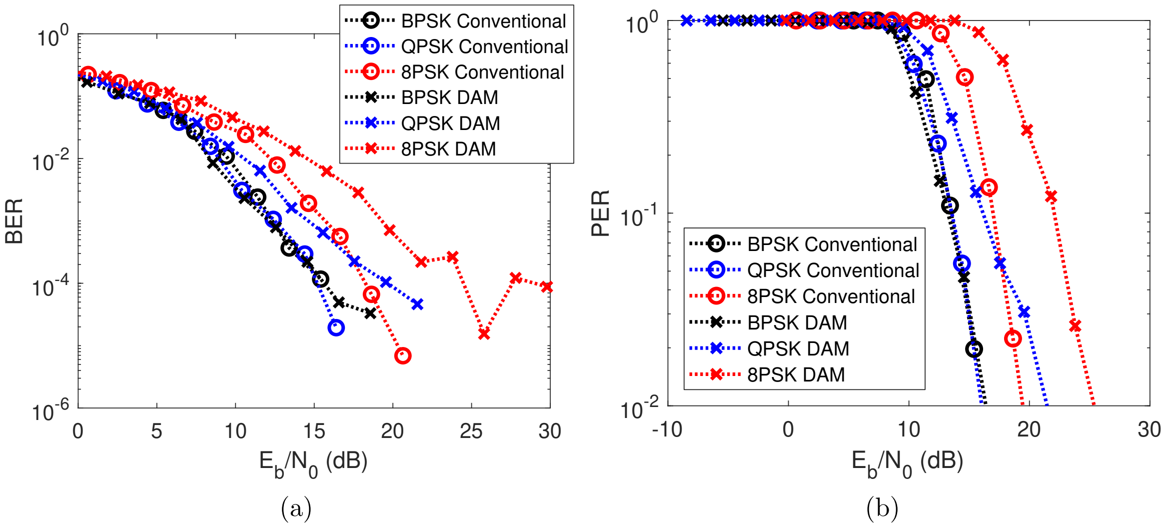

(a) (b)

Figure 6.22: Measured (a) BER, and (b) PER, for CPDSSS with the length $N = 4$ Barker sequence and a CP of $Q = 3$ in a $L = 4$ Rayleigh fading channel, using DAM (crosses) and conventional (circles) transmitters

Channel Emulator. The short spacing minimised any reflections from the environment, allowing the Channel Emulator to produce the desired multipath fading on the input signal, which is downconverted and sampled by the Rohde & Schwarz Signal Analyzer. This digital data was then processed in MATLAB. A photograph of this testbed is shown in Fig. 6.21.

The slight difference between this testbed and the conventional CPDSSS testbed should be noted. In order to investigate the DAM transmitter, the signal must be transmitted over the air, while in the previous testbed the RF is kept within cables. Most significantly, this means the transmit powers required to obtain the same received power are higher in this testbed, though this is still well within the dynamic range of the Rohde & Schwarz signal generator. However, extra reflections may be introduced from the environment when signals are transmitted over the air. This was mitigated by keeping the distance between the DAM unit and receive antenna small and ensuring it is a line-of-sight channel. This could be explored by transmitting the conventionally modulated CPDSSS signal between two passive antennas, but will be assumed to have a minimal influence here.

6.6.2 The perfect binary sequence

Again, the first scenario examined was the length $N = 4$ Barker sequence, which has an ideal periodic autocorrelation function. In analogy with the experiments performed in the previous Section, the channel emulated was $L = 4$ independently Rayleigh fading paths, each with a relative delay of 1μs and equal average power. The chip rate produced by the DAM transmitter was 1Mchip/s, so each path emulated was resolved separately by the receiver. The Barker sequence was preceded by a CP of length $Q = 3$ to provide the CPDSSS format.

BER and PER measurements were taken for BPSK, QPSK and 8PSK, and the results are shown compared with the measured results from the previous Section in Fig. 6.22.

BPSK using DAM performs similarly to the conventional transmitter, similar to the performance of balanced DAM BPSK in the AWGN channels discussed in Chapter 5.4.3. This suggests that the use of a spreading sequence is again reducing the EVM at the receiver output, as the Manchester code did previously. As such, BER performance below 10^{-5} is obtained with little discernable difference from using conventional transmitters. QPSK, however, suffers due to the impairments produced by DAM, reaching 10^{-4} BER at an E_b/N_0 3.8dB greater than with a conventional transmitter. This suggests that the ideal autocorrelation has broken down due to the imperfect constellation produced by DAM, reintroducing the interference term seen in Equation 6.15. 8PSK performs worse still, with a minimum BER of 1.5×10^{-5}, crossing 10^{-4} at an E_b/N_0 6dB greater than with a conventional transmitter, similar to the degradation experienced by QPSK. This is both due to the breakdown in the perfect performance of the length 4 Barker code, and the unbalanced nature of this code providing less mitigation of variable constellation amplitude than the balanced Manchester code. Applying Equation 5.4 to the 8PSK constellation suggests the minimum and maximum amplitudes of the resultant desired despread signal will be 0.575 and 0.845, respectively, rather than 0.70 and 0.83. This disparity increases the probability of error.

There is also degradation noticeable in the PER measurements (Fig. 6.22b). QPSK reduces the PER below 10^{-2}, though with a penalty of 3dB. The PER for 8PSK falls below 1% for a degradation of 6dB in comparison with the performance of an instrument grade transmitter. The extreme nature of the channels under test here should be emphasised, with equal power multipath across almost the entire length of the sequence. That the non-ideal constellations produced by DAM should suffer more in these situations than instrument grade modulation is unsurprising. The robustness and quality of the BPSK constellation produced by the DAM unit, however, gives little or no degradation in PER compared with instrument grade modulation. Further, the reduction of all modulation orders tested below a PER of 1%suggests that CPDSSS with DAM transmitters is still a viable system for transmission in wideband channels.

Greater understanding of this drop in performance can be found by analysing the autocorrelation functions produced by each distorted constellation point spread across the DAM magnitude-phase trace of Fig. 5.22 by the length 4 Barker sequence. Using the measured constellation amplitude distortion previously described in Tables 5.5, 5.6 and 5.7, the equivalent distorted code $\boldsymbol{c'}$ for each constellation point was correlated with the ideal length 4 Barker sequence $\boldsymbol{c} = [1, 1, 1, -1]$ to give the distorted correlation function

$$W'(\Lambda) = \sum_{m=0}^{N-1} c'_m c^*_{m+\Lambda} \tag{6.22}$$

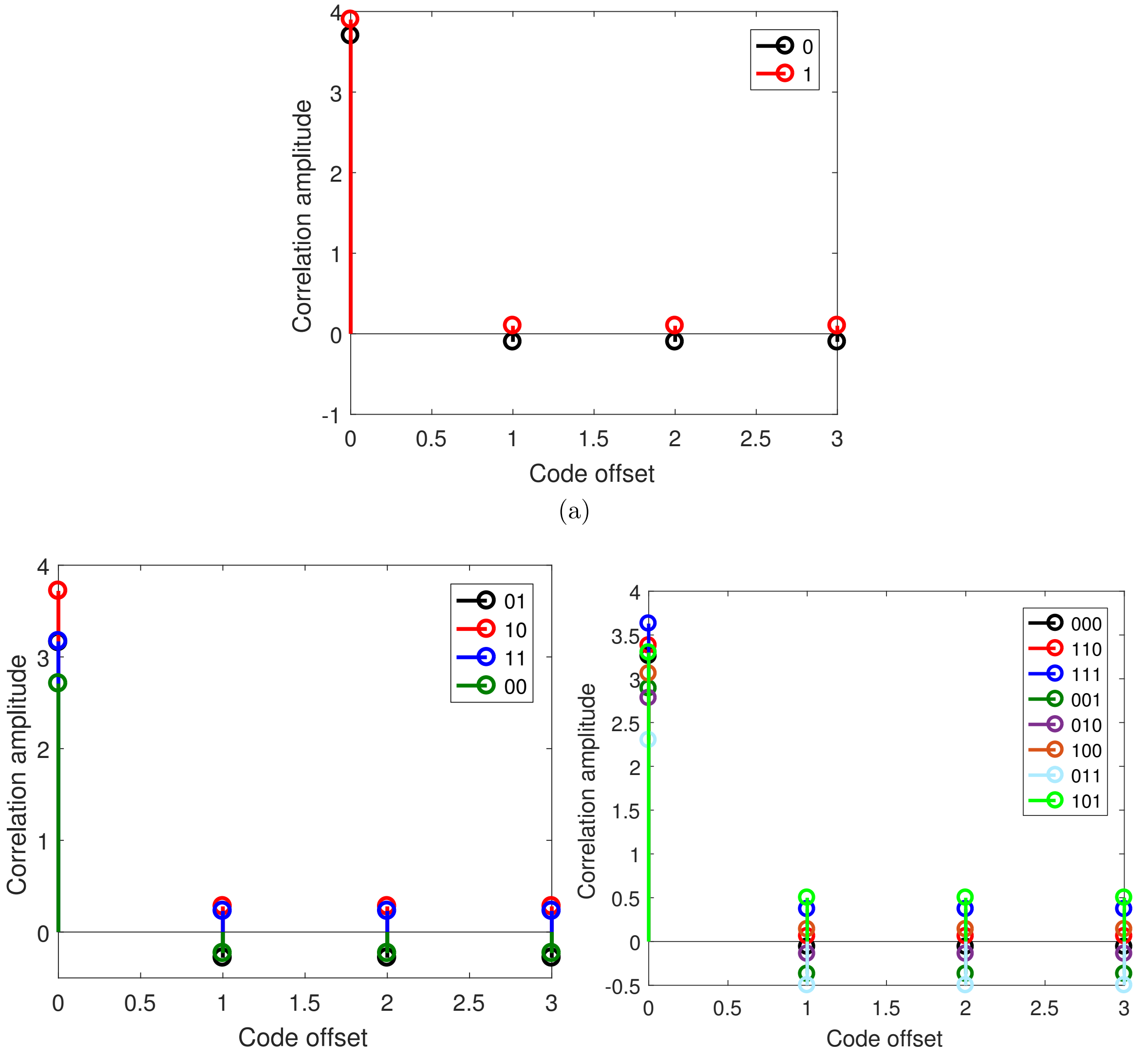

(a)

(b)

(c)

Figure 6.23: Autocorrelation function of length 4 Barker sequence when distorted by DAM constellation. (a) BPSK, (b) QPSK, (c) 8PSK

for different shifts Λ, in analogy with Equation 2.23. The correlation values are shown for each modulation order in Fig. 6.23. These can be compared with the ideal autocorrelation function shown earlier in Fig. 6.6a. The varying values at zero shift represent the amplitude of each constellation point at the output of the receiver's correlator. This shows that the unbalanced nature of the length 4 Barker sequence means there is quite a lot of variation in the relative constellation amplitude for QPSK and 8PSK, with the smallest point 73% and 63% of the largest constellation point in each case. This increases the chance of errors occuring compared with CPDSSS with a conventional transmitter due to the decreased Euclidean distance between constellation points. However, the most important effect shown by these correlation values is that the sequence is no longer ideal, with IntraSI emerging from the non-ideal correlation. The larger increase in IntraSI from the more distorted higher order modulation of 8PSK compared with BPSK is what produces the larger degradation in error rates at 8PSK.

This demonstrates that the special advantages of the length 4 Barker sequence are mostly lost when used with a distorting DAM transmitter, due to the loss of the ideal correlation property and so the introduction of symbol-dependent IntraSI. However, using CPDSSS with a DAM transmitter still eliminates InterSI, and so the PER has been shown to drop below 1% for all three modulation orders examined with RAKE reception in highly dispersive channels, suggesting this combination could be used in an IoT communications system.

6.6.3 Imperfect binary sequences

In order to evaluate the performance of DAM CPDSSS with imperfect binary sequences, similar comparison can be performed using the length $N = 7$ m-sequence $[1, 1, 1, -1, -1, 1, -1]$. As in the previous Section, a CP of length $Q = 4$ is added to the sequence, and the packet is passed through a length $L = 5$ wideband Rayleigh fading channel.

The results of BER measurement with DAM CPDSSS, compared with CPDSSS using an instrument grade transmitter are shown in Fig. 6.24. BPSK again has little discernable difference between the BER performance of DAM and instrument grade transmitters. As before, QPSK shows some degradation due to the distorted constellation of DAM, though it is significantly less than in the previously examined case. Here, an error rate of 10^{-4} is reached at less than 1dB greater E_b/N_0 than with a conventional transmitter, similar to the performance of QPSK DAM in AWGN when using a Manchester code (Chapter 5.4.3). 8PSK requires 3dB greater E_b/N_0 to cross 10^{-4} BER. The greater similarity between instrument grade and DAM BER performance in this experiment is likely due to the pseudo-balanced property of the length 7 m-sequence providing better amelioration of the distorted DAM constellations, and due to the relative difference between an increase in intracode interference, as with the m-sequence, and its introduction having previously eliminated it,

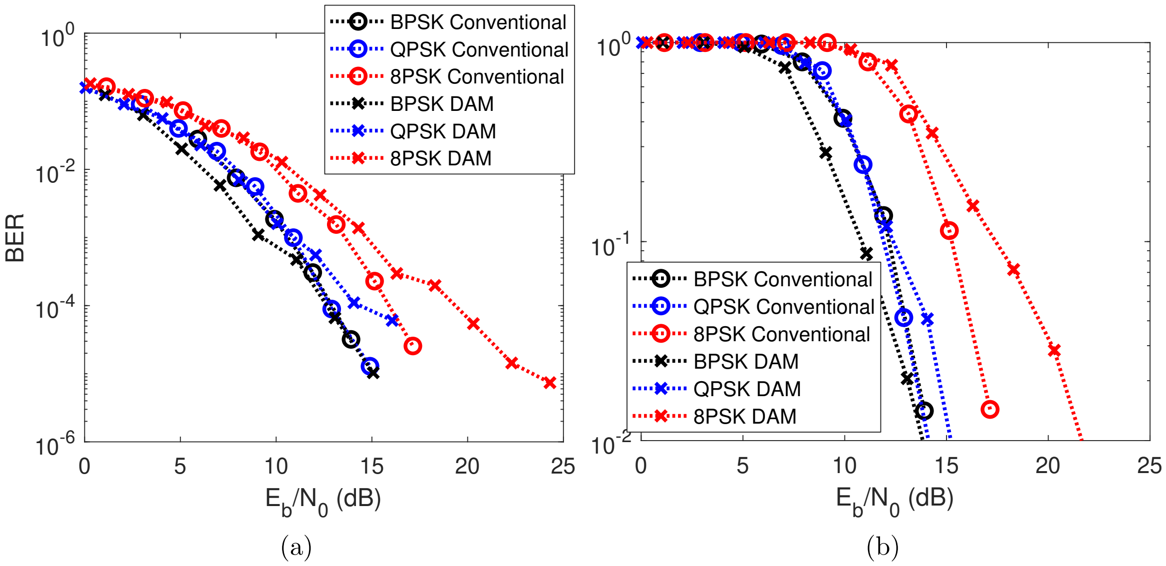

Figure 6.24: Measured (a) BER, and (b) PER, for CPDSSS with the length $N = 7$ Barker sequence and a CP of $Q = 4$ in a $L = 5$ Rayleigh fading channel, using DAM (crosses) and conventional (circles) transmitters

as with the length 4 Barker sequence.

The PER is shown to reduce below 1% for all modulation orders examined (Fig. 6.24b). BPSK again shows no obvious difference between DAM and instrument grade modulation. QPSK DAM CPDSSS experiences a small degradation in performance compared with instrument grade modulation, of less than 1dB. 8PSK reduces the PER below 1% with 4dB greater E_b/N_0 required for the DAM transmitter compared with instrument grade modulation. Again, that the PER is able to reduce below 1% suggests that DAM CPDSSS may be a suitable solution for IoT connectivity in wideband channels.

The effect on both the constellation and the IntraSI due to the impaired DAM constellations can be further investigated through analysis of the correlation between the impaired transmission and the ideal code (Fig. 6.25). Using an ideal code, the peak would be 7, and all sidelobes -1 (Fig. 6.6b). In the BPSK case, there is only a small departure from the ideal, with the smallest in-phase peak being 6.6 and the sidelobe peaks being either -1 or -0.9 (Fig. 6.25a). This leads to the similar performance between DAM and conventional CPDSSS discussed previously (Fig. 6.24). There is only a slight increase in IntraSI relative to the peak values, which further explains the similarities in results.

In all, the performance of DAM CPDSSS with the length 7 m-sequence is similar to that achieved by CPDSSS with conventional modulation. This is particularly true when a RAKE receiver is used, as it reduces the effect of IntraSI by taking advantage of interfering paths, rather than merely coping with them. Further, it allows the reduction of the BER below 10^{-4} and the PER below 1% in the majority of examined cases, suggesting that it is suitable for use in wideband channels. The difference is significantly less than when the length 4

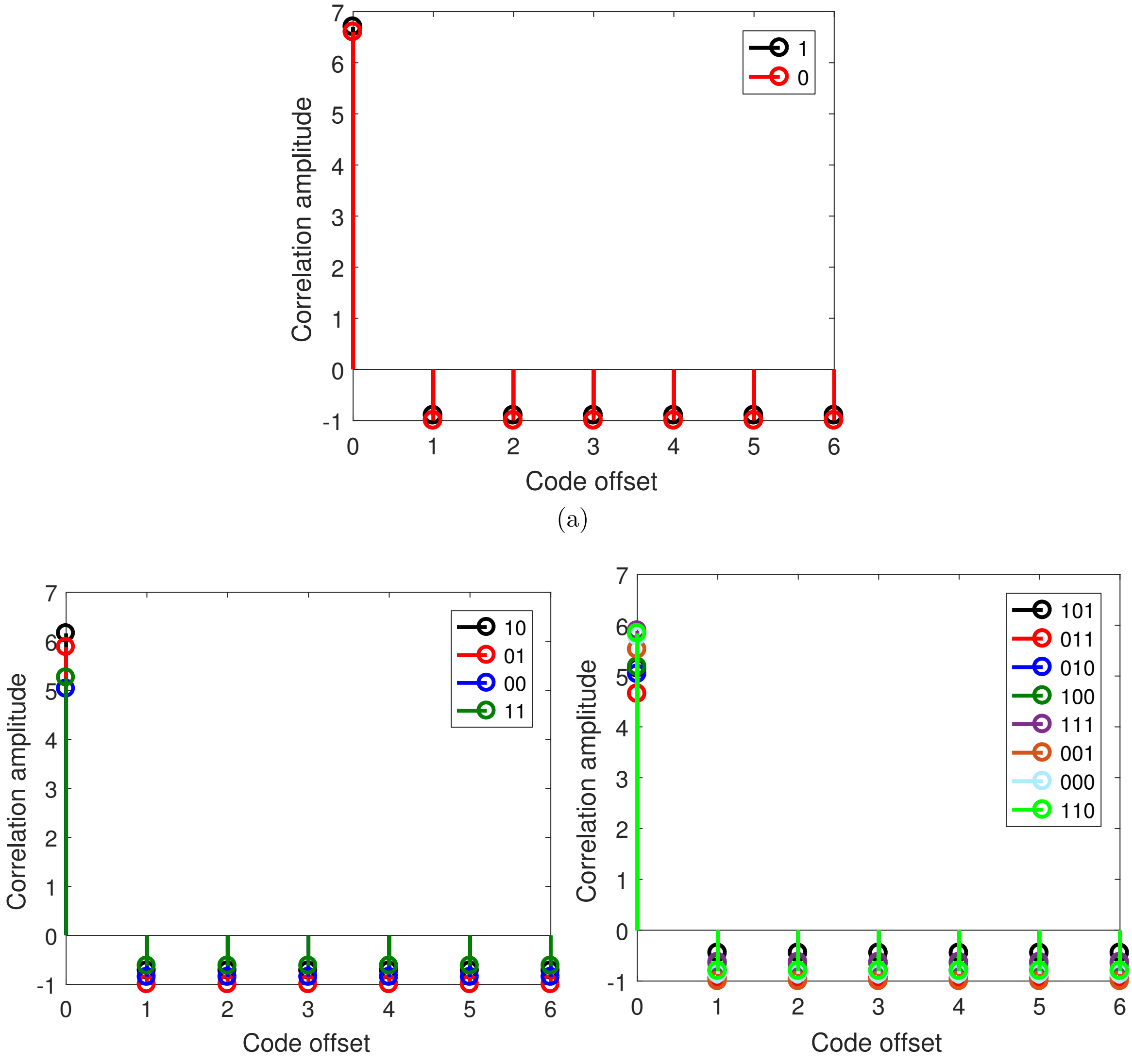

(a)

(b)

(c)

Figure 6.25: Autocorrelation function of length 7 m-sequence sequence when distorted by DAM constellation. (a) BPSK, (b) QPSK, (c) 8PSK

Barker sequence was used. This is for two reasons: firstly, the difference between eliminating interference with conventional modulation and reducing it significantly with DAM, as occurs when using the ideal binary sequence is much larger than the difference between mitigating interference by a different amount, as occurs when using imperfect sequences. Secondly, the imbalance of the length 4 Barker sequence leads to larger variation in the amplitude of constellation points after correlation than when the pseudo-balanced m-sequence is used, resulting in a higher probability of error. However, most importantly, DAM has been demonstrated performing satisfactorily in wideband fading channels by using the newly developed CPDSSS communications system. This opens DAM to use in IoT communications links in non-ideal channel conditions.

6.7 Discussion

Cyclic Prefix Direct Sequence Spread Spectrum has been presented, analysed mathematically, simulated in MATLAB, and experimentally implemented with both conventional modulation and FSS DAM. By placing a cyclic prefix at the front of the spreading sequence, which is then discarded at the receiver, intersymbol interference is eliminated, and intrasymbol interference is entirely defined by the periodic autocorrelation function of the sequence. This allows operation in wideband fading channels, and is the first demonstration of FSS DAM producing effective modulation in these channels. This system has been designed for IoT communications, as using short spreading codes could allow robust transmission of high data rates for short periods of time in dispersive channels, allowing the transfer of small amounts of information with high energy but low power and supporting large numbers of devices through contention based random multiple access methods.

When using the length 4 Barker sequence, which has ideal periodic autocorrelation properties and so eliminates inter and intrasymbol interference in CPDSSS, mathematical analysis was shown to have very good agreement with numerical simulation, especially at high E_b/N_0 values. Here CPDSSS allows multiple paths to add diversity to the system, improving performance over single-path Rayleigh fading. Through simulation, it was shown that CPDSSS outperforms conventional DSSS when both the kernel sequence or an equivalent length sequence are used, reliably reducing the BER of BPSK, QPSK and 8PSK below 10^{-6}. Further, in all examined cases, the PER was reduced below 1%. As in contention multiple access schemes a failed packet will be retransmitted, this is the key parameter for the performance of CPDSSS and other contention based IoT technologies.

These simulated results were then experimentally validated, first with conventional instrument grade modulation. Good agreement was found between simulation and experiment for both the length 4 Barker sequence and the length 7 m-sequence.

	Modulation format	Multiple access	Processing gain
EC-GSM-IoT	GMSK, 8PSK	TDMA, RMA	1
NB-IoT	BPSK, QPSK	OFDMA (128), SC-FDMA	1
LTE-M	QPSK, 16QAM	OFDMA (128), SC-FDMA	1
Sigfox	DBPSK	RMA	1
Weightless-P	GMSK, QPSK	FDMA, TDMA	1
Ingenu	DBPSK	RPMA	16 - 8192
LoRaWAN	CSS	RMA	64 - 4096
CPDSSS	BPSK, QPSK, 8PSK	RMA, TDMA	4, 7

Table 6.5: Comparison of CPDSSS with existing IoT technologies

CPDSSS compares favourably as a mid-point between higher throughput, more complex cellular IoT standards, which require use of OFDM waveforms even while reducing bandwidth to mitigate energy consumption, and low power wide area network (LP-WAN) technology, which sacrifice maximum throughput to support huge numbers of devices (Table 6.5). CPDSSS is a wideband technology, but uses a CP to allow small processing gains (PGs) of 4 and 7, tested here, to overcome highly dispersive channels, which would otherwise require the narrow bandwidths of Sigfox, Weightless-P and EC-GSM-IoT to overcome. This is significantly less than the PG of Ingenu and LoRa technologies, though the robustness of short CPDSSS codes against interference should be subject to further work. The modulation format is also comparable, with three PSK orders investigated. This technique could be extended to higher order modulation, accounting for complexity. The combination of short codes and more spectrally efficient modulation formats means the throughput of CPDSSS is greater than most LP-WAN approaches, though still less than LTE-M, which uses a significantly more complex OFDM waveform and high peak-to-average power ratio (PAPR) format. Further, CPDSSS does not use the equaliser required by EC-GSM-IoT, reducing complexity. The multiple access scheme suggested is RMA on the uplink and TDMA on the downlink, which is also used by many other IoT technologies. In future work, larger codesets may open the way to using code division multiple access (CDMA) to increase the number of devices supported, or the achievable data rate through code shift keying (CSK) modulation.

However, it is the codesign of CPDSSS with the properties of FSS DAM that make it a candidate for cost effective dense IoT networks. The autocorrelation of the perfect binary sequence breaks down due to the impairments inherent in FSS DAM, however the PER always reduced below 1%, and the BER below 10^{-4}. The performance of FSS DAM CPDSSS with the length 7 m-sequence is much closer to the performance of conventional modulation CPDSSS, due to the pseudo-balanced nature of the sequence reducing both variation in the amplitude of constellation points, and additional IntraSI. Again, the PER was always reducible below 1% and the BER below 10^{-4}. This demonstrates that FSS DAM can reliably transmit information over wideband channels using CPDSSS.

The low complexity and high efficiency of FSS DAM makes it an ideal transmitter for use at wireless access points in increasingly dense IoT networks. By modulating within the antenna, the majority of RF electronics are removed, reducing the size and weight of transmitter units. While the FSS DAM unit is larger than conventional antennas, the size of the whole equipment is reduced, making it suitable to be installed on small sites and street furniture. Further, the efficiency of the transmitter is improved by requiring the power amplifier (PA) to amplify only a single carrier wave, which can be done at peak efficiency. This also reduces the size and cost of the PA required. When transmitting CPDSSS modulation, FSS DAM units can reliably transmit data over wideband channels, allowing them to be used in practical scenarios. This setup compares favourably with both cellular IoT, which must make use of portions of the mobile infrastructure and often use complex waveforms to overcome fading, and LP-WAN technologies, which can support thousands of devices over a large area but do not scale easily and affordably through densification due to the costs of each access point. As such, FSS DAM with CPDSSS emerges as a scalable, low cost solution to supporting increasing numbers of IoT devices.

6.8 Conclusion

CPDSSS has been presented as a wideband waveform for IoT communications with FSS DAM transmitters. Mathematical analysis, simulation and experimental implementation demonstrated CPDSSS with conventional transmitters is able to leverage the diversity of dispersive channels with short spreading sequences by adding a CP of similar length to the channel. The technique was then demonstrated with an FSS DAM transmitter, showing that the use of balanced spreading sequences in CPDSSS systems overcomes the systematic amplitude distortion produced by FSS DAM, allowing good transmission. This suggests that the low complexity FSS DAM transmitters can be used with CPDSSS to provide low cost, energy efficient dense networks for implementing the Internet of Things.

Chapter 7

Conclusions

7.1 Summary

This thesis has sought to find a solution to the increasing numbers of connected wireless devices required to realise the promises of the Internet of Things (IoT), and the associated increase in wireless capacity. It has looked to do this through the codesign of a low complexity, energy efficient transmitter suitable for deploying in dense networks of wireless access points, and a new waveform that leverages the advantages of this new transmitter while mitigating the disadvantages.

The new transmitter technology is a form of direct antenna modulation (DAM), where modulation occurs at or after the antenna rather than in radio frequency (RF) electronics at low power. This allows the power amplifier (PA), which otherwise would have to amplify broadband and peaky signals, to amplify the carrier wave only. This can be done by a non-linear PA, reducing the cost and size of the transmitter, and also with a significant increase in efficiency over linear PAs. This, along with the reduction of the amount of bulky and inefficient RF electronics, which are replaced with electronics operating at the data rate, makes a DAM transmitter low complexity and low cost. Chapter 2 showed that, while multiple DAM technologies have been developed, none is suitable for use as transmitters in dense IoT networks.

As such, Chapter 3 looked to design a new DAM technology for this purpose, using transmissive reconfigurable frequency selective surfaces (FSS). This produced an outline design consisting of a multi-layer square-loop aperture FSS integrated with variable capacitors, the varying of which produces phase change in an incident RF wave. Multiple layers are required to achieve the amount of phase change needed for modulation while minimising the magnitude variation with phase change, in trade-off with loss increasing exponentially with increasing numbers of layers. The FSS was enclosed in a cavity to limit the physical size, with a monopole feed to inject energy into the cavity. This formed a complete DAM unit capable of producing phase modulation.

Chapters 4 and 5 then used this generic design to produce DAM units capable of QPSK and continuous phase modulation respectively. Chapter 4 produced a proof-of-principle DAM transmitter which was then implemented in a complete end-to-end communications system. QPSK modulation was achieved at 1MSymbol/s using a length 15 m-sequence to mitigate the distortion caused by the three-layer FSS modulator. However, it had peak gain of only 0.15dBi, suggesting a poor efficiency, which was simulated to be below 10%, and suffered 4dB degradation in BER performance in comparison with instrument grade modulation. To improve this, Chapter 5 increased the number of FSS layers to 4, potentially allowing continuous phase modulation to be performed. Improved choice of variable capacitors led to improvements in efficiency to give peak gain 2.3dBi, and use of low loss substrates could increase simulated efficiency to over 50%. This new DAM unit was demonstrated with BPSK, QPSK and 8PSK modulation, with only up to 1.5dB BER degradation between DAM and instrument grade modulation when Manchester code pulse shaping was used. The minimum EVM obtained was 2.4%, suggesting good quality modulation is produced by the DAM transmitter.

In order to transmit information reliably in non-line-of-sight channels, such as those found in the majority of realistic communications systems, a suitable waveform had to be chosen to overcome frequency selective fading. A modification of DSSS called cyclic prefix DSSS (CPDSSS) was designed in Chapter 6, where adding a cyclic prefix (CP) to the beginning of each spread symbol removes the effects of intersymbol interference (InterSI) while allowing time diversity to be exploited. This was explored through mathematical analysis, simulation and experimental implementation using instrument grade modulation. The new scheme was then shown with DAM transmitters, which was, to the author's knowledge, the first demonstration of DAM operating in wideband fading channels. Note that this is because of the codesign approach taken in this thesis, where the demonstration of FSS DAM using a suitable waveform was of interest. When pseudobalanced sequences are used, the distortion of FSS DAM is mitigated, giving maximum 3dB degradation compared with instrument grade modulation in wideband channels, suggesting this new waveform is suitable for use in IoT systems with DAM transmitters.

This new combination of FSS DAM and CPDSSS appears to be a suitable candidate for low complexity, energy efficient implementation of a dense network of IoT wireless access points. The final DAM unit is compact and self-enclosed, being $0.68\times0.68\times1.71\ \lambda_0^3$. While this has a significantly greater depth than either integrated switch DAM or reflective metasurface DAM, it contains its own feed, unlike [59], as well as being smaller in the other two dimensions. As such, FSS DAM is more suited to being installed on street furniture than reflective metasurface DAM, allowing it to be used in denser networks. While integrated switch DAM is smaller in every dimension than FSS DAM, it is only capable of simple on off keying (OOK) modulation, limiting its use in IoT communications [42]. The modulation complexity of up to 8PSK demonstrated by FSS DAM is equivalent to reflective metasurface DAM, and means the unit can achieve most low power wide area network (LPWAN) communications signalling, as well as the newly developed CPDSSS waveform. The demonstrated symbol rates are also similar to the maximum rates required for most IoT standards, and similar to competing DAM technologies. All of these techniques can be considered low complexity compared with conventional transmitters, which require a large amount of radio frequency (RF) electronics and linear amplification. FSS DAM has also been shown to have greater efficiency than a conventional transmitter with a linear PA, though an in-depth cost to efficiency study has not been carried out. As such, FSS DAM is a suitable technology for the wireless access point transmitter in dense IoT networks.

When FSS DAM is combined with CPDSSS, it may be a solution to the scalability problem of increasing numbers of IoT devices. The complexity of waveform is similar to Ingenu and LoRa, though it has significantly lower processing gain due to the use of a CP allowing much shorter spreading sequences to be used. The different modulation orders available suggests a range of data rates could be used, making it a flexible approach to IoT connectivity. While LTE-M and NB-IoT look to coexist with densifying cellular networks, the complexity of the waveforms limits the efficiency of their application, and it may be that densifying for IoT devices only, particularly in industrial use cases, is more cost effective than relying on mobile networks. LP-WAN technologies, meanwhile, have aimed to reduce the need for densification by supporting huge numbers of devices from single sites, though this approach does not scale without stringent limits on capacity, as Sigfox have implemented. As such, FSS DAM with CPDSSS provides an affordable approach to densification, with a waveform capable of supporting varying throughputs and numbers of devices produced by low complexity, energy efficient transmitters, which can be deployed at low cost in dense networks of wireless access points.

7.2 Future work

This thesis has presented both the first demonstration of FSS DAM as a new transmitter, and CPDSSS as a new waveform for IoT. As such, there is a large potential scope for developing this research further.

7.2.1 Pulse shaping for DAM

At present, the DAM transmitters demonstrated have been unable to keep their emissions within the standard frequency masks required by IoT standards. This could be achieved through filtering the bias control signal, though without an equivalent filter at the receiver the EVM increases significantly, impacting BER performance. As such, future work should investigate both how simple filters applied at the transmitter might be reproduced on baseband I and Q at the receiver to reduce the EVM, and how precise control of the DAM bias voltage may mimic the effects on the transmitted signal of conventional pulse shaping filters, which could then be used at the receiver. The first approach adds complexity at the receiver, and the second at the transmitter. They may have applications in different circumstances.

7.2.2 Multiple antenna transmitters

As has been particularly mentioned in discussions about load modulation, DAM presents an opportunity to reduce the complexity of multiple antenna transmitters [158]. Increasingly, capacity increasing multiple-in multiple-out (MIMO) techniques require large numbers of antennas- potentially over 100- at each base station [159]. However, at present each transmit antenna requires a complete RF chain to produce full digital modulation. This means that MIMO transmitters have large form factors and are often inefficient, using low cost components rather than expensive and efficient ones.

DAM provides a possible response to this. By modulating at the antenna, the RF chains are removed and low cost PAs can be run efficiently in their non-linear region. Electronics providing the modulating signal operate at baseband rates rather than RF, allowing them to be smaller and more efficient. Preliminary work has been carried out by the author to show that FSS DAM may be suitable for multiple antenna techniques [160]. Simulation was carried out to demonstrate that two DAM units of the design examined in Chapter 4 fed by the same source were capable of producing a standard transmit diversity scheme. Reflections back from the antennas were found to be minimal due to always operating in the transmissive region of the FSSs, as were cross-coupling effects on the antenna constellation.

Much more work is still to be performed, however, including studying the effect of the FSS DAM distortion on the performance of diversity schemes, and whether certain schemes have any mitigating effect. This could then be extended to larger numbers of antennas, where phase-only MIMO precoding could be used to allow multiple access and large capacities while reducing the complexity of the system [161].

7.2.3 High frequency operation

The work in this thesis has focused on operation at microwave frequencies, as these are the frequencies of interest for IoT applications. In particular, the designs have operated at 1.8GHz, though across most sub-6GHz ranges the design can be expected to function similarly. However, interest has been growing in the utilisation of higher frequency bands, particularly those known as mm-Wave, between 26GHz and 100GHz [6], due to the large amount of currently unused bandwidth at these frequencies.

One key problem with the move upwards in frequency is the cost and efficiency of RF electronics, in particular PAs. State-of-the-art mm-Wave PAs have been designed with peak 40% efficiency, which must then operate at back-off [162]. This is due to both the high carrier frequencies and the large bandwidths, which must be amplified. As such, the potential gains from FSS DAM are significant, as non-linear PAs could still be used at mm-Wave frequencies to efficiently amplifier the constant envelope carrier. Further, the physical size of the DAM unit reduces in proportion to the increase in frequency. As such, a unit which may have a restrictive form factor at microwave frequencies, as is often the case with multiple layers of FSS required for DAM, reduces to a chip-size unit. This allows large arrays of DAM units to be realised in small space.

While the physics of using FSS to phase modulate scales simply to mm-Wave frequencies, there is much research to be carried out for the implementation. In particular, the variable capacitors would be a focus of study, as they must be low loss at mm-Wave and fast switching to provide wide bandwidths. Fabrication techniques at the small scale required will also need to be investigated. However, with increasing numbers of mm-Wave transmitters and the need for energy efficiency, FSS DAM could provide a simple and cost effective solution.

7.2.4 Quadrature modulation using FSS

All study and discussion here has been focussed on producing phase modulation using FSS. However, controlling the amplitude of incident RF using FSS is a well-established technique [100]. As such, combining the work of this thesis with these amplitude modulating FSS may allow higher orders of modulation to be produced, in particular QAM. Further, continuous amplitude modulation in conjunction with continuous phase modulation would allow a DAM unit to produce any point on a complex plane, allowing it to produce any form of modulation with full digital control, including multiple access techniques other than spread spectrum approaches. This would allow FSS DAM to be a viable low complexity, efficient transmitter for a wide variety of applications.

7.2.5 Electrical characteristics of DAM units

Many of these potential applications discussed require the DAM unit to produce modulation with very high bandwidths, which requires fast variation of the capacitances of the unit. Until the development of FSS DAM, there was little need to understand the electrical characteristics of FSS, as the required tuning speeds were often in the order of ms rather than sub-μs. However, as the rates increase, an understanding of how these arrays of active devices on possible electrically large conducting planes behave in response to varying voltages becomes more important. Methods for driving these FSS, and multiples of them in DAM units, effectively and at high speeds must be considered. Further, an understanding of how the reconfigurable FSS's electrical characteristics respond to incident RF may lead to a method of direct reception or detection using FSS.

7.2.6 Multi-user CPDSSS

CPDSSS has been analysed and measured in this thesis as a single user communications system. However, it could be extended to allow large numbers of IoT devices to connect to a network through RMA. This should be investigated, in order to determine the number of devices which can connect to a single wireless access point, giving greater understanding of the amount of densification required for proper support of IoT networks.

7.2.7 Extended mathematical analysis of CPDSSS

The analysis presented here of CPDSSS was limited to an expression of a binary system, and BER results were derived only for the case of codes with perfect periodic autocorrelation functions. Further work should extend this to higher order modulation schemes, such as QPSK, 8PSK and beyond to QAM formats. Also, expressions for calculating the BER of CPDSSS with imperfect codes should be derived, possibly treating intraSI as a process defined by the periodic autocorrelation function of the code being investigated. This would give greater understanding of the effect of different code properties on the performance of CPDSSS, and further validate the simulation results obtained here.

7.2.8 M-ary CPDSSS and CPCDMA

In this thesis, only simple, short binary codes have been examined for use in CPDSSS. The ones examined have codesets of size one, which limits them to allowing only a single user to access the channel at any one time, and limits the data rate. Using longer sequences with larger codesets could allow multiple access to the channel through a form of code division multiple access (CDMA) with the CP enhancing the performance of the system. Larger codesets could also allow M-ary signalling, where different codes represent different data sets, increasing the potential data rate significantly. Research would be required into large codesets, and finding codes that balance their periodic autocorrelation and cross-correlation functions.

7.2.9 Polyphase codes for CPDSSS

Extending the codesets under investigation from binary codes to polyphase codes is another potential research direction. They often have large codesets for relatively short code lengths while maintaining good autocorrelation and cross-correlation characteristics, such as the polyphase complementary codes [163]. Further, the unit magnitude of polyphase codes lends them to the phase modulation produced by FSS DAM.

Polyphase codes with perfect autocorrelation characteristics are also of interest, as they can be much longer than the length 4 Barker sequence. For example, Frank-Zadoff-Chu sequences can have any length, though their largest sets have length equal to prime numbers. However, they consist of a number of constellation points one less than their length, so can become complex to produce as their length increases [164]. The Frank sequences, which are used in RADAR pulses, consist of the number of phases equal to the square root of their length, meaning they can be long while retaining simplicity, though the lengths available are more limited [165]. The exploration of CPDSSS with all these sequences should consider all these points.

7.2.10 Multiple antenna CPDSSS

In addition to the time diversity obtained by CPDSSS, the useful properties may be utilised in multiple antenna systems. This could be in the form of adapted transmit diversity schemes, or in utilising the codes for point-to-point MIMO communications. The simple nature of the sequences investigated could lead to simple, high rate data transmission.

Appendix A

MATLAB code for QPSK FSS DAM

A.1 TestMultitest.m

```
% Multitest- 20/01/16
% To be used in conjunction with QPSK_ContinuousRun
% For finding BER of large amounts of data in QPSK DAM system

clear all
close all
instrreset;
%CODE FOR REPEATED QPSK: Started 20/01/16

%% VARIABLES
pilotLen=222; %Select length of pilot. This is spread by a
   factor (15 default).
ambLen=1; %Length of post-amble(*15)
numDataBits=888; %Defines the number of data bits per packet
freq='1.8GHz'; %Baseband frequency
sRate=2e6; %Sample rate (2*chip rate)
lengthseq=15;  %length of the spread sequence
testBits=5e6; %No. bits required for reasonable BER measurement
% numPackets=1; %Number of packets to be send to acquire
   reasonable BER measurement
numPackets=ceil(testBits/numDataBits); %Determine no. packets
   to send using required no. bits to test
```

```
level=-60:1:-45; %Transmit power (dBm). Can also set a range (eg. -20:2:-10)

%----------------------------%

g1=visa('agilent','GPIB0::2::INSTR'); %Address of spectrum analyzer
g2=visa('agilent','GPIB0::28::INSTR'); %Address of signal generator
bufsize=((numDataBits/2)+pilotLen+ambLen)*lengthseq*18*2*2;% Analyzer result buffer size: totbits*seq length*wordlength*commas
g1.InputBufferSize=bufsize;
g2.OutputBufferSize= 5000000; %Arbitrary large input buffer
fopen(g1); %to establish connection
fopen(g2);

%% Establishing connection
%-spectrum analyzer-%
fprintf(g1,'*RST;*CLS'); %Reset and clear analyzer
fprintf(g1,'*IDN?'); %get ID
instID=fscanf(g1);

if isempty(instID) %Error messages
        throw(MException('RSAIQCapture:ConnectionError','Unable to connect to instrument'));
        end
disp(['Connection established with: ' instID]);

%-------------%
%-signal gen-%

fprintf(g2,'*CLS');
fprintf(g2,'*IDN?'); %get ID
instID=fscanf(g2);
if isempty(instID)
```

```
        throw(MException('RSAIQCapture:ConnectionError','Unable
            to connect to instrument'));
        end
disp(['Connection established with: ' instID]); %Confirmation

%% setting up
fprintf(g1,'inst iq'); %Display IQ window
fprintf(g1,['freq:center ' freq]);%Set frequency
fprintf(g1,'trac:iq:set norm,10MHz,22.5MHz,ext,pos,0,4080'); %
   -,-,sample rate,trigger source,trigger slope,pretrigger
   samples, number of samples
fprintf(g1,['trac:iq:rlen ' num2str(bufsize/(sRate/2e6))]); %
   Expected result length at analyzer
fprintf(g1,'system:disp:upd on');
fprintf(g1,'trac:iq:stat on'); %Enables aquisition of IQ data
fprintf(g1,['trac:IQ:SRAT ' num2str(sRate)]); %Sample at 2*
   symbol rate for Nyquist
fprintf(g1,'trac:iq:data:form iqp'); %Defines format of data
   return (IQIQIQ)

fprintf(g2,['sour:bb:dm:srat ' num2str(sRate/2)]); %Symbol rate
fprintf(g2,['freq ' freq]); %Transmit frequency
fprintf(g2,'sour:bb:dm:filt:type rect'); %Rectangular filter on
    baseband data
fprintf(g2,'sour:bb:dm:sour dlis'); %Set location of data file
   in sig gen

%% M sequences
mseq15lse=[1;0;0;1;1;0;1;0;1;1;1;1;0;0;0]*2-1;%lse
mseq15mse=[0;0;1;1;0;1;0;1;1;1;1;0;0;0;1]*2-1;%mse
periodicseq=[1;0;1;0;1;0;1;0;1;0;1;0;1;0]*2-1; %length 14
onlyoneseq =[1;1;1;1;1;1;1;1;1;1;1;1;1;1;1]*2-1;%length 15
sprdSeqConv=mseq15lse; %Choose spreading sequence

%% preallocate calculations
dataChips=(numDataBits*length(sprdSeqConv))/2; % No. data chips
    : data bits times length mseq divided into I and Q stream
```

```
pilotChips=pilotLen*length(sprdSeqConv); % No. pilot chips :
   pilot bits times length mseq
ambChips=ambLen*length(sprdSeqConv);  % No. postamble chips :
   postamble bits times length mseq
streamLen=dataChips+pilotChips; % Length of used chips stream (
   I&Q)
totValues=2*streamLen+2*ambLen; % Length of total input

%% Preallocation
pilot=ones(1,pilotLen); %Pilot: string of 1s (Spread later)
postAmb=ones(1,ambLen); %Postamble: string of 1s (Spread later)

totSprdData=zeros(length(sprdSeqConv),numDataBits);
dataString=blanks(totValues);
estData=zeros(1,numDataBits);
pilotQ=zeros(1,pilotLen);
sprdData=-ones(1,totValues);
errOut=-ones(1,numPackets);

allChanEst=zeros(numPackets,lengthseq);
errorsCONV=zeros(1,numPackets);
totErrorsCONV=zeros(length(level),1);
erRateCONV=zeros(length(level),1);
throughput=zeros(length(level),1);

%% Call function and collect data
for levelInd=1:length(level) %Loop through transmit powers
        fprintf(g2,['level ' num2str(level(levelInd))]); %Set
           transmit power
        QPSKContinuousRun; %Call m file and perform operations
           within
        display(['Cycles completed: ' num2str(levelInd) '/'
           num2str(length(level))]); %Update

        totErrorsCONV(levelInd)=sum(errorsCONV); %Store
           calculations
        erRateCONV(levelInd)=errRateTot;
```

```
end

for cv=1:length(level) %Display results for each transmit power
        display(['---| Results for ' num2str(level(cv)) ' dBm |---']);
        display(['Errors CONV: ' num2str(totErrorsCONV(cv)) ' - Error Rate CONV: ' num2str(erRateCONV(cv))]);
        display(' ');
end

if length(level)>2 %Plot results
        figure;
        semilogy(level,erRateCONV,'bx-');
        title('Bit Error Rates');xlabel('Level (dBm)');ylabel('Error Rate');
        legend('','Conventional','Location','sw');
        axis([min(level) max(level) 10^-4 1]);
end
```

A.2 QPSKContinuousRun

```
% QPSK_ContinuousRun  20/01/16
% For use with Testmultitest
% To get BER of large amount of data in DAM system

for p=1:numPackets %Cycle through transmit packets
        %% Generating random data
        randBits=randi([0 1],1,numDataBits)*2-1;%Generates string of random bits

        dataIstream= randBits(1:2:end); %Split into I and Q
        dataQstream= randBits(2:2:end);

        %% Spreading
        sprdPilot=sprdSeqConv*pilot; %Matrix multiplication to spread
        sprdAmb=sprdSeqConv*postAmb;
        sprdDataI=sprdSeqConv*dataIstream;
```

```matlab
sprdDataQ=sprdSeqConv*dataQstream;

%% Assembling data packet
totSprdI=[sprdPilot,sprdDataI,sprdAmb]; %Concatenate packet
totSprdQ=[sprdPilot,sprdDataQ,sprdAmb];

inputI=([reshape(totSprdI,1,streamLen)]+1)*0.5; % Reshape and convert back to 1s and 0s for sig gen
inputQ=([reshape(totSprdQ,1,streamLen)]+1)*0.5;
sprdData(1:2:end)=inputI; %Interleave I and Q
sprdData(2:2:end)=inputQ;

%% Transmitting data
for count=1:totValues %Convert all chips to char string of 1s and 0s, separated by commas
        dataString(2*count-1)=num2str(sprdData(count));
        dataString(2*count)=',';
end

%% Receiving Data
listIn=dataString(1:totValues*2-1);%Drop final comma
sigDur=num2str(totValues/2); %Sets the signal duration (total number of chips) to a string value

fprintf(g2,['sour:bb:dm:trig:slen ' sigDur]); %Send sig duration to sig gen
fprintf(g2,['bb:dm:dlis:data ' listIn]); %Sent data to sig gen file
display(['Sent ' num2str(p) ' of ' num2str(numPackets) ' packets']);

pause(1) %Delay to allow transmit&read of signal

%% Data gathering into I and Q components
clrdevice(g1); %Clear buffers
clrdevice(g2);
```

```
fprintf(g1,'trac:iq:data?');  %Expect data at analyzer
fprintf(g2,'sour:bb:dm:trig:exec'); %Trigger sig. gen.
   to send data
DataIn=fscanf(g1); %Store string of data from sig
   analyser

dataI=zeros(totValues/2,1); %Preallocation
dataQ=zeros(totValues/2,1);

[samplesI,samplesQ]=strDataConv2(DataIn); %Call
   function strDataConv2 to convert string to I and Q
   vectors
dataI(2:end)=samplesI(3:2:end)+samplesI(2:2:totValues
   -1); %Recombination of oversampled data
dataI(1)=samplesI(1)+samplesI(totValues); %As delay
   causes 1st sample to be at wrong end of data stream
dataQ(2:end)=samplesQ(3:2:end)+samplesQ(2:2:totValues
   -1);
dataQ(1)=samplesQ(1)+samplesQ(totValues);
rxDataI=dataI((pilotChips)+1:(pilotChips+dataChips)); %
   Remove the pilot and postamble from data
rxDataQ=dataQ((pilotChips)+1:(pilotChips+dataChips));
rxPilotI=dataI(1:pilotChips); %Extract pilot
rxPilotQ=dataQ(1:pilotChips);

%% Channel estimate
chanEst=-ones(1,lengthseq-1); %Preallocation
for x=1:length(sprdSeqConv)-1  %Cycle through delays of
    spread sequence
        re=circshift(sprdSeqConv',[0,x-1])*reshape(
           rxPilotI(1:pilotChips),length(sprdSeqConv),
           pilotLen); %Correlate with entire pilot
        im=circshift(sprdSeqConv',[0,x-1])*reshape(
           rxPilotQ(1:pilotChips),length(sprdSeqConv),
           pilotLen);
        chanEst(x)=(sum(re(1:pilotLen-1))/pilotLen)+(
           sum(im(1:pilotLen-1))/pilotLen)*1i; %Combine
```

```
            I and Q
end
[~,ind]=max(chanEst); %Choose strongest path to latch
   onto (expect 1st, LoS)

%% Convolution
%---despread & estimate---%
rxDataIbts=reshape(rxDataI(1:dataChips), length(
   sprdSeqConv),numDataBits/2); %Reshape for
   correlation with spread sequence
rxDataQbts=reshape(rxDataQ(1:dataChips), length(
   sprdSeqConv),numDataBits/2);

RxSymConv=rxDataIbts+1i*rxDataQbts; %Form complex Chip
   Symbols
RxdataConv=RxSymConv*max(chanEst)'; %Equalise with
   channel estimate

desprdDataI=sprdSeqConv'*real(RxdataConv); %Correlate
   with and integrate over spread sequence
desprdDataQ=sprdSeqConv'*imag(RxdataConv);
desprdDataConv=desprdDataI+desprdDataQ*1j; %Combine I
   and Q

estData=-ones(1,numDataBits); %Preallocation

for x=1:2:numDataBits %QPSK threshold detector
        if (angle(desprdDataConv((x+1)/2))>-pi/4)&&(
           angle(desprdDataConv((x+1)/2))<pi/4)
                estData(x)=1;
                estData(x+1)=1;
        elseif (angle(desprdDataConv((x+1)/2))>-3*pi/4)
           &&(angle(desprdDataConv((x+1)/2))<-pi/4)
                estData(x)=0;
                estData(x+1)=1;
        elseif (angle(desprdDataConv((x+1)/2))<3*pi/4)
           &&(angle(desprdDataConv((x+1)/2))>pi/4)
```

```
                        estData(x)=1;
                        estData(x+1)=0;
                elseif (angle(desprdDataConv((x+1)/2))<-3*pi/4)||(angle(desprdDataConv((x+1)/2))>3*pi/4)
                        estData(x)=0;
                        estData(x+1)=0;
                else disp((x+1)/2)
                end
        end

        %------Error count--------%
        errorsConv=sum(xor(estData,(randBits+1)*0.5)); %Sum errors
        erRateConv=errorsConv/length(randBits); %Calculate BER
        errOut(1,p)=erRateConv; %Store

        %---------------------------------%
        if ind~=1
                display('first path not strongest'); %Prints to MATLAB screen if first path not strongest: suggests error in system
        end
end

errRateTot=sum(errOut)/numPackets; %Calculations and data storage at end of each level transmission
errPacket=errOut>zeros(1,numPackets);
errPacketTot=sum(errPacket);
```

A.3 strDataConv2.m

```
%Converts string of data from the R&S spectrum analyser to numerical data array.
%Note that all variables declared here are private

function [dataI,dataQ]=strDataConv2(dataString) %Return dataI and dataQ from function
        bufferSize=length(dataString); %Set buffer
```

```
numberValues=floor(bufferSize/18); %No. values received
    from the R&S sig analyser
%18 is the number of characters per 1 piece of received
    data (1 character is a comma)
data=zeros(numberValues,1);%Preallocate space for data
mod=0; %allows an offset if a block of characters
   shorter than 18 occurs
for i=1:numberValues
        tmpdata=blanks(17); %Set array size
        k=0; %Reset counter to 0
        for j=(i-1)*18+1-mod:i*18-1-mod %Cycles 17
           times
                k=k+1; %Increment k
                tmpdata(k)=dataString(j); %Store
                   characters (not commas) into temp
                   variable
        end
        if tmpdata(13)==',' %When sample value 0, 13
           characters returned- account for this
                        tmpdata(13:17)='E+000'; %adds '
                           E+000' (missing section for
                           0 sample)
                        mod=mod+5; %Account for fewer
                           characters by adding an
                           offset
                end

                data(i)=str2double(tmpdata); %Convert
                   string to double
        end
        %Separate the I and Q data, received IQIQIQIQIQ
           ...
        dataI=data(1:2:end);
        dataQ=data(2:2:end);
end
```

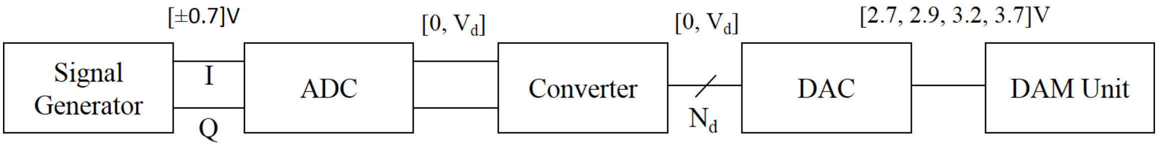

Figure B.1: Schematic of stages required of control electronics

Appendix B

Design of control electronics for FSS DAM

In order to convert the I and Q voltage signals into the 4-level PAM signal for the DAM unit, a set of control electronics was designed. The required stages of this system are shown in Fig. B.1. First, the signal generator I and Q values must be converted to a digital signal by some form of analogue to analogue to digital converter (ADC). As there are only 4 states, this can be represented by 2 digital lines, each of which takes the values 0 or V_d Volts, where V_d is the digital voltage high. These must then be converted into a digital signal representing the required bias voltages for the DAM unit to produce a QPSK constellation, which will require some N_d bits depending on the precision of the output voltage required. Finally, this digital signal is converted by a digital to analogue converter (DAC) into the bias voltages and sent to the DAM unit over a coaxial cable.

The first step was implemented by placing a LT1711 high-speed comparator on each baseband feed line, producing two parallel digital signals taking the values V_d=+5V or 0V. The comparators have rise and fall times of 4.5ns, so can operate at high symbol rates. The second and third steps, of Converter and DAC, are implemented using a non-linear DAC. This has the advantage of performing both steps at once while limiting the amount of digital electronics required, which can be expensive at the high frequency and high output voltages required. A ladder network was chosen as an implementation for its high speed of operation and flexibility. A linear ladder network, as described in Fig. B.2, has M digital

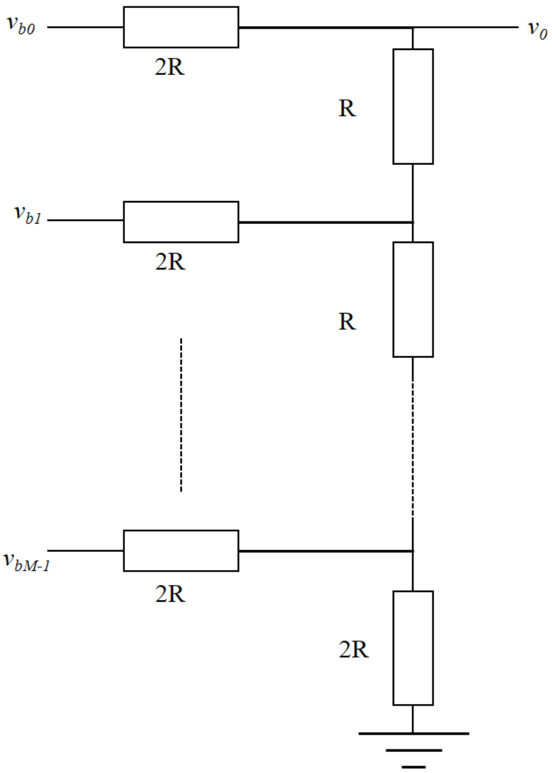

Figure B.2: Circuit diagram of classical R-2R resistive ladder network linear DAC

inputs v_{bm}=[0, V_d]V, representing binary bits b_m, with b_0 being the most significant bit. The network consists of $M-1$ resistors of some value $R\Omega$, and $M+1$ resistors of value $2R\Omega$. The voltage output is

$$v_0 = \sum_{m=0}^{M_{mod}-1} \frac{v_{bm}}{2^{M-m-1}} \tag{B.1}$$

This configuration gives a linear output in steps of $\frac{V_d}{2^{M_{mod}}}$, with a minimum output of 0V and a maximum output of $V_d(1-\frac{1}{2^M})$. However, if a non-linear response over a different range of voltages is required, different values of resistors should be used at different points in the ladder. While the output voltage can be calculated using nodal analysis, when all $2M_{mod}$ resistors and M_{mod} input voltages are variables, the equations quickly becomes unwieldy as M_{mod} increases. Further, not all combinations of output voltages are achievable using a ladder network, so many input values may cause the equations to suggest negative resistances are required.

Some design questions can be approached analytically, in particular the required number of inputs to the ladder network. The signal generator is limited to two outputs with two states each. However, using only digitised versions of these as the only two inputs would produce an output waveform with value V_{00}=0V when both I and Q are 0V. The minimum voltage required, however, is 2.7V. As such, the bottom input to the network should be

Digital word	Input from sig gen (V)	Desired output (V)	Simulated output (V)	Measured output (V)
V_{00}	-0.7,-0.7	2.7	2.65	2.63
V_{01}	-0.7,+0.7	2.9	2.95	2.93
V_{10}	+0.7,-0.7	3.7	3.64	3.57
V_{11}	+0.7,+0.7	3.2	3.18	3.18

Table B.1: Desired and achievable simulated output voltages for DAM bias conversion in response to different input voltages from the signal generator

a constant voltage to ensure that V_{00}=2.7V. While this could be any voltage input, for simplicity of circuit design V_s=5V was used. With these three inputs, the voltage output when both comparators output 5V would be $V_{01} + V_{10} - V_{00}$. However, due to the non-linear behaviour of the varactor diode, a larger jump in voltage is required to produce the desired capacitance value. As such, an AND gate formed of two diodes and a pull-up resistor was used to take the output of both comparators, and provide another input to the ladder network when both comparators produced 5V. In particular, Vishay 1N4148 diodes were used for their fast recovery time of 4ns. Note that this input will be less than 5V due to the forward voltage drop across the diodes, which here is 1V.

The circuit design for this implementation is shown in Fig. B.3. The required values of resistors to achieve the desired output voltages were explored through a Simulink model. For simplicity, the resistors between inputs were kept fixed at 20Ω. Low resistances were chosen to minimise the RC constant of the circuit once connected to the DAM unit, and so improve the rate of operation. The values of the input resistors were then explored through trial and error. First the resistor R_3 was chosen to achieve the desired minimum voltage V_{00}=2.7V, as this resistor has the greatest effect on the overall output. The values of R_0 and R_1 were then varied to give V_{01} and V_{10}, and finally R_2 was modified to find V_{11}. As the later changes can affect all output voltages, this process was iterated several times. The desired and achieved voltages are shown in Table B.1. Note that V_{11} is furthest from its desired value. This is because the rate-of-change of phase with respect to voltage is lowest at higher voltages due to the non-linear voltage-capacitance characteristic of the varactor diodes, so the constellation produced is more accurate when voltage error occurs at higher voltages. The quality of the constellation produced will be discussed in detail later in this chapter.

Through experimentation, it was found that the changing impedance of the DAM unit in response to the changing bias voltage affected the ladder network output. As such, at the output of the circuit, a unity gain buffer, made from a OPA354 op-amp, was used to isolate the ladder network from the changing impedance of the diodes in the FSS. The output was connected to the FSS layers in the DAM unit using a coaxial cable and twisted pairs of wires via a resistor, to limit the op-amp output current during voltage switching.

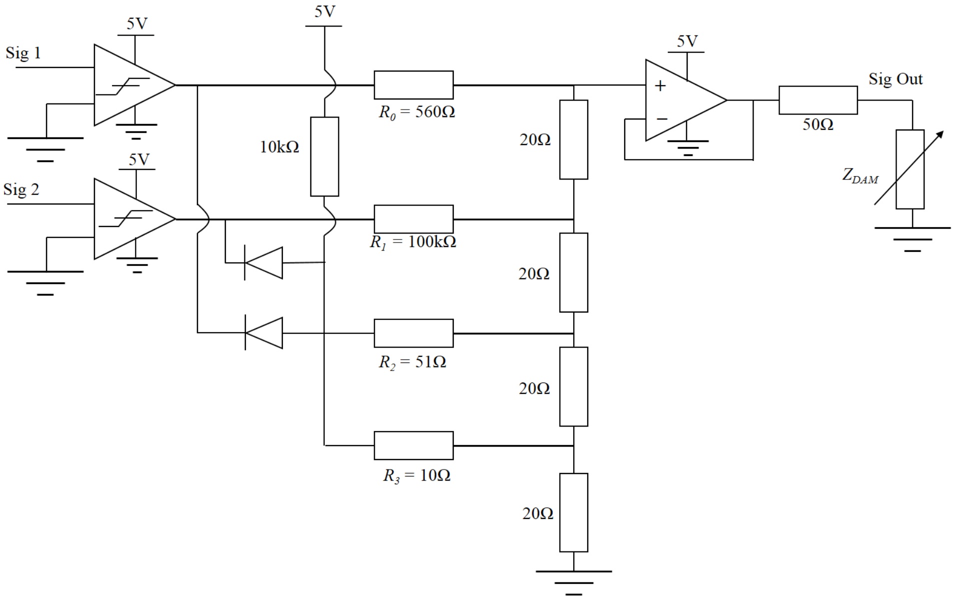

Figure B.3: Circuit diagram of control electronics for converting signal generator signals into FSS bias voltages

Appendix C

Standard Operating Procedure for Rohde & Schwarz Signal Generator and Signal Analyzer

Inserted below is the Standard Operating Procedure for the Rohde & Schwarz measurement equipment used in this thesis. While focussed on health and safety aspects, the document also includes setup procedures allowing the running of experiments in this thesis, with MATLAB code performing instrument control as outlined in Appendix A, Appendix D and Appendix E.

SOP Title: Use of Rohde and Schwarz Equipment for Signal Measurements

Stephen Henthorn **16/10/17**

Contents

1. PURPOSE

This SOP covers health and safety considerations for safe use of the Rohde and Schwarz (R&S) SMBV1000a Vector Signal Generator and FSV 30 Vector Signal Analyzer, located in the EEE Communications Research Labs (C34, C27) in the Portobello Centre.

2. INTRODUCTION

The R&S signal generator and signal analyzer are high performance design, test and measurement equipment. The setup is designed for the design, test and analysis of wireless communication systems. Both pieces of equipment may be used individually, together, or in conjunction with a PC running Windows OS. The details of the potential risks, relevant control measures and risk reduction procedures are detailed in risk assessment.

This SOP describes safe methods of use for the R&S test and measurement equipment, and setup procedures for conducting measurement of communications systems.
This SOP should be implemented and used in conjunction with local and University policies (where applicable), using relevant PPE and adhering to relevant legislation (such as the Health and Safety at Work act). Before operation of the R&S signal measurement kit users should have attended the necessary training course on operation of the equipment, be fully conversant with the content of this document and any appendices, and where necessary have made themselves familiar with the manufacturer's users' manual.

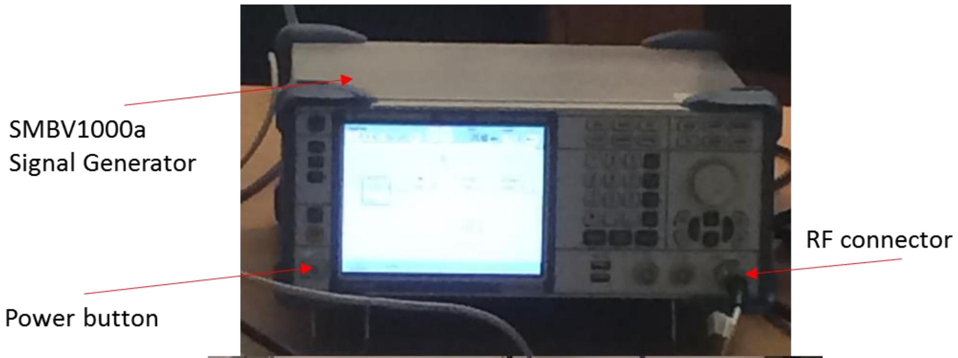

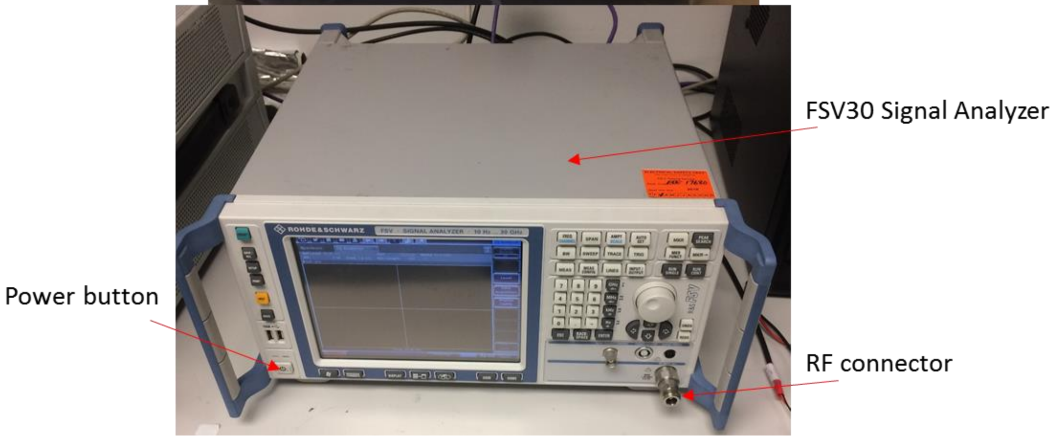

3. SCOPE

This SOP is intended for use by all EEE staff and students with permission from the Head of Department to use this equipment:

- R&S SMBV1000a Signal Generator and/or R&S FSV30 Signal Analyzer, EEE Communications laboratories, The Portobello Centre.

4. DEFINITIONS

SOP- Standard Operating Procedure

PPE – Personal Protective Equipment

R&S – Rohde and Schwarz

5. SPECIFIC PROCEDURE(S)

<u>Before using the R&S signal measurement equipment:</u>

1. Each operator should have performed a risk assessment of the activity.
2. Ensure that you have suitable PPE in place as outlined in the risk assessment.

3. Each operator should have read and reviewed the relevant operating/installing procedures and user manual for the specific module of the R&S kit.

4. Each operator will have received the appropriate training for the safe operation of the R&S kit and been signed off for use of the equipment. For training purpose, please get in touch with Stephen Henthorn or Prof Timothy O'Farrell.

5. Each operator will have successfully completed the Manual Handling course before moving the equipment.

6. Ensure that the Signal Generator, Signal Analyzer and controlling PC have been PAT tested and that their air vents are clear from obstruction.

7. Ensure that each individual piece of equipment is safely positioned on a suitable laboratory bench or table. The R&S equipment is designed to be stackable to reduce bench space.

8. Ensure that the area around the equipment is clear of obstructions to allow easy access to the front/back panels of the equipment.

9. Prior to connecting RF cables/antennas and connectors to the RF connector(s) of the signal analyzer and signal generator, ensure that they have been cleaned in accordance with the associated risk assessment.

10. Ensure that the coaxial cables and any other equipment (such as tripods) do not form a trip hazard during the test and measurements. Use appropriate fencing and hazard labels.

Turning ON the equipment:

11. Ensure that the vents in the equipment in use are not obstructed at any time.

12. Ensure the power cable in connected and turned on, and the master power switch at the rear of the required instrument(s) is turned "ON".

13. Use the power button on the front of the required instrument(s) to turn the equipment "ON".

14. The instrument(s) will boot up and begin operating the required software for operation.

Turning OFF the equipment:

15. Press the power button on the front of the instrument(s).

16. The software running on the instrument(s) will close down and the instrument(s) will power down. DO NOT REMOVE THE POWER UNTIL SHUTDOWN HAS COMPLETED.

17. Turn OFF the power switch on the rear of the instrument(s) and unplug the system.

18. Disconnect the coaxial cables. Store the cables and any other parts in a suitable location.

<u>Key connections:</u>

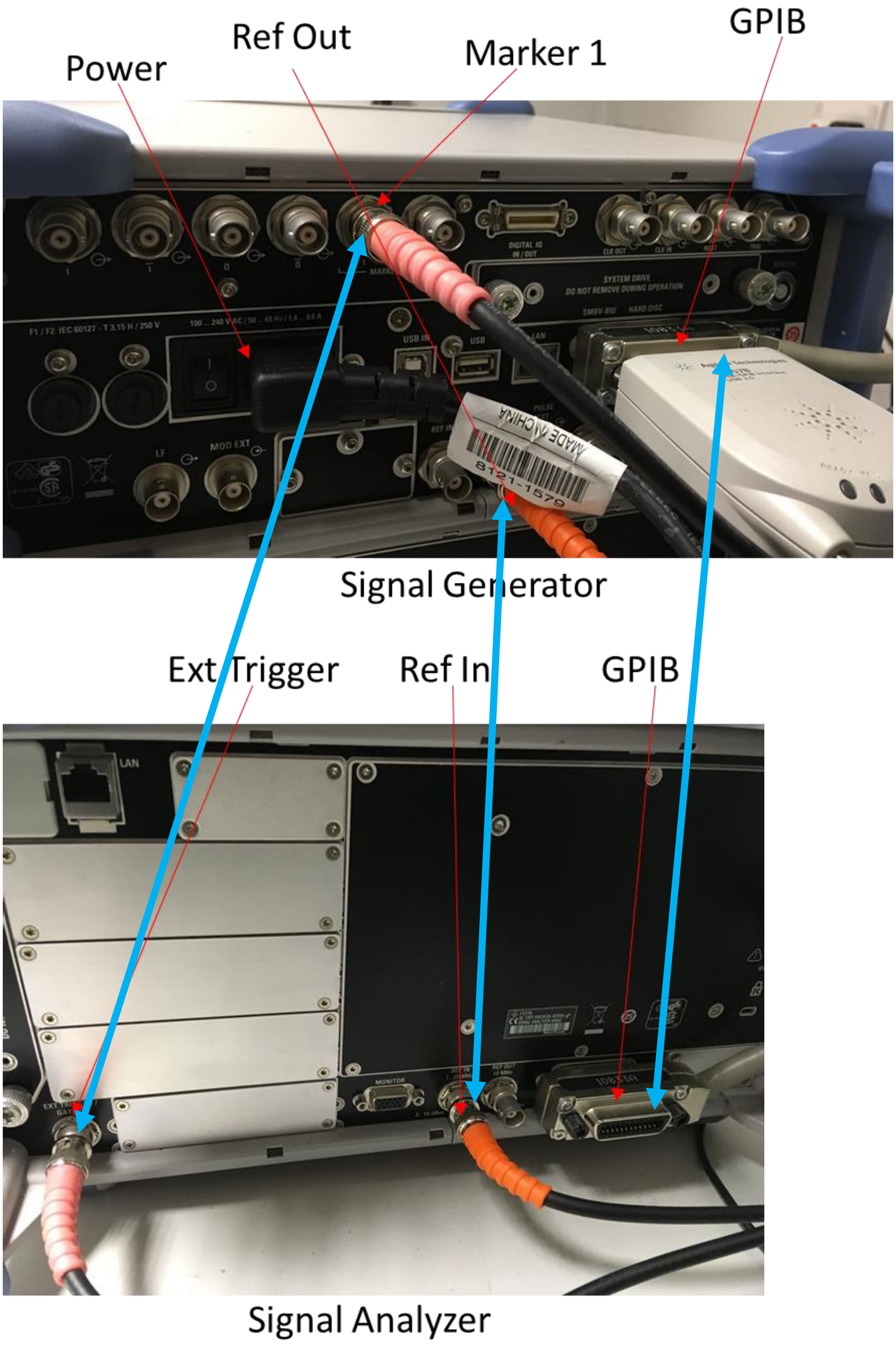

19. Sig Gen GPIB : Sig Analyzer GPIB : PC
20. Sig Gen Ref Out : Sig Analyzer Ref In

21. Sig Gen Marker 1 : Sig Analyzer Ext Trigger

<u>Sig Gen Setup:</u>

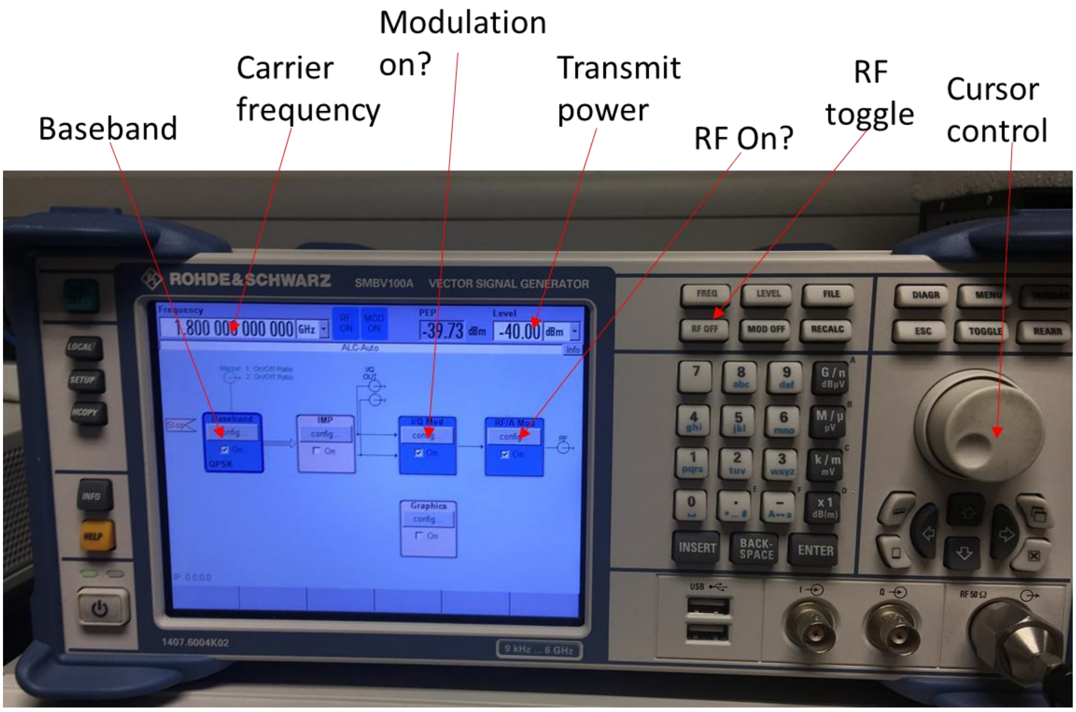

22. Check carrier frequency, transmit power (controlled by MATLAB)

23. Turn on RF (Box Blue for On)

24. Modulation: On for Conventional, Off for DAM

25. Baseband:

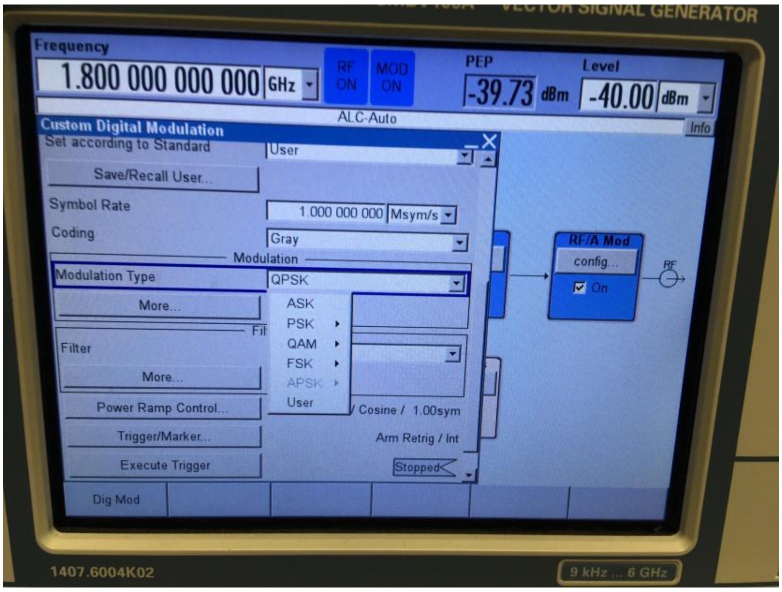

Frequency 1.800 000 000 000 GHz
PEP -39.73 dBm
Level -40.00 dBm
Custom Digital Modulation
Set according to Standard: User
Symbol Rate: 1.000 000 000 Msym/s
Coding: Gray
Modulation Type: QPSK

a. Choose modulation type
b. Choose coding (if appropriate)

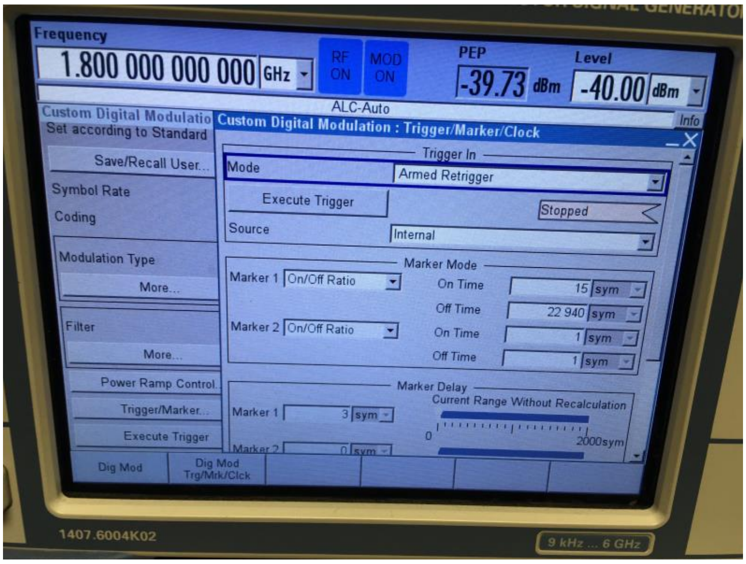

Frequency 1.800 000 000 000 GHz

PEP -39.73 dBm

Level -40.00 dBm

Custom Digital Modulation : Trigger/Marker/Clock

Trigger In

Mode: Armed Retrigger

Stopped

Source: Internal

Marker Mode

Marker 1: On/Off Ratio — On Time 15 sym, Off Time 22 940 sym

Marker 2: On/Off Ratio — On Time 1 sym, Off Time 1 sym

Marker Delay

Marker 1: 3 sym

Marker 2: 0 sym

c. Set Trigger to Armed Retrigger
d. Check Symbol Rate, Filter (controlled by MATLAB)

Signal Analyzer Setup:

26. After switch-on, all settings in the Signal Analyzer are controlled by MATLAB.

Emergency Procedures:

- Sudden operator illness e.g. stroke or heart attack.
- No other events have been defined as an emergency as a direct use of using this equipment.

27. Call for an ambulance using 999.

28. If anyone has been injured contact 4444 and inform the control room, request an ambulance if the injury is severe.

29. Notify other staff working in the workshop.

30. First aiders should administer appropriate first aid as required until the paramedics arrive.

31. Switch off the equipment at the mains power supply.

6. RESPONSIBILITIES

All EEE staff and students using the NI PXIe Test and Measurements equipment are responsible for adhering to the steps outlined in this SOP as well as the safety precautions outlined in the risk assessment.

Appendix D

MATLAB code for Continuous Phase FSS DAM

D.1 TestMultitestNumErrors

```
% Multitest- 07/18
% To be used in conjunction with EightPSKContinuousRun
% For finding BER and Throughputs of large amounts of data in
   DAM system

clear all
close all
instrreset;

tic %Keep track of time taken
%% VARIABLES
pilotLen=50; %Number of spread pilots
ambLen=15; %Length of postamble.
numDataBits=8000; %defines the number of data bits per packet.
   +1 for 8-PSK
freq='1.8GHz'; %Transmit frequency
sRate=2e6; %Sample rate (2*symbol rate)
modOrder=2; %Order of PSK modulation
lengthPilotSeq=15;  %Length of the pilot spread sequence
lengthPulseSeq=2; %Length of pulse shaping sequence
errRequired=100; %Number of bit errors required to get valid
   result
```

```
packErrRequired=10; %Number of packet errors required for valid result
numPackLimit=10000; %Limit to prevent running forever

numDataChips=numDataBits*lengthPulseSeq/modOrder; %Data length in chips
lengthIn=pilotLen*lengthPilotSeq*modOrder+numDataChips*modOrder*lengthPulseSeq+ambLen; %Length of the dataList in SigGen

level=-60:1:-40; %transmitting power (dBm). Can also set a range (eg. -20:2:-10)

if modOrder==2 %Set a phase offset for QPSK (pilots expected e^(jpi/4) & e^(-3jpi/4) not +/-1)
        pskOffset=pi;
elseif modOrder==1 || modOrder==3
        pskOffset=0;
else
        disp('Error in modOrder input: Value must be 1, 2 or 3'); %Check validity of modOrder input
end


%-----------------------------%

g1=visa('agilent','GPIB0::2::INSTR'); %Address spectrum analyser
g2=visa('agilent','GPIB0::28::INSTR'); %Address signal generator
bufsize=(numDataChips+pilotLen*lengthPilotSeq+ambLen)*18*2*2;%Sig gen buffer size totbits*seq length*wordlength*commas
g1.InputBufferSize=bufsize;
g2.OutputBufferSize= 5000000; %Arbitrary sig gen buffer
fopen(g1); %Open visa objects
fopen(g2);

%% Establishing connection
```

```matlab
%-spectrum analyser-%
fprintf(g1,'*RST;*CLS');
fprintf(g1,'*IDN?');
instID=fscanf(g1);
if isempty(instID)
        throw(MException('RSAIQCapture:ConnectionError','Unable to connect to instrument'));
end
disp(['Connection established with: ' instID]);

%-signal gen-%
fprintf(g2,'*CLS');
fprintf(g2,'*IDN?');
instID=fscanf(g2);
if isempty(instID)
        throw(MException('RSAIQCapture:ConnectionError','Unable to connect to instrument'));
end
disp(['Connection established with: ' instID]);

%% setting up
fprintf(g1,'inst iq');
fprintf(g1,['freq:center ' freq]);
fprintf(g1,'trac:iq:set norm,10MHz,22.5MHz,ext,pos,0,4080'); % -,-,sample rate,trigger source,trigger slope,pretrigger samples, number of samples
fprintf(g1,['trac:iq:rlen ' num2str(bufsize/(sRate/2e6))]); % Expected result length (time)
fprintf(g1,'system:disp:upd on');
fprintf(g1,'trac:iq:stat on');
fprintf(g1,['trac:IQ:SRAT ' num2str(sRate)]); %Sample at 2*symbol rate for Nyquist
fprintf(g1,'trac:iq:data:form iqp'); %Data format IQIQ

fprintf(g2,['sour:bb:dm:srat ' num2str(sRate/2)]);
fprintf(g2,['freq ' freq]);
```

```
fprintf(g2,'sour:bb:dm:filt:type rect'); %Rectangular filter on
    baseband data
fprintf(g2,'sour:bb:dm:sour dlis');

%% Sequences
mseq15lse=[1;0;0;1;1;0;1;0;1;1;1;1;0;0;0]*2-1;%lse
mseq15mse=[0;0;1;1;0;1;0;1;1;1;1;0;0;0;1]*2-1;%mse
periodicseq=[1;0;1;0;1;0;1;0;1;0;1;0;1;0]*2-1; %length 14
onlyoneseq =[1;1;1;1;1;1;1;1;1;1;1;1;1;1;1]*2-1;%length 15
if lengthPulseSeq == 2 %Pulse sequence 1 or [+ -]
        pulseSeq=[1,-1];
elseif lengthPulseSeq == 1
        pulseSeq=1;
else
        display('Spread sequence length error');
        break
end
pilotSeq=mseq15lse; %Pilot sequence

if modOrder==3 %Data describing BPSK (ie. opposite) pilots in
   each mod order
        pilot1=[0;0;0];
        pilot0=[1;1;0];
elseif modOrder==2
        pilot1=[1;1];
        pilot0=[0;0];
elseif modOrder==1
        pilot1=0;
        pilot0=1;
end

%% Preallocation calculations
pilotChips=pilotLen*length(pilotSeq);
ambChips=ambLen*length(pulseSeq);
streamLen=numDataChips+pilotChips;
sigGenBits=streamLen*modOrder+ambLen;
totValues=streamLen+ambLen; %Number of received samples
```

```
%% Preallocation
pilotSort=ones(modOrder,pilotLen);
postAmb=ones(1,ambLen); %Postamble: string of 1s
totSprdData=zeros(length(pulseSeq),numDataBits);
dataString=blanks(totValues);
estData=zeros(1,numDataBits);
pilotQ=zeros(1,pilotLen);
sprdData=-ones(1,totValues);
errOut=-ones(1,numPackLimit);
numErr=zeros(1,length(level));
numSymErr=zeros(1,length(level));

%% Find pilots
sprdPilot=reshape(pilotSeq*ones(1,pilotLen),1,pilotLen*length(
   pilotSeq)); %Pilot as +/- representation
for indPilot=1:pilotLen*length(pilotSeq) %Assign appropriate
   data sequence for desired pilots
        if sprdPilot(indPilot)==1
                pilotSort(:,indPilot)=pilot1;
        elseif sprdPilot(indPilot)==-1
                pilotSort(:,indPilot)=pilot0;
        else
                display('Error: Unexpected pilot inputs');
                return
        end
end
pilot=reshape(pilotSort,pilotLen*modOrder*length(pilotSeq),1);
   %Reshape as appropriate

%% Result preallocation
errorsCONV=zeros(1,numPackLimit);
totErrorsCONV=zeros(length(level),1);
erRateCONV=zeros(length(level),1);
throughput=zeros(length(level),1);

%% Fills allocated space with data
```

```
for levelInd=1:length(level) %Cycle through transmit powers
        fprintf(g2,['level ' num2str(level(levelInd))]);
        EightPSKContinuousRun; %Call m file to transmit and
          receive packets for this power
        display(['Cycles completed: ' num2str(levelInd) '/'
          num2str(length(level))]);

        erRateCONV(levelInd)=numErr(levelInd)/(p*numDataBits);
          %Calculate error rate for given transmit power
        symErRate(levelInd)=numSymErr(levelInd)/(p*numDataBits/
          modOrder); %Symbol error rate
        pErRate(levelInd)=errPacketTot/p; %Packet error rate
        throughput(levelInd)=(sRate/2/lengthPilotSeq)*log2(4)
          *(1-errPacketTot/numPackLimit);
        save('DataTemp','erRateCONV','symErRate','pErRate'); %
          Save to preserve data
        if(pErRate(levelInd))==0 %End cycle when no errors
          detected at transmit power
                display(['Zero error rate for ' num2str(
                  errRequired) ' bits at power level ' num2str
                  (levelInd)]);
        break
        end
end

for cv=1:levelInd %Display data for all transmit powers
        display(['---| Results for ' num2str(level(cv)) ' dBm
          |---']);
        display([' - Bit Error Rate     : ' num2str(erRateCONV(
          cv))]);
        display([' - Symbol Error Rate : ' num2str(symErRate(cv
          ))]);
        display([' - Packet Error Rate : ' num2str(pErRate(cv))
          ]);
        display(' ');
end
```

```
if length(level)>2 %Plot results
        figure;
        semilogy(level,erRateCONV,'bx-');
        title('Bit Error Rates');xlabel('Level (dBm)');ylabel('
           Error Rate');
        legend('','Conventional','Location','sw');
        axis([min(level) max(level) 10^-4 1]);
        figure
        semilogy(level(1:levelInd),symErRate)
        figure
        semilogy(level(1:levelInd),pErRate)
end
toc %Time for total measurement
```

D.2 EightPSKContinuousRun

```
% EightPSKContinuousRun  07/18
% For use with TestmultitestNumErrors
% To get BER and throughput of large amount of data in multi-
   order DAM system

for p=1:numPackLimit
        %% Generating random data
        randBits=randi([0 1],1,numDataBits); %1s and 0s here,
           easier for modulation function

        %% Modulation and spreading
        sprdAmb=postAmb; %Postamble isn't spread here

        data=reshape(randBits,modOrder,numDataBits/modOrder); %
           Reshape for modulation
        dataDec=bi2de(data.'); %Convert binary data to decimal
           for modulation
        dataMod=pskmod(fliplr(dataDec),2^modOrder,0,'gray'); %
           MATLAB modulation function, symbol stream out
        sprdDataMod=dataMod*pulseSeq; %Pulse shaping of symbol
           stream
        sprdDataDec=pskdemod(sprdDataMod,2^modOrder,0,'gray');
```

```
   %Convert shaped symbol stream to decimal
   representation
sprdDataBin=fliplr(de2bi(reshape(sprdDataDec.',
   numDataBits*length(pulseSeq)/modOrder,1),modOrder));
    %Convert decimal to binary shaped symbol stream
sprdDataBinReshape=reshape(sprdDataBin.',1,numDataBits*
   length(pulseSeq)); %Reshape to linear sequence

%% Assembling data packet
dataIn=[pilot;sprdDataBinReshape.';sprdAmb.'];

%% Transmitting data
for count=1:length(dataIn) %Convert stream to char
   string of 1s and 0s, separated by commas
        dataString(2*count-1)=num2str(dataIn(count));
        dataString(2*count)=',';
end

%% Receiving Data
listIn=dataString(1:length(dataIn)*2-1);%Remove last
   comma
sigDur=num2str(totValues/2); %Signal duration
ind=2; %Ensure run while loop at least once
while ind~=1 %While so can resend packet if sync error
   occurs
        fprintf(g2,['sour:bb:dm:trig:slen ' sigDur]);
        fprintf(g2,['bb:dm:dlis:data ' listIn]); %Data
           into sig gen
        display(['Sent ' num2str(p) ' packets']);

        pause(1) %Delay to allow transmit&read of
           signal

        %% Data gathering into I and Q components
        DataIn='';
        while(size(DataIn)==0) %Ensure data received
                clrdevice(g1); %Clears buffers
```

```
        clrdevice(g2);
        fprintf(g1,'trac:iq:data?'); %Expect
           data at analyzer
        fprintf(g2,'sour:bb:dm:trig:exec'); %
           Trigger sig gen to transmit data
        DataIn=fscanf(g1); %Collect char string
            from analyzer
end

[samplesI,samplesQ]=strDataConv2(DataIn); %Call
    function strDataConv2 to convert string to
   I and Q vectors of doubles

dataI1=samplesI(1:2:end); %Recombination of
   samples: Which has most power? Varies due to
    delay
dataQ1=samplesQ(1:2:end);
dataI2=samplesI(2:2:end);
dataQ2=samplesQ(2:2:end);

powr1=sum(dataI1.^2+dataQ1.^2); %Power of each
powr2=sum(dataI2.^2+dataQ2.^2);

if powr1>powr2 %Choose set of samples with
   greatest amount of power
        dataI=dataI1;
        dataQ=dataQ1;
        powrHold(p)=powr1;
else
        dataI=dataI2;
        dataQ=dataQ2;
        powrHold(p)=powr2;
end

rxDataI=dataI((pilotChips)+1:(pilotChips+
   numDataChips)); %Remove pilot and postamble
   from data
```

```
        rxDataQ=dataQ((pilotChips)+1:(pilotChips+
           numDataChips));
        rxPilotI=dataI(1:pilotChips); %Extract pilot
        rxPilotQ=dataQ(1:pilotChips);

        %% Channel estimate
        chanEst=-ones(1,lengthSprdSeq-1);
        for x=1:length(pilotSeq)-1 %Cycle through
           delays of pilot sequence
                re=circshift(pilotSeq',[0,x-1])*reshape
                   (rxPilotI(1:pilotChips),length(
                   pilotSeq),pilotLen); %Correlate with
                    pilot
                im=circshift(pilotSeq',[0,x-1])*reshape
                   (rxPilotQ(1:pilotChips),length(
                   pilotSeq),pilotLen);
                chanEst(x)=(sum(re(1:pilotLen-1))/
                   pilotLen)+(sum(im(1:pilotLen-1))/
                   pilotLen)*1i; %Calculate channel
                   estimate
        end
        [~,ind]=max(chanEst); %Choose strongest path
                if abs(max(chanEst))<1.5*abs(max(
                   chanEst(chanEst~=max(chanEst)))) %
                   Check that strongest path
                   significantly stronger than 2nd
                   strongest- should be true for LoS
                ind=2; %To force reprocessing
        end
                if ind~=1
                disp('Sync error: 1st path not the
                   strongest, reprocessing');
        end
end

%% Convolution
%---despread & estimate---%
```

```
rxDataIbts=reshape(rxDataI(1:numDataChips), length(
   pulseSeq),numDataBits/modOrder); %Shape data for
   correlation with pulse
rxDataQbts=reshape(rxDataQ(1:numDataChips), length(
   pulseSeq),numDataBits/modOrder);

RxSymConv=rxDataIbts+1i*rxDataQbts;%Form complex
   symbols
RxdataConv=RxSymConv*max(chanEst)'; %Equalise with
   channel estimate

desprdDataConv=pulseSeq*RxdataConv; %Correlate with
   pulse shaping sequence

demodData=pskdemod(desprdDataConv,2^modOrder,pskOffset,
   'gray'); %MATLAB PSK demodulation function
estDataOrg=de2bi(demodData,modOrder); %Convert data to
   binary from decimal
estData=reshape(estDataOrg.',numDataBits,1);

%------error count--------%
compare=xor(estData,randBits.'); %Find any errors
errorsConv=sum(compare); %Sum errors
erRateConv=errorsConv/length(randBits); %Calculate BER
errOut(levelInd,p)=erRateConv;
numErr(levelInd)=numErr(levelInd)+errorsConv;

display([num2str(errOut(levelInd,p)*numDataBits) '
   errors in Packet ' num2str(p)]);

compareOrder=reshape(compare,modOrder,numDataBits/
   modOrder);
symErrOut=sum(compareOrder,1)>0; %Find symbol errors
numSymErr(levelInd)=sum(symErrOut)+numSymErr(levelInd);
errPacket=errOut(levelInd,:)>zeros(1,numPackLimit); %If
    errors present, packet error recorded
```

```
        %---------------------------------------%
        if ind~=1
                display('first path not strongest'); %prints to
                    MATLAB screen indicating the first path is
                   not the strongest
        end

        if sum(numErr(levelInd))>=errRequired && sum(errPacket)
           >=packErrRequired && p>=minPackets %Bit-error
           requirement
                measPacks(levelInd)=p;
                display([num2str(sum(numErr(levelInd))) '
                   errors found after ' num2str(p) ' packets
                   transmitted']);
                break %Exit loop when enough bit errors found
        end

        toc %Keep track of time taken every packet
end

errRateTot=sum(errOut)/p; %Store data at end of loop (transmit
   power)
errPacketTot=sum(errPacket);
display([num2str(sum(numErr(levelInd))) ' bit errors and '
   num2str(errPacketTot) ' packet errors found after ' num2str(
   p) ' packets transmitted']);
```

Appendix E

MATLAB code for CPDSSS

E.1 Multitest

```
% Multitest- 01/19
% To be used in conjunction with DSSCPContinuousRun
% For finding BER, PER of CDSSS scheme in multipath channels,
   with and without DAM transmitter

clear all
close all
instrreset;

tic
%% VARIABLES
pilotLen=10; %Pilot repetitions
ambLen=6; %Length of post-amble.
numDataBits=1002; %Number of data bits per packet
freq='1.8GHz'; %Transmit frequency
sRate=1e6; %Symbol rate
overSample=2; %Oversampling rate
modOrder=3; %PSK modulation order
lengthPilotSeq=15;  %Pilot sequence length
lengthSprdSeq=7; %Length of spreading sequence
chanLength=5; %Channel length, for synchronisation error check
cpLength=4; %Length of CP
numFingers=1; %Number of RAKE fingers (1, chanLength)
errRequired=100; %Number of bit errors required to get valid
```

```
   result (For fading channel should be packet based)
packErrRequired=60; %Number of packet errors required for valid
    result
numPackLimit=10000; %Limit to prevent running forever

numDataChips=numDataBits*(lengthSprdSeq+cpLength)/modOrder;
lengthIn=pilotLen*lengthPilotSeq*modOrder+numDataChips*modOrder
   *(lengthSprdSeq+cpLength)+ambLen; %Length of the dataList in
    SigGen

level=-70:2:-40; %transmitting power (dBm). Can also set a
   range (eg. -75:2:-50)

%% Sequences
% sprdSeq=[0;0;0;1].'*2-1; %Barker 4
sprdSeq=[1,1,1,0,0,1,0]*2-1; %Barker 7
% sprdSeq=[1,1,1,0,0,0,1,0,0,1,0]*2-1; %Barker 11
pilotSeq=[0;0;1;1;0;1;0;1;1;1;1;0;0;0;1]*2-1; %Pilot sequence (
   m15)

%% Offset
if modOrder==2 %Offset for QPSK modulation
        pskOffset=pi;
elseif modOrder==1 || modOrder==3
        pskOffset=0;
else
        disp('Error in modOrder input: Value must be 1, 2 or 3'
           );
end


%--------------------------------%

g1=visa('agilent','GPIB0::2::INSTR'); %Address sig analyzer
g2=visa('agilent','GPIB0::28::INSTR'); %Address sig gen
bufsize=(numDataChips+pilotLen*lengthPilotSeq+ambLen)*18*2*
   overSample;%Analyzer result buffer, totchips*wordlength*
```

```
   commas*oversample
g1.InputBufferSize=bufsize;
g2.OutputBufferSize= 5000000; %Abitrary sig gen buffer
fopen(g1); %Open VISA objects
fopen(g2);

%% Establishing connection
%-spectrum analyser-%
fprintf(g1,'*RST;*CLS');
fprintf(g1,'*IDN?');
instID=fscanf(g1);

if isempty(instID)
        throw(MException('RSAIQCapture:ConnectionError','Unable
            to connect to instrument'));
        end
disp(['Connection established with: ' instID]);

%-signal gen-%
fprintf(g2,'*CLS');
fprintf(g2,'*IDN?'); %get ID
instID=fscanf(g2);

if isempty(instID)
        throw(MException('RSAIQCapture:ConnectionError','Unable
            to connect to instrument'));
        end
disp(['Connection established with: ' instID]);

%% Set up
fprintf(g1,'inst iq');
fprintf(g1,['freq:center ' freq]);
fprintf(g1,'trac:iq:set norm,10MHz,22.5MHz,ext,pos,0,4080'); %
   -,-,sample rate,trigger source,trigger slope,pretrigger
   samples, number of samples
fprintf(g1,['trac:iq:rlen ' num2str(bufsize/(sRate/2e6))]); %
   Expected result length at receiver (time)
```

```
fprintf(g1,'system:disp:upd on');
fprintf(g1,'trac:iq:stat on');
fprintf(g1,['trac:IQ:SRAT ' num2str(sRate*overSample)]); %
   Sample at oversample*symbol rate
fprintf(g1,'trac:iq:data:form iqp'); %Data format IQIQ

fprintf(g2,['sour:bb:dm:srat ' num2str(sRate)]);
fprintf(g2,['freq ' freq]);
fprintf(g2,'sour:bb:dm:filt:type rect'); %Rectangular filter on
    baseband data
fprintf(g2,'sour:bb:dm:sour dlis');

%% Pilots
if modOrder==3 %Define data sequence for pilot symbols
        pilot1=[0;0;0];
        pilot0=[1;1;0];
elseif modOrder==2
        pilot1=[1;1];
        pilot0=[0;0];
elseif modOrder==1
        pilot1=0;
        pilot0=1;
end

%% Preallocation calculations
pilotChips=pilotLen*length(pilotSeq);
streamLen=numDataChips+pilotChips;
sigGenBits=streamLen*modOrder+ambLen;
totValues=streamLen+ambLen; %Number of received samples

%% Fill matrices
pilotSort=ones(modOrder,pilotLen); %Pilot all ones, spread
   later
postAmb=ones(1,ambLen); %Postamble 1s only
totSprdData=zeros(length(sprdSeq),numDataBits);
dataString=blanks(totValues);
```

```
estData=zeros(1,numDataBits);
pilotQ=zeros(1,pilotLen);
sprdData=-ones(1,totValues);
numErr=zeros(1,length(level));
numSymErr=zeros(1,length(level));

%% Find pilots
sprdPilot=reshape(pilotSeq*ones(1,pilotLen),1,pilotLen*length(
   pilotSeq)); %Pilot sequence on pilots as +/-
for indPilot=1:pilotLen*length(pilotSeq) %Assign appropriate
   data sequence (1s and 0s) for spread pilot
        if sprdPilot(indPilot)==1
                pilotSort(:,indPilot)=pilot1;
        elseif sprdPilot(indPilot)==-1
                pilotSort(:,indPilot)=pilot0;
        else
                display('Error: Unexpected pilot inputs');
                return
        end
end
pilot=reshape(pilotSort,pilotLen*modOrder*length(pilotSeq),1);

%% Preallocation
errorsCONV=zeros(1,numPackLimit);
totErrorsCONV=zeros(length(level),1);
erRateCONV=zeros(length(level),1);
throughput=zeros(length(level),1);
symErrHold=zeros(length(level),numDataBits/modOrder);

%% Fills allocated space with data
for levelInd=1:length(level) %Cycle through transmit powers
        fprintf(g2,['level ' num2str(level(levelInd))]); %Set
           transmit power
        errPacket=zeros(1,numPackLimit);
        DSSSCPContinuousRun; %Call m file and cycle through
           packets
        display(['Cycles completed: ' num2str(levelInd) '/'
```

```
           num2str(length(level))]);

        erRateCONV(levelInd)=numErr(levelInd)/(p*numDataBits);
           %Store error rate data
        symErRate(levelInd)=numSymErr(levelInd)/(p*numDataBits/
           modOrder);
        pErRate(levelInd)=errPacketTot/p;
        throughput(levelInd)=(sRate/lengthPilotSeq)*log2(4)*(1-
           errPacketTot/numPackLimit);
        save('DataTemp','erRateCONV','symErRate','pErRate','
           symErrHold','level'); %Save data

        if(errPacketTot)<packErrRequired  %Break when not
           enough packet errors found for statistical
           siginificance
                display(['Statistically insignificant packet
                   error rate for ' num2str(errRequired) ' bits
                    at power level ' num2str(levelInd)]);
                break
        end
end

for cv=1:levelInd %Display all results
        display(['---| Results for ' num2str(level(cv)) ' dBm
           |---']);
        display([' - Bit Error Rate    : ' num2str(erRateCONV(
           cv))]);
        display([' - Symbol Error Rate : ' num2str(symErRate(cv
           ))]);
        display([' - Packet Error Rate : ' num2str(pErRate(cv))
           ]);
        display(' ');
end

if length(level)>2 %Plot error rates
        figure;
        semilogy(level,erRateCONV,'bx-');
```

```
        title('Bit Error Rates');xlabel('Level (dBm)');ylabel('
           Error Rate');
        legend('','Conventional','Location','sw');
        axis([min(level) max(level) 10^-4 1]);

        figure
        semilogy(level(1:levelInd),symErRate)

        figure
        semilogy(level(1:levelInd),pErRate)
end

toc
```

E.2 DSSSCPContinuousRun

```
% DSSSCPContinuousRun  01/19
% For use with Multitest
% For finding BER, PER of CDSSS scheme in multipath channels,
   with and without DAM transmitter


for p=1:numPackLimit %Keeps from running forever
        %% Generating random data
        randBits=randi([0 1],1,numDataBits); %Data as 1s and 0s

        %% Spreading
        sprdAmb=postAmb; %Postamble not spread

        if cpLength==0 %If no CP, spread sequence is spread
           sequence
                sprdSeqCP=sprdSeq;
        else %If CP present, define extended cyclic spread
           sequence
                sprdSeqCP=[sprdSeq(:,length(sprdSeq)+1-cpLength
                   :end),sprdSeq];
        end
```

```
data=reshape(randBits,modOrder,numDataBits/modOrder); %
   Reshape binary data into modOrder nibbles
dataDec=bi2de(data.'); %Convert nibbles to decimal
dataMod=pskmod(fliplr(dataDec),2^modOrder,0,'gray'); %
   MATLAB PSK modulation function

sprdDataMod=dataMod*sprdSeqCP; %Spread with extended
   sequence
sprdDataDec=pskdemod(sprdDataMod,2^modOrder,0,'gray');
   %Demodulate spread symbols into decimal data
sprdDataBin=fliplr(de2bi(reshape(sprdDataDec.',
   numDataBits*length(sprdSeqCP)/modOrder,1),modOrder))
   ; %Convert back to binary
sprdDataBinReshape=reshape(sprdDataBin.',1,numDataBits*
   length(sprdSeqCP)); %Vector of cyclically spread
   binary data


%% Assembling data packet
dataIn=[pilot;sprdDataBinReshape.';sprdAmb.'];

%% Transmitting data
for count=1:length(dataIn) %Convert data into char
   string of 1s, 0s and commas for sig gen
        dataString(2*count-1)=num2str(dataIn(count));
        dataString(2*count)=',';
end

%% Receiving Data
listIn=dataString(1:length(dataIn)*2-1);%Remove comma
sigDur=num2str(totValues/2); %Define length of
   transmitted signal
checkSync=0; %1==sync correct; 0==sync not established
while checkSync~=1 %While loop so can resend packet if
   sync error occurs
        fprintf(g2,['sour:bb:dm:trig:slen ' sigDur]);
```

```
fprintf(g2,['bb:dm:dlis:data ' listIn]); %Send
   data to sig gen
display(['Sent ' num2str(p) ' packets']);

pause(1) %Delay to allow transmit&read of
   signal

%% Data gathering into I and Q components
DataIn=''; %Clear variable from previous loop
while(size(DataIn)==0) %Ensure data collected
        clrdevice(g1); %Clear device buffers
        clrdevice(g2);
        fprintf(g1,'trac:iq:data?'); %Analyzer
           ready for data
        fprintf(g2,'sour:bb:dm:trig:exec'); %
           Trigger sig gen to transmit
        DataIn=fscanf(g1); %stores string of
           data from sig analyser
end

[samplesI,samplesQ]=strDataConv2(DataIn); %Call
    function strDataConv2 to convert char
   string data to double vectors

dataISet=zeros(length(samplesI)/overSample,
   overSample); %Preallocate
dataQSet=zeros(length(samplesQ)/overSample,
   overSample);
for iD=1:overSample %Sort data into samples
        dataISet(:,iD)=samplesI(iD:overSample:
           end);
        dataQSet(:,iD)=samplesQ(iD:overSample:
           end);
end

powr=sum(dataISet.^2+dataQSet.^2,1);
[maxPowr,powrInd]=max(powr); %Choose set of
```

```
  samples with maximum power- ie. best chip-
  level sync

dataI=dataISet(:,powrInd);
dataQ=dataQSet(:,powrInd);

adjustSync=1; %Ensure loop runs at least once
while adjustSync==1 %While loop for adjusting
  bad sync, bad while adjustSync=1
      rxDataI=dataI((pilotChips)+1:(
        pilotChips+numDataChips)); %Extract
        received data chips
      rxDataQ=dataQ((pilotChips)+1:(
        pilotChips+numDataChips));
      rxPilotI=dataI(1:pilotChips); %Extract
        received pilot
      rxPilotQ=dataQ(1:pilotChips);

      %% Channel estimate
      chanEst=-ones(1,lengthSprdSeq-1);
      for x=1:length(pilotSeq)-1 %From 1 to
        14
            re=circshift(pilotSeq',[0,x-1])
              *reshape(rxPilotI(1:
              pilotChips),length(pilotSeq)
              ,pilotLen); %Correlate with
              pilot sequence
            im=circshift(pilotSeq',[0,x-1])
              *reshape(rxPilotQ(1:
              pilotChips),length(pilotSeq)
              ,pilotLen);
            chanEst(x)=(sum(re(1:pilotLen
              -1))/pilotLen)+(sum(im(1:
              pilotLen-1))/pilotLen)*1i; %
              Complex channel estimate
      end
      [~,ind]=max(chanEst); %Find strongest
```

```
                   path

                        if abs(chanEst(1))<abs(chanEst(
                           chanLength+1)) %If 1st path
                           less than chanLength+1th
                           path, assume sync error (
                           delayed by 1 chip): adjust
                           by one and check again
                        dataI=circshift(dataI,-1,1);
                        dataQ=circshift(dataQ,-1,1);
                        display('Adjustment made');
                else
                        adjustSync=0;
                end
        end

        if sum(abs(chanEst(1:chanLength)))>sum(abs(
           chanEst(chanLength+1:chanLength*2+1)))
        checkSync=1; %If more power in expected channel
            length than equivalent no. paths after it,
           good sync
        end

        if checkSync~=1 %If sync is bad, reprocess:
           Back to start of while loop
        disp('Sync error: Strongest path not strong
           enough, reprocessing');
        end
end

%% Assemble and remove CP
rxDataIbtsCP=reshape(rxDataI(1:numDataChips), length(
   sprdSeqCP),numDataBits/modOrder);
rxDataQbtsCP=reshape(rxDataQ(1:numDataChips), length(
   sprdSeqCP),numDataBits/modOrder);
rxDataCP=rxDataIbtsCP+1j*rxDataQbtsCP; %Complex chip
   symbols
```

```
rxData=rxDataCP(cpLength+1:end,:); %Remove CP

%% Channel equalisation
if numFingers == 1 %Where no RAKE, use strongest path
        rxDataConv=circshift(rxData,-ind+1,1)*chanEst(
           ind)'; %Circshift occurs within each spread
           symbol
else %Where RAKE, gather energy from 1st path to
   numFingersth path
        filtEach=zeros([size(rxData),numFingers]);
        for pathInd=1:numFingers
                filtEach(:,:,pathInd)=circshift(rxData
                   ,-pathInd+1,1)*chanEst(pathInd)';
        end
        rxDataConv=squeeze(sum(filtEach,3));
end

%% Correlation with sequence
desprdDataConv=sprdSeq*rxDataConv; %Despread and
   integrate chips over sequence length

demodData=pskdemod(desprdDataConv,2^modOrder,pskOffset,
   'gray'); %MATLAB function for PSK demodulation
estDataOrg=de2bi(demodData,modOrder); %Decimal to
   binary data
estData=reshape(estDataOrg.',numDataBits,1); %Reshape
   for error finding

%------error count--------%
compare=xor(estData,randBits.'); %Find any errors
errorsConv=sum(compare);
erRateConv=errorsConv/length(randBits); %Calculate BER
numErr(levelInd)=numErr(levelInd)+errorsConv; %Running
   total of errors
display([num2str(errorsConv) ' errors in Packet '
   num2str(p)]);
```

```
        compareOrder=reshape(compare,modOrder,numDataBits/modOrder);
        symErrOut=sum(compareOrder,1)>0; %Find symbol errors
        numSymErr(levelInd)=sum(symErrOut)+numSymErr(levelInd);
        errPacket(p)=errorsConv>0; %If errors, packet error recorded
        display([num2str(sum(errPacket)) ' packet errors measured']);

        %----------------------------------%
        if ind~=1
                display('first path not strongest'); %prints to MATLAB screen indicating the first path is not the strongest
        end

        if sum(numErr(levelInd))>=errRequired && sum(errPacket)>=packErrRequired && p>=minPackets %Bit-error requirement
                measPacks(levelInd)=p;
                display([num2str(sum(numErr(levelInd))) ' errors found after ' num2str(p) ' packets transmitted']);
                break %End loop when enough packet errors found
        end

        toc
end

errPacketTot=sum(errPacket);
display([num2str(sum(numErr(levelInd))) ' bit errors and ' num2str(errPacketTot) ' packet errors found after ' num2str(p) ' packets transmitted']);
```

Appendix F

Standard Operating Procedure for Spirent SR5500 Wireless Channel Emulator

Inserted below is the Standard Operating Procedure for the Spirent 5500 Wireless Channel Emulator used in Chapter 6 of this thesis. While focussed on health and safety aspects, the document also includes setup procedures allowing the production of repeatable broadband fading channels for evaluating wireless communications systems. In conjunction with the Rohde & Schwarz equipment, with standard operation defined in Appendix C, and the MATLAB code in Appendix E, this gives an overview of procedures for carrying out the experiments described in Chapter 6.

SOP Title: Use of Spirent SR5500 Wireless Channel Emulator for production of repeatable wireless channels

Stephen Henthorn **10/07/19**

Contents

1. PURPOSE

This SOP covers health and safety considerations for safe use of the Spirent SR5500 Wireless Channel Emulator, located in the EEE Communications Research Labs (C34, C27) in the Portobello Centre.

2. INTRODUCTION

The Spirent SR5500 Wireless Channel Emulator is a highly accurate emulator of complex wideband channel characteristics. Used in conjunction with the Rohde & Schwarz Signal Generator and Signal Analyzer, it may be used to provide highly repeatable channels for the measurement of wireless communications systems. It is run in conjunction with a laptop PC operating Spirent proprietary software. The details of the potential risks, relevant control measures and risk reduction procedures are detailed in risk assessment.

This SOP describes safe methods of use for the Spirent channel emulator to produce wideband fading channels.
This SOP should be implemented and used in conjunction with local and University policies (where applicable), using relevant PPE and adhering to relevant legislation (such as the Health and Safety at Work act). Before operation of the Spirent Wireless Channel Emulator users should have attended the necessary training course on operation of the equipment, be fully conversant with the content of this document and any appendices, and where necessary have made themselves familiar with the manufacturer's users' manual.

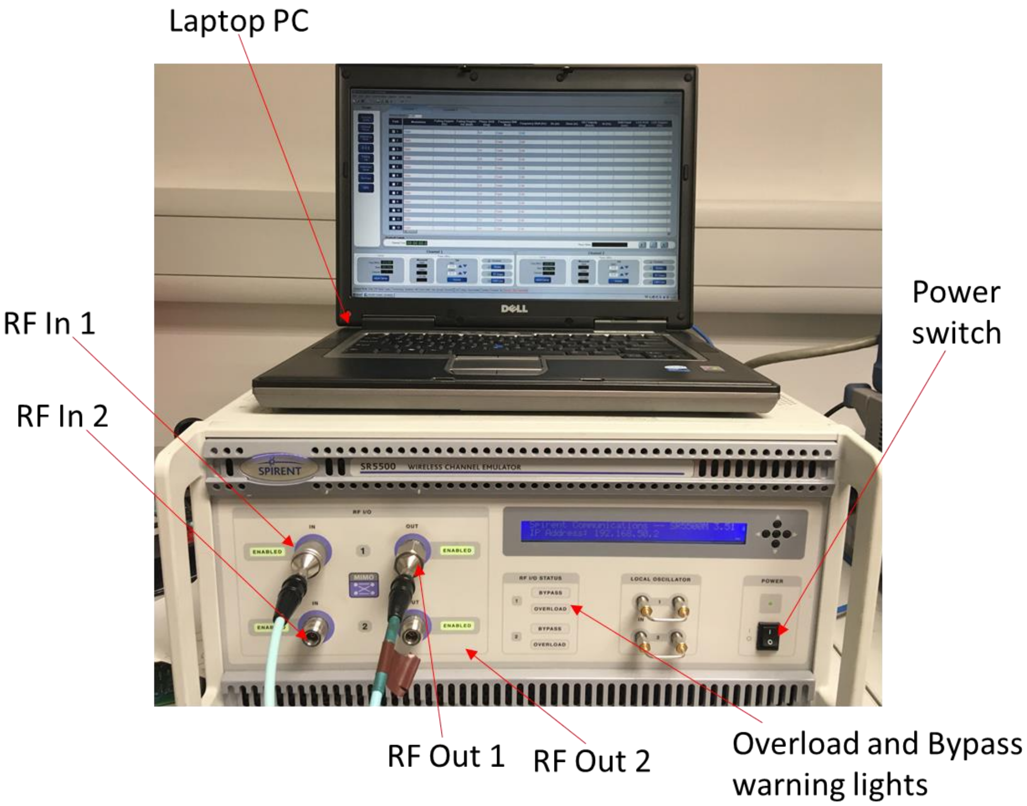

3. SCOPE

This SOP is intended for use by all EEE staff and students with permission from the Head of Department to use this equipment:

- Spirent SR5500 Wireless Channel Emulator, EEE Communications laboratories, The Portobello Centre.

4. DEFINITIONS

SOP- Standard Operating Procedure

PPE – Personal Protective Equipment

5. SPECIFIC PROCEDURE(S)

<u>Before using the Channel Emulator:</u>

1. Each operator should have performed a risk assessment of the activity.
2. Ensure that you have suitable PPE in place as outlined in the risk assessment.
3. Each operator will have received the appropriate training for the safe operation of the Channel Emulator and been signed off for use of the equipment. For training purpose, please get in touch with Stephen Henthorn or Prof Timothy O'Farrell.

4. Each operator will have successfully completed the Manual Handling course before moving the equipment.

5. Ensure that the Channel Emulator and controlling PC have been PAT tested and that their air vents are clear from obstruction.

6. Ensure that each individual piece of equipment is safely positioned on a suitable laboratory bench or table. The laptop PC may sit on top of the Channel Emulator as long as vents are clear.

7. Ensure that the area around the equipment is clear of obstructions to allow easy access to the front/back panels of the equipment.

8. Prior to connecting RF cables/antennas and connectors to the RF connector(s) of the Channel Emulator, ensure that they have been cleaned in accordance with the associated risk assessment.

9. Prior to injecting RF into Channel Emulator, ensure power levels below -30dBm.

10. Ensure that the coaxial cables and any other equipment (such as tripods) do not form a trip hazard during the test and measurements. Use appropriate fencing and hazard labels.

Turning ON the equipment:

11. Ensure that the vents in the equipment in use are not obstructed at any time.

12. Ensure the power cable in connected and turned on, and the master power switch at the rear of the required instrument is turned "ON".

13. Use the power button on the front of the required instrument to turn the equipment "ON".

14. The instrument will boot up and begin operating the required software for operation.

Turning OFF the equipment:

15. Press the power button on the front of the instrument.

16. The software running on the instrument will close down and the instrument(s) will power down. DO NOT REMOVE THE POWER UNTIL SHUTDOWN HAS COMPLETED.

17. Turn OFF the power switch on the rear of the instrument and unplug the system.

18. Disconnect the coaxial cables. Store the cables and any other parts in a suitable location.

Key connections:

19. RF In 1/2 : RF source(s)
20. RF Out 1/2 : RF sink(s)

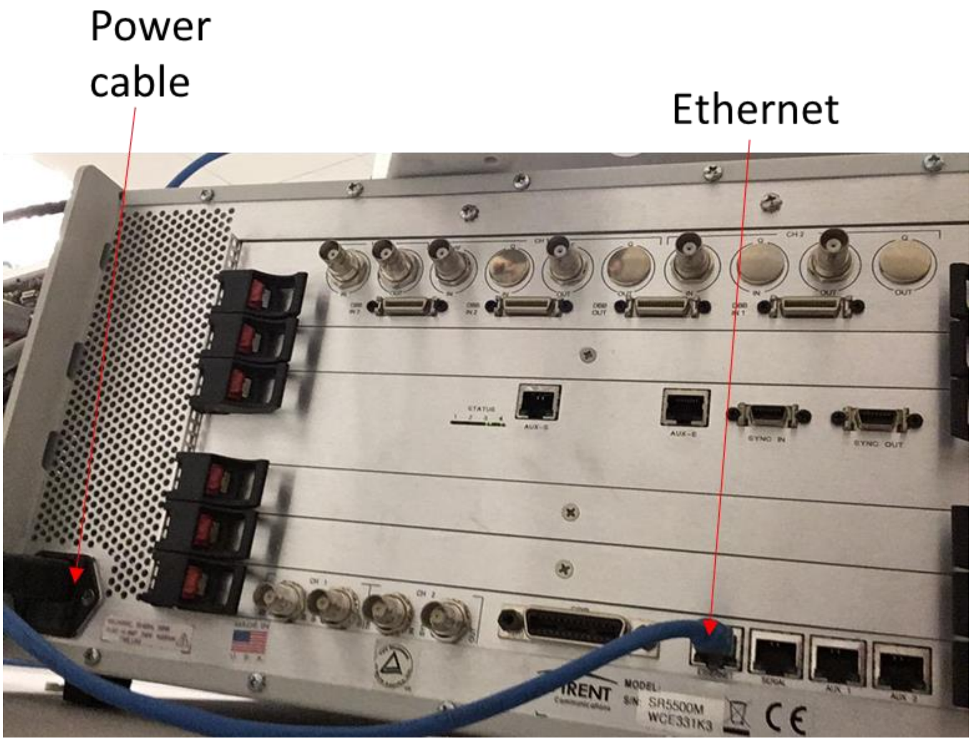

21. Emulator Ethernet : PC Ethernet

Emulator PC Setup for Channel 1 operation:

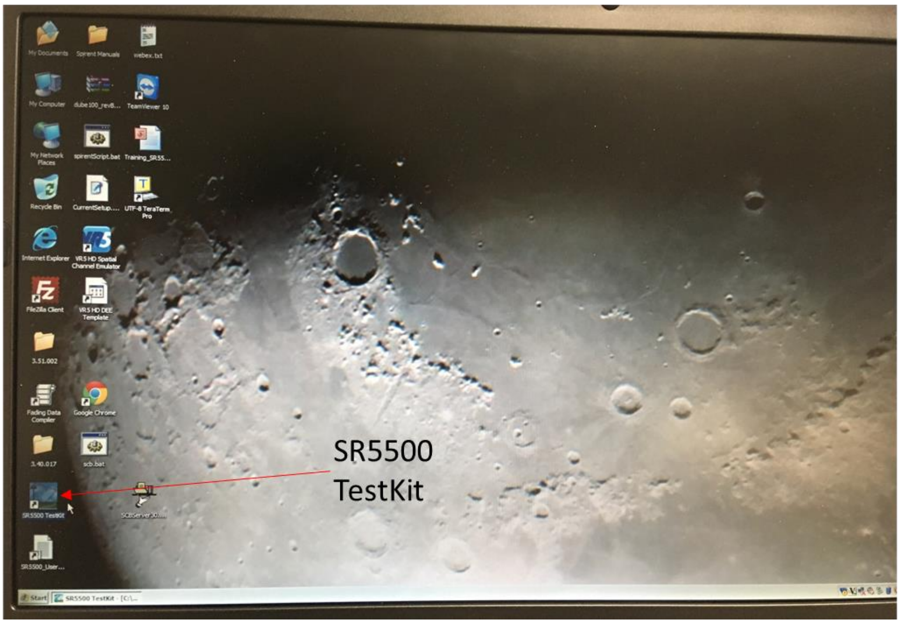

22. On PC, open SR5500 TestKit program

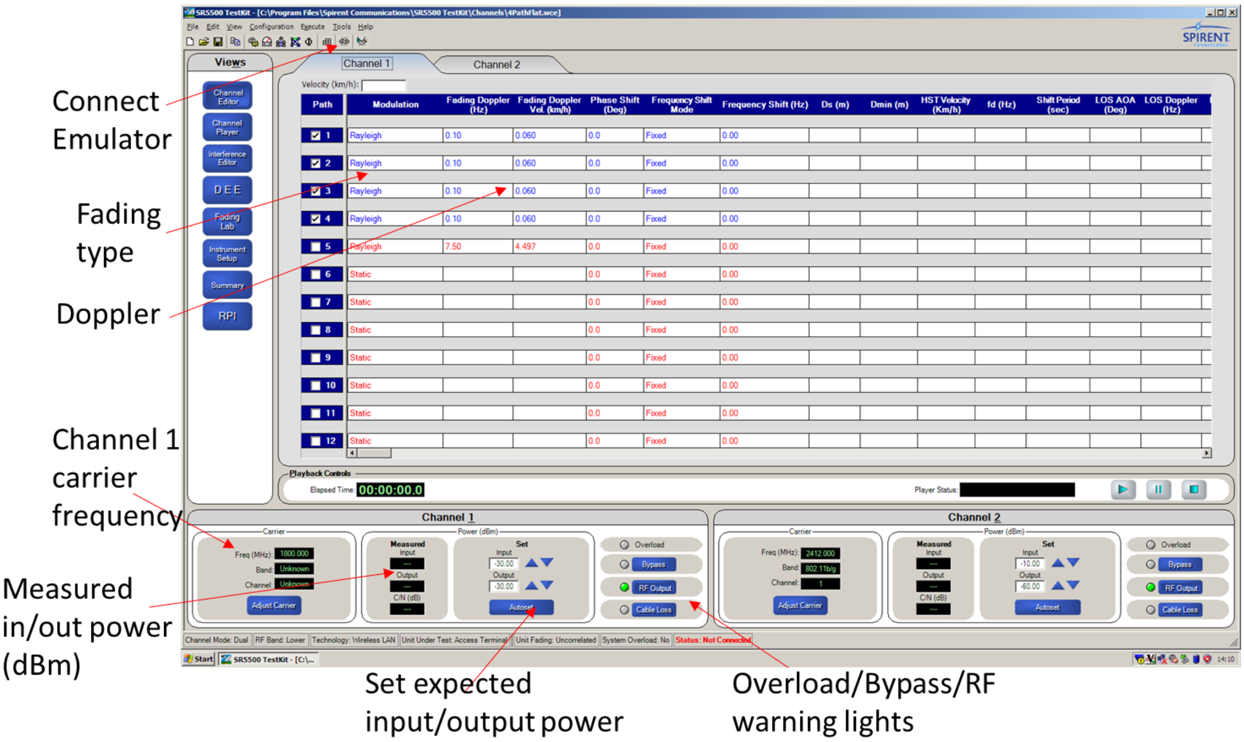

SR5500 TestKit - [C:\Program Files\Spirent Communications\SR5500 TestKit\Channels\4PathFlat.wce]

Velocity (km/h):

Path	Modulation	Fading Doppler (Hz)	Fading Doppler Vel. (km/h)	Phase Shift (Deg)	Frequency Shift Mode	Frequency Shift (Hz)	Ds (m)	Dmin (m)	HST Velocity (Km/h)	fd (Hz)	Shift Period (sec)	LOS AOA (Deg)	LOS Doppler (Hz)
☑ 1	Rayleigh	0.10	0.060	0.0	Fixed	0.00							
☑ 2	Rayleigh	0.10	0.060	0.0	Fixed	0.00							
☑ 3	Rayleigh	0.10	0.060	0.0	Fixed	0.00							
☑ 4	Rayleigh	0.10	0.060	0.0	Fixed	0.00							
☐ 5	Rayleigh	7.50	4.497	0.0	Fixed	0.00							
☐ 6	Static			0.0	Fixed	0.00							
☐ 7	Static			0.0	Fixed	0.00							
☐ 8	Static			0.0	Fixed	0.00							
☐ 9	Static			0.0	Fixed	0.00							
☐ 10	Static			0.0	Fixed	0.00							
☐ 11	Static			0.0	Fixed	0.00							
☐ 12	Static			0.0	Fixed	0.00							

Playback Controls
Elapsed Time: 00:00:00.0
Player Status:

Channel 1
Carrier: Freq (MHz): 1800.000; Band: Unknown; Channel: Unknown
Power (dBm): Measured Input: ---; Output: ---; C/N (dB): ---
Set Input: -30.00; Output: -30.00

Channel 2
Carrier: Freq (MHz): 2412.000; Band: 802.11b/g; Channel: 1
Power (dBm): Measured Input: ---; Output: ---; C/N (dB): ---
Set Input: -10.00; Output: -60.00

Channel Mode: Dual | RF Band: Lower | Technology: Wireless LAN | Unit Under Test: Access Terminal | Unit Fading: Uncorrelated | System Overload: No | Status: Not Connected

23. Click ‘Connect Emulator’ shortcut. Wait while connection established.

24. Check Channel carrier frequency. Click ‘Adjust Carrier’ to alter if necessary.

25. Ensure expected input/output power set to -30/-30: maximum values, no desired loss in system.

26. Check Measured in/out power. Should have readings >-80dBm if RF signal present on input in expected band.

27. If Overload warning light on, turn off RF source and ensure input power -30dBm or lower when next connected.

<u>Key channel definitions:</u>

28. For L desired paths, check L ‘Paths’ checkboxes on left of display.

29. For each path, choose fading type (static, Rayleigh, Rician).

30. For each path, choose Fading Doppler (in Hz or km/h).

31. For each path, choose Delay values in µs. For independently resolvable paths, incremental delay = 1/symbol rate.

32. For each path, choose Relative path loss in dB. For equal average power, all set at 0dB.

33. Press Begin Emulation (‘Play’) to start emulating channel in equipment.

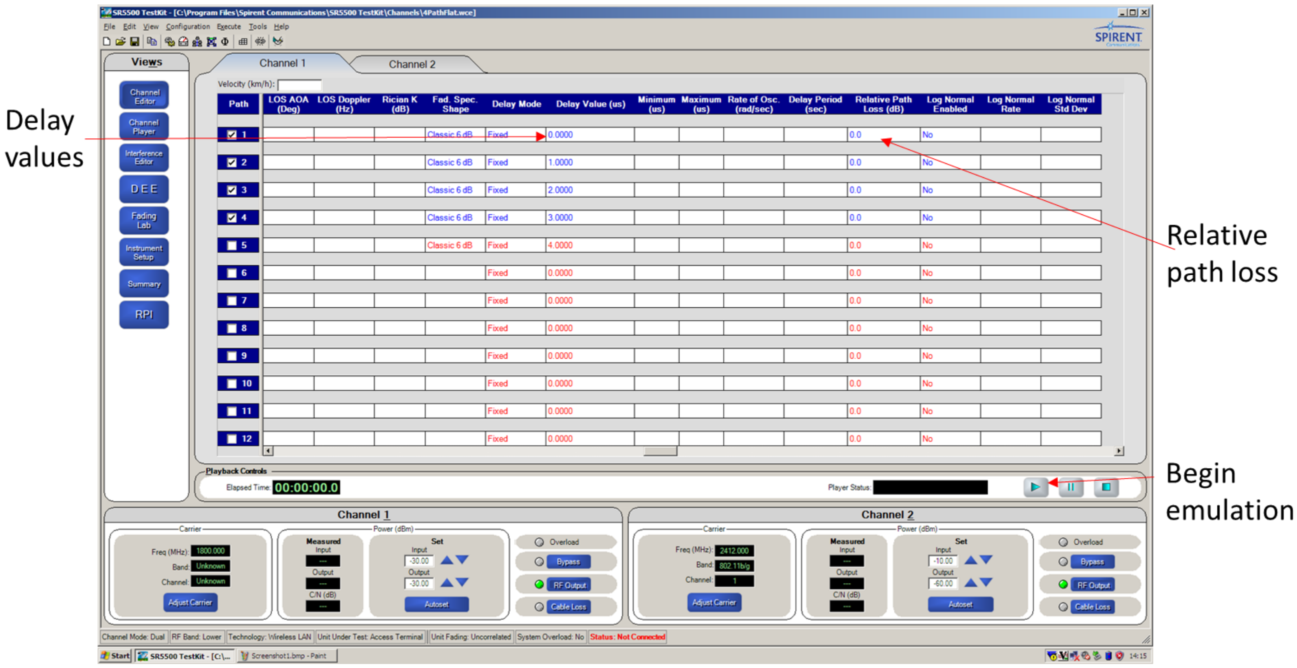

SR5500 TestKit - [C:\Program Files\Spirent Communications\SR5500 TestKit\Channels\4PathFlat.wce]

Velocity (km/h):

Path	LOS AOA (Deg)	LOS Doppler (Hz)	Rician K (dB)	Fad. Spec. Shape	Delay Mode	Delay Value (us)	Minimum (us)	Maximum (us)	Rate of Osc. (rad/sec)	Delay Period (sec)	Relative Path Loss (dB)	Log Normal Enabled	Log Normal Rate	Log Normal Std Dev
☑ 1				Classic 6 dB	Fixed	0.0000					0.0	No		
☑ 2				Classic 6 dB	Fixed	1.0000					0.0	No		
☑ 3				Classic 6 dB	Fixed	2.0000					0.0	No		
☑ 4				Classic 6 dB	Fixed	3.0000					0.0	No		
☐ 5				Classic 6 dB	Fixed	4.0000					0.0	No		
☐ 6					Fixed	0.0000					0.0	No		
☐ 7					Fixed	0.0000					0.0	No		
☐ 8					Fixed	0.0000					0.0	No		
☐ 9					Fixed	0.0000					0.0	No		
☐ 10					Fixed	0.0000					0.0	No		
☐ 11					Fixed	0.0000					0.0	No		
☐ 12					Fixed	0.0000					0.0	No		

Elapsed Time: 00:00:00.0
Player Status:

Channel 1
Carrier: Freq (MHz): 1800.000; Band: Unknown; Channel: Unknown
Power (dBm): Measured Input: ---; Output: ---; C/N (dB): ---; Set Input: -30.00; Output: -30.00

Channel 2
Carrier: Freq (MHz): 2412.000; Band: 802.11b/g; Channel: 1
Power (dBm): Measured Input: ---; Output: ---; C/N (dB): ---; Set Input: -10.00; Output: -60.00

Channel Mode: Dual | RF Band: Lower | Technology: Wireless LAN | Unit Under Test: Access Terminal | Unit Fading: Uncorrelated | System Overload: No | Status: Not Connected

SR5500 TestKit - [C:\... | Screenshot1.bmp - Paint | 14:15

Emergency Procedures:

- Sudden operator illness e.g. stroke or heart attack.
- No other events have been defined as an emergency as a direct use of using this equipment.

34. Call for an ambulance using 999.

35. If anyone has been injured contact 4444 and inform the control room, request an ambulance if the injury is severe.

36. Notify other staff working in the workshop.

37. First aiders should administer appropriate first aid as required until the paramedics arrive.

38. Switch off the equipment at the mains power supply.

6. RESPONSIBILITIES

All EEE staff and students using the NI PXIe Test and Measurements equipment are responsible for adhering to the steps outlined in this SOP as well as the safety precautions outlined in the risk assessment.

Bibliography

[1] Cisco, "Cisco visual networking index: Global mobile data traffic forecast update, 2016–2021 white paper," March 2017. [Online]. Available: https://www.cisco.com/c/en/us/solutions/collateral/service-provider/visual-networking-index-vni/mobile-white-paper-c11-520862.html

[2] IHS, "IoT platforms: Enabling the Internet of Things," March 2016. [Online]. Available: https://cdn.ihs.com/www/pdf/enabling-IOT.pdf

[3] G. A. Akpakwu, B. J. Silva, G. P. Hancke, and A. M. Abu-Mahfouz, "A survey on 5G networks for the Internet of Things: Communication technologies and challenges," *IEEE Access*, vol. 6, pp. 3619–3647, 2018.

[4] M. Agiwal, A. Roy, and N. Saxena, "Next generation 5G wireless networks: A comprehensive survey," *IEEE Communications Surveys & Tutorials*, vol. PP, no. 99, pp. 1–1, 2016.

[5] G. Intelligence, "Understanding 5G: Perspectives on future technological advances in mobile," GSMA, Report, 2014. [Online]. Available: https://www.gsmaintelligence.com/research/?file=141208-5g.pdf&download

[6] C. Dehos, Gonza, x, J. L. lez, A. De Domenico, Kte, D. nas, and L. Dussopt, "Millimeter-wave access and backhauling: the solution to the exponential data traffic increase in 5G mobile communications systems?" *Communications Magazine, IEEE*, vol. 52, no. 9, pp. 88–95, 2014.

[7] T. L. Marzetta, "Massive MIMO: An introduction," *Bell Labs Technical Journal*, vol. 20, pp. 11–22, 2015.

[8] A. H. Jafari and T. O. Farrell, "Performance evaluation of spatial complementary code keying modulation in MIMO systems," in *2015 IEEE 81st Vehicular Technology Conference (VTC Spring)*, Conference Proceedings, pp. 1–5.

[9] R. Y. Mesleh, H. Haas, S. Sinanovic, C. W. Ahn, and S. Yun, "Spatial modulation," *IEEE Transactions on Vehicular Technology*, vol. 57, no. 4, pp. 2228–2241, 2008.

[10] S. Alamouti, “A simple transmit diversity technique for wireless communications,” *Selected Areas in Communications, IEEE Journal on*, vol. 16, no. 8, pp. 1451–1458, 1998.

[11] M. R. Palattella, M. Dohler, A. Grieco, G. Rizzo, J. Torsner, T. Engel, and L. Ladid, “Internet of Things in the 5G era: Enablers, architecture, and business models,” *IEEE Journal on Selected Areas in Communications*, vol. 34, no. 3, pp. 510–527, March 2016.

[12] W. Guo and T. O. Farrell, “Capacity-energy-cost tradeoff in small cell networks,” in *2012 IEEE 75th Vehicular Technology Conference (VTC Spring)*, Conference Proceedings, pp. 1–5.

[13] D. Muirhead, M. A. Imran, and K. Arshad, “A survey of the challenges, opportunities and use of multiple antennas in current and future 5G small cell base stations,” *IEEE Access*, vol. 4, pp. 2952–2964, 2016.

[14] B. Badic, T. O’Farrrell, P. Loskot, and J. He, “Energy efficient radio access architectures for green radio: Large versus small cell size deployment,” in *2009 IEEE 70th Vehicular Technology Conference Fall*, Sep. 2009, pp. 1–5.

[15] S. Wang, W. Guo, and T. O’Farrell, “Energy efficiency evaluation of SISO and MIMO between LTE-femtocells and 802.11n networks,” in *2012 IEEE 75th Vehicular Technology Conference (VTC Spring)*, May 2012, pp. 1–5.

[16] S. D. Keller, W. D. Palmer, and W. T. Joines, “Electromagnetic modeling and simulation of a directly modulated patch antenna,” *Antennas and Wireless Propagation Letters, IEEE*, vol. 9, pp. 779–782, 2010.

[17] A. Babakhani, D. B. Rutledge, and A. Hajimiri, “Near-field direct antenna modulation,” *Microwave Magazine, IEEE*, vol. 10, no. 1, pp. 36–46, 2009.

[18] Z. Jun and X. Xiaowen, “Study of the effect of a finite FSS radome on a horn antenna,” in *Microwave Technology & Computational Electromagnetics (ICMTCE), 2011 IEEE International Conference on*, Conference Proceedings, pp. 74–76.

[19] L. Bin, B. Sanz-Izquierdo, E. A. Parker, and J. C. Batchelor, “A frequency and polarization reconfigurable circularly polarized antenna using active EBG structure for satellite navigation,” *Antennas and Propagation, IEEE Transactions on*, vol. 63, no. 1, pp. 33–40, 2015.

[20] J. Roberts, K. L. Ford, and J. M. Rigelsford, “Secure electromagnetic buildings using slow phase-switching frequency-selective surfaces,” *Antennas and Propagation, IEEE Transactions on*, vol. 64, no. 1, pp. 251–261, 2016.

[21] R. Arvind, S. Nuttapong, and L. Joy, *Modeling and Design Techniques for RF Power Amplifiers.* IEEE, 2008, p. 1. [Online]. Available: http://ieeexplore.ieee.org/document/6130111

[22] S. C. Cripps, *RF Power Amplifiers for Wireless Communications, Second Edition (Artech House Microwave Library (Hardcover)).* Artech House, Inc., 2006.

[23] G. Auer, V. Giannini, C. Desset, I. Godor, P. Skillermark, M. Olsson, M. A. Imran, D. Sabella, M. J. Gonzalez, O. Blume, and A. Fehske, "How much energy is needed to run a wireless network?" *IEEE Wireless Communications*, vol. 18, no. 5, pp. 40–49, 2011.

[24] A. Raghavan, N. Srirattana, and J. Laskar, *Efficiency Enhancement of RF Power Amplifiers.* Wiley-IEEE Press, 2008, pp. 173–198. [Online]. Available: http://ieeexplore.ieee.org/xpl/articleDetails.jsp?arnumber=6130105

[25] A. Augustin, J. Yi, T. Clausen, and W. M. Townsley, "A study of LORA: Long range & low power networks for the Internet of Things," *Sensors (Basel, Switzerland)*, vol. 16, no. 9, p. 1466, 2016. [Online]. Available: http://www.ncbi.nlm.nih.gov/pmc/articles/PMC5038744/

[26] T. J. Myers, "Random phase multiple access system with meshing," US Patent 7773664B2, 2010.

[27] A. Goldsmith, *Spread Spectrum Wireless Communications.* Cambridge University Press, 2005.

[28] D. L. Sengupta and T. K. Sarkar, "Maxwell, Hertz, the Maxwellians, and the early history of electromagnetic waves," *IEEE Antennas and Propagation Magazine*, vol. 45, no. 2, pp. 13–19, 2003.

[29] H. Sungook, *Inventing the Invention of Wireless Telegraphy: Marconi versus Lodge.* MITP, 2014, p. 1. [Online]. Available: http://ieeexplore.ieee.org/document/6940541

[30] J. S. Belrose, "Reginald Aubrey Fessenden and the birth of wireless telephony," *IEEE Antennas and Propagation Magazine*, vol. 44, no. 2, pp. 38–47, 2002.

[31] R. A. Fessenden, "Wireless telephony," *Proceedings of the American Institute of Electrical Engineers*, vol. 27, no. 7, pp. 1283–1358, 1908.

[32] L. de Forest, "Space telegraphy," US Patent 879532, 1908.

[33] L. C. N. de Vreede, R. Gajadharsing, and W. C. E. Neo, “On the bandwidth performance of Doherty amplifiers,” in *2013 IEEE International Wireless Symposium (IWS)*, April 2013, pp. 1–4.

[34] F. H. Raab, P. Asbeck, S. Cripps, P. B. Kenington, Z. B. Popovic, N. Pothecary, J. F. Sevic, and N. O. Sokal, “Power amplifiers and transmitters for RF and microwave,” *IEEE Transactions on Microwave Theory and Techniques*, vol. 50, no. 3, pp. 814–826, March 2002.

[35] I. Tatsuo, H. George, and H. James, *Power Amplifier Approaches for High Efficiency and Linearity.* IEEE, 2001, p. 1. [Online]. Available: http://ieeexplore.ieee.org/document/5236706

[36] C. A. Balanis, *Antenna Theory: Analysis and Design.* USA: Wiley-Interscience, 2005.

[37] V. F. Fusco and C. Qiang, “Direct-signal modulation using a silicon microstrip patch antenna,” *Antennas and Propagation, IEEE Transactions on*, vol. 47, no. 6, pp. 1025–1028, 1999.

[38] Y. Weijun and Y. Wang, “Direct antenna modulation - a promise for ultra-wideband (UWB) transmitting,” in *Microwave Symposium Digest, 2004 IEEE MTT-S International*, vol. 2, Conference Proceedings, pp. 1273–1276 Vol.2.

[39] S. Chang-Sin, P. Jun-Seok, C. Hong-Goo, and J.-B. Lim, “A novel variable-impedance microstrip circuit and its application to direct antenna modulation,” in *Microwave Conference, 2005 European*, vol. 3, Conference Proceedings, p. 4 pp.

[40] S. D. Keller, W. D. Palmer, and W. T. Joines, “Switched antenna circuit with increased information bandwidth,” *IEEE Antennas and Wireless Propagation Letters*, vol. 9, pp. 1045–1048, 2010.

[41] W. Lin, Y. Mengqing, X. Tian, W. T. Joines, and L. Qing Huo, “Broadband electromagnetic radiation modulated by dual memristors,” *Antennas and Wireless Propagation Letters, IEEE*, vol. 10, pp. 623–626, 2011.

[42] S. Srivastava and J. J. Adams, “Analysis of a direct antenna modulation transmitter for wideband OOK with a narrowband antenna,” *IEEE Transactions on Antennas and Propagation*, vol. 65, no. 10, pp. 4971–4979, 2017.

[43] K. Schab and J. Adams, “Calculation of radiation transients in direct antenna modulation systems,” in *2017 IEEE International Symposium on Antennas and Propagation & USNC/URSI National Radio Science Meeting*, Conference Proceedings, pp. 521–522.

[44] M. Salehi and M. Manteghi, “Self-contained compact transmitter for high-rate data transmission,” *Electronics Letters*, vol. 50, no. 4, pp. 316–318, February 2014.

[45] M. Manteghi, “A wideband electrically small transient-state antenna,” *IEEE Transactions on Antennas and Propagation*, vol. 64, no. 4, pp. 1201–1208, 2016.

[46] J. P. Santos, F. Fereidoony, Y. Huang, and Y. E. Wang, “High bandwidth electrically small antennas through BFSK direct antenna modulation,” in *MILCOM 2018 - 2018 IEEE Military Communications Conference (MILCOM)*, Oct 2018, pp. 1–9.

[47] A. Babakhani, D. B. Rutledge, and A. Hajimiri, “Transmitter architectures based on near-field direct antenna modulation,” *Solid-State Circuits, IEEE Journal of*, vol. 43, no. 12, pp. 2674–2692, 2008.

[48] A. H. Chang, A. Babakhani, and A. Hajimiri, “Near-field direct antenna modulation (NFDAM) transmitter at 2.4GHz,” in *Antennas and Propagation Society International Symposium, 2009. APSURSI ’09. IEEE*, Conference Proceedings, pp. 1–4.

[49] J. P. Santos, F. Fereidoony, Y. Huang, and Y. E. Wang, “High bandwidth electrically small antennas through BFSK direct antenna modulation,” in *MILCOM 2018 - 2018 IEEE Military Communications Conference (MILCOM)*, Oct 2018, pp. 1–9.

[50] M. P. Daly and J. T. Bernhard, “Directional modulation technique for phased arrays,” *Antennas and Propagation, IEEE Transactions on*, vol. 57, no. 9, pp. 2633–2640, 2009.

[51] H. Z. Shi and A. Tennant, “An experimental two element array configured for directional antenna modulation,” in *2012 6th European Conference on Antennas and Propagation (EUCAP)*, March 2012, pp. 1624–1626.

[52] S. Hongzhe and A. Tennant, “Simultaneous, multichannel, spatially directive data transmission using direct antenna modulation,” *Antennas and Propagation, IEEE Transactions on*, vol. 62, no. 1, pp. 403–410, 2014.

[53] S. Mufti, J. Parrón, and A. Tennant, “Hardware implementation of directional modulation system with a 2 element antenna array,” in *2017 11th European Conference on Antennas and Propagation (EUCAP)*, March 2017, pp. 3239–3242.

[54] G. I. Kiani, T. S. Bird, and K. L. Ford, “60 GHz ask modulator using switchable FSS,” in *Antennas and Propagation Society International Symposium (APSURSI), 2010 IEEE*, Conference Proceedings, pp. 1–4.

[55] G. I. Kiani, T. S. Bird, and K. Y. Chan, "MEMS enabled frequency selective surface for 60 GHz applications," in *Antennas and Propagation (APSURSI), 2011 IEEE International Symposium on*, Conference Proceedings, pp. 2268–2269.

[56] G. I. Kiani and T. S. Bird, "ASK modulator based on switchable FSS for THz applications," *Radio Science*, vol. 46, no. 02, pp. 1–8, April 2011.

[57] G. D. Bai, J. Zhao, J. C. Ke, J. Y. Dai, N. H. Qi, S. Liu, Q. Cheng, T. J. Cui, X. Yang, X. Li, S. Jin, and A. Alù, "Programmable time-domain digital-coding metasurface for non-linear harmonic manipulation and new wireless communication systems," 11 2018. [Online]. Available: https://doi.org/10.1093/nsr/nwy135

[58] J. Dai, W. Tang, J. Zhao, X. Li, Q. Cheng, J. Chen Ke, M. Zheng Chen, S. Jin, and T. Jun Cui, "Wireless communications through a simplified architecture based on time-domain digital coding metasurface," *Advanced Materials Technologies*, p. 1900044, 02 2019.

[59] W. Tang, "Programmable metasurface-based rf chain-free 8PSK wireless transmitter," *Electronics Letters*, vol. 55, pp. 417–420(3), April 2019. [Online]. Available: https://digital-library.theiet.org/content/journals/10.1049/el.2019.0400

[60] R. C. McPhedran, I. V. Shadrivov, B. T. Kuhlmey, and Y. S. Kivshar, "Metamaterials and metaoptics," *Npg Asia Materials*, vol. 3, p. 100, 2011. [Online]. Available: https://doi.org/10.1038/asiamat.2011.146

[61] E. Nader and R. W. Ziolkowski, "A positive future for double-negative metamaterials," *IEEE Transactions on Microwave Theory and Techniques*, vol. 53, no. 4, pp. 1535–1556, 2005.

[62] C. L. Holloway, E. F. Kuester, J. A. Gordon, J. O. Hara, J. Booth, and D. R. Smith, "An overview of the theory and applications of metasurfaces: The two-dimensional equivalents of metamaterials," *IEEE Antennas and Propagation Magazine*, vol. 54, no. 2, pp. 10–35, 2012.

[63] G. Oliveri, D. H. Werner, and A. Massa, "Reconfigurable electromagnetics through metamaterials—a review," *Proceedings of the IEEE*, vol. 103, no. 7, pp. 1034–1056, 2015.

[64] B. Munk, *Frequency selective surfaces : theory and design.* New York: New York : John Wiley, c2000, 2000.

[65] D. J. Kern, D. H. Werner, A. Monorchio, L. Lanuzza, and M. J. Wilhelm, "The design synthesis of multiband artificial magnetic conductors using high impedance frequency selective surfaces," *IEEE Transactions on Antennas and Propagation*, vol. 53, no. 1, pp. 8–17, 2005.

[66] Y. Fan and Y. Rahmat-Samii, "Reflection phase characterizations of the EBG ground plane for low profile wire antenna applications," *IEEE Transactions on Antennas and Propagation*, vol. 51, no. 10, pp. 2691–2703, 2003.

[67] L. Li, Q. Chen, Q. Yuan, K. Sawaya, T. Maruyama, T. Furuno, and S. Uebayashi, "Frequency selective reflectarray using crossed-dipole elements with square loops for wireless communication applications," *IEEE Transactions on Antennas and Propagation*, vol. 59, no. 1, pp. 89–99, Jan 2011.

[68] G. Wu, S. Qu, Y. Wang, and S. Yang, "Nonuniform FSS-backed reflectarray with synthesized phase and amplitude distribution," *IEEE Transactions on Antennas and Propagation*, vol. 66, no. 12, pp. 6883–6892, Dec 2018.

[69] M. R. Chaharmir, J. Shaker, and H. Legay, "Dual-band Ka/X reflectarray with broadband loop elements," *IET Microwaves, Antennas Propagation*, vol. 4, no. 2, pp. 225–231, Feb 2010.

[70] F. Costa and A. Monorchio, "A frequency selective radome with wideband absorbing properties," *IEEE Transactions on Antennas and Propagation*, vol. 60, no. 6, pp. 2740–2747, 2012.

[71] L. Guo Qing, H. Wei, T. Hong Jun, C. Ji Xin, Y. Xiao Xin, K. Zhen Qi, and W. Ke, "Filtenna consisting of horn antenna and substrate integrated waveguide cavity FSS," *Antennas and Propagation, IEEE Transactions on*, vol. 55, no. 1, pp. 92–98, 2007.

[72] E. A. Parker, *The gentleman's guide to frequency selective surfaces*, 1991.

[73] B. Sanz-Izquierdo, E. A. Parker, J. Robertson, and J. C. Batchelor, "Singly and dual polarized convoluted frequency selective structures," *IEEE Transactions on Antennas and Propagation*, vol. 58, no. 3, pp. 690–696, 2010.

[74] R. J. Langley and E. A. Parker, "Equivalent circuit model for arrays of square loops," *Electronics Letters*, vol. 18, no. 7, pp. 294–296, 1982.

[75] A. Babinet, "Memoires d'optiques meteorologique," *Comptes rendus de l'Academie de Sciences*, vol. 4, pp. 638–648, 1837.

[76] H. G. Booker, "Slot aerials and their relation to complementary wire aerials (Babinet's principle)," *Journal of the Institution of Electrical Engineers - Part IIIA: Radiolocation*, vol. 93, no. 4, pp. 620–626, 1946.

[77] P. Callaghan, E. A. Parker, and R. J. Langley, "Influence of supporting dielectric layers on the transmission properties of frequency selective surfaces," *IEE Proceedings H - Microwaves, Antennas and Propagation*, vol. 138, no. 5, pp. 448–454, 1991.

[78] C. Mias, "Waveguide and free-space demonstration of tunable frequency selective surface," *Electronics Letters*, vol. 39, no. 11, pp. 850–852, 2003.

[79] F. Costa, A. Monorchio, and G. Manara, "Analysis and design of ultra thin electromagnetic absorbers comprising resistively loaded high impedance surfaces," *IEEE Transactions on Antennas and Propagation*, vol. 58, no. 5, pp. 1551–1558, 2010.

[80] L. Zhu and Q. Wang, "Novel ferroelectric polymers for high energy density and low loss dielectrics," *Macromolecules*, vol. 45, no. 7, pp. 2937–2954, 2012. [Online]. Available: https://doi.org/10.1021/ma2024057

[81] K. Fuchi, J. Tang, B. Crowgey, A. R. Diaz, E. J. Rothwell, and R. O. Ouedraogo, "Origami tunable frequency selective surfaces," *IEEE Antennas and Wireless Propagation Letters*, vol. 11, pp. 473–475, 2012.

[82] W. Hu, R. Dickie, R. Cahill, H. Gamble, Y. Ismail, V. Fusco, D. Linton, N. Grant, and S. Rea, "Liquid crystal tunable mm wave frequency selective surface," *IEEE Microwave and Wireless Components Letters*, vol. 17, no. 9, pp. 667–669, 2007.

[83] T. K. Chang, R. J. Langley, and E. Parker, "An active square loop frequency selective surface," *IEEE Microwave and Guided Wave Letters*, vol. 3, no. 10, pp. 387–388, 1993.

[84] M. Haghzadeh, L. M. Bhowmik, C. Armiento, and A. Akyurtlu, "Printed tunable miniaturized frequency selective surface with BST/polymer composite filled interdigital capacitors," in *Radio Science Meeting (Joint with AP-S Symposium), 2014 USNC-URSI*, Conference Proceedings, pp. 154–154.

[85] M. Mavridou, A. P. Feresidis, P. Gardner, and P. S. Hall, "Tunable millimetre-wave phase shifting surfaces using piezoelectric actuators," *IET Microwaves, Antennas Propagation*, vol. 8, no. 11, pp. 829–834, August 2014.

[86] M. Mavridou and A. P. Feresidis, "Dynamically reconfigurable high impedance and frequency selective metasurfaces using piezoelectric actuators," *IEEE Transactions on Antennas and Propagation*, vol. 64, no. 12, pp. 5190–5197, Dec 2016.

[87] S. Rotenberg, M. Poveda-Garcia, J. L. Gomez-Tornero, and C. Mateo-Segura, "Dual-band Ku-band scanning leaky-wave antenna for satellite communications," in *2018 IEEE-APS Topical Conference on Antennas and Propagation in Wireless Communications (APWC)*, Sep. 2018, pp. 810–813.

[88] T. K. Chang, R. J. Langley, and E. A. Parker, "Frequency selective surfaces on biased ferrite substrates," *Electronics Letters*, vol. 30, no. 15, pp. 1193–1194, 1994.

[89] A. C. d. Lima, E. A. Parker, and R. J. Langley, "Tunable frequency selective surface using liquid substrates," *Electronics Letters*, vol. 30, no. 4, pp. 281–282, Feb 1994.

[90] S. Ghosh and S. Lim, "Fluidically reconfigurable multifunctional frequency-selective surface with miniaturization characteristic," *IEEE Transactions on Microwave Theory and Techniques*, vol. 66, no. 8, pp. 3857–3865, Aug 2018.

[91] E. A. Parker and S. B. Savia, "Active frequency selective surfaces with ferroelectric substrates," *IEE Proceedings - Microwaves, Antennas and Propagation*, vol. 148, no. 2, pp. 103–108, April 2001.

[92] G. Meier and A. Saupe, "Dielectric relaxation in nematic liquid crystals," *Molecular Crystals*, vol. 1, no. 4, pp. 515–525, 1966. [Online]. Available: https://doi.org/10.1080/15421406608083290

[93] J. A. Bossard, X. Liang, L. Li, S. Yun, D. H. Werner, B. Weiner, T. S. Mayer, P. F. Cristman, A. Diaz, and I. C. Khoo, "Tunable frequency selective surfaces and negative-zero-positive index metamaterials based on liquid crystals," *IEEE Transactions on Antennas and Propagation*, vol. 56, no. 5, pp. 1308–1320, May 2008.

[94] Y. Zhang, J. Wang, T. Dong, and J. Yin, "A frequency and polarization reconfigurable frequency selective surface based on liquid crystal," in *2018 International Workshop on Antenna Technology (iWAT)*, March 2018, pp. 1–4.

[95] J. R. Reis, N. Copner, A. Hammoudeh, Z. M. E. Al-Daher, R. F. S. Caldeirinha, T. R. Fernandes, and R. Gomes, "FSS-inspired transmitarray for two-dimensional antenna beamsteering," *IEEE Transactions on Antennas and Propagation*, vol. 64, no. 6, pp. 2197–2206, 2016.

[96] T. K. Chang, R. J. Langley, and E. Parker, "An active square loop frequency selective surface," *IEEE Microwave and Guided Wave Letters*, vol. 3, no. 10, pp. 387–388, 1993.

[97] A. Edalati and T. A. Denidni, "High-gain reconfigurable sectoral antenna using an active cylindrical FSS structure," *IEEE Transactions on Antennas and Propagation*, vol. 59, no. 7, pp. 2464–2472, July 2011.

[98] P. S. Taylor, E. A. Parker, and J. C. Batchelor, "An active annular ring frequency selective surface," *IEEE Transactions on Antennas and Propagation*, vol. 59, no. 9, pp. 3265–3271, Sep. 2011.

[99] G. I. Kiani, K. L. Ford, L. G. Olsson, K. P. Esselle, and C. J. Panagamuwa, "Switchable frequency selective surface for reconfigurable electromagnetic architecture of buildings," *IEEE Transactions on Antennas and Propagation*, vol. 58, no. 2, pp. 581–584, Feb 2010.

[100] A. Tennant and B. Chambers, "A single-layer tuneable microwave absorber using an active FSS," *IEEE Microwave and Wireless Components Letters*, vol. 14, no. 1, pp. 46–47, Jan 2004.

[101] K. K. Tantwai, "Microwave-frequency non-linear universal model for PIN diode," in *2007 International Workshop on Physics of Semiconductor Devices*, Dec 2007, pp. 119–122.

[102] C. T. . Nguyen, L. P. B. Katehi, and G. M. Rebeiz, "Micromachined devices for wireless communications," *Proceedings of the IEEE*, vol. 86, no. 8, pp. 1756–1768, Aug 1998.

[103] B. Schoenlinner, A. Abbaspour-Tamijani, L. C. Kempel, and G. M. Rebeiz, "Switchable low-loss RF MEMS Ka-band frequency-selective surface," *IEEE Transactions on Microwave Theory and Techniques*, vol. 52, no. 11, pp. 2474–2481, Nov 2004.

[104] O. Bayraktar, O. A. Civi, and T. Akin, "Beam switching reflectarray monolithically integrated with RF MEMS switches," *IEEE Transactions on Antennas and Propagation*, vol. 60, no. 2, pp. 854–862, 2012.

[105] Y. E. Erdemli, K. Sertel, R. A. Gilbert, D. E. Wright, and J. L. Volakis, "Frequency-selective surfaces to enhance performance of broad-band reconfigurable arrays," *IEEE Transactions on Antennas and Propagation*, vol. 50, no. 12, pp. 1716–1724, Dec 2002.

[106] T. G. S. M. Rijks, J. T. M. v. Beek, P. G. Steeneken, M. J. E. Ulenaers, J. D. Coster, and R. Puers, "RF MEMS tunable capacitors with large tuning ratio," in *17th IEEE International Conference on Micro Electro Mechanical Systems. Maastricht MEMS 2004 Technical Digest*, Conference Proceedings, pp. 777–780.

[107] M. Safari, C. Shafai, and L. Shafai, "X-band tunable frequency selective surface using MEMS capacitive loads," *IEEE Transactions on Antennas and Propagation*, vol. 63, no. 3, pp. 1014–1021, March 2015.

[108] A. Alpaslan and P. Edenhofer, "Electronically tunable frequency selective surfaces," in *Int. Symp. on Electromagnetic Theory, U.R.S.I., Thessaloniki, Greece.*

[109] F. Costa, A. Monorchio, and G. P. Vastante, "Tunable high-impedance surface with a reduced number of varactors," *IEEE Antennas and Wireless Propagation Letters*, vol. 10, pp. 11–13, 2011.

[110] F. Bayatpur and K. Sarabandi, "A tunable metamaterial frequency-selective surface with variable modes of operation," *IEEE Transactions on Microwave Theory and Techniques*, vol. 57, no. 6, pp. 1433–1438, June 2009.

[111] D. Li, T. Li, R. Hao, H. Chen, W. Yin, H. Yu, and E. Li, "A low-profile broadband bandpass frequency selective surface with two rapid band edges for 5G near-field applications," *IEEE Transactions on Electromagnetic Compatibility*, vol. 59, no. 2, pp. 670–676, April 2017.

[112] A. H. Abdelrahman, A. Z. Elsherbeni, and F. Yang, "Transmission phase limit of multilayer frequency-selective surfaces for transmitarray designs," *IEEE Transactions on Antennas and Propagation*, vol. 62, no. 2, pp. 690–697, 2014.

[113] B. Chambers and A. Tennant, "A smart radar absorber based on the phase-switched screen," *IEEE Transactions on Antennas and Propagation*, vol. 53, no. 1, pp. 394–403, Jan 2005.

[114] J. Roberts, K. L. Ford, and J. M. Rigelsford, "Secure electromagnetic buildings using slow phase-switching frequency-selective surfaces," *IEEE Transactions on Antennas and Propagation*, vol. 64, no. 1, 2016.

[115] A. Abdelrahman, F. Yang, A. Elsherbeni, and P. Nayeri, *Analysis and Design of Transmitarray Antennas*, 01 2017, vol. 6.

[116] H. Kaouach, L. Dussopt, J. Lantéri, T. Koleck, and R. Sauleau, "Circularly-polarized discrete lens antennas in the 60-GHz band," in *2010 Conference Proceedings ICECom, 20th International Conference on Applied Electromagnetics and Communications*, Sep. 2010, pp. 1–4.

[117] R. Milne, "Dipole array lens antenna," in *1980 Antennas and Propagation Society International Symposium*, vol. 18, June 1980, pp. 576–579.

[118] S. V. Hum and J. Perruisseau-Carrier, "Reconfigurable reflectarrays and array lenses for dynamic antenna beam control: A review," *IEEE Transactions on Antennas and Propagation*, vol. 62, no. 1, pp. 183–198, Jan 2014.

[119] I. Russo, D. Gaetano, L. Boccia, G. Amendola, and G. Di Massa, "Investigation on the transmission beam-steering capabilities of tunable impedance surfaces," in *2009 European Microwave Conference (EuMC)*, Sep. 2009, pp. 1033–1036.

[120] T. Jiang, Z. Wang, D. Li, J. Pan, B. Zhang, J. Huangfu, Y. Salamin, C. Li, and L. Ran, "Low-DC voltage-controlled steering-antenna radome utilizing tunable active metamaterial," *IEEE Transactions on Microwave Theory and Techniques*, vol. 60, no. 1, pp. 170–178, Jan 2012.

[121] M. Sazegar, Y. Zheng, C. Kohler, H. Maune, M. Nikfalazar, J. R. Binder, and R. Jakoby, "Beam steering transmitarray using tunable frequency selective surface with integrated ferroelectric varactors," *IEEE Transactions on Antennas and Propagation*, vol. 60, no. 12, pp. 5690–5699, Dec 2012.

[122] W. Pan, C. Huang, P. Chen, M. Pu, X. Ma, and X. Luo, "A beam steering horn antenna using active frequency selective surface," *IEEE Transactions on Antennas and Propagation*, vol. 61, no. 12, pp. 6218–6223, Dec 2013.

[123] J. R. Reis, R. F. S. Caldeirinha, A. Hammoudeh, and N. Copner, "Electronically reconfigurable FSS-inspired transmitarray for 2-d beamsteering," *IEEE Transactions on Antennas and Propagation*, vol. 65, no. 9, pp. 4880–4885, Sep. 2017.

[124] T. M. Cover and J. A. Thomas, *Elements of Information Theory.* New York, NY, USA: Wiley-Interscience, 1991.

[125] R. H. Clarke, "A statistical theory of mobile-radio reception," *The Bell System Technical Journal*, vol. 47, no. 6, pp. 957–1000, July 1968.

[126] R. Scholtz, "The origins of spread-spectrum communications," *IEEE Transactions on Communications*, vol. 30, no. 5, pp. 822–854, May 1982.

[127] H. Holma and A. Toskala, *WCDMA for UMTS: HSPA Evolution and LTE.* New York, NY, USA: John Wiley & Sons, Inc., 2007.

[128] F. Adachi, M. Sawahashi, and H. Suda, "Wideband DS-CDMA for next-generation mobile communications systems," *IEEE Communications Magazine*, vol. 36, no. 9, pp. 56–69, Sep. 1998.

[129] N. Y. Yu and G. Gong, "The perfect binary sequence of period 4 for low periodic and aperiodic autocorrelations," in *Proceedings of the 2007 International Conference on Sequences, Subsequences, and Consequences*, ser. SSC'07. Berlin, Heidelberg: Springer-Verlag, 2007, pp. 37–49. [Online]. Available: http://dl.acm.org/citation.cfm?id=1785660.1785664

[130] M. J. Mossinghoff, "Wieferich pairs and barker sequences," *Designs, Codes and Cryptography*, vol. 53, no. 3, pp. 149–163, Dec 2009. [Online]. Available: https://doi.org/10.1007/s10623-009-9301-3

[131] S. W. Golomb, *Shift Register Sequences.* Laguna Hills, CA, USA: Aegean Park Press, 1981.

[132] J. A. Gutierrez, M. Naeve, E. Callaway, M. Bourgeois, V. Mitter, and B. Heile, "IEEE 802.15.4: a developing standard for low-power low-cost wireless personal area networks," *IEEE Network*, vol. 15, no. 5, pp. 12–19, Sep. 2001.

[133] B. E. Benhiba, A. A. Madi, and A. Addaim, "Comparative study of the various new cellular IoT technologies," in *2018 International Conference on Electronics, Control, Optimization and Computer Science (ICECOCS)*, Dec 2018, pp. 1–4.

[134] U. Raza, P. Kulkarni, and M. Sooriyabandara, "Low power wide area networks: An overview," *IEEE Communications Surveys Tutorials*, vol. 19, no. 2, pp. 855–873, Secondquarter 2017.

[135] 3rd Generation Partnership Project, "Technical specification group GSM/EDGE radio access network; cellular system support for ultra-low complexity and low throughput internet of things (CIoT) (release 13)," vol. 1, 11 2015.

[136] 3rd Generation Partnership Project; Technical Specification Group Radio Access Network, "Study on provision of low-cost machine-type communications (MTC) user equipments (UEs) based on LTE (release 12)," vol. 1, 10 2018.

[137] ——, "Evolved universal terrestrial radio access (E-UTRA); NB-IoT; technical report for BS and UE radio transmission and reception," vol. 1, 06 2016.

[138] S. Yi, S. Chun, Y. Lee, S. Park, and S. Jung, *Overview of LTE and LTE-Advanced New Features.* Wiley, 2013. [Online]. Available: https://ieeexplore.ieee.org/document/8043424

[139] C. Fourtet and T. Bailleul, "Method for using a shared frequency resource, method for manufacturing terminals, terminals and telecommunication system," 2013, uS Patent 9049732. [Online]. Available: https://patents.google.com/patent/US9049732B2/en?oq=+9049732

[140] R. Gold, "Optimal binary sequences for spread spectrum multiplexing (corresp.)," *IEEE Transactions on Information Theory*, vol. 13, no. 4, pp. 619–621, October 1967.

[141] Ingenu, *How RPMA Works: The making of RPMA.* Ingenu, 2016.

[142] C. A. Hornbuckle, "Fractional-n synthesized chirp generator," 2008, uS Patent 7791415B2. [Online]. Available: https://patents.google.com/patent/US7791415

[143] B. Reynders and S. Pollin, “Chirp spread spectrum as a modulation technique for long range communication,” in *2016 Symposium on Communications and Vehicular Technologies (SCVT)*, Nov 2016, pp. 1–5.

[144] L. Vangelista, “Frequency shift chirp modulation: The LORA modulation,” *IEEE Signal Processing Letters*, vol. 24, no. 12, pp. 1818–1821, Dec 2017.

[145] S. Solutions, “Design with PIN diodes,” Report, 2012. [Online]. Available: http://www.skyworksinc.com/uploads/documents/Design_With_PIN_Diodes_200312D.pdf

[146] N. Marcuvitz, *Waveguide handbook*. Institution of Electrical Engineers, 1986.

[147] F. Debarros, P. Lemaître-Auger, V. G. de Menezes, Alysson, R. Siragusa, T.-P. Vuong, G. E. P. Tourtollet, and G. Fontgalland, “Characterization of frequency-selective surface spatial filters in a rectangular waveguide,” *International Journal of Microwave and Wireless Technologies*, vol. 4, no. 1, pp. 59–69, 02 2012. [Online]. Available: https://search.proquest.com/docview/920297218?accountid=13828

[148] S. Henthorn, K. L. Ford, and T. O’Farrell, “Frequency selective surface loaded antenna for direct antenna modulation,” in *2017 11th European Conference on Antennas and Propagation (EUCAP)*, March 2017, pp. 731–734.

[149] S. Henthorn, K. L. Ford, and T. O’Farrell, “Bit-error-rate performance of quadrature modulation transmission using reconfigurable frequency selective surfaces,” *IEEE Antennas and Wireless Propagation Letters*, vol. 16, pp. 2038–2041, 2017.

[150] S. Henthorn, L. Ford, and T. O’Farrell, “Direct antenna modulation with frequency selective surfaces,” in *5th Colloquium on Antennas, Wireless and Electromagnetics (CAWE 2017)*, June 2017, pp. 1–16.

[151] V. S. Alliance, “Visa specifications,” Report, 1995. [Online]. Available: http://www.ivifoundation.org/specifications/default.aspx

[152] S. Henthorn, K. L. Ford, and T. O’Farrell, “A low-loss reconfigurable frequency selective surface based antenna for direct antenna modulation,” in *Loughborough Antennas Propagation Conference (LAPC 2017)*, Nov 2017, pp. 1–4.

[153] T. Instruments, “LM7171 very high speed, high output current, voltage feedback amplifier,” Report, 2014. [Online]. Available: http://www.ti.com/lit/ds/symlink/lm7171.pdf

[154] A. Al-Fuqaha, M. Guizani, M. Mohammadi, M. Aledhari, and M. Ayyash, "Internet of Things: A survey on enabling technologies, protocols, and applications," *IEEE Communications Surveys Tutorials*, vol. 17, no. 4, pp. 2347–2376, Fourthquarter 2015.

[155] B. Muquet, Zhengdao Wang, G. B. Giannakis, M. de Courville, and P. Duhamel, "Cyclic prefixing or zero padding for wireless multicarrier transmissions?" *IEEE Transactions on Communications*, vol. 50, no. 12, pp. 2136–2148, Dec 2002.

[156] J. Proakis, *Digital Communications*, ser. McGraw-Hill series in electrical and computer engineering : communications and signal processing. McGraw-Hill, 2001. [Online]. Available: https://books.google.co.uk/books?id=aUp2QgAACAAJ

[157] D. Tse and P. Viswanath, *Fundamentals of Wireless Communication.* Cambridge University Press, 2005.

[158] M. A. Sedaghat, R. R. Mueller, and G. Fischer, "A novel single-RF transmitter for massive MIMO," in *Smart Antennas (WSA), 2014 18th International ITG Workshop on*, Conference Proceedings, pp. 1–8.

[159] E. G. Larsson, O. Edfors, F. Tufvesson, and T. L. Marzetta, "Massive MIMO for next generation wireless systems," *IEEE Communications Magazine*, vol. 52, no. 2, pp. 186–195, 2014.

[160] S. Henthorn, K. L. Ford, and T. O'Farrell, "A low-complexity array of directly phase modulating antennas," in *12th European Conference on Antennas and Propagation (EuCAP 2018)*, April 2018, pp. 1–4.

[161] F. Wiffen, M. Z. Bocus, A. Doufexi, and A. Nix, "Phase-only OFDM communication for downlink massive MIMO systems," in *2018 IEEE 87th Vehicular Technology Conference (VTC Spring)*, June 2018, pp. 1–5.

[162] N. Rostomyan, M. Özen, and P. Asbeck, "28 GHz doherty power amplifier in CMOS SoI with 28% back-off PAE," *IEEE Microwave and Wireless Components Letters*, vol. 28, no. 5, pp. 446–448, May 2018.

[163] R. Sivaswamy, "Multiphase complementary codes," *IEEE Transactions on Information Theory*, vol. 24, no. 5, pp. 546–552, Sep. 1978.

[164] D. Chu, "Polyphase codes with good periodic correlation properties (corresp.)," *IEEE Transactions on Information Theory*, vol. 18, no. 4, pp. 531–532, July 1972.

[165] R. Frank, "Polyphase codes with good nonperiodic correlation properties," *IEEE Transactions on Information Theory*, vol. 9, no. 1, pp. 43–45, January 1963.